Investigation of the evolution of dark clouds

THESIS SUBMITTED TO THE UNIVERSITY OF DELHI

for the degree of

DOCTOR OF PHILOSOPHY

By

Ekta Sharma

Department of Physics & Astrophysics

University of Delhi

Delhi-110 007

November 2020

Dedicated to

My Parents & Family

"....he warned me against getting too deeply involved with dark nebulae and their problems. He indicated to me that it would have been wiser if I had avoided the dark nebulae. He suggested that it might have been better to concentrate on the regions in between dark clouds where one can explore the fine structure of our Galaxy more directly than in regions in which one is bothered by obscuring nebulosity. I hope to show you tonight that it has proved very useful to have paid attention to the dark nebulae, which have a very special place of their own in the study of our home galaxy, the Milky Way System."

–Bok 1977

Department of Physics and Astrophysics
University of Delhi
Delhi-110007, India

Date : _____

Declaration

It is certified that the work presented in this thesis entitled **"Investigation of the evolution of dark clouds"** has been carried out by **Ekta Sharma** during his tenure as Ph.D. student at the Department of Physics and Astrophysics, University of Delhi, Delhi, India under the supervision of Prof. T. R. Seshadri and Prof. Maheswar Gopinathan. The work reported in this thesis is original and it has not been submitted earlier for any degree to any University or Institute.

Candidate: _____

Ekta Sharma

Supervisor: _____

Prof. T.R. Seshadri

Co – Supervisor : _____

Prof. Maheswar Gopinathan

Head of the Department: _____

Prof. Brajesh Choudhary

Department of Physics and Astrophysics
University of Delhi
Delhi-110007, India

Date : _____

Certificate of Originality

This is to certify that the work incorporated in this thesis entitled **"Investigation of the evolution of dark clouds"** has been carried out by me at the **Department of Physics and Astrophysics**, University of Delhi, Delhi, India. The work has been subjected to plagiarism check by **Urkund** software. The work submitted for consideration of award of Ph.D. is original.

Candidate: _____

Ekta Sharma

Supervisor: _____

Prof. T.R. Seshadri

Co – Supervisor : _____

Prof. Maheswar Gopinathan

Head of the Department: _____

Prof. Brajesh Choudhary

P[1]>p1 M[1]>m1

Student Approval Form

Name of the Author	**Ekta Sharma**
Department	Department of Physics and Astrophysics
Degree	Doctor of Philosophy
University	University of Delhi
Supervisor	Prof. T. R. Seshadri
Co-Supervisor	Prof. Maheswar Gopinathan
Thesis Title	Investigation of the evolution of dark clouds
Year of Award	

Agreement

1. I hereby certify that if appropriate, I have obtained and attached hereto a written permission/statement from the owner(s) of each third party copyrighted matter to be included in my thesis/dissertation, allowing distribution as specified below.

2. I hereby grant to the university and its agents the non-exclusive license to archive and make accessible, under the conditions specified below, my thesis/dissertation, in whole or in part in all forms of media, now or hereafter known. I retain all other ownership rights to the copyright of the thesis/dissertation. I also retain the right to use in future works (such as articles or books) all or part of this thesis, dissertation, or project report.

Conditions:

1. Release the entire work for access worldwide
2. Release the entire work for 'My University' only for 1 Year 2 Year 3 Year and after this time release the work for access worldwide.
3. Release the entire work for 'My University' only while at the same time releasing the

following parts of the work (e.g. because other parts relate to publications) for worldwide access. (a) Bibliographic details and Synopsis only (b) Bibliographic details, synopsis and the following chapters only. (c) Preview/Table of Contents/24 page only.
4. View Only (No Downloads) (worldwide)

Signature of the Scholar (Signature and seal of the Guide)

Co – Supervisor : _____

Prof. Maheswar Gopinathan
(Signature of the Co-Guide)

Place: _____

List of Publications

Publications in refereed journal

1. Distance, magnetic field, and kinematics of the filamentary cloud LDN 1157 **Sharma Ekta**; Gopinathan M.; Soam A.; Lee C.W.; Kim S.; Ghosh T.; Kim G.; Sharma N and Saha P. , 2020, **A&A** 639, A133 **(Impact factor : 5.7)**

2. A census of young stellar population associated with the Herbig Be star HD 200775 Saha P., Gopinathan M., Kamath U., Lee C.W., Purvankara M., Mathew B. And **Sharma Ekta**, 2020, **MNRAS**, 494, 4 **(Impact factor : 5.35)**

3. First Sub-pc Scale Mapping of Magnetic Fields in the Vicinity of a Very Low Luminosity Object, L1521F-IRS arXiv:1908.01018

   Archana Soam, Chan Won Lee, B-G Andersson, Maheswar Gopinathan, Mika Juvela, Tie Liu, Gwanjeong Kim, Ramprasad Rao, Eun Jung Chung, Woojin Kwon, **Ekta Sharma**, 2018, **ApJ**, 883, 9S **(impact factor : 5.7)**

4. *Tracing the magnetic field morphology of LDN 1172/1174 cloud complex*
   Piyali Saha, Maheswar G., **Ekta Sharma**, Chang Won Lee, Tuhin Ghosh and Kim, Shinyoung, 2020, **submitted in A&A (Impact factor : 5.7)**

To be submitted

1. Cloud motion and Magnetic fields: Four clouds in Cepheus Flare region
   Ekta Sharma, Maheswar Gopinathan, Sami Dib (2020) to be submitted in A&A

2. Dynamical state of gas surrounding HD 200775 (To be submitted)
   Ekta Sharma, Maheswar Gopinathan, Piyali Saha, Shinyoung Kim, Chang W. Lee (2020), to be submitted in A&A

List of talks/poster presentations in Conferences

- Astronomical Society of India 2016 held in Kashmir (Srinagar) from 10-14th May 2016 (Poster)
- Star and Planet Formation (SPF-2017) held in IIST, Trivandrum from 5-8th December 2016 (Talk and Poster)
- First Belgo-Indian Network for Astronomy astrophysics (BINA) workshop, held in Nainital (India), 15-18 November 2016. (Talk and Poster)
- ARIES training school in Observational Astronomy (ATSOA)- 2017 (Talk)
- Astronomical Society of India (ASI) 2019, held from 16-19th February 2019 in Bangalore (Talk)
- Star Formation in Different Environments (SFDE) in Vietnam from 6th August-10th August 2017 (Talk)
- Zooming in to Star formartion held in Napflio, Greece from 10-14th June 2019 (Poster)
- Young Astronomers' Meet (YAM) 2019, held in Kodaikanal Solar Observatory, IIA (Talk and Poster)

Conferences and Workshops attended

- Radio Astronomy School (RAS) 2017 in NCRA-TIFR.
- 10th international workshop on H1 studies -PHISCC 2017 held in NCRA-TIFR, Pune from 5-11th February 2017.

ACKNOWLEDGMENTS

The milestone of finishing a PhD is incomplete without paying gratitude to all those who have supported me in any possible way. I feel extremely fortunate to have had the guidance and support of so many people during my tenure of doing a PhD.

First of all, I would like to thank Almighty God for showering his blessings on me in making me capable to finish my thesis. I owe my deepest gratitude to Prof. Maheswar Gopinathan for enlightening me to the first phase of research and for being a very supportive mentor throughout the years of my PhD. His calm demeanour has been immeasurably helpful during the stressful times, and he has been a pleasure to work with. His brilliant ideas about any given topic and approach for encouraging me to go beyond the problems is something I always look forward to.

It is my great pleasure to acknowledge my sincere thanks to my supervisor Prof. T.R. Seshadri (Sesh) who has been a incredible support in all difficult times. I really get inspired by his holistic approach he takes in guiding his students. The submission of thesis would not have been possible without his tireless and continuous efforts.

I am sincerely thankful to Prof. Chang Won Lee with whom I had the pleasure of collaborating in my research work. His deep knowledge about the subject of Radio Astronomy and his constant feedback on my molecular line work has helped me a lot in growing my knowledge about the subject. I also highly grateful to Shinyoung Kim without whom I could not have completed my radio observations. I also owe thanks to Prof. Anandmayee Tej from IIST, Trivandrum for a fruitful discussion on far-infrared data analysis. I also wish to acknowledge Tuhin Ghosh for assisting me in Planck data analysis. I would also like to acknowledge Rekhesh Mohan for useful discussions on GMRT observations.

I also convey my thanks to the Director Prof Annapurni Subramaniam, IIA for giving me the opportunity and the facilities to finish my research. I am really thankful to the whole staff of 104 cm Sampurnanand telescope for being very helpful during the observations. Special thanks to Ashok Kumar Singh ji and Dr. Biman for always being ready in any assistance. I also wish to acknowledge the staff at CREST, IAO for their supportive role in observations.

Friends have been an integral part of my PhD life. I am really grateful to the constant support I got from many good people. Thanks to the girls gang Priyanka, Prerna, Priya for a family at IIA. I also thank Panini, Ritesh and Manoj for being available for any help in IIA. I thank Ambily and Priyanka Jalan for being very supportive roommates. I also convey my special thanks to all my seniors Archana Soam, Neha Sharma, Piyush, Suvendu, Mukesh, Mridweeka who has taught me many things academically and non-academically. I thank all my fellow friends Anjasha, Pankaj, Raya, Piyali, Kuldeep, Sapna and Vineet.

I would like to convey special thanks to my friends Aakanksha and Ashwani Pandey for being an all time listener in all thick and thins of my life. I also thank Asaj and Saikant for being available always during the course of thesis wrirting.

I convey my thanks to all the members at IRC: Sunil, Ram, Nidhi, Bidhisha, Arun in Delhi University for always being so welcoming and helping out for any administration process. A special thanks to Sandhya, Sapna and Raya for guiding me in the official work of my thesis submission. I thank all the staff at Department of Physics for their help in getting administrative things finished.

Last but not least definitely, a thankyou is very small word to express the gratitude towards my parents. Being there always like a pillar and believing me has always given me a boost to look forward to and keep working hard. I could not have finished the thesis without their unconditional love and encouragement. I express my deep gratitude to my sister and brother-in-law for full-times source of motivation and tolerating me during thesis writing. A special thanks to my younger sister, Surbhi for going through all the chapters of my thesis at the last moment.

I may have missed mentioning some people here, but I whole-heartedly owe my gratitude to all those who have contributed in completing this journey.

−Ekta

Abstract

Stars form in the densest regions of molecular clouds which are actually gravitationally unstable cores that resides at the junction of filaments. Before the onset of the gravitational collapse in cores, the build up of filaments and further substructures takes place. The formation of dense cores and the filaments is a crucial step in the star formation process. The question involving how the diffuse gas transforms to dense regions decides the star formation rate and the mass distribution of stars in molecular clouds. The association of cores with the filaments which turn into cores indicates that the filaments play a central role in the process of forming stars. However, even with a plethora of observational and theoretical information available, the role of turbulence, self-gravity and magnetic fields in the formation of filamentary structures is still a debated topic. Understanding the connection of the molecular cloud structure with its formation mechanism is crucial in knowing the intricacies of star formation process.

In this thesis, we investigated the characteristics, dynamics, and the global evolution of filamentary structures formed in two different scenarios either by isolated star formation or triggered star formation. In order to characterise observationally the process of filament and dense core formation with different physical effects in molecular clouds, we studied two regions in detail, L1172/L1174 and L1157/L1158. These regions are located in Cepheus constellation at higher galactic latitude. The striking difference between the ongoing star formation activity in both the regions makes them the favourable testbeds for studying the filaments formation in isolated or clustered sites. We studied each of these regions by means of large-scale molecular line observations in the range of millimeter or sub-millimetre wavelengths by choosing tracers sensitive to different density structures in clouds. The results were complimented with the dust continuum emissions. We first extracted the filaments and cores using and estimated their geometric properties and further estimated the detailed velocity structure of all the filaments and cores. The large scale magnetic field morphology was inferred either from ground based optical polarization or from the *Planck* polarization maps.

One part of the regions studied, L1172/L1174 resembles the hub-filament morphology. The presence of intermediate mass star can significantly influence the surrounding gas by interaction of stellar winds with the neutral molecular cloud. Our detailed characterization of the gas kinematics of filaments and cores around massive star showed the presence of high velocity gas is affecting the high density gas. The gas show spectral signatures of expansion or contraction through blue or red-skewed profiles. We further explored the origin behind the hub-filament morphology of L1172/L1174 complex

by studying the physical conditions of high density gas and its comparison with the dust emission in the long filament associated to the complex. Our results reveal the presence of velocity gradients which may be responsible for the accretion of gas towards the high massive core. Based on the correlation of magnetic field lines with the filament orientation, the same is found to be dynamically important for the morphology of the filament.

To understand the physical state of gas in the filaments and the cores in L1147/L1158 complex which is in close proximity to L1172/L1174 and share similar radial velocity and distances but low star formation efficiency, we studied the molecular line mapping of the whole region at 0.1 km s^{-1}spectral resolution. The velocity structure of each of the filament was investigated in detail. The kinematical information on both the complexes will help in understanding the difference in star formation activity and testing various theories of turbulent magnetized medium. The large scale gas dynamics in both the complexes suggest that the filaments indeed preserve the initial condition of star formation.

The next part of the thesis explores the importance of motion of the cloud with the respect the magnetic fields. We also studied the distribution of core orientation over a sample of molecular clouds which builds up a link between cloud-scale magnetic field and core orientation. We established the distribution of offsets between core orientation and motion of the complexes in the galaxy. We also studied a set of nearby clouds with asymmetric dust emission using magnetic fields using starlight polarization and the thermal dust emission using *Planck* and the relative orientation of cores with the magnetic fields.

NOTATIONS AND ABBREVIATIONS

The most commonly used notations and abbreviations in the thesis are given below. If a symbol has been used in a different connection than listed here, it has been explained at the appropriate place.

Notations

Å	Angstrom
α, RA	Right Ascension
A_V	Visual extinction
d	Distance to the star/cluster from earth in parsec (pc)
$^\circ$, deg	Degree
δ, Dec	Declination
I_e, I_o	Extraordinary and ordinary intensities
I_{pol}, I_{unpol}	Polarized and unpolarized intensities
$J2000$	Epoch of observation
Jy	Jansky
K	Wdth parameter
kpc	Kiloparsec(unit of distance)
λ	Wavelength
λ_{max}	Wavelength at which maximum polarization observed
l, b	Galactic longitude and latitude
$M_\odot$	Mass of the Sun
Myr	Million Years
pc	Parsec (unit of distance)
$'$, arcmin	Arc minute
$''$, arcsec	Arc second
P_{max}	Maximum polarization corresponds to λ_{max}
Q_{ext}	Extinction efficiency factor
mG	Milli Gauss
μG	Micro Gauss
μm	Micro meter
$M_\star$, $T_\star$	Mass and Temperature of a star
$n(H), n(H_2)$	H, H_2 column density
$P_{BVRIJHK}$	Polarization in B, V, R, I, J, H, and K-bands
$\rho(r)$	Stellar surface density as a function of radius
Q_{BVRI}	Stoke parameter 'Q' in B, V, R, and I-bands
q_{fg}, u_{fg}	Normalized Stokes parameters for the foreground
q, u, q_1, u_1	Normalized Stokes parameters at four positions of HWP

R_V	Ratio of total to selective extinction
$\sigma_{P_{BVRIJHK}}$	Uncertainty in the polarization in B, V, R, I, J, H, and K-bands
$\sigma_{\theta_{BVRIJHK}}$	Uncertainty in the polarization angle in B, V, R, I, J, H, and K-bands
sr	Steradian
$\theta_{BVRIJHK}$	Polarization position angle in B, V, R, I, J, H, and K-bands
τ	Optical depth
V_{LSR}	Velocity of observer relative to local standard of rest
X	Air mass
yr	Year/Years
Z	Solar metallicity

Abbreviations

ADF	Angular Dispersion Function
AIMPOL	ARIES IMaging POLarimeter
ALMA	Atacama Large Millimeter Array
ARIES	Aryabhatta Research Institute of observational SciencES
Be	Berkeley
BRC	Bright Rimmed Cloud
CB	Clemens & Barvainis
CCD	Charge-Couple Device
CLASS	Continuum and Line Analysis Single Dish Software
CMD	Color-Magnitude Diagram
DSS	Digitized Sky Survey
EUV	Extreme Ultraviolet
ESO	European Southern Observatory
FIR	Far Infrared
FUV	Far Ultraviolet
FWHM	Full Width at Half Maximum
GAIA	Global Astrometric Interferometer for Astrophysics
GHz	Giga Hertz
GMCs	Giant Molecular Clouds
GP	Galactic Parallel
M/L	Mass per unit length
HGBS	Herschel Gould Belt Survey

HWP	Half Wave Plate
IAO	Indian Astronomical Observatory
IBL	Ionized Boundary Layer
IC	Index Catalogue
ICM	Intra Cluster Medium
IF	Ionization Front
IIA	Indian Institute of Astrophysics
IMF	Initial Mass Function
IR	Infra-Red
IRAC	Infra Red Array Camera
IRAF	Image Reduction and Analysis Facility
IRAS	Infrared Astronomical Satellite
IRS	Infrared Spectrograph
IRSF	Infra-Red Survey Facility
ISM	Interstellar Matter/Medium
K-S	Kolmogorov-Smirnov
LDN	Lynd's Dark Nebula
LOSFR	Lambda-Orinis Star Forming Region
LTE	Local Thermodynamic Equilibrium
mag	magnitude (stellar)
MF	Mass Function
MIR	Mid-infrared
Myr	Million year
NGC	New General Catalogue
OTF	On-The-Fly
PAH	Polycyclic Aromatic Hydrocarbons
PDR	Photo Dissociation Region
PLW	Photometer Long Wavelength Array
PMS	Pre-Main Sequence
PSW	Photometer Short Wavelength Array
PSF	Point Spread Function
RDI	Radiation Driven Implosion
RGB	Red Green Blue
SED	Spectral Energy Distribution
SEQUOIA	SEcond QUabbin Observatory Imaging Array
SFR	Star Forming Region
SIMBAD	Set of Identifications, Measurements, and Bibliography for Astronomical Data
SMA	Sub-millimeter Array

SSC	*Spitzer* Science Center
ST	Sampurnanand Telescope
TRAO	Taeduk Radio Astronomy Observatory
TTS	T Tauri Star
UV	Ultraviolet
WDP	Wavelength Dependent polarization
WISE	Wide-field Infrared Survey Explorer
YSO	Young Stellar Object

Table of contents

List of figures

List of tables

Chapter 1

INTRODUCTION

1.1 The interstellar medium

Stars are the homes for planetary systems and provide the necessary energy for maintenance of life. Stellar evolution is central to the processes in star clusters in galaxies. Stars also maintain the chemical evolution and the energy budget of the Universe. Knowledge of the physical mechanism for the formation of stars is essential for understanding the evolution of the galaxies and the universe from the earliest times after the Big Bang to the current epoch of cosmic history. Therefore, understanding star formation or the origin of the stars is one of the most important processes in understanding galaxy formation and its evolution.

Field et al. (1969) suggested a two-phase structure of the interstellar medium (ISM) if the atomic gas HI is in thermal equilibrium. One of the phases is cold dense phase termed as Cold Neutral Medium (CNM) and the other is the warm diffuse medium defined as Warm Neutral Medium (WNM). McKee & Ostriker (1977) extended the model stating that there is another Hot Ionized Medium (HIM) where the gas cools very slowly possessing a temperature of 10^6 K. The energy and momentum injected by Supernovae explosions would create large, ionized bubbles which gets filled with very hot gas. Simulations suggest that the formation and evolution of the molecular clouds involve two step process. The cold neutral medium (CNM) is constituted by neutral hydrogen (HI) atom. When the molecularization happens from atomic hydrogen to molecular hydrogen, that is defined as Molecular Clouds (MCs). They are the nurseries where the diffuse gas transforms to the high density gas, thereby, forming stars. Understanding star formation (SF) in turn depends on the deep understanding of the structure, formation, dynamics and evolution of molecular clouds. MCs are the densest, darkest and coldest regions of the ISM. The physical conditions favourable for the formation of molecules are found in the *molecular clouds*, and hence the name. These clouds are made up of molecules of Hydrogen, Helium and trace gases with their mass fraction 78%, 20% and 2%, respectively.

Molecular clouds possess typical temperatures of 10-20 K and span a range of sizes between $\sim$ 1 pc and $\sim$ 200 pc. A fractal nature of MCs has been suggested by Elmegreen & Scalo (2004) where

there exists an inherent hierarchy at each spatial scale of the cloud. Small and dense structures are found at each scale which can be catalogued on the basis of their masses and sizes as:

- giant molecular clouds (GMCs) with masses above 10^5 M$\odot$ and sizes $\sim$ 30 pc and up to 100-200 pc.
- MCs, with mass range of 10^2 to 10^4 M$\odot$ and sizes of about 10-20 pc.
- clumps, with mass range of 10-10^2 M$\odot$ and sizes of few pcs.
- cores, with masses below few 10 M$\odot$ and sizes of 0.1 pc or less. (Blitz, 1993; Heyer & Dame, 2015). They are the smallest possible relevant scales at which stars are forming.

Current understanding of star formation:

How is the star formation rate determined by the larger scale ISM in the Galaxy? What determines the mass distribution of the stars? Is it the Initial Mass Function (IMF) or the Core Mass Function (CMF)? How do stars form in the dense environments where the feedback from the massive stars or young stellar objects affect the gas?

The IMF suggests that there can be low as well as high mass stars that can be formed from the molecular clouds. There are two competing scenarios for the massive star formation. They can be the scaled up version of low-mass stars (Shu et al., 1987) where the mass of the formed star is determined by the mass of the cloud core which has collapse under the effect of self-gravity. The other possibility could be that the mass of the stars is affected by the environment through competitive accretion or mergers in clusters.

1.2 Modes of star formation: Spontaneous and Triggered star formation

While there are multiple processes that can cause the gas to become gravitationally unstable and collapse, it is believed to have two possible paradigms of star formation: *Spontaneous star formation* and *Triggered star formation*.

1.2.1 Spontaneous Star formation

In this mode, the regions which can possibly collapse are caused by the overdensities due to the natural turbulent gas motions. It is also called as *Stochastic* star formation. The dissipation of energies is responsible for the collapse of the material in the cores. The energy dissipation time for the large-scale turbulence is of the order of 10^6 yr which is comparable to the free fall time scale (Offner et al., 2008; Stone et al., 1998). The collapse will happen in such a way that the time scale for spontaneous star formation is the dissipation time scale or ambipolar diffusion time scale or free-fall time scale.

This is the slowest step in the star formation. The spontaneous star formation is further categorised in two scenarios: magnetically dominated and turbulence dominated star formation scenarios. In magnetically dominated star formation, a slow quasistatic evolution of the core takes place where it becomes more centrally condensed by ambipolar diffusion with a time scale of 10^7 year. The time scale of diffusion is higher than the free fall time scale where the evolution becomes quasi-static. The dynamics of the core becomes magnetically supported (McKee et al., 1993; Mouschovias, 1991; Mouschovias & Ciolek, 1999; Nakano, 1984) and the centrally condensed material flattens along the field lines under the effect of increasing density. The cloud core eventually collapse when the self-gravity dominates over the magnetic support near the center. The central density of the cloud core corresponding to the collapse is typically $\sim 10^5$-10^6 cm^{-3}, which is similar to the volume density of prestellar cores (Ciolek & Basu, 2000).

On contrary to the above scenario, Nakano (1998) stated that the magnetic pressure through the ambipolar diffusion model may not be sufficient to stabilise the cloud against gravity if the fields are not strong enough. This points to the turbulent dominated star formation where the support of the molecular clouds is attributed to the random supersonic motions in them which is responsible for the low star formation efficiencies and the relatively long lifetime of the clouds higher by an order of free-fall time. The presence of broad line-widths implies the turbulent supersonic motion in the clouds. Klessen et al. (2000) has studied the dissipation of turbulence as a stage where the dynamical collapse will start taking place. These two scenarios are two competing approaches to explain the star formation theory.

1.2.2 Triggered star formation

The feedback processes can be of two types: positive feedback or negative feedback. The former is related to the creation of local density enhancements which could be triggered by several external factors like supernova explosions, stellar feedback. Once the collapse is initiated, it is expected to follow the same path as in the case of spontaneous star formation. If the external agents are responsible for dispersing the ambient material, it is considered as the negative feedback. The energetic radiation and stellar wind emanating from massive stars (>8 $M_\odot$) can have either positive effect and thus trigger new star formation (e.g., Dibai, 1958; Elmegreen, 1998; Sandford et al., 1982) or may also have a negative effect by efficiently dispersing the surrounding material and halt further star formation (e.g., Ali et al., 2018; Dale et al., 2013; Pabst et al., 2019; Zamora-Avilés et al., 2019). Several numerical studies have been conducted to understand the aspects of positive feedback or the triggered mode of star formation (e.g., Bisbas et al., 2011; Elmegreen et al., 1995; Haworth et al., 2012, 2013; Miao et al., 2006) and the negative feedback or dispersal of material to inhibit star formation (e.g., Colín et al., 2013; Geen et al., 2016; Kim et al., 2018; Whitworth, 1979).

Very young stellar objects are deeply embedded in their parent gas and dust and they can be detected in the far-infrared wavelengths. The Herbig Ae/Be (HAeBe) stars (originally identified by (Herbig, 1960)), are the intermediate mass stars in the mass range of 2-10 M⊙ which lie in the

pre-main sequence region and hence belong to the early evolutionary stages of the star. But since these stars are still embedded in the natal parent cloud, the further evolution will depend on the distribution of circumstellar material or how the mass is being dispersed. At the onset of star formation, the dense core material collapses turning it into a hydrostatic core with a massive gas and dust envelope around the central object. Fuente et al. (1998a) predicted that the time scale of the dispersal of the envelope is 1 Myr in the case of intermediate-mass stars.

The massive stars with extremely high luminosities in excess of 10^5 L$\odot$ produce stellar winds and they can significantly affect the region around them by evaporating the surrounding clouds. The shock waves from a supernova explosion can compress the material of molecular clouds and induce next generation of star formation. When the extreme ultraviolet radiation (EUV) ionizes the stars' surroundings by heating the gas to 10^4 K, expansion takes place at the sound speed. The resulting regions of ionized gas containing mainly hydrogen ions is considered as HII region. Because of the available luminosity, there is limited region in the surrounding cloud that can be ionised and there is simultaneous combination of electrons and protons to create neutral hydrogen creating a possible equilibrium. The spread of ionization takes place isotropically and the volume filled out is defined as Stromgrén sphere. The triggered star formation is further classified into two categories, *Collect and collapse* and *Radiative driven implosion*.

1.2.2.1 Collect and Collapse model

This scenario of star formation is triggered by an expanding HII region created by the radiation from massive stars. Elmegreen & Lada (1977) proposed the collect and collapse model. The spherical ionisation front is expanding at the supersonic speeds, much higher than the sound speeds. The front will sweep away an increasingly massive and dense shell of cold neutral material, which is the *collect* phase of this process and the HII regions acts like a snowplough. Depending on the longevity of the expansion of the HII region, the surface density of the shell may increase to a stage where it becomes self-gravitating. The shell further fragments into small structures which if acquire non-linear collapse stage, will possibly form stars. Therefore, the massive condensations near to HII regions are interesting sites to explore this scenario of triggered star formation.

1.2.2.2 Radiative Driven Explosion

The energetic radiation from OB stars can trigger the birth of new stars through different processes. The stellar winds, expanding HII regions and supernova explosions from the massive stars are the main sources can effect the natal clouds by sweeping and compressing the surrounding material. The ionized layer of the radiation from the nearby OB stars heats the surface layer of the parent cloud and as a result the high pressure waves driven by ionized heating compresses the cold molecular cloud into high density core. This could be the new potential site for the star formation. This process of star formation triggered by ionizing radiation is termed as *Radiative driven implosion* (Bertoldi, 1989; Bertoldi & McKee, 1990).

HAeBe stars are intermediate-mass counterparts of low-mass T Tauri stars (Herbig, 1960; The et al., 1994). These sources are important as they form a link between the low-mass star formation and the formation of highly enigmatic massive stars. The photons from them are not energetic enough to ionize hydrogen molecules in a large region of parent cloud and therefore mitigate the difficulties that exist in the study of massive star formation. Sources having masses in the range of ~ 5 - 10 $M_{\odot}$ or B- spectral types are classified as HBe stars which are easily discernible as majority of them are associated with reflection nebulosity (Herbig, 1960; Perez & Grady, 1997; The et al., 1994; Waters & Waelkens, 1998). Based on a study conducted on a sample of 34 HAeBe stars of different ages and luminosities, Fuente et al. (1998a) classified them into three groups depending on their association with gas material. According to their classification, HD 200775, a Herbig Be (B2/3Veq) star (The et al., 1994) is classified as a Type III source implying that the source is located in a cavity and that it has already dispersed material from within a region of ~ 0.1 pc. However, in a recent study conducted by (Saha et al., 2020), a number of young stellar population are found to be associated with it. Numerical simulations of shell formation and collapse around HII regions have been done by (Dale et al., 2007a,b). A classic example of compression of material from HII region and formation of high density core is found in the Eagle nebula. Fukuda et al. (2002) observed molecular lines ^{13}CO , C^{18}O (J=1-0) and 2.7 emission and found the formation of high density molecular core at the end of the pillars.

1.3 Filamentary structure of the ISM

Over many past years, the filamentary morphology of the ISM has been revealed using observations of dust, starlight extinction, CO and HI line emission (Bally et al., 1987; Hennebelle & Falgarone, 2012) in the nearby molecular clouds such as Orion, Taurus, Aquila, Ophiuchus, Musca-Chamaeleon, Serpens, Perseus, Cepheus, Polaris, Pipe nebula etc. (Abergel et al., 1994; André et al., 2010; Cambrésy, 1999; Goldsmith et al., 2008; Johnstone & Bally, 1999). These gravitationally bound structures have been considered as the loci where star formation takes place (André et al., 2010). Generally more massive "Infrared dark clouds" (IRDCs) which are at larger distances and are seen as absorption against the Galactic mid-infrared background, also exhibit clear filamentary structures (Egan et al., 1998; Peretto & Fuller, 2009). Therefore, the observed filamentary morphology in nearby clouds and the IRDCs cover the range from low- to high-mass star forming regions.

Specifically over the last decade, extensive observations using the *Herschel* space observatory at far-infrared wavelengths have shown the ubiquity of filaments in the ISM. The dust continuum maps given by the Herschel have shown these structures in detail and with good sensitivity from large scale molecular clouds (~ 10 pc) to the small scale structures to the cloud cores (≤ 0.1 pc).

Furthermore, the *Herschel* results indicate that the characteristic inner width of the filaments id quasi-universal at value of ~0.1 pc (Arzoumanian et al., 2011). The value of mentioned filament width corresponds to within a factor of ~ 2 to the sonic scale where the transition occurs from supersonic to

subsonic turbulent motions in the diffuse gas and consequently, a change in the slope of linewidth-size relation is also observed (Falgarone et al., 2009). This suggests that the formation of filaments may happen as a result of turbulent compression of the interstellar gas in low-velocity shocks (Padoan et al., 2001). Turbulent simulations have also shown the universality of the characteristic width of the filaments (Federrath, 2016). The other reason behind the typical value of width could be the case if the interstellar filaments are formed as quasi-equilibrium structures as a consequence of pressure balance with the diffuse ambient ISM $P_{ext} \sim 2\text{-}5 \times 10^4$ K cm^{-3} (Fischera & Martin, 2012). As most of the star-forming cores are found embedded in the filamentary structures, it suggests a strong link between the two which is important in the star forming process and the existing initial mass function (IMF) of the stars. In a general scenario, cold dense structures form hierarchically out of gravitational instabilities where the filaments condense out of sheets and cores form in the filaments. The filamentary clouds are pressure confined with the surrounding medium.

Therefore understanding the formation of filaments and their properties is crucial to the deep understanding of star-formation.

Prior to Herschel era, Myers (2009) has found a specific morphology of the filaments, *Hub-filament morphology* where the gas is concentrated in the form of hubs with the column density higher than 10^{22} cm^{-2} and several low density filaments branching out. Many star-forming regions are found to be threaded by a network of filaments which are connected to a central hub of dense gas and star clusters (André et al., 2010; Myers, 2009). The gas in these filaments are arranged in the form of fibrous substructures as shown in position-position velocity space (Hacar et al., 2013). Filaments form first and feed the matter towards the hub. These filament-hub systems are considered as transition stage connecting parsec-scale filaments and proto-clusters. The study of the interplay of different mechanisms like gravity and kinematics will provide useful insights into the possible factors involved in the origin of these structures.

Molecular filaments are the best places for the birth of young stars as it is found that all the cores are embedded in these structures (André et al., 2014, 2010). Könyves et al. (2015) studied the Aquila complex using the Herschel data and found that 75% of the cores are embedded in the filamentary structures. Similarly, Palmeirim et al. (2013) have analysed the dust continuum in Taurus molecular cloud.

1.4 Mechanism of filament formation: current accepted scenario

There are various processes that have been proposed to explain the formation of filaments observed in the ISM. Simulations of supersonic turbulence suggests that the gas is rapidly compressed into hierarchy of sheets and filaments and on inclusion of gravity, the dense gas in the filaments becomes gravitationally fragmented and collapses to form stars.

The interstellar medium involves multiple scales and different varieties of energetic phenomenon like the end stage of stars, the stellar feedback and the energetic stellar winds which can give rise to the formation of filaments. The formation of filaments in the interstellar medium have been considered in the theoretical models of supernova ejecta (Melioli et al., 2006; Stone & Norman, 1992), HII regions (Mellema et al., 2006) and tidally-disrupted clouds. Winds play an important role in shaping the dynamics and chemistry of the molecular clouds, characteristics, formation and global evolution of filamentary structures. Magnetohydrodynamic simulations by Banda-Barragán et al. (2016) suggest that the interactions between supersonic winds and interstellar clouds also play a significant role in formation of filaments.

- **Role of magnetic fields**
  Magnetic fields are ubiquitous on various scales of astronomical objects and they are considered as playing a significant role in star and galaxy formation. The role of the magnetic field in the formation of filaments is likely important because it makes the flow more coherent therefore allowing the existing filaments to survive longer. In a related way, the flows tend also to be more organized when they are magnetized. For example several studies have concluded that velocity and magnetic field are preferentially aligned (see for example ((Banerjee et al., 2009; Iffrig & Hennebelle, 2017; Matthaeus et al., 2008).

  Various connected sub-structures have also been observed which are found out to be parallel to the high density filaments (Goldsmith et al., 2008; Inutsuka et al., 2015). The magnetic field is found out to be preferentially aligned along these diffuse low density structures which are representation of striations in molecular clouds (Heyer et al., 2016). They are the streamlines of the flow of material on the high dense filaments. Based on the numerical simulations, Tritsis & Tassis (2016) have identified the possible origin as the result of coupling of non-linear coupling of MHD waves from inhomogeneous density fields. Once these structures become super-critical ($M \geq 16\ M_{\odot}/pc$), they will become self-gravitating and may collapse depending on the density enhancements along the length.

  Recent findings suggest that the magnetic field direction and the density gradients are clearly correlated (Planck Collaboration et al., 2016b; Soler & Hennebelle, 2017; Stephens et al., 2013). These studies conclude that the magnetic fields and velocity fields are well aligned in the cases of low feedback and stellar feedback. A major question to understand the role of the magnetic field in molecular cloud evolution is how it correlates with the other factors and in particular with the density. Two aspects are particularly important, first how the mean magnetic intensity varies with the density and second how the magnetic field direction correlates with structures like filaments and more generally how the magnetic field direction correlates with density gradients.

- **Role of instabilities**
  The instabilities occur when the gas is in thermally unstable state, i.e., when there is a transition

between the warm neutral medium to cold neutral medium. Basically, the formation of dense molecular gas depends on how the temperature and density has changed from CNM to WNM. In a region having tens of particles per cm^{-3}, the atomic cooling of the ISM (mainly H, O, CII) is not dependent on the temperature rather proportional to the square of density. However, the extent of heating is linearly proportional to the density. At the thermal equilibrium, gas cannot exist at the intermediate densities between 1-30 cm^{-3} and becomes thermally unstable. As a result, the WNM enters the thermally unstable regime where the gas starts contracting and reaches the thermal equilibirium where it becomes CNM.

- **Role of gravity and turbulence**
  Turbulence is a multiscale process where the kinetic energy cascades from large scale to the smallest possible scales. In case of molecular clouds, it is dynamically important from the scales of Giant Molecular Clouds to the cores as shown by various simulations and observations (Hennebelle & Falgarone, 2012; Mac Low & Ossenkopf, 2000; Scalo & Elmegreen, 2004). The effect of turbulence is seen in the extent of fragmentation in the clouds.

  The level and extent of fragmentation is controlled by the turbulence. Previous studies have shown that the velocity dispersions of each region is dependent on mass and size and it satisfies the Kolmogroff law of subsonic turbulence (Larson, 1981). The hierarchy of the condensations will end up with the objects so small that their internal motions are not supersonic.

  It is likely the case that together with gravity, turbulence is playing a significant role in the evolution of molecular clouds for example by creating strong density fluctuations, owing to its supersonic nature, that may serve as seed for the mass reservoir of future stars. More generally, interstellar turbulence is an agent that imposes order in the form of coherent structures and correlations between the various fields of the flows. Turbulence is likely responsible of many, if not almost all, of the observed motions. Therefore, by assessing the dynamical state of the clouds, it is possible to understand the effect and origin of the turbulence. It is also believed that the rich structure observed in molecular clouds can be understood by the interplay of the magnetic fields and the supersonic turbulence.

1.5 Energy budget and virial theorem

Molecular clouds are observed to have line-widths that are substantially larger than the sound velocity of the gas molecules within them. These motions correspond to the random, as opposite to the systematic motions in the cloud (Zuckerman & Evans, 1974). In a given cloud, this kinetic energy is comparable to the gravitational energy of the material and these motions are important in supporting the cloud against gravitational collapse (Larson, 1981). The Virial Theorem is an important tool in measuring the work done by the external forces on the medium and its resulting kinematic effects on the cloud. The observational quantities that allows us to quantify the total energy budget of the

cloud are line-profiles and/or the integrated emission over a solid angle. This allows an estimate of the physical state and possibly evolutionary state of the molecular cloud.

The physical properties of the filaments and the process of their evolution are mainly controlled by the interplay of factors like magnetic fields, turbulence and self-gravity.

1.6 Tools to study the different properties of the material in filaments

As mentioned, the dynamics and evolution of filaments are believed to be governed by magnetic pressure, turbulence and self-gravity. The main constituents of molecular clouds are dust grains and gas molecules. In the further sections, the observational probes for the molecular clouds will be discussed.

1.6.1 Dust continuum emission

The interstellar dust grains are solid, macroscopic particles which are composed of dielectric and refractory material. There are two ways by which the presence of dust grains in ISM can be determined observationally. The interaction of dust grains with starlight either through wavelength-dependent extinction of starlight through absorption or scattering by dust grains or reflection of light by dusty clouds located behind bright stars leading to the reflection nebulae tells about the presence of dust grains. Other observational evidence is the thermal continuum emission from dust grains at mid- to far-infrared wavelengths. The nature of emission from dust in thermal equilibrium is well described by blackbody spectrum modified by wavelength-dependent emissivity factor (λ^{-2}). The mass fraction of dust with respect to the present gas in the ISM is 0.02 (Draine, 2011). Although the content of dust is small, still the dust grains are the primary sites of molecular formation, and are thought to be responsible for all of the H_2 in the ISM. Being an important tracer of ISM and main constituent of molecular clouds, far-infrared emission maps from *Herschel* has revolutionised the current understanding of molecular cloud physics. The observations were taken in wavelengths from 70 μm to 500 μm. The Hydrogen column density maps were constructed by fitting a modified blackbody model to each pixel emission. The dust emission maps are actually useful in giving total integrated emission along the line-of-sight.

1.6.2 Importance of molecular line observations:probe of turbulent motions

The formation of molecules take place with the chemistry driven by ultraviolet rays from interstellar radiation field. The formation of molecular hydrogen, being the main ingredient in the formation of molecular clouds can be inherited from the large-scale convergence flows. Although the main

constituent of ISM is 78% Hydrogen molecule and 20% Helium, these gases do not emit at lower temperatures. The molecular hydrogen do not have a non-zero dipole moment, so the rotational transitions $\Delta J = \pm 1$ corresponds to forbidden states. Also, the temperature required to excite the vibrational or electronic transitions is 512 K which are not the typical temperatures of molecular clouds. It is the second most abundant molecule which gets readily excited at low temperatures. Therefore, CO molecule has been used as a popular tracer of the cold dense ISM. The central frequency at which ^{12}CO molecule gets excited is 115.27 GHz. Because the gas and dust in "typical" molecular clouds has a temperature of 10-100 K, the radiation of emission lies mostly in the range of millimetre (10-1 mm), sub-millimetre (1-0.1 mm) and far-infrared wavelengths (200-300 μm). The interaction of electromagnetic radiation with the rotational motion of dipolar molecules like ^{12}CO , HCN, HCO^+ etc. is the maximum (where the necessary condition with the non-zero dipole moment).

One important tool for the observations of MCs is the molecular line emissions of several tracer molecules, like e.g. CO, $C^{18}O$, N_2H^+, NH_3, CS, C_2S, which are also hosted within the molecular material of Molecular clouds (Caselli et al., 2002b). These lines can give additional spectral information about the velocities of the gas and its temperature. The most abundant molecule is the Hydrogen, H_2 molecule but it cannot be directly observed since it is a homonuclear molecule with no dipole moment. The second abundant molecule is ^{12}CO with a dipole moment emitting at a frequency of 115 GHz. There is a proportionality factor between the H_2 and CO density with a value of X = 1.8. 10^{20} cm^{-2} K km s^{-1}, (Dame et al., 2001). Though this factor is not constant but dependent on various conditions like metallicity, temperature variations. Bolatto et al. (2013) has proposed a constant value within the solar neighbourhood of the Milky Way.

1.6.3 Importance of polarization observations

To map the magnetic field structure in the clouds, various techniques like polarization using background starlight or thermal emission from dust grains can be used. The main difference between both the techniques is that background starlight polarimetry depends on the discrete lines of sight selected by the availability of the background stars whereas the polarization using thermal dust emission is measured at the position of dust structures which is integration along the line of sight. Linear polarization of the light provides a probe of magnetic field morphology in the molecular clouds. The alignment of asymmetric shaped dust grains with the magnetic field is the condition necessary for the polarization to occur. A number of various mechanisms have been proposed for producing grain alignment like paramagnetic relaxation (Davis, 1951), mechanical alignment (Gold, 1952) and the Radiative alignment torque (RAT) (Lazarian & Hoang, 2007). The latter one was considered as a promising theory successful in explaining the alignment of the dust grains. RAT depends on the interaction of the radiation with the spinning dust grains (Hoang & Lazarian, 2008, 2009). The dichroic extinction of the starlight by the asymmetric dust grains with reference to the magnetic field was recognized as interstellar polarization at visible wavelengths (Hiltner, 1949). The technique of optical polarimetry has been used in a number of observational studies involving filaments in dark

clouds at the densities corresponding to optical extinction, $A_v \sim$ 1-2 mag. Goodman et al. (1990) has summarized the magnetic field morphology in the outer parts of the molecular clouds like Taurus, Ophiuchus and Perseus using optical polarizations.

In addition to attenuating starlight, the dust grains also emit thermal radiation. The very first successful attempt to measure polarized thermal dust emission in the far infrared wavelengths was made by Cudlip et al. (1982) towards the object M42. Hence, the technique at millimeter and sub-millimeter wavelengths has become a powerful standard observational tool for studying magnetic field morphologies at the larger optical extinction (or higher hydrogen column densities of $\sim 10^5$ cm^{-3}) corresponding to molecular cores and clumps (Hull et al., 2014; Matthews et al., 2009; Ward-Thompson et al., 2009). Depending on the requirement of tracing B-field at various spatial scales, different set of polarization measurements were carried out , e.g., archive of data using Hertz polarimeter at 350 μm in 56 Galactic objects and 2 galaxies (Dotson et al., 2010b), polarization maps for 16 high mass star forming regions using Submillimetre Common-User Bolometer Array (SCUBA) on the James Clark Maxwell Telescope (JCMT) (Curran & Chrysostomou, 2007).

1.6.4 Strength of magnetic field

The modified Chandrasekhar-Fermi (CF) relation estimate the projected magnetic field strength in the plane-of-sky. It assumes an equipartition between the kinetic and the disturbed magnetic energies. The plane-of-the-sky component of magnetic field strength could be estimated using the velocity dispersion due to isotropic turbulence and the dispersion in polarization position angle (Chandrasekhar & Fermi, 1953). The plane-of-the-sky component of magnetic field strength (B_{pos}) can be found out using the following relation (Chandrasekhar & Fermi, 1953; Crutcher, 2005; Ostriker et al., 2001):

$$B_{pos} = 9.3 \sqrt{n(H_2)} \frac{\Delta V}{\delta\theta} \tag{1.1}$$

, where the ΔV is the velocity dispersion obtained from the Gaussian fitting of the lines and $\delta\theta$ is the dispersion in polarization angle. The CF method can only be used for the cases when $\delta\theta < 25°$. The strength of the plane of the sky component of the magnetic field was estimated using the expression (Franco & Alves, 2015),

$$B_{\rm pos} = 9.3 \left[\frac{2\, n_{H_2}}{cm^{-3}}\right]^{1/2} \left[\frac{\Delta V}{kms^{-1}}\right] \left[\frac{b}{1°}\right]^{-1} \quad \mu G \tag{1.2}$$

The above expression was derived by modifying the CF relation proposed by Chandrasekhar & Fermi (1953) where it was suggested that the analysis of the small-scale randomness of the magnetic field could be utilised to estimate the field strength.

1.7 Results obtained from the observations in Galactic star forming sites

A cloud hierarchy has been observed in the filamentary molecular clouds starting from cloud scale to core scale structures. Dense cores are believed to be the last stage of the molecular cloud fragmentation and the cradles of the star and binary of stars. There is an evidence of hierarchy in the mass distribution in the ISM. That involves cores to be at the bottom of hierarchy in a Giant molecular cloud and as seen in observations, to be associated with the dense filaments as seen in dust continuum and molecular lines. Herschel observations show that the dense cores are embedded in the thermally supercritical filaments that is the structures with mass per unit length exceeding $2c_s^2/G$ (Ostriker, 1964). Theoretically also, Inutsuka & Miyama (1992) concluded that the isothermal self-gravitating filaments are unstable to any longitudinal perturbation which will fragment the filament into dense cores. The fragmentation process will depend on the initial physical conditions present in the cloud. The distribution of cores in the cloud, their mass function, shapes, morphology (in other words the evolution from cores to stars) are important factors to understand the star formation rate. Previous molecular line observations have shown that the velocity gradient in the structures is a proxy of plane-of-sky motion present in the filaments. The results from the kinematical studies for various nearby star-forming regions are interesting but quite diversified. Hacar et al. (2016) has found the Musca filament as velocity coherent and subsonic turbulent motions using line observations. Arzoumanian et al. (2013) investigated the velocity dispersions of gas in a sample of filaments in nearby interstellar clouds IC 5146, Aquila, and Polaris using tracers of ^{13}CO , $C^{18}O$, and N_2H^+ (1-0). The authors concluded that the there is an increase in the velocity dispersion with the column density of filaments which could be a consequence of gravitational accretion not the interstellar turbulence.

The physical factors which decide the fate of filaments and their possible conversion to cores are still under debate. Cepheus constellation is also a part of the Gould belt which has signposts of active star formation. This region was considered as distant constellation in previous studies. Thanks to Gaia Dr2 (Bailer-Jones et al., 2018) distance measurements, the location of the complex has been accurately constrained now. To address these physical properties of molecular clouds and the interplay of these different factors in molecular clouds, Cepheus constellation is the appropriate laboratory which will be discussed in the next section.

1.8 Importance of Cepheus Flare Region and the cloud complexes

The Gould Belt is a distribution of stars and MCs that forms a circular pattern in the sky having an inclination of $\sim 20^\circ$ with respect to the Galactic plane (Gould, 1879). The minimum and the maximum Galactic latitudes of the Gould Belt are toward the Orion and the Scorpio-Centaurus

constellations respectively. The Cepheus Flare region is considered to be a part of the Gould Belt (e.g., Kirk et al., 2009). This region is identified as having a complex of nebulae that extends 10°-20° out of the plane of the Galactic disk at a Galactic longitude of 110° (Clemens & Barvainis, 1988; Dobashi et al., 2005; Dutra & Bica, 2002; Hubble, 1934; Lynds, 1962; Taylor et al., 1987). Five associations of dark clouds are found towards this region, namely, L1148/1157, L1172/1174, L1228, L1241, and L1247/1251. There are signposts of current star formation in these cloud complexes (e.g., Kirk et al., 2009).

Several shells and loops are identified in the direction of the Cepheus Flare. The Cepheus Flare Shell with its center at the Galactic coordinates of $l \sim 120°$ and $b \sim 17°$, is considered as an expanding supernova bubble at distance of ~ 300 pc (Grenier et al., 1989; Olano et al., 2006). This supernova remnant seems to be 4×10^4 yr old. Based on a study of the HI distribution in the region of the Cepheus Flare, Heiles (1969) speculated the possibility of the presence of two sheets most likely representing an expanding or colliding system at a distance range of 300-500 pc. Presence of a giant radio continuum region *Loop III* centered at $l = 124 \pm 2°$, $b = +15.5 \pm 3°$ and extending across 65° (Berkhuijsen, 1973), possibly formed as a consequence of multiple supernova explosions, and identification of an HI shell by Hu (1981) at $l = 105°$and $b = +17°$ suggest that the ISM towards the Cepheus Flare region is in a state of energetic motion. Yonekura et al. (1997) has studied the kinematics of the whole Cepheus Flare shell using ^{13}CO (1-0) observations. The observations were taken using 4 m Nagoya telescope using 2.7′ beam at a grid size of 8′. The velocity resolution used was 0.1 km s^{-1}.

The main reasons of selecting these clouds is strikingly different star-formation efficiencies with high in L1172/L1174 and less in L1147/L1158 cloud though both of them are at same distances and similar radial velocities. To understand the details of velocity information of each high density structures present, we do need a map at better spatial and spectral resolution. We made detailed kinematical observations of two complexes in Cepheus Flare Shell using single dish radio telescope. Along with the kinematical information, studies of the molecular cloud cores using molecular line observations will also provide the information on the mass and stability estimates. The work presented in this thesis discusses the physical properties of filaments and cores at a spatial resolution of 44″ with a grid size of 20″ and a velocity resolution of 0.1 km s^{-1}. We studied the physical properties of the gas clumps and filaments along with their environment using the line profiles.

Along with the microscopic motion of the material in the molecular clouds, there is a transverse motion also of each cloud in the galaxy. Owing the fact that magnetic fields are ubiquitous in astrophysical environments, there can be a significant effect on the formation mechanism of cloud when it is moving through the magnetized tenuous medium. In general, moving clouds are shaped up by the magnetic tension when the cloud motion is oblique to the magnetic field lines. Based on the 3-dimensional simulations of the moving cloud, Gregori et al. (1999), in the presence of magnetic field suggests that the head on interaction of the cloud with the generated magnetic tension supports the creation of Rayleigh-Taylor instabilities and thereby enhancing cloud disruption. The direction of motion may give hints on the structural evolution of the clouds in the galaxy. I studied four clouds

in Cepheus Flare region L1172/1174, L1147/1158, L1251 and L1228 complex. The details will be discussed in the chapter 7.

Clump shapes may be an indicator of the dynamical processes that govern clump internal dynamics. For example, early models of magnetized, self-gravitating clouds (e.g., (Mouschovias & Spitzer, 1976)) have oblate spheroidal isodensity contours that are flattened in a plane perpendicular to the mean magnetic field. Observers have looked for evidence of such oblate structures in molecular line maps of clouds. A statistical analysis in a set of 24 clouds to relate the intrinsic shapes and magnetic field orientations was done using Hertz polarimeter data. The orientation between cloud major axis and magnetic field direction has recently gained much attention (Law et al., 2019; Li et al., 2013). The relative offsets between their angles the magnetic field are found to be important in deciding various properties like the star formation rate, linear mass distributions. They found a bimodal distribution of orientation of filamentary clouds and magnetic fields. We expect that there might be an intrinsic relation of the core orientation with the magnetic field as the cores are believed to be embedded in the filamentary structures (André et al., 2014).

1.9 Tools used to study the clouds in this thesis

In this work, the observations of molecular line emission were used to study the kinematics of the selected clouds. The choice of tracers used depends on the density structure that needs to be studied. We used optically thick ^{12}CO (1-0) and optically thin C^{18}O (1-0) lines to study the filamentary structure of the clouds. The high density tracers like N_2H^+ (1-0) and CS (2-1) were used to investigate the core-scale structures in one of the clouds. Because of the limited observation time, the high density tracers were not observed towards another complex. The dust column density and temperature maps were taken from the Herschel Gould Belt Survey Archive. To characterize the physical properties of the filaments and the cores in the Cepheus Flare region, we have used a number of algorithms such as Filfinder, Astrodendro and Radfil. The details of all these methods will be discussed further in chapter 2. We used R-band optical polarization measurements and constructed Planck polarization maps from the data archive to study the magnetic field structure of the clouds.

1.10 Overview and structure of thesis

The thesis is structured in nine chapters, and its organization is as follows:

Chapter 1: This chapter gives the comprehensive view of star formation by giving an introduction of ISM and dust properties in ISM, extinction, interstellar dust polarization, and the interpretation of magnetic fields from the interstellar polarization in different wavelengths. It also explains the processes of star formation and the role played by the magnetic fields in the evolution of molecular clouds and subsequent star formation. Finally we introduced the region of which the results are presented in this chapter.

Chapter 2: This chapter explains about the various telescopes and instruments used for the acquisition of data for this thesis. There is an explanation of data reduction processes and the software used. The detailed procedures of estimating the results from the acquired data with the help of different programming languages are also explained. To map the magnetic fields in the star forming regions in different environments, we have used the polarization technique extensively. Optical polarization observations were carried using the polarimeter attached to 1-m class telescope at Aryabhatta Research Institute of Observational Sciences (ARIES), Nainital (India). We have also carried out single dish radio observations using 14-m radio telescope located at Taeduk Radio Astronomy Observatory (TRAO), KASI, Daejeon, Korea. We described radio data reduction using Continuum and Line Analysis Single-dish Software (CLASS).

Chapter 3: This chapter discusses the interaction between stellar winds and the material surround a Herbig Be star, HD 200775. We have used a sample of high density (N_2H^+) and low density tracers (^{12}CO and C^{18}O (1-0)) to probe the kinematics of the ambient gas around this intermediate mass star.

Chapter 4: This chapter discusses the relative importance between the dynamics and magnetic field morphology of the long filamentary complex. We studied the set of tracers ^{12}CO, C^{18}O (1-0) and N_2H^+ (1-0), CS (2-1) to probe the high extinction regions. The triggered mode of star formation will be explored in this chapter. How the radiation field is really affecting the ambient cloud emission in form of stellar winds.

Chapter 5: We studied the kinematics of L1157 complex with the optical polarization which was obtained using Aries Imaging Polarimeter.

Chapter 6: In this chapter, we studied the large scale kinematics of L1147/1158 complex using ^{13}CO and C^{18}O (1-0) regions. We extracted a set of filaments and set of clumps on dust emission maps. The velocity field of the filaments and clumps has been established.

Chapter 7: This chapter deals with the motion of the complexes in the Cepheus Flare region: L1147/L1158, L1172/L1174, L1228 and L1251. We calculated the core orientation and background magnetic field using Planck polarization in all four clouds.

Chapter 8: In this chapter, we studied magnetic field structure using Planck polarization and optical polarization techniques on a set of clouds which exhibit asymmetric emission. We found out the clumps in all the selected clouds and studied the relative orientation of B-field with the core major axis.

Chapter 9: Finally, in this chapter, we have summarized the main results which are obtained based on the various aforesaid studies carried out in this thesis. We concluded the key findings in this chapter and also gave a brief picture of the future perspectives.

Chapter 2

Observations & Data Reduction

2.1 Introduction

As mentioned in previous chapter, the understanding of star formation comes from the detailed study of the different physical processes involved in the dynamics of the cloud. To investigate the magnetic structure at the perpiphery of the molecular clouds, we mapped the region with optical polarimetric observations using ARIES Imaging Polarimeter (AIMPOL) mounted at 104-cm optical telescope. We performed detailed molecular line mapping towards two complexes L1172/L1174 and L1147/L1158 complex. In addition, we also used the archival data in far-infrared (FIR) using Herschel, optical using GAIA and polarization using Planck archive. A number of algorithms were also employed to characterise the dust properties of the filaments and cores which will be discussed in the last section of this chapter.

The structure of this chapter is organized as follows. We explain about the telescopes used for the work and further the detailed descriptions of each back-end instrument in section 2.2. Then, the details of the software used for data reduction are discussed. Then, we further explain the details about Archival data and the steps including the further analysis done on the archival data in the section 2.6. Finally, in the last section, the methodology of each algorithm used in each chapter is explained.

2.2 Telescopes used

There are two ground-based telescopes which we used for our observations:

- **104-cm Sampurnanand Telescope (ST):** This telescope works in optical wavelengths and is located at Aryabhatta Research Institute of Observational Sciences (ARIES), Manora Peak, Nainital (India). It is one of the main observing facility in optical wavelengths. The Telescope was commissioned by Carl Zeiss, Germany and installed at Manora Peak in 1972. The telescope is a Ritchey-Chretien (RC) reflector with a Cassegrain focus (f/13) and Coude (f/13) focii with

plate scales of 15.5 and 6.5 arcsec/mm, respectively. The telescope is mounted on an equatorial 2-pier English mount that can produce a field of $45^{'}$ with a corrector at the Cassegrain end. The achieved tracking accuracy is $7^{''}$/hr without the use of guider and is $0.7^{''}$ with the use of guider.

A technical and detailed description of the telescope can be found in Sagar et al. (2013). The telescope has been equipped with a 2k×2k CCD camera which covers 13×13 arcmin^2 region and an ARIES Imaging Polarimeter (AIMPOL) covering a region of 8′ field-of-view (FOV). Table 2.1 show the technical parameters of the telescope.

2.2.1 ARIES Imaging Polarimeter (AIMPOL)

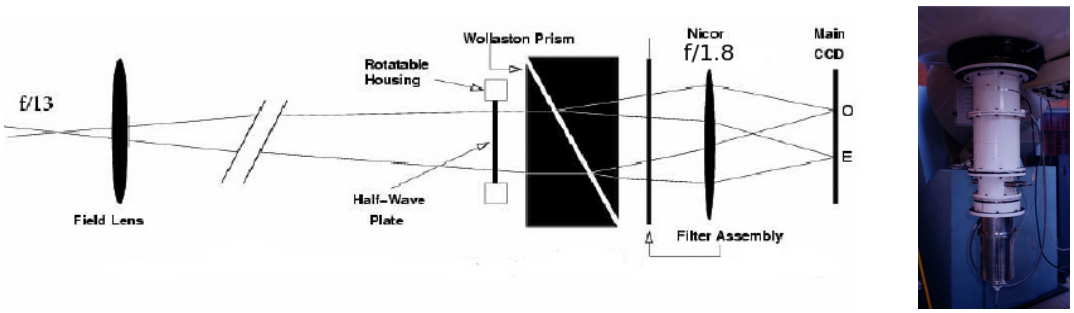

Figure 2.1: *Left*: Optical layout of the backend instrument, ARIES Imaging Polarimeter (AIMPOL) ((Rautela et al., 2004)). *Right*: The polarimeter with filters holder and 1024×1024 CCD attached.

We carried out optical linear polarimetric observations using the ARIES IMaging POLarimeter (AIMPOL), mounted at the Cassegrain focus of the 104-cm Sampurnanand telescope of ARIES. The instrument measures linear polarisation in five bands U, B, V, I and has a field of view of $\sim 8^{'}$. A 13-magnitude star can be observed for the polarization in an exposure time of 2 min with 0.18% accuracy. This polarimeter uses Tek-1k x 1k CCD as detector.

Fig.2.1 shows the optical layout of the AIMPOL. It consists of a camera lens (85mm, f/1.8) and a field lens with an achromatic, rotatable half-wave plate (HWP) in between. The HWP is used as a modulator and a Wollaston prism beam-splitter as an analyzer. The Wollaston prism splits the incoming light into ordinary (O-ray) and extra-ordinary rays (E-ray) which are separated by 28 pixels along the direction of north-south on the sky plane. The HWP provides the components of electric vector polarized orthogonally with different intensities after emerging out of the Wollaston prism. The orientation of the optic axis of Wollaston prism is aligned to the north-south axis of the telescope. Also, the HWP is kept in such a way that the axis of the prism is along the fast axis of the plate.

This polarimeter is used with the Charged Coupled Device (CCD) cooled by liquid-N_2. The plate scale of the CCD is $1.48''$/pixel for a pixel size of 24μm and the field of view is $\sim 8'$ in

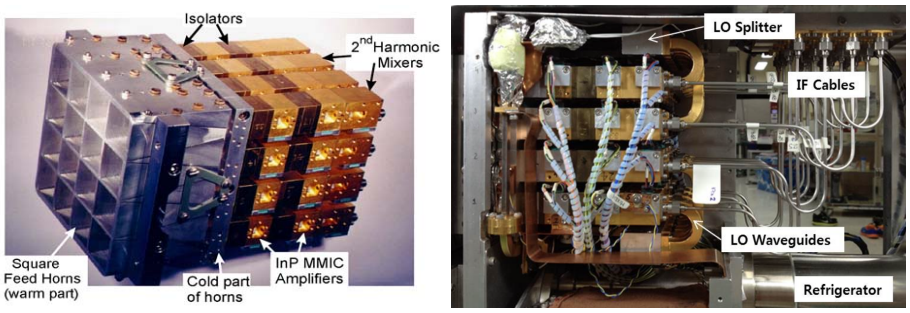

Figure 2.2: *Left panel:* The assembled 16-pixel array. *Right panel:* Inside view of the SEQUOIA dewar with 16-pixels installed. Image Credit: http://radio.kasi.re.kr/trao/receiver.php.

diameter. The full width at half maximum (FWHM) of the point source function (PSF) varies from two to three pixels. The parameters such as read-out noise and the gain of the CCD are 7.0 e^{-1} and 11.98 e^{-1}/ADU, respectively. The instrument measures the linear polarization in broad B, V, R and I bands and has a field of view ~8′ arcmin in diameter. The instrumental polarization is found out to be ~0.04% by observing unpolarized standard stars. The instrument can be used to measure the linear polarization of different celestial objects having the fraction of polarization more than 0.1%. A detailed description of the instrument and the techniques of the polarization measurements are given in Rautela et al. 2004.

- **14-m Single dish radio Telescope:** The telescope operates at a frequency range of 86 GHz to 115 GHz and is located at Taeuduk Radio Astronomy Observatory (TRAO), KASI, Daejeon, Korea. The modes of observations where the telescope will work depends on the science requirements. One of the observing modes is OTF (On-The-Fly) as a main observing mode, second is the position switching mode and the frequency switching mode. In the front-end, it is equipped with SEQUOIA-TRAO and in the backend a FFT (Fast Fourier transform) spectrometer is attached. Further information about this 14-m radio telescope is available on http://radio.kasi.re.kr/trao/telescope.php website. Table 2.1 show the technical parameters of the telescope.

2.3 Instruments

2.3.1 SEcond QUabbin Observatory Imaging Array (SEQUOIA)

SEQUOIA-TRAO is a new back-end system instrument to the telescope and operates at in the frequency of 85-115.6 GHz range. It consists of high-performing 16 pixel MMIC preamplifiers in a 4×4 array and can observe 4×4 points in the sky at a time in vertical and horizontal direction. The

Table 2.1: Details about the optical telescopes used for observation.

Telescopes	**Sampurnanand Telescope (ST)**	**Radio Telescope**
Place	ARIES, Nainital, India Deajeon, Republic of Korea	TRAO
Longitude	79°27′24″ (E)	127°22′18.77″ (E)
Latitude	29°21′42″ (N)	36°23′53″ (N)
Altitude (m)	1951	109
System	Richey-Chreteian	–
focus	Cassegrain	–
f-ratio	f/13	f/4.074
Diameter of primary mirror (m)	1.04	13.716
Plate-scale	15.5″/mm	–
Mount	Equatorial	Alt-Azimuth

pointing accuracy was achieved to be $\leq 5''$ using a standard X Cygnus source in the SiO line. The position-switch mode was employed to subtract the sky signals. At 115 GHz, the beam size (half-power beam width, HPBW) or the angular resolution of the telescope is about $45''$ and the fraction of the beam pattern subtending main beam (beam efficiency) is 51±2% . The system temperature was 550 K-600 K during the observations. The back-end system with Fast Fourier Transform (FFT) spectrometer has 4096 × 2 channels at 15 kHz resolution (~0.05 km s^{-1}at 110 GHz). Because the optical system provides two side-bands, two different lines can be observed simultaneously. The value of noise temperature varies from 50-80 K over almost full band. The intermediate frequency (IF) preamplifier at each pixel is merged by a single-sideband (SSB) mixer with an IF band covering 5–20 GHz. The new local oscillator developed for SEQUOIA can generate the response at 40 GHz and 60 GHz.

An image of SEQUOIA instrument is shown in Fig.2.3. Details about this instrument can be found at http://radio.kasi.re.kr/trao/receiver.php.

2.4 Observation and Data Reduction

2.4.1 Polarimetric Observations

The optical linear polarization observations were performed with the ARIES IMaging POLarimeter (AIMPOL) which is coupled with TK 1024×1024 $pixels^2$ CCD camera. Only the central region containing 325×325 $pixels^2$ out of 1024×1024 $pixels^2$ was used. The total intensity of the incoming light (I) is represented by the following equation: $I^2 = Q^2+U^2+V^2$, where Q and U are the Stokes parameters and give information about the linearly polarized light and V gives the information about the circularly polarized light. Using Q and U, we can estimate results of polarization: the degree of polarization (P) and polarization position angle (θ). The stokes parameters were calculated at different position angles of HWP.

Alignment of polarimeter with North-South axis of telescope: At the onset, the optical axis of the polarimeter is aligned with the North-South(N-S) axis of the telescope. The polarization angle is 0° which is in the north direction as the reference direction is with respect to north counterclockwise towards east. We point the telescope towards any bright star, then the telescope is directed either in the north or south direction with sufficient exposure time. The optic axis of polarimeter is considered to be aligned with the NS of the telescope when the elongated images of ordinary and extraordinary rays appear in one line and are not separated. This procedure is repeated a number of times to make proper adjustments so that the images of ordinary and extraordinary rays overlap each other. In order to measure polarization, we observed at four positions (i.e. α = 0.0°, 22.5°, 45.0°, 67.5°) by rotating HWP. The α is the angle of the HWP makes with the N-S direction of the telescope. The extraordinary (e-ray) is polarized in the direction parallel to the crystal principal axis, and the ordinary (o-ray) gets polarized in the perpendicular direction.

We observe a number of frames to get a good SNR. Besides the object frames, we also observe bias frames. In 104-cm Sampurnanand Telescope, the raw data of polarimetric observations are saved in .pmi format. We convert this .pmi format to the Flexible Image Transport System (FITS) format using a script file 'pmi2fits' written in Fortran languages.

2.4.2 Radio Observation

We mapped the star-forming regions in sub-millimetre wavelengths using 13.7 m single dish radio telescope located at Taeduek Radio Astronomical Observatory (TRAO), Daejeon, South Korea. On-The-Fly (OTF) is a technique which is used to perform mapping observations where the antenna is driven continuously in a region to be mapped, and the data are taken at every short interval, instead of observing at discrete positions on the sky such as point swicthing technique. With this technique, the observing efficiency is improved because the dead time of the telescope gets reduced, and a large number of on-source integration can be made per off-source reference integration. Also, the data is taken more frequently than the Nyquist sampling rate, so the spatial information is not lost. The details about the telescope system and its observations can be found in Jeong et al. (2019). The details of On-The-Fly imaging technique can be found in Mangum et al. (2007).

We select SEQUOIA as the instrument from the receiver window. Then the appropriate frequencies were selected for the two channels of LOA and LOB using Lovas Line Catalog appears at the click of relevant frequency value. We click 'Cal' at intervals which estimate the 'Tsys' using chopper wheel technique. This process requires the change in the IF value. To calculate the τ_0 value, the 'SKYDIP' process has to be executed. The RA & DEC of the source has to be entered according to the celestial coordinate system. As we carried out observations in OTF mode, it determines the pointing direction using Ra, Dec, Elevation (El), Longitude (L) and Latitude (B). After it we set the number of OTF observations. We use OTFTOOL which is developed in the languages MYSQL and GTK+1.2. This tool is specifically customized for TRAO. There are three steps for the preliminary data reduction: a data file Selection, data assessment and re-gridding of data. First, we import the file from the OTF

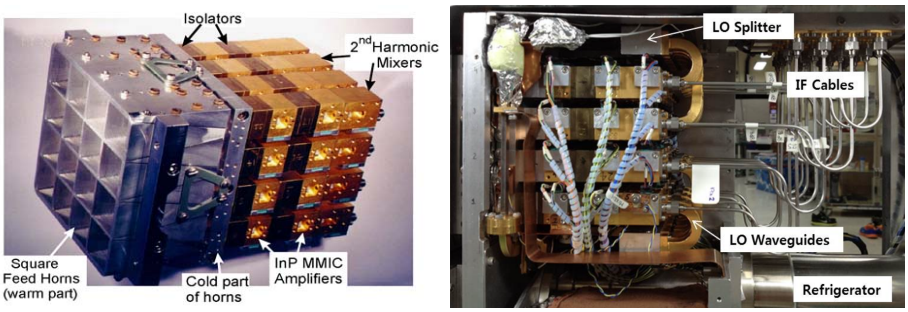

Figure 2.3: *Left panel:* The assembled 16-pixel array arrangement for SEQUOIA. *Right panel:* Inner parts of the SEQUOIA dewar installed with 16-pixels.
Image Credit: "http://radio.kasi.re.kr/trao/receiver.php".

data folders. In data assessment tab, we subtract the baseline first and regrid the data to create the fits cube using convolution and cell size entered by the users. The data reduction of the data has been performed using Continuum and Line-Analysis Single Dish Software (CLASS).

2.5 Softwares

2.5.1 Optical Photometric data reduction using IRAF

Optical Photometry: We used *Image Reduction & Analysis Software* (IRAF) for preliminary reduction of the images. First we performed the cleaning of raw images, in which the following steps were included:

- **Bias Level Subtraction:** This is used to provide an estimate of the value produced by an empty or unexposed pixel within a CCD. Using Bias images, we measure the zero noise level of a CCD. Several bias frames were observed in proper intervals during whole night observations and a master bias frame was made by median combining. Then the master bias frame was subtracted from each science and flat frames. To perform this step of bias subtraction, a task called *zerocombine* in IRAF is used.

- **Flat Fielding:** To remove the effect of varying sensitivity of each pixel to incoming photons, we observed the uniformly illuminated sky for short exposures and they are called as flat frames. The flat frames were taken during the twilight times in all the filters and the master bias was subtracted from flat frames. Master flat frame was made by median combining these flat frames in each filter. Each obtained image was divided by this normalized master flat to remove the effect of non-uniform sensitivity of the pixels. To perform flat-fielding we used the IRAF tasks *flatcombine*.

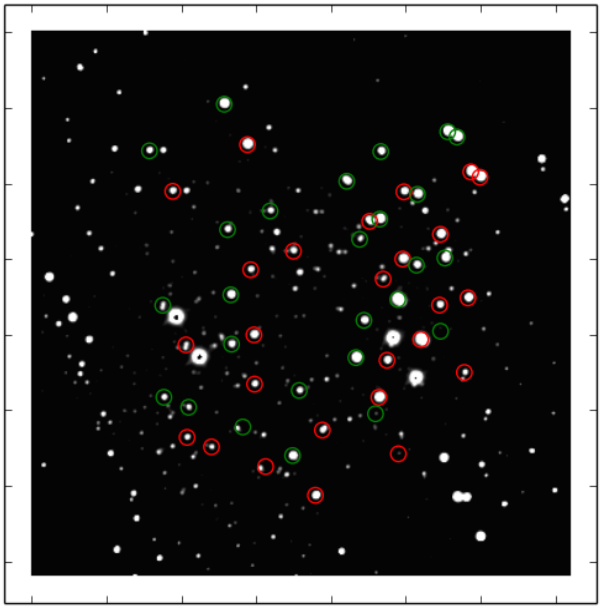

Figure 2.4: Ordinary (red circles) and extraordinary (green circles) images of stars obtained with AIMPOL observation.

- **Aligning and combining:** We align all the images by using task *imalign* at each plate position with respect to a reference image to get rid of any effects due to tracking of the telescope. We then combined images of field at each plate position for photometry to have good SNR by using task *imcombine*.

Photometry: With four images in final, we extracted the fluxes of stars in both the images of ordinary and extra ordinary rays using a technique called photometry. On the selected stars, we performed aperture photometry by using *phot* task of IRAF software.

Calibration: There are two effects that have to be corrected for, namely the effect of atmospheric extinction and the discrepancies between the instrumental and target standard system. The effect of atmospheric extinction arises due to the scattering and absorption of the star radiation when it passes through Earth's atmosphere. We calibrated the magnitudes of the stars after measuring the instrumental magnitudes. The calibration needs to be applied to convert the measured instrumental magnitudes to a standard photometric system.

Estimation of polarization values: Because of the split of the incoming light rays into two perpendicular components, we can estimate the polarization using the intensities of the ordinary and extra-ordinary images. The intensities of the extraordinary and ordinary images can be explained as,

$$I_e(\alpha) = \frac{I_{unp}}{2} + I_{pol} \times cos^2(\theta - 2\alpha) \tag{2.1}$$

$$I_o(\alpha) = \frac{I_{unp}}{2} + I_{pol} \times sin^2(\theta - 2\alpha) \tag{2.2}$$

where I_o and I_e represent the fluxes of ordinary and extraordinary rays, I_{unp} and I_{pol} are the unpolarized and polarized fluxes, respectively. The angles θ and α are the angle of polarization and the angle of HWP fast axis with respect to the axis of the Wollaston prism, respectively.

We used aperture photometry in the IRAF package to acquire the fluxes of extraordinary (I_e) and ordinary (I_o) rays for all the observed stars which has SNR ≥ 3. We define a ratio *R(α)* as:

$$R(\alpha) = \frac{\frac{I_e(\alpha)}{I_o(\alpha)} - 1}{\frac{I_e(\alpha)}{I_o(\alpha)} + 1} = P \times cos(2\theta - 4\alpha), \tag{2.3}$$

where P is the degree of polarization and θ is the polarization position angle of the plane of linear polarization. The angle α represents the angle of HWP fast axis at four different positions, 0.0°, 22.5°, 45.0°, and 67.5°. They represent the four normalized Stokes parameters, q[R(0.0°)], u[R(22.5°)], q_1[R(45.0°)], and u_1[R(67.5°)], respectively.

2.5.2 Continuum and Line Analysis Single-dish Software (CLASS)

CLASS is a software package under GILDAS[1] used for analysing spectroscopic data observed with the single dish telescope. It also has basic functionalities to correct for the continuum drifts like pointing or focus. The default extension of files saved in TRAO observation systems is .raw which is converted later after using OTFtool mounted in local server of observatory.

The raw OTF data for each acquired map for each pointing of observation were read and converted into a map using a Jinc-Gaussian function after fitting baseline with first order in OTFTOOL. The resulting cell size was given as 22″ and noise weighting was applied. The further reduction and inspection of the data was done in CLASS package. Because of non uniform shape of baseline on both the ends of the band and the velocity range ($\sim$ 170 km s^{-1}) is larger than the emission contributed in the observed sources (less than 20 km s^{-1}), we carry out baseline fittings in two steps. First we make a shorter velocity range by cutting the spectra on both sides so that the range becomes around 120 km s^{-1}. Then, we subtract the baseline with the second order polynomial. Finally, the spectra were resampled with a channel width of 0.06 km s^{-1}. Both the ends were cropped again, resulting in a velocity range of 60 km s^{-1}, and the baseline subtraction was repeated again with a first-order polynomial. After this step, all the velocity channel maps were examined, and the maps which show a high noise level gradient due to rapid change in the system temperature were excluded. Finally, the final fits cube were made with 44″ cell size and 0.1 km s^{-1}as spectral resolution for $C^{18}O$, ^{13}CO lines. For N_2H^+ (1-0) and CS (2-1), we used a cell size of 20″ and $\sim$ 0.06 km s^{-1}velocity channel width.

[1] http://www.iram.fr/IRAMFR/GILDAS

2.6 Other archival data used in the thesis

2.6.1 Herschel Far-infrared telescope

In order to study the far-infrared emission from the molecular clouds, we have used archival data from *Herschel* space satellite. Herschel is a space based observatory, launched on May 14 2009 and operated nearly for four years. It hosted the largest and most powerful infrared telescope ever flown space, and three sensitive scientific instruments which operated at temperatures close to zero. The Herschel observations were completed on April 29 2014 when the tank of liquid helium used to lower down the temperature of the system. Herschel was the first space observatory to observe from the far-infrared to the sub-millimetre waveband, allowing us to study the invisible dusty and colder regions of the Universe. The telescope's primary mirror was 3.5 m in diameter which is four times larger than any previous infrared telescope and almost one and half times than that of Hubble Space Telescope. There are four main parts to the satellite- the telescope, the payload (the hosted instruments and the cryostat which cooled everything), the service module (electronics, satellite pointing), and the sun shield to protect the payload from direct solar illumination. The payload had three advanced science instruments: two cameras and a very high resolution spectrometer; their detectors were cooled to temperatures close to absolute zero by a sophisticated cryogenic system.

2.6.2 GAIA data

GAIA mission is the successor mission of European Space Agency (ESA) after HIPPARCOS satellite measured the absolute parallax of stars with milli-arcsecond accuracy with a great influence on various areas of astronomy (Perryman, 2009). The main motivation behind GAIA is to acquire three-dimensional spatial and velocity distribution of stars, their physical properties like surface gravity and effective temperature.

The first release of data GAIA DR1 was done in 2016 (Gaia Collaboration et al., 2016). GAIA DR2 is the second data release of the mission executed by GAIA. In addition to the photometric data in various optical bands G (400-1000 nm), G_{RP} (640–1000 nm), G_{BP} (330–680 nm), it provides the proper motion and parallax measurements of 1.3 billion stars in the sky. The limiting fainter magnitude is G $\sim$ 21 mag and the brightest limit is $\sim$ 3 mag.

In this work, we have incorporated both parallax and proper motion measurements from GAIA DR2 and their uncertainties to find out the space velocity and distance of the molecular clouds studied in this work. The more accurate calculated distance values were taken from catalog generated by Bailer-Jones et al. (2018).

2.6.3 Planck sub-mm magnetic field map

The Planck satellite was a space observatory, having small angular resolution and high sensitivity, operated by the European Space Agency (ESA) from 2009 to 2013. The satellite performed wide

variety of observations, e.g., the Milky Way observations, measurements of the Galactic magnetic field and distributed synchrotron emission. The satellite had two instruments: (i) the Low Frequency Instrument (LFI) and (ii) the High Frequency Instrument (HFI). Both the instruments were able to measure both the total intensity and polarization of photons. These instruments jointly cover a frequency range from 30 GHz to 857 GHz. The LFI had three frequency bands 30 GHz, 44 GHz and 70 GHz, covering the microwave to infra-red wavelengths with an angular resolution of 33′, 24′ and 14′, respectively. The HFI had six frequency bands 100 GHz, 143 GHz, 217 GHz, 353 GHz, 545 GHz and 857 GHz, covering the far-infrared to sub-millimeter (sub-mm) wavelengths with an angular resolution of 10′, 7.1′, 5.5′, 5′, 5′ and 5′, respectively. Only the last four frequency bands were capable to measure the polarization of incoming radiation because of Galactic dust. The Planck survey provided a unique full-sky coverage of the sub-mm polarized emission from Galactic dust.

2.6.4 Methodology used to make polarization map

The *Planck* satellite has mapped the microwave sky from 30 to 353 GHz with unprecedented sensitivity and angular resolution (Planck Collaboration et al., 2014) and produced the all-sky map of the polarized emission from dust at sub-mm wavelengths. We extracted the *Planck* released whole sky map which is bandpass leakage corrected from *Planck* Legacy Archive (http://www.cosmos.esa.int/web/planck/pla/) at 353 GHz frequency band. This is the highest frequency channel with the polarization capabilities with best signal-to-noise ratio (SNR) for dust polarization (Planck Collaboration et al., 2015a). The contribution of the polarization of the CMB is negligible at 353 GHz therefore, it was ignored in the calculation of sky polarization towards molecular clouds. The I,Q and U maps were constructed at $8^{'}$ resolution using the gnomic projection of the HEALPix [2] (Górski et al., 2005) all sky maps. We derived stokes parameters I,Q and U from *Planck* observations. We have used *healpy* (Zonca et al., 2019) to analyze data for calculation of percentage of polarization and position angle.

The Stokes parameters, I is the total polarized intensity and Q and U, the stokes parameters, are the two components of the linearly polarized dust emission obtained from line-of-sight (LOS) integration and are related as

$$
\begin{aligned}
Q &= I * p * \cos 2 * \phi, \\
U &= I * p * \sin 2 * \phi, \\
P &= \sqrt{Q * Q + U * U}, \\
p &= \frac{P}{I}, \\
\phi &= 0.5 * \arctan U, Q,
\end{aligned}
$$

[2] http://healpix.sourceforge.net

where P is the total polarized intensity, p is the polarization fraction, and ϕ is the polarization angle given in IAU convention (Planck Collaboration et al., 2015a). The $\arctan U, Q$ is used to calculate $\arctan \frac{U}{Q}$ to avoid π ambiguity. In *Planck* polarization, the plane-of-sky (POS) magnetic field orientation is found by adding 90° to the polarization angle. The cut out maps of polarization fraction and angle were rebinned to increase the signal-to-noise.

2.7 Algorithms used in the analysis of dust-continuum Herschel maps

We aim here to study the overall physical properties of filaments, clumps and their physical properties like column density profile, orientation, curvature, widths, lengths. So, we used the following algorithms to quantify all the filament properties.

1. **Filfinder:** FilFinder is a Python based package for the extraction and the charaterization of filamentary structure in molecular clouds. We can uniformly extract the structure over a large dynamical range in intensity or column density. In this section, we discuss the multiple steps involved in running the algorithm which are based on various user inputs. The segmentation of filamentary structure is done by the adaptive thresholding over local neighborhoods. Determining filament mask is a crucial step. It is constructed by applying morphological conditions to remove extra small regions. It involves the following steps:

   (a) Flatten the image using an arctan transform which will remove the effects of small bright maxima from effecting the filament mask.

   (b) Smoothing the image with a small median filter and it is usually taken as half the size of the expected filament widths. In our case, we used around 40 pixels for the Herschel images.

   (c) Applying the adaptive threshold where the patch size is taken to be the expected filament width (0.1 pc).

   (d) Supplying a threshold of the area for the final mask.

   The final regions are reduced to skeletons via Medial Axis Transform for further analysis. Pixels within each skeleton are classified by the number of connecting pixels. The skeletons are broken up into a set of branches to determine the length. The length of the filament is determined by converting the set of branches into a graph. The skeletons are then further pruned by removing the branches which are not in the main length on the basis of the branch length or the relative intensity. The width of the filament is derived by building a radial profile using the distance from the skeleton. A measure of filament direction and curvature is found using the technique of Rolling Hough Transform. This method returns a distribution of angles,

from which the mean and variance are defined. Finally, it gives the position angle of the filaments and their curvature. These are the basic steps of this algorithm, which will give the main filament properties such as the local amplitude and background intensity, width, length, orientation and curvature.

2. **Radfil:** The Radfil workflow can be broken down into three stages: data input, filament profile building, and filament profile fitting. The first step in the Radfil workflow includes on taking the data input and the image at any wavelength can be used to run Radfil. All of the data are stored in a radfil class object. It takes the image in form of Python image array which shows the intensity of the filament. This is typically taken in as a FITS file. The corresponding FITS header for the image which contains the WCS information and the distance to the filament are given as optional inputs. If no header is provided then the analysis will be carried out in pixel units of the image. If a distance is not provided but the header, the analysis is carried out in angular units. If both are given, the analysis will be carried out in physical units (i.e. parsecs).

   The users can choose to input a filament mask and/or a filament spine of the same shape as the image array that can be used in the profile building procedure. The filament mask gives two purposes. In the first case the user does not have a pre-built spine, the mask can be used to create a filament "spine" which is a one-pixel wide representation of the filament mask. The skeleton is created by using medial axis skeletonization technique using the FilFinder package (Koch & Rosolowsky, 2015). The FilFinder algorithm then derives the shortest structure from end-to-end using the set of skeletons to give the final spine. This skeletonization procedure is performed via Radfil method make fil_spine(). The mask can also be used to define the extent of the image array for further analysis like including profile shifting. Instead of this, we can feed in any user-defined spine of filament.

   The derived average profile of a filament is fitted by a Plummer-like function and Gaussian function. We give the choice of function via the "fitfunc" argument which can be either "Gaussian" or "Plummer". The Gaussian function is given by H(r) = a((rμ)/ 2σ^2), where r is the radial distance, H is the height of the profile, and the free parameters are the amplitude (a), the standard deviation (σ) and the mean value (μ). In the Gaussian case, we can decide whether to fit for the mean by giving parameter "fix mean", which fixes the mean to zero when True or making it flexible by giving option as False. The Plummer function is the same as that found in (Cox et al., 2016). We assume here that the inclination of the filament to the plane-of-the-sky is zero. We obtain the best-fit parameters, peak intensity (I_o), R_{flat} is the flattening radius, and p is the index of the density profile.

3. **Astrodendrogram** This algorithm works on hierarchical structures in the molecular cloud. It finds out isocontours in the intensity gas emission (Rosolowsky et al., 2008). This algorithm works with the input of three parameters min_value, min_delta and min_npix. The min_value is the threshold in the emission map which is decided by the rms noise across the emission map.

If a single local maximum exceeds the minimum value then it is considered as the *leaf*. The second parameter, min_delta is defined as the minimum height of the local maxima with respect to the nearby local maxima. Only those structures will be considered as leaves which have local maxima higher than min_delta and they form continuous branches with the neighbours which are considered as filaments. If the height of any emission structure is less than min_delta, it will become part of other leaf structure. This will avoid identifying the local peak produced by the noise spikes. These two parameters min_value and min_delta are taken in terms of noise level of the dataset, σ_{rms}. The third parameter, min_pix, determines the number of pixels a structure should have to be considered as a real leaf. The method gives a catalog of central coordinates of each source, effective radius, area contained in an ellipse, total flux within the structure if appropriate units of flux and beam width are supplied. The radius of each source identified is calculated by R = 1.91 $\sqrt{R_{max}}\mathrm{R}_{min}$ as stated by Rosolowsky et al. (2008). We expect that that a particular concentration of emission from the cloud is included within a spherical cloud having equivalent radius R.

Chapter 3

Dynamical state of gas surrounding Herbig Be star HD 200775

3.1 Introduction

The L1172/1174 complex is a region containing a number of dark clouds showing signature of ongoing star formation in some of them. The complex is situated in the Cepheus constellation. It consists of two dark clouds LDN 1172 (hereafter L1172), LDN 1174 (hereafter L1174) catalogued by (Lynds, 1962). The spatial location of L1174 coincides with the reflection nebula NGC 7023 (also called Iris nebula) which is powered by an HAeBe star HD 200775 (R.A. (J2000)= 21h01m39s, Dec(J2000)= $+68°09'47''$) of spectral type B2Ve (Guetter, 1968).

The complex shows a head-tail morphology where L1174 high density core along with NGC 7023 lies in the head part which is parallel to the celestial equator and L1172 lies in the tail part of the complex south of the head. The region which is a stem to the complex is considered as L1172 region which extends towards southern part of the complex. Fig. 3.1 shows the dust column density map[1] obtained from the *Herschel Gould Belt Archive* (Di Francesco et al., 2020). There are high density regions in the complex. This complex has been a target of many molecular line and dust emission studies.

Myers (2009) has identified several clouds having a hub-filament shaped morphology and having an active star formation of which NGC 7023 is considered a classical example. It is one of the hub-filament systems in which there is a single but long filament attached to the hub along with a number of smaller ones.

To characterize the formation of the filaments and the cores, we observed the whole complex using ^{12}CO , C^{18}O and high density regions using N_2H^+ and CS (2-1) molecular lines. Fig. 3.1 shows the fields that were observed using 13.7 m single dish radio TRAO telescope. The white boxes show

[1]The images of dust temperature and column density at 36″ were available on the http://www.herschel.fr/cea/gouldbelt before the publication of the paper.

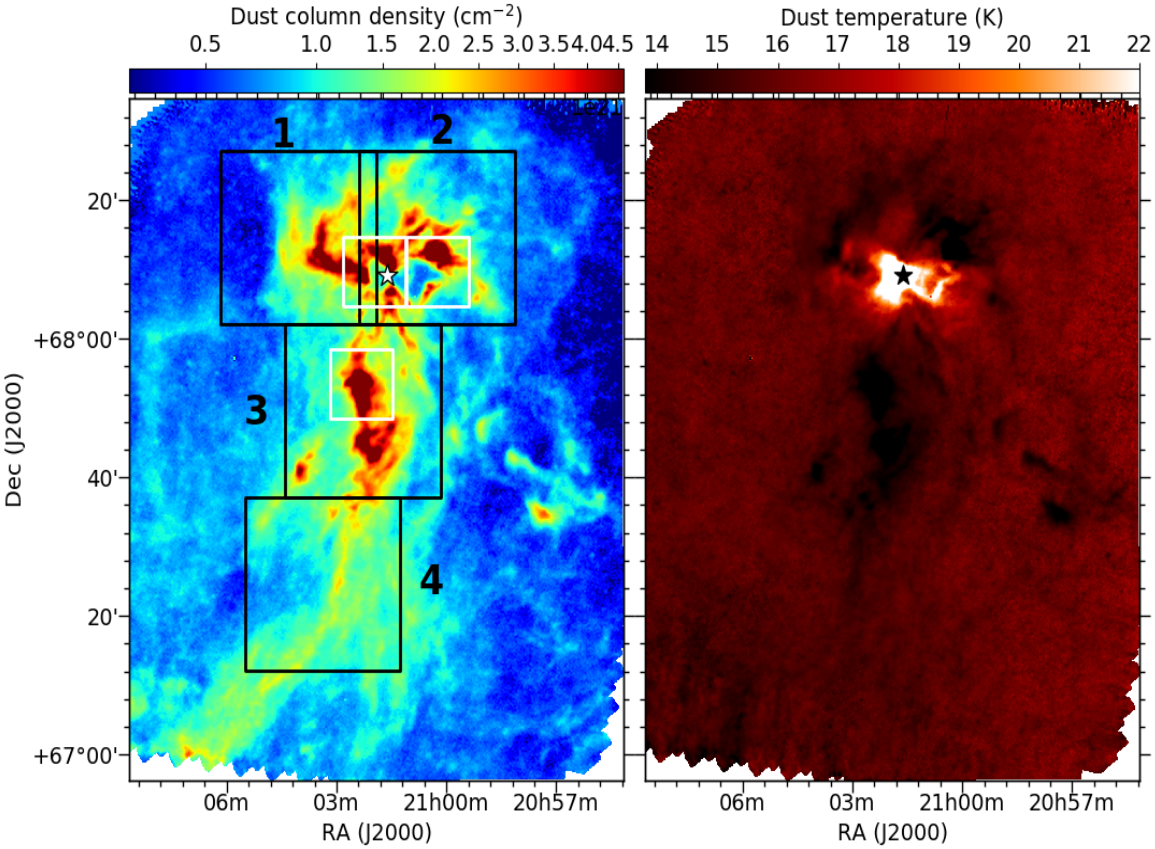

Figure 3.1: Dust column density (left panel) and temperature map (right panel) of the L1172/1174 complex. The black squares represents the pointings used for ^{12}CO and C^{18}O (1-0) molecular lines using TRAO. The white squares mark the regions observed for N_2H^+ (1-0) and CS (2-1) line emission. Each of the three white boxes is of size $10' \times 10'$. The star represents shows the position of central star HD 200775.

the pointings for ^{12}CO and C^{18}O lines having size of 25′ and the black boxes represent the regions observed for N_2H^+ (1-0) and CS (2-1) lines. Since the head region hosts HD 200775 where the gas dynamics might have effect from the stellar radiation, we divided the region in two parts and inspected the average profiles. The fields numbered as 1 and 2 are identified as head and the fields 3, 4 are identified as tail region of L1172/L1174 complex. We will study the properties of the tail region in the next chapter. The temperature map is shown in right panel of Fig. 3.1. There is bright emission around the central star showing high temperature (higher than 20 K) and there are dark structures around the head region and towards the southern part of the complex with temperature around $\sim$ 14 K.

Fig. 6.2 shows the average spectrum for the head in the left panel and tail in the right panel. In both the regions, there is presence of single peaked profile in C^{18}O line which implies that there is a single cloud component along the line-of-sight. The ^{12}CO profiles show high velocity wings towards

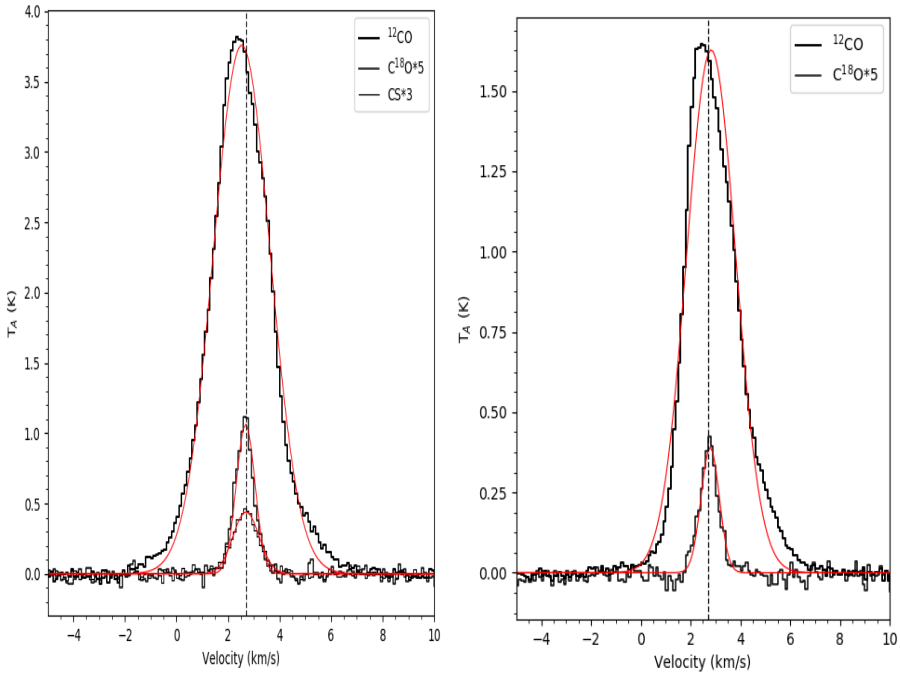

Figure 3.2: ^{12}CO (J = 1-0), C^{18}O (J = 1-0), CS (2-1) averaged spectra of the head region (left) and tail region (right panel). The black dashed line represents the intensity peak at systematic velocity of the cloud $\sim$ 2.7 km s^{-1}. The x-axis is labelled with the velocity in units of km s^{-1}.

the lower and the high velocity ends whereas in the tail region the ^{12}CO profile is relatively narrower. The averaged ^{12}CO (1-0) and C^{18}O (1-0) spectra of the whole mapped region where line profiles have emission higher than 3σ are shown in Fig. 6.2. The C^{18}O line is scaled up by a factor of 5. Based on a Gaussian fit to the ^{12}CO (1-0) line, we obtained a peak velocity of 2.5 km s^{-1}. There is no evidence of any additional foreground or background component along the line-of-sight. The averaged spectrum of C^{18}O also shows a single peak at 2.7 km s^{-1}. The line width of ^{12}CO is found to be ~2.35 km s^{-1}while C^{18}O is comparatively narrower with a line width of ~0.7 km s^{-1}. An averaged profile of the CS (2-1) line (scaled by a factor of 3) is also shown in Fig. 6.2. The CS (2-1) line is mapped over a smaller region of $20' \times 11'$ size around HD 200775.

The peak velocity of ~2.7 km s^{-1}found for the CS (2-1) line matches well with that of the C^{18}O , but is found to be relatively broader with a line width of ~ 1.2 km s^{-1}.

In this chapter, we will be discussing the kinematics of the structures in the upper part, NGC 7023 and the tail region having an elongated structure will be discussed in chapter 4.

NGC 7023 is a bright reflection nebula in the Cepheus constellation illuminated by the HD 200775 having a total luminosity of ~1500 L$_\odot$ (Hernández et al., 2004) and an effective temperature of 17,000 K (Baschek et al., 1982). This star is identified as a double-line spectroscopic binary system having primary and secondary masses of 10.7±2.5 M$_\odot$ and 9.3±2.1 M$_\odot$, respectively (Alecian et al., 2008). An outflow from the HD 200775, currently defunct, is believed to be responsible for the generation of an asymmetric east-west bi-conical cavity that is filled with hot atomic gas (Fuente et al., 1998b). The cavity and the structures found associated with the edges of the cavity have been the focus of several multi-wavelength observations ranging from optical to radio (An & Sellgren, 2003; Berné et al., 2008; Fleming et al., 2010; Fuente et al., 2000, 1998b; Gerin et al., 1998; Habart et al., 2011; Köhler et al., 2014; Lemaire et al., 1999; Rapacioli et al., 2005; Werner et al., 2004; Witt et al., 2006; Yuan et al., 2013). Several low mass young stellar objects (YSOs) have been identified around HD 200775 and majority of them are found to lie within ~1 pc distance from the star (reference). The dark region in the west of the nebula is the obscured region L1174 (Lynds, 1962; Myers et al., 1988, 1983). Rector & Schweiker (2013) detected four new Herbig-Haro (HH) objects in L1174 implying that star formation is still active. Based on near-IR imaging of the fields containing HAeBe stars, Testi et al. (1997) and have found a richness in the stellar density as a function of spectral type of the stars.

Recently, based on the *Gaia* parallax and proper motion values of individual YSOs identified towards the direction of NGC 7023 by Kun et al. (2009), Kirk et al. (2009) and Yuan et al. (2013), Saha et al. (2020) estimated a distance of 335±11 pc to it.

Myers et al. (1983) conducted one of the first molecular line mapping observations in ^{13}CO J=1-0 and C^{18}O J=1-0. The observations were carried out with a half power beam width of ~ 2″ and velocity resolution of 0.1 km s^{-1}. Bontemps et al. (1996); Myers et al. (1988); Wu et al. (1992) found the presence of CO outflow in L1174. Based on NH_3 (J, K) = (1, 1) Goodman et al. (1993) measured an average velocity gradient of 0.87±0.32 in L1174. Subsequently, L1174 was observed in several molecular line (DCO^+, H^{13}CO, CH_3OH, c-C_3H_2, DCN, N_2H^+) (Buckle & Fuller, 2002; Walsh et al., 2004; Williams et al., 1998).

Table 3.1: Log of molecular line observations

Molecule	ν_{rest} (GHz)	θ_{FWHM} ($''$)	Size of a field ($'$)	δv (km s^{-1})	T$_{rms}$ (K)
^{12}CO (1-0)	110.201353	47	$26^{'} \times 26^{'}$	0.1	0.3
C^{18}O (1-0)	109.782160	47	$26^{'} \times 26^{'}$	0.1	0.1
N_2H^+ (1-0)	93.173764	56	$10^{'} \times 10^{'}$	0.06	0.06
CS (2-1)	97.980953	52	$10^{'} \times 10^{'}$	0.06	0.1

In this chapter we present results of molecular line observations of the region surrounding the star HD 200775. The main goals of this study is to understand, (1) What is the kinematics of gas around HD 200775? (2) The dynamical state of cores found surrounding the star and (3) Is there local and global velocity gradient in the gas. The chapter is organized in the following manner.

First we explain the dust emission over the full complex in terms of extraction of filaments and clumps over the head region of the complex. Further, we explain the gas distribution over the full complex in terms of channel maps. The velocity distribution of all the cores and filaments will be discussed. The magnetic field (B-field) is discussed with the polarization measurements. Finally, we discuss the individual regions by inspecting their line profiles.

3.2 Observations and data reduction

3.2.1 Molecular Line Observations

In molecular clouds, ^{12}CO is the second most abundant molecule after H_2. Therefore, it can trace the basic cloud structure reasonably well. On contrary to this, spectral lines of molecules made of rare isotopologues like C^{18}O can trace relatively denser gas with densities of 10^3 - 10^4 cm^{-3}. In order to trace the dense cold gas, N_2H^+ molecule is observed with a critical density of 10^5 cm^{-3}, particularly in the prestellar phase, very well (Caselli et al., 2002a; Punanova et al., 2016). In order to trace the structure of the whole cloud L1172/L1174 at different density regimes, it was observed in ^{12}CO , C^{18}O , N_2H^+ (1-0) and CS (2-1) transitions using On-The-Fly (OTF) mapping technique. Observations were made with the 14 m diameter single-dish telescope of Taedeuk Radio Astronomy Observatory in Daejeon, South Korea between November 16-28, 2018. The pointing accuracy achieved was $\leq 5''$ using a standard X Cygnus source in the SiO line. As mentioned in chapter 2, the optical system provides 2-side-band, two different lines can be observed simultaneously. C^{18}O line which reveals the dynamics of high density regions of a cloud was simultaneously observed with ^{12}CO line and similarly, N_2H^+ was observed with CS (2-1) transition as the former is an optically thin line and the latter is an optically thick line.

Table 3.1 shows the details of line observations observed for L1172/1174 complex. Column 1 and 2 shows the line tracer used with the rotational transition and their respective frequencies in GHz.

Third column gives the angular resolution of each molecular line and fourth one gives the size of each pointing used to cover the whole complex. As also shown in 3.1, there are four pointings covered in ^{12}CO and C^{18}O lines whereas three pointings in N_2H^+ (1-0) and CS (2-1) tracers. Column 5 and 6 shows the final velocity resolution of each data cube and average standard deviation in Kelvins for emission in each line. The map is sampled at a grid size of 20″ which corresponds to spatial resolution of ~0.033 pc at a distance of 335 pc. Spectral resolution of 0.05 kms^{-1} was used and the typical rms noise in one channel was ~0.09 K for C^{18}O and ~0.35 K for ^{12}CO lines. The data was reduced and visualised with the CLASS and GREG programs of GILDAS software. The baselines were fitted with first order polynomial and removed in each line. More details about the telescope and its back end instruments can be found in (Jeong et al., 2019).

3.2.2 Dust continuum data

The dust column density and temperature maps were taken from the *Herschel Gould Belt Survey Archive* which were obtained by fitting spectral energy distribution (SEDs) of each pixel over a wavelength range of 160 μm and 500 μm with a modified blackbody function. The Planck offsets at each wavelength has been added to each Herschel PACS-SPIRE image. The details have been taken from (Di Francesco et al., 2020). The modified blackbody used in the SED fitting includes a dust opacity, τ = 0.144 cm^2 g^{-2} at 250 μm (incorporating a dust-to-gas ratio of 100) with a power-law dependence with wavelength of index, β = 2.0 Hildebrand (1983). Here the mean molecular weight per H_2 molecule, is assumed to be μ= 2.8 (Koenig et al., 2008) to convert gas surface density into H_2 column density. Each data point in SED fit was weighted by $1/\sigma^2$, where σ was calculated using the pixel values in emission-free region of the map in each wavelength and the calibration uncertainties were also included. The two free parameters, T_d and N(H_2) were derived from the grey-body fit to the four wavelength points for all pixels. The pixels having bad or unreliable fits were assigned the median value of the dust temperature of those pixels having good fits.

3.2.3 Planck polarization measurements in sub-mm

We estimated the Stokes I, Q and U parameters from the smoothed *Planck* map of a region obtained from the *Planck* 353 GHz image centered at HD 200775. Stokes I (total dust intensity) and Q, U (two components of the linearly polarized dust emission) parameters are related as Q = Ipcos(2ψ), U = Ipsin(2ψ). The total polarization P is related to the Q and U values as P = $\sqrt{Q^2 + U^2}$ and the fraction of the polarization fraction as P/I. The polarization angle, ψ, is related to Q and U values as ψ = 0.5 arctan(U, Q). The ψ is measured with respect to the Galactic coordinates with -90° < ψ < +90°, ψ = 0° toward Galactic north, increasing toward Galactic west (HEALPix convention). The angle of B_{POS} (χ) can be obtained by adding 90° to the polarization angle ($\chi = \psi + 90°$). The Stokes parameter maps are shown in accordance with the IAU convention (ψ = 0° toward the Galactic north,

increasing toward the Galactic east) (Hamaker, J. P. & Bregman, J. D., 1996), using the relation U = -Ipsin(2ψ).

We extracted the Planck polarization maps for the 1.5°×1.5 ° square size using at an angular resolution of 4.8′. The details of the extraction and the final construction of map is explained in chapter 2. The polarization sensitivity was expected to be such that, at a resolution of 15′, ISM structures with A_V = 1 mag would be detected with a relative uncertainty on the polarization fraction ∼ 40% and an uncertainty on the polarization angle ∼ 30° (Pelkonen et al., 2009).

3.3 RESULTS

3.3.1 Spatial distribution of dust around HD 200775

Using the *Herschel* images obtained with the instruments, the PACS (Poglitsch et al., 2010) at 160μm and the SPIRE (Griffin et al., 2010) from 250μm to 500 μm wavelengths, a dust temperature (T_d) map and a column density (N_{H_2}) map of the entire L1172/1174 complex were produced by (Di Francesco et al., 2020). The maps are produced at a spatial resolution of 36″ with a pixel grid of 3″. Since the beam size of TRAO is 44″, we have used the images at almost similar resolution to compare the dust and gas emission at same angular scale.

The modified blackbody used in the Spectral Energy Distributions (SEDs) fitting of each pixel includes a dust opacity, τ = 0.144 cm^2 g^{-1} at 250 μm (incorporating a dust-to-gas ratio of 100) with a power-law dependence with wavelength of index, β = 2.0 Hildebrand (1983). In addition, the mean molecular weight per H_2 molecule of μ = 2.8 is assumed here (Kauffmann et al., 2008) to convert gas surface density into H_2 column density.

In Fig. 3.3 we present the dust column density and the temperature maps of the region surrounding HD 200775 (identified using a star symbol in white). The dust emission is found to show distinct high density and low density structures around the star. The spatial distribution of material around HD 200775 is found to be asymmetric with more material lying to the north of the star delineating the asymmetric east-west biconical cavity studied in detail by Fuente et al. (1998b) which is conspicuous in Fig. 3.3. The value of N(H_2) varies from $\sim 3.3\times10^{20}$ cm^{-2} to $\sim 2.8\times10^{22}$ cm^{-2}. The temperature map of the region surrounding HD 200775 is presented in Fig. 3.3 (right panel). T_d is found to range from 11 K to 42 K. The T_d is found to be maximum around HD 200775. The bicanonical cavity surrounding HD 200775, in general, shows higher temperatures. The low temperatures are seen towards the dense structures seen in Fig. 3.3 (left panel).

- **Extraction of Filaments around HD 200775:**
  To identify the filaments around HD 200775, we used the *Filfinder* algorithm (Koch & Rosolowsky, 2015) on the column density map at the resolution of 36″.

  Details of how the algorithm works are given in chapter 2. To derive a mask (a crucial factor in determining the filaments), a global threshold of 3 times the background column density (N_{bg}

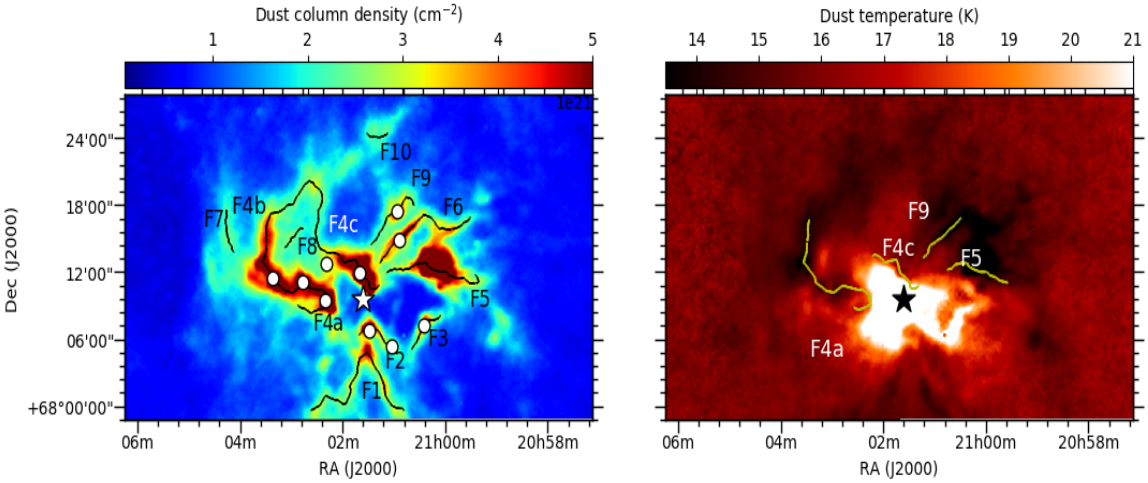

Figure 3.3: The dust column density map (left) and the temperature map (right) of the region surrounding HD 200775. The position of HD 200775 is identified using a star symbol in black.

$\sim 0.7 \times 10^{21}$ cm^{-2}) was used with an adaptive threshold of 0.2 pc (twice the expected filament width (Arzoumanian et al., 2011)). The size threshold corresponds to an area of ellipse with a width of 0.1 pc and an aspect ratio of 5.

We obtained a total of 10 filaments around HD 200775 using the *Filfinder* algorithm that are identified using solid curves in black in Fig. 3.3. Six of the 10 filaments (F1, F2, F4, F5, F6, F9) are oriented radially with respect to HD 200775. Filament F4 is the longest of all with a total length of $\sim$ 4 pc. The filament presents a loop structure with its end points terminating at the dense structures lying to the north and to the east of HD 200775. For the convenience of analysis we divided F4 into two parts as F4a and F4b which form the eastern and the northern arms of F4 respectively. The cloud L1174 is located on the filament F5. Filaments F3, F7, F8 and F10 are shorter (0.5, 0.4, 0.3 and 0.3 pc) and oriented orthogonal to the direction of radiation from HD 200775.

- **Radial profile distribution of extracted filaments:**
  The radial profiles of the filaments having a column density contrast of 5 are derived. The background column density is a local property of every filament and varied through the full column density map. The fitting of average profile with Plummer function could not be fit if the column density contrast is less than a factor of 5 because the background column density for some of the filaments is higher than the peak column density. This happens because of the close proximity of the filaments to each other. The filament F4 splits into two F4a and F4c towards the north and east of HD200775 at the threshold of 5 times the background column density. We fitted a Plummer-like function (Nutter et al., 2008) and a Gaussian function to the average column density profiles on three filaments which are shown with yellow color

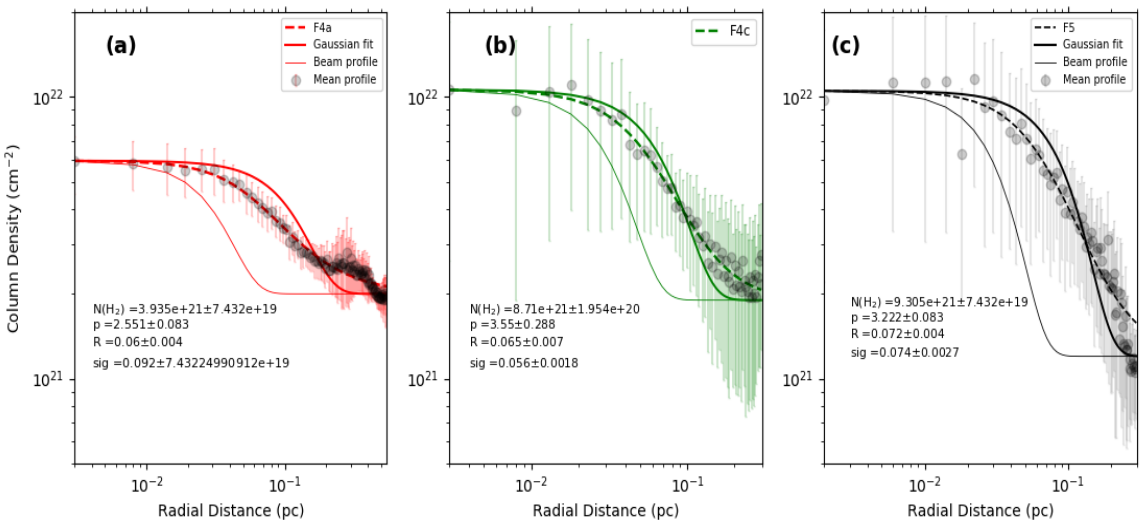

Figure 3.4: Mean radial column density profiles of three filaments F4a (a), F4c (b), F5 (c) in gray filled dots. In all the three panels, dashed curve in the respective color represents the best-fit of Plummer model. The solid thick curve shows the Gaussian fit while thin solid curve shows the beam profile. The best-fit parameters for each filament are shown in plot itself.

curves in right panel of Fig. 3.3. The resulting mean radial column density profiles for the three filaments are shown in Fig. 3.4. The fitting radius was taken as 0.3 pc for F4a and local background density was taken as 0.7× 10^{21} cm^{-2}. We then sampled the radial profile with cuts perpendicular to the crest. The positions of the cuts along the crest were separated by 20 pixels to ensure that the profiles at the crest position are not correlated. The presence of high density peaks of cores along the length of filament may effect the estimation of filament properties and should be removed. Therefore, the cuts over the crest of filament was taken as two times the beam width spread over the length of filament. This decreases the effect of nearby clumps and local column density peaks. Consequently, the 0.72 pc long filament was sampled with 12 profiles. We sampled the filament F5 towards the western part of it since it does not overlap with the local clumps or high density peaks. The background subtracted data was further used to fit it using the Plummer-like function to determine N° (amplitude), p (spectral power index), R_{flat} (flattening radius). Depending on the initial estimate of the background level near the crest of the filaments, a range of fitting radii was tried and fixed to a value. The second filament was fitted with a radius of 0.5 pc. We restricted the fitting distance to 0.3 pc. The filaments, which are not centrally condensed enough, are not fitted with the Plummer-like and the Gaussian function.

- **Extraction of Clumps around HD 200775:**
  We used *Astrodendro* algorithm to identify high density clumps in the column density map. We chose the minimum threshold value as 2.8×10^{21} cm^{-2}, which is four times the background

column density value. The other parameter is min-delta which is defined as the minimum difference in temperature or intensity of two structures before it gets combined into a single entity. We set min-delta as 0.7×10^{21} cm^{-2} which is the background threshold value. The high density regions extracted are called leaves in dendrogram. We extracted 12 clumps in the head part of the complex. The advantage of using Astrodendrogram is that it also gives information on the orientation of identified clumps.

A total of 10 clumps (C1-C10) are identified around HD 200775 which are marked and labelled in Fig. 3.3 (a) with filled circles in white. Three clumps are identified towards the filament F4a, one clump over F4c. Filament F2 has two clumps. F4c has one clump. F3, F6 and F9 have one clump each. There is a clump in between F4a and F4c which does not lie on any extracted filaments. We found two clumps towards the cloud LDN 1174 which are located on the filament F5. These clumps were removed from the sample on the basis of area covered by pixels. The core has resolved into two peaks as seen in *Herschel* dust emission map with $N(H_2) \sim 3 \times 10^{22}$ cm^{-2}. We will explain the dust and gas properties of the core separately in discussion.

3.3.2 Spatial distribution of gas around HD 200775

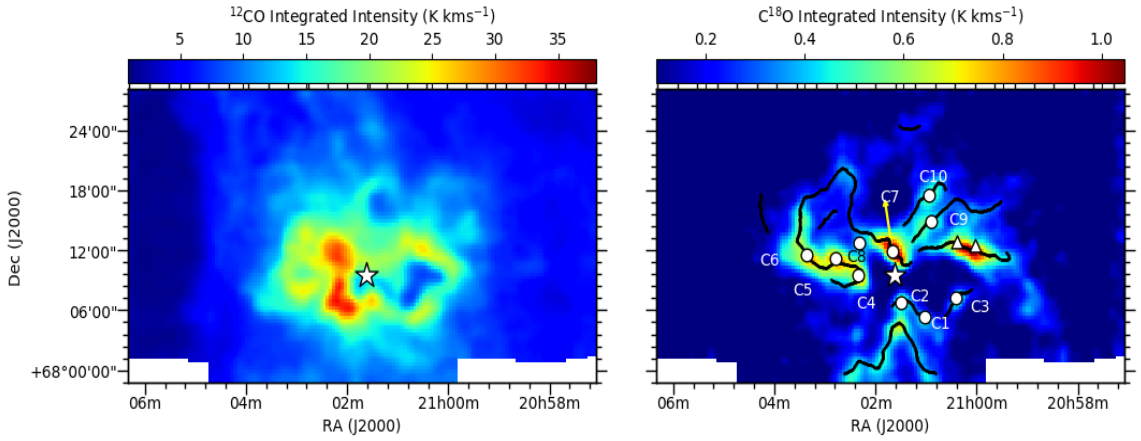

Figure 3.5: Integrated intensity images of ^{12}CO (left) and the C^{18}O (right) gas emission. The position of HD 200775 is identified using a star symbol in black. The positions of the cores are labelled from 1-10 using white filled circles. White triangles show the resolved peaks around L1174 core.

Fig. 6.3 shows the distribution of ^{12}CO and C^{18}O gas around the central star HD 200775. The moment maps for ^{12}CO and C^{18}O are created by using those channels having temperature values exceeding 0.3 K and 0.1 K (approximately 3 times the rms level per channel) respectively. The integrated intensity distribution of ^{12}CO towards HD 200775 is shown in Fig. 6.3 (a). The ^{12}CO is

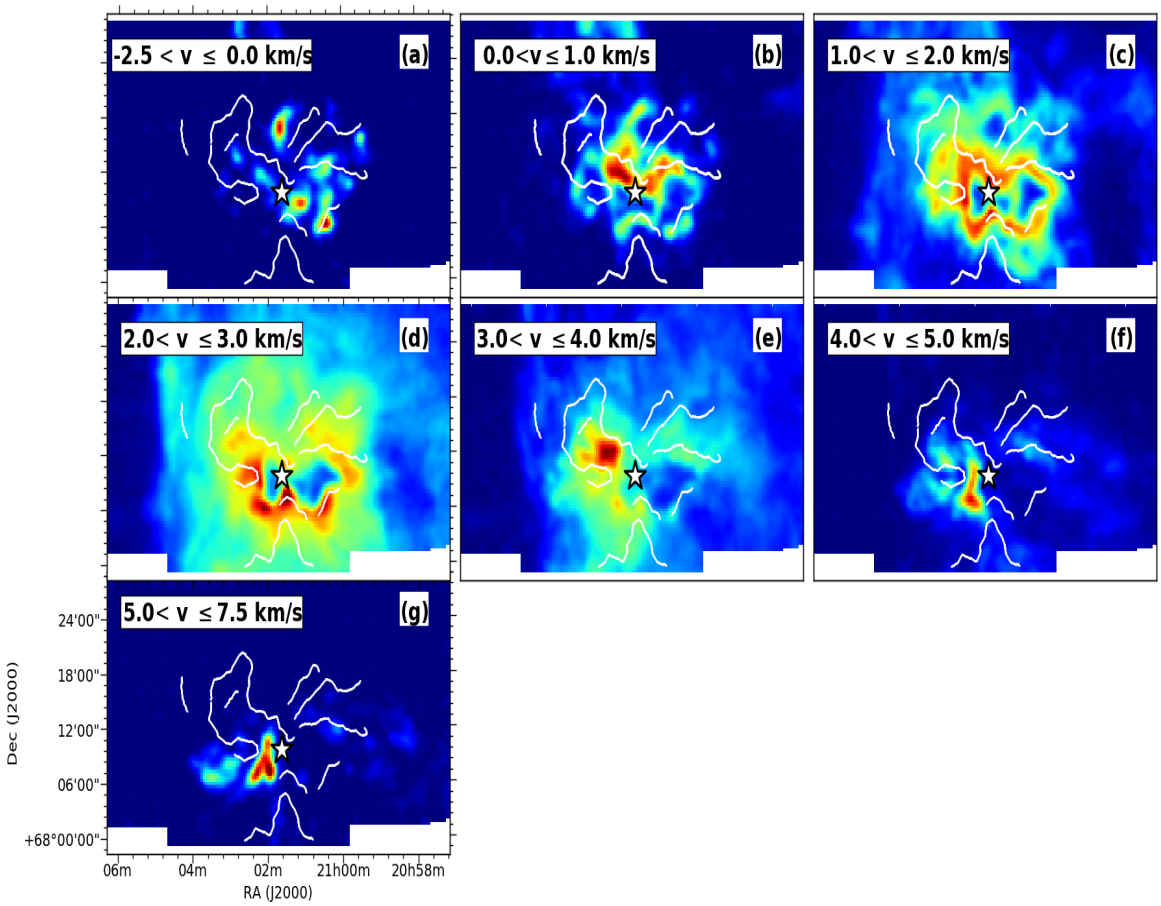

Figure 3.6: Channel maps for ^{12}CO line. Each channel shows the velocity range used for the integrated emission. The intensity is in the units of K km s^{-1}.

integrated over a velocity range of -2.5 - +7.5 km s^{-1}. The ^{12}CO emission intensity is found to be maximum along the rim of the biconical cavity identified by Fuente et al. (1998b). Within the cavity, the distribution of ^{12}CO emission intensity is found to be asymmetric with more intense emission emerging from the eastern parts of the cavity than the west.

The distribution of C^{18}O (1-0) emission is shown in Fig. 6.3 (b) in units of K kms^{-1}. The intensity levels are taken from 0.1-1.3 K kms^{-1} in steps of 3σ= 0.1 K kms^{-1}. The velocity channels used for the summation are in the range of 1.5-3.6 km s^{-1}. The C^{18}O appears to correlate very well with the high dust column density regions shown in Fig. 3.3. The bipolar cavity (Fuente et al., 1998b) seen around HD 200775 seems to be devoid of C^{18}O gas as reported in the earlier studies (Fuente et al. (1998b)). The spatial region of ^{12}CO emission (greater than 3 σ) is much more extended than the C^{18}O gas emission. The C^{18}O emission is quite structured around the central star and shows multiple high density peaks identified as clumps in Fig. 3.3 with white filled circles.

Velocity structures of the gas around HD 200775 are very complex as evident in the velocity channel maps of ^{12}CO and C^{18}O emission shown in Fig. 6.4 and Fig. 6.5. The ^{12}CO gas is distributed

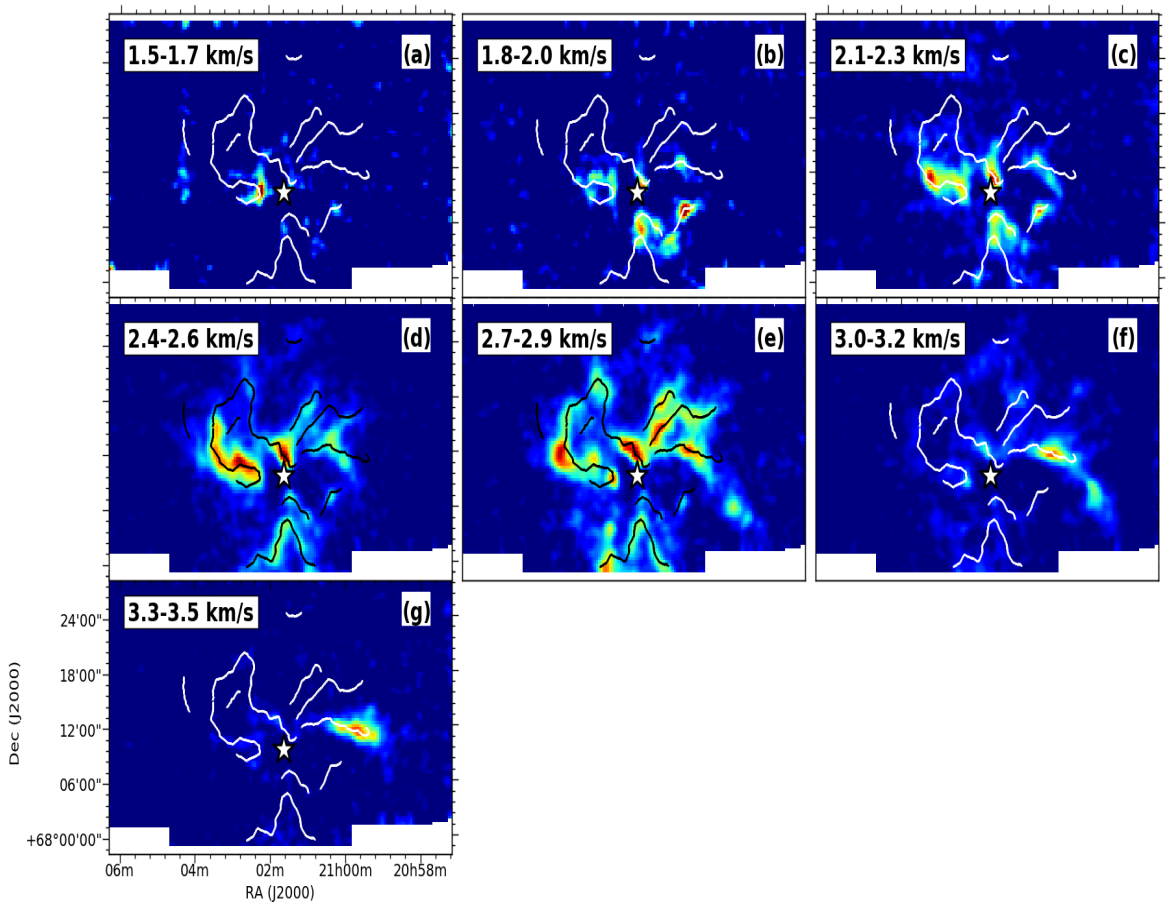

Figure 3.7: Channel maps for $C^{18}O$ lines. The solid black lines represent high density skeletons derived from *Filfinder*. Each channel shows the velocity range used for the integrated emission. The intensity is in the units of K km s^{-1}. The background intensity is 0.02 K km s^{-1}.

over multiple velocity channels from -2.5 to 7.5 km s^{-1}in Fig. 6.4. Only those values of the integrated intensities are shown which are greater than σ of the region ($\sigma \sim \sqrt{N} T_{rms} V_{res}$), where N is the number of channels, V_{res} is the velocity resolution and T_{rms} is the rms of the data cube. We noticed the presence of blue-shifted high velocity gas in the velocity range -2.5 to 0 km s^{-1}that resides towards the cavity as shown in panel (b). The integrated intensity varies from 0.15 to 4.7 K km s^{-1}. The emission shows bright clumps seen towards the northern and the western end of the nebula which is in the vicinity of the cavity. The structure of the gas extends first symmetrically towards the northern side of the central star in velocity range 0-1 km s^{-1}in panel (c) and then the southern side of central star in panel (e). The panel (d) shows the most prominent structure of bipolar asymmetrical shape of emission in the direction of the cavity. The maximum intensity of ^{12}CO emission is present on the eastern side of the central star with value $\sim$ 10 K km s^{-1}whereas the minimum intensity is found around the cavity on the western side. There is a clear evidence of difference in the integrated intensity of ^{12}CO emission towards the central star than in the diffuse regions. The presence of red-shifted high velocity gas in the velocity range from 5.0 to 7.5 km $s^{-1}$is much more localised residing to the eastern side of the central star with integrated intensity values varying from 0.2 to 9 K km s^{-1}. This high velocity gas has the potential to affect the high density structures around the nebula which are traced by C^{18}O line.

Fig. 6.5 shows channel maps of C^{18}O line from 1.5-3.5 km s^{-1} in steps of 0.2 km s^{-1} (twice the isothermal sound speed). The high density skeletons are represented by solid white lines from 1 to 10 in panel (g). Red solid lines shown in panel (f) marks the location of the high density skeletons derived with threshold greater than $5\sigma \sim 3.5 \times 10^{21}$ cm^{-2}. In panel (a) from 1.5-1.7 km s^{-1}, the dominant feature is coming from north-eastern side of HD 200775 which appears like a bright rim turning in the form of filament F4a. The emission in panel (b) from 1.8 to 2.0 km $s^{-1}$is localised towards the south-west region of HD 200775 on one side of the cavity. In panels (d) and (e), the gas looks originating radially away from HD 200775 in the direction of the crests of filaments. The gas emission from F4a and F4c are more prominent in panel (d). In panel (e), the shell like structure is observed tracing filament 4 which splits up into three filaments 4a, 4b, 4c as the column density varies from 3 to 5 times the threshold used in Filfinder algorithm. The channels around the cloud's velocity from 2.7 to 2.9 km $s^{-1}$are strongly dominated by cloud emission. Most of the high density structures in the neighbourhood of HD 200775 appear in this velocity range. In panel (f) from 3.0 to 3.2 km s^{-1}, the gas emission is predominantly observed on eastern side and in panel (g) 3.3 to 3.5 km s^{-1}, the red-shifted emission is completely associated with the filament F5. Overall, the C^{18}O emission has a variation from east towards west of HD 200775. The structures are not velocity coherent and the positions of the peak intensities are shifted in position and in velocity space. The filaments F7, F8 and F10 do not show significant gas emission. Therefore, we will not consider them in characterizing the filament properties using gas.

Estimation of physical parameters of the gas: A single velocity component is seen in C^{18}O line emission, suggesting that there is a single cloud component along the line-of-sight. Although the

average spectrum of ^{12}CO represents a single peak over the mapped region, it exhibits multiple velocity components at different positions due to contamination from the low density regions. The kinematic information of the gas emission in the cloud has been extracted by fitting a Gaussian model to C^{18}O profiles. We examined individual spectrum and fitted independently using one component at each individual position in C^{18}O lines.

To investigate the physical status of the clumps, we derived various fundamental properties like excitation temperature, optical depth, and the number density are derived using spectral data obtained at different positions of the cloud. Two assumptions have been made to estimate the column density (N_{18}) based on C^{18}O and ^{12}CO lines; the molecules along the line of sight possess a uniform excitation temperature for J = 1 − 0 transition and the J = 1 − 0 excitation temperatures of the two isotopic species are equal (e.g., Dickman, 1978; Sato et al., 1994). The emission from ^{12}CO molecule is optically thick and common excitation temperature (T_{ex}) is calculated from the peak ^{12}CO brightness temperature using the expression, $T_b = T_R^{12}/\eta_{eff}$, where η_{eff} is the beam efficiency of TRAO telescope. The brightness temperature, T_b^{12}, is calculated as follows,

$$T_b^{12} = T_0^{12}[f_{12}(T_{ex}) - f_{12}(2.7)], \tag{3.1}$$

where T_0^{12} is the temperature corresponding to the energy difference between the two levels given by $T_0^{12} = h\nu_{12}/k$, here ν_{12} is the frequency for J = 1 − 0 transition. In the same manner, the optical depth of the C^{18}O line (τ_0^{18}) is also calculated from the peak brightness temperature and the excitation temperature (T_{ex}) using the expression,

$$T_R^{18} = T_0^{18}[f_{18}(T_{ex}) - f_{18}(2.7)][1 - \exp(-\tau_0^{18})]. \tag{3.2}$$

The column density along the line of sight is calculated as follows,

$$N_{18} = \frac{3h\triangle\nu_{18}}{8\pi^3\mu^2}\frac{\tau^{18}Q}{[1 - \exp - \frac{T_0}{T_{ex}}]}, \tag{3.3}$$

where Δv_{18} is the line full width at half maxima in velocity units, μ is the permanent dipole moment of the molecule, h is the Planck constant and Q is the partition function. Again an assumption has been made regarding the partition function, which depends upon the excitation temperatures of all significantly populated states of the molecule like:

$$Q = 1 + \sum_{L=1}^{+\infty}(2L+1)\prod_{J=0}^{L}\exp[-h\nu(J)/kT_{ex}(J)], \tag{3.4}$$

where ν(J) and T_{ex}(J) are the frequency and excitation temperature of the transition J = 1 − 0, respectively. So we assume that all the levels have same T_{ex}. The partition function can be written as Q= $\frac{2T_{ex}^{18}}{T_0^{18}}$. But all the lines are not fitted to a perfect Gaussian. Thus the chi-square minimization has been done to determine the goodness-of-fit. We obtained integrated intensity (moment 0) maps of ^{12}CO,

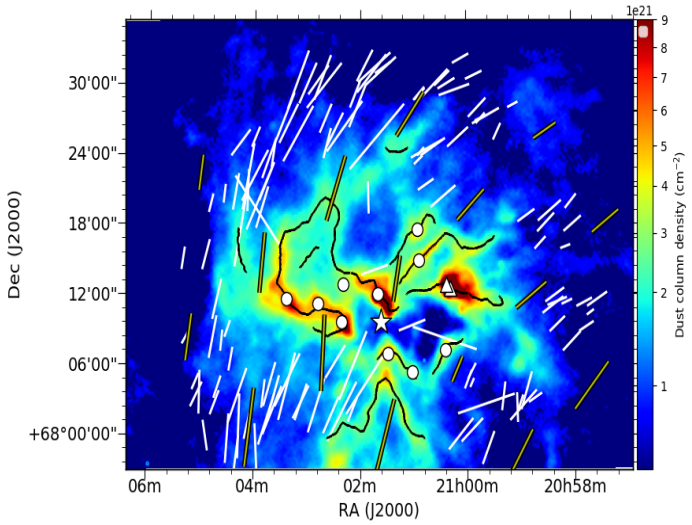

Figure 3.8: The dust column density map of the region (in colorscale) surrounding HD 200775. The position of HD 200775 is identified using a star symbol in white. The curves lines in black marks the positions of skeletons derived using Filfinder algorithm and white filled circles represent the cores derived using Astrodendrogram. Yellow bold lines represent the Planck vectors and the white lines represent the R-band polarization vectors.

$C^{18}O$ using spectral data cubes with position-position velocity information. The values below 3σ were not considered to obtain summation over the channels. The rms value of each line map was calculated as $\sim \sqrt{N}\delta \mathrm{v} \mathrm{T}_{rms}$, where N is the number of channels used for integrating the emission, δv is the velocity resolution and T_{rms} is the noise of the line profile.

3.3.3 Polarization measurements:

Fig. 3.8 shows the results of the *Planck* polarization and optical polarization measurements which are overplotted on the dust column density map. The selective extinction of starlight by dust grains and thermal re-radiation in the longer wavelengths are the ways through which we can infer effects of dust grains. The spinning grains are believed to get oriented with their longer axis perpendicular to the magnetic field lines (Davis & Greenstein, 1951; Lazarian, 2003). When the unpolarized starlight passes through a series of aspherical dust grains, the electromagnetic wave is absorbed maximum along the long axis of grain. The transmitted radiation becomes partially plane polarized and lies along the plane-sky (B_{POS}) projection of magnetic field (Whittet, 2005). When the dust grains re-radiate, it is maximum along the longer axis, thus becomes polarized perpendicular to B_{POS}. Since dust grains are coupled with the magnetic field, measurements of dust polarization provide information on the structure and the strength of the B-field. The value of θ depends on the orientation of the B_{POS} and the efficiency of the dust grain alignment with the field. The length of the polarization vectors

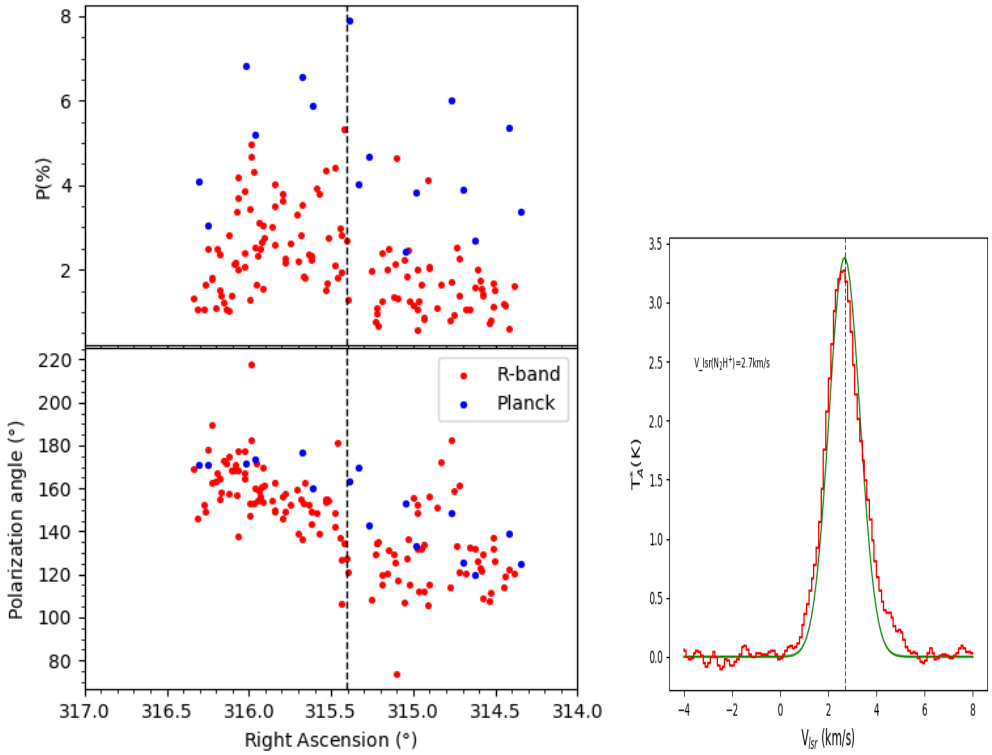

Figure 3.9: *Left:* Variation of degree of polarization and position angles with respect to the right ascension (in degree) around HD 200775 (position indicated with a dashed line).The polarization values obtained from our R-band and from the *Planck* are shown in red and blue filled circles. *Right:* Average profile of the ^{12}CO line at the position of the background stars at Right Ascension $\leq 315°$.

corresponds to the degree of polarization (P%) and the orientations correspond to the position angle (θ_P) measured from the north increasing towards east.

All these stars are lying background to the cloud as suggested by the distances of the stars obtained from the *Gaia* DR2 (Bailer-Jones et al., 2018) are larger than 335 pc. The polarization measurements in the optical bands trace the B_{POS} only in the outskirts of the molecular clouds where the extinction (A_V) is relatively low (Guetter & Vrba, 1989; Harjunpää et al., 1999) while the polarization measurements in sub-millimeter or millimeter can infer the B_{POS} inside the cloud where A_V is relatively high (e.g., Goodman, 1995; Greaves et al., 1999; Hildebrand et al., 1984). Far-infrared and submillimeter polarimetric observations made by the *Planck* have been used not only to infer the direction of the Galactic magnetic field but also to put new constraints on the properties of dust (Planck Collaboration et al., 2016a, 2015b, 2016b). The optical polarization vectors are well correlated with the Planck polarization measurements. A change in the values of θ_P is also apparent in both optical and Planck as the B-field on the eastern side is perpendicular to the filaments F4a and F4c. On the contrary, the structures on western side, F6, F7 and F9 are following the global field lines.

The change in the polarization angle and the degree of polarization as a function of their Right Ascension is further investigated in Fig. 3.9. In upper panel, we show the $P\%$ and in lower panel, θ_P obtained from both the R-band observations (red circles) and the *Planck* (blue circles). We find a good correlation between the orientation of the projected magnetic fields inferred from both the optical and the *Planck* data given the large uncertainty in the polarization values obtained from the *Planck* (Pelkonen et al., 2009). The location of HD 200775 is identified with a black line at right ascension of 315°. We find a systematic variation in both $P\%$ and θ_P as a function of positions with respect to HD 200775. The stars to the west of HD 200775 show relatively low values of $P\%$ when compared to those to the east.

It could be that the dust grains to the eastern side of HD 200775 are more aligned than to the western side as a result of the presence of their interaction with high velocity gas. The right panel of Fig.3.9 shows the signatures of high velocity red-shifted gas on the western side of HD 200775. Also, there is less polarization and angle is oriented more along the high density structures. This low polarization fraction is considered to be a well known phenomenon, *depolarization* in molecular cloud structures. The fraction of polarization is dependent on the dust grain properties such as composition, size and shape of dust grains (Lee & Draine, 1985). In addition, the efficiency of grain alignment and the magnetic field structure are also contributing factors in determining the polarization intensity (Hildebrand, 1988). The widely accepted reason for the low polarization in high density structures include the changes in the magnetic field orientation in the high density regions. We notice that the polarization angles shows higher dispersion which suggests that the B-field orientation is relatively disturbed on the western side ($\delta\theta \sim 22°$) as compared to the eastern side ($\Delta\theta \sim 18°$). The depolarization can happen because of more variations in B-field component. Our findings are similar to the ones suggested by Seifried et al. (2018) where the depolarization can be a consequence of the strong variation is the B-field component along the line-of-sight due to turbulent motions.

3.4 Discussion

3.4.1 Presence of high-velocity gas around HD 200775

The kinematical study of the molecular and atomic gases associated with HD 200775 was conducted by Fuente et al. (1998b). The presence of the bipolar outflow associated with this star was first proposed by Watt et al. (1986) by carrying out J=1-0 ^{12}CO and ^{13}CO observations at a spatial scale of 0.1 pc and 0.67 km s^{-1}spectral resolution. They found the presence of a ridge of emission in the north-south direction in their ^{12}CO maps with intensity peaks on either ends. From the channel maps of ^{12}CO presented in Fig. 6.4, the gas components at different velocity ranges show discernible structures particularly towards the high velocity ends. In Fig. 3.10 we show the distribution of high velocity gas around HD 200775. The colour composite image is made using high velocity gas in the velocity range of -2.5 to 0 km s^{-1}(blue) and 5.0 <v≤ 7.5 km s^{-1}shown in blue and red while the distribution of dust column density is shown in green colour. The position of HD 200775 is identified with a star symbol. The outflow is not isotropic but is confined primarily into two lobes with the blue- and red-shifted lobes lying predominantly on the western and eastern sides of HD 200775 respectively.

The dust column density map shows several discrete high density structures most of which are oriented radially pointing towards the central star. The column density structures that are often seen around massive stars are created as a result of the escape routes carved out by the wind as it blows away low density material revealing the pre-existing high density density structures. This creates cavities and channels of material as seen around HD 200775 in Fig.6.4. Numerical simulations performed to understand the effects of massive stars on their surrounding medium do show the creation of such structures (e.g., Dale et al., 2005; Fierlinger et al., 2012).

There are bright arc-shaped structures observed in channel maps as we move to larger velocities from systematic velocity of the cloud. We used ^{12}CO integrated intensity map over the velocity range in which the shells were clearly detected. Fig. 3.11 shows the color composite image where red represents ^{12}CO channel map from 1-2 km s^{-1}, green represents dust column density emission and blue represents the ^{12}CO emission in the velocity range 3-4 km s^{-1}. There is a presence of red-shifted high velocity gas predominantly on the eastern side and blue-shifted on the western side. The high density gas in filament F4a is seen to be highly influenced by the high velocity emission as it is being engulfed by the emission in red-shifted high velocity. Different shells are identified on either side of central star. There could be evidence of high velocity shells lying symmetrically with respect to HD 200775.

The position velocity (P-V) diagram shown in Fig. 3.12 is produced by plotting position and velocities along a cut shown using a white line in Fig.3.11. The origin of the cut is taken from east increasing towards the west. The distance of the star position is marked in PV diagram which is at ∼ 0.44 pc from the east. Along the cut, there is evidence of blue-shifted and red-shifted components in ^{12}CO emission. The three white lines mark the extent of the cloud velocity where bulk of the cloud emission is obtained between 1.7 and 3.7 km s^{-1}. High velocity peaks identified as shells are found

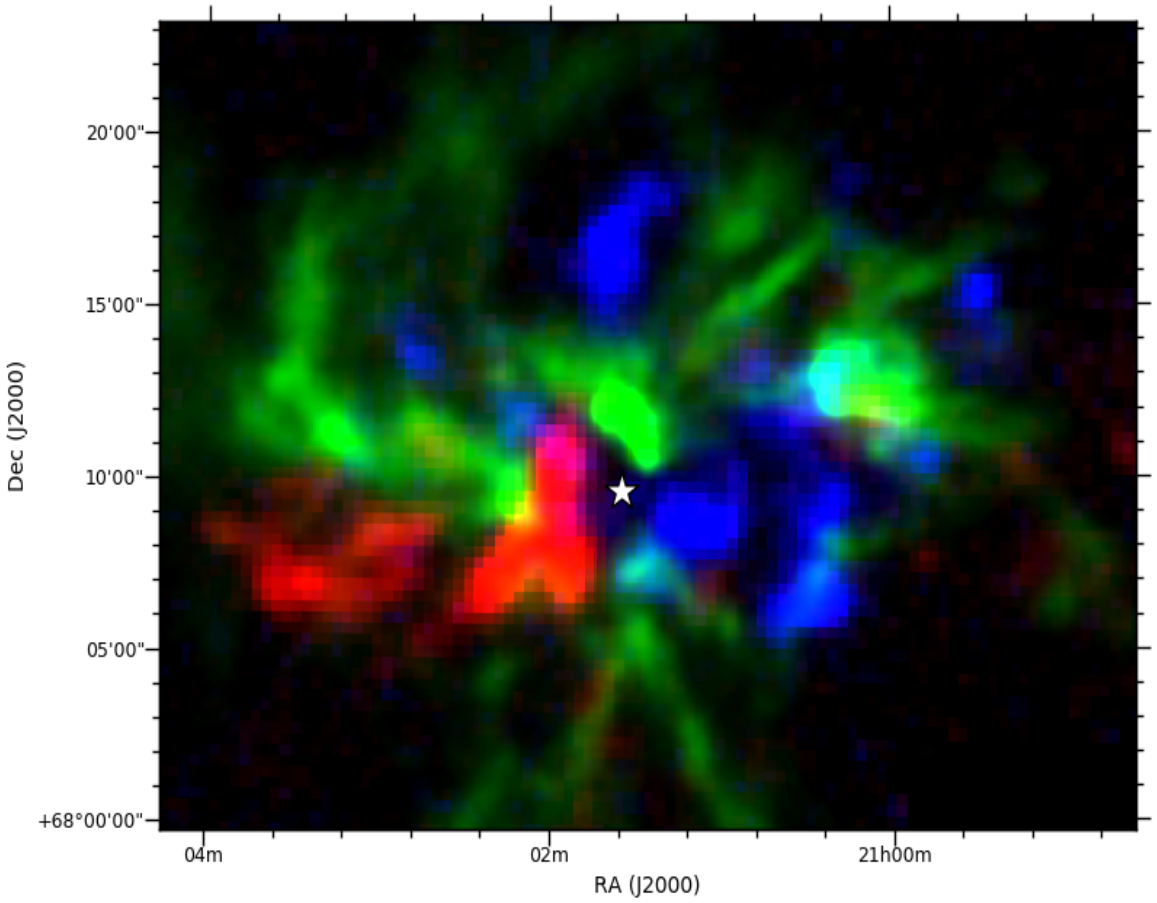

Figure 3.10: The colour composite image of the region around HD 200775. The image is made using ^{12}CO gas in the velocity range of -2.5 to 0 km s^{-1}(blue), 5.0 <v≤ 7.5 km s^{-1}(red) and dust column density map (green).

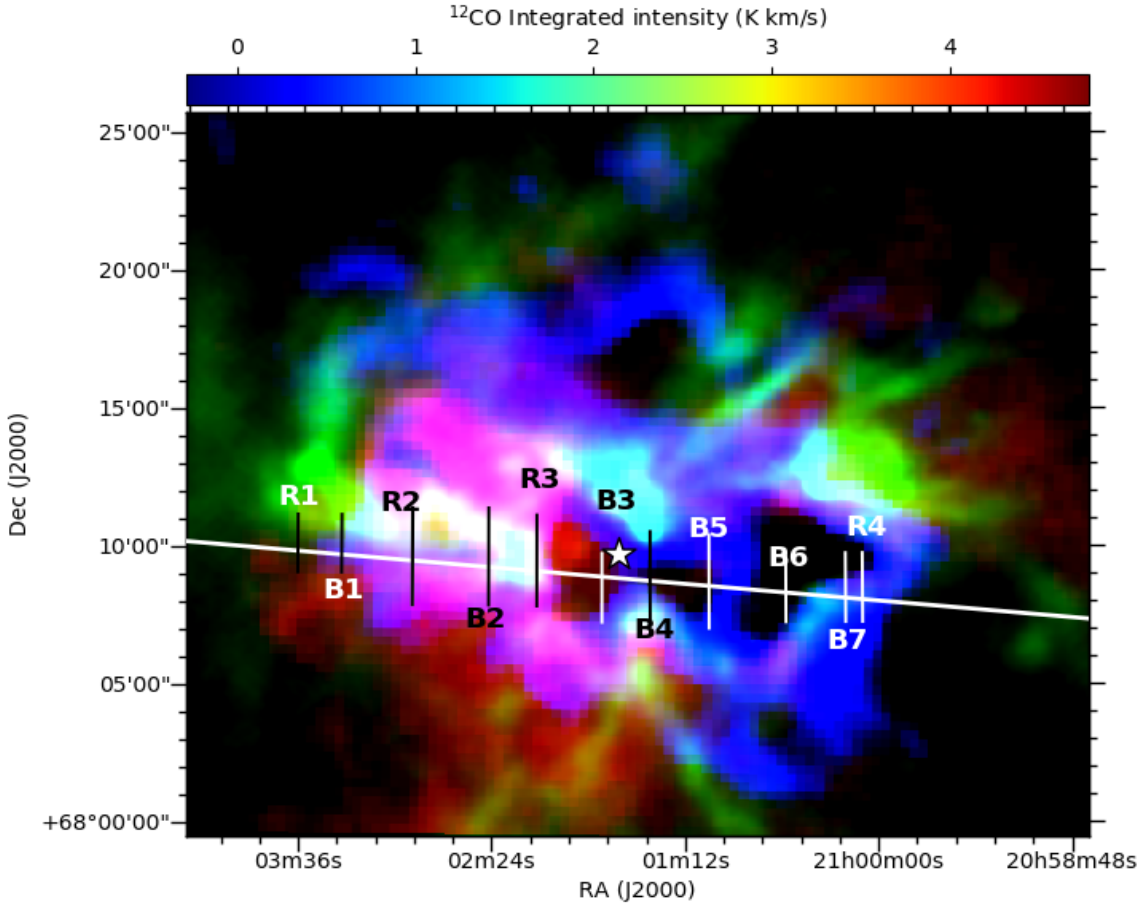

Figure 3.11: Channel map of ^{12}CO line in the velocity range from 1.0 to 2.0 km s^{-1}. The location of shell is identified by black line.

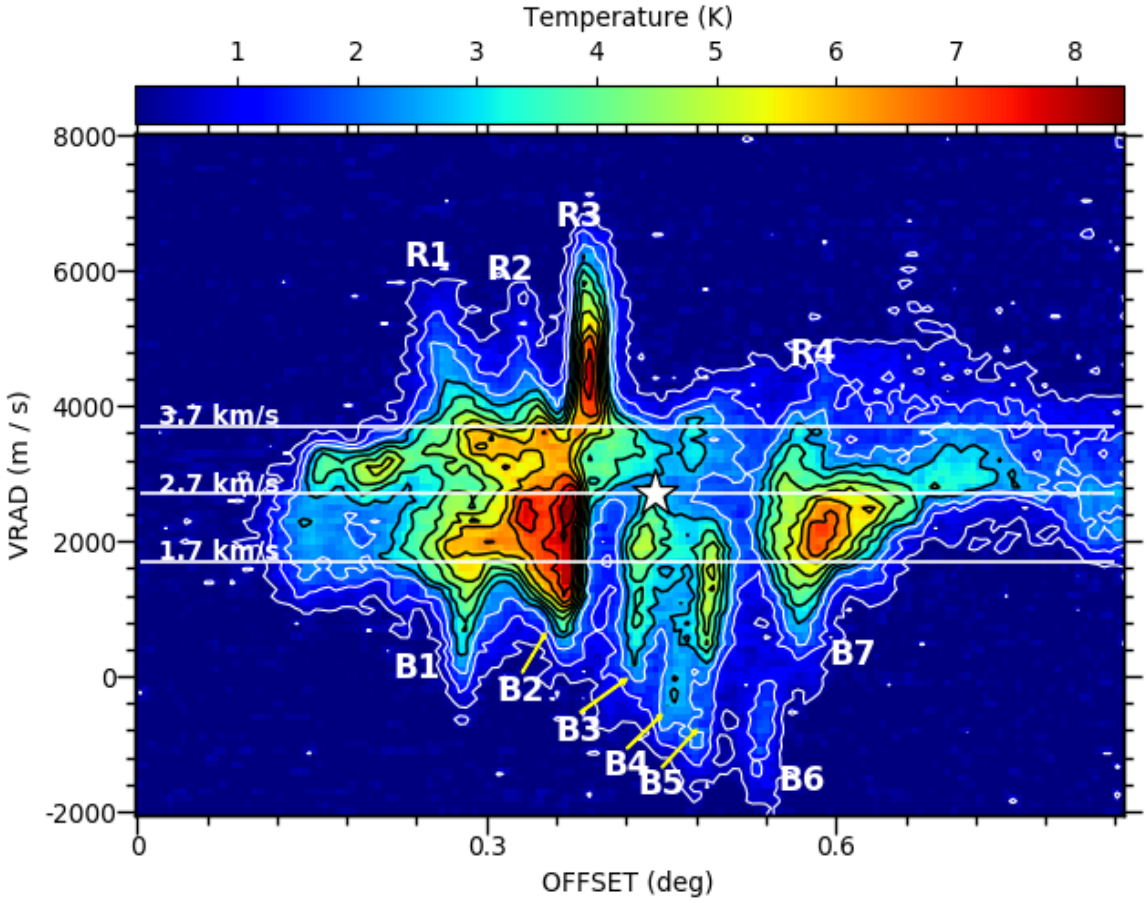

Figure 3.12: Position velocity diagram for ^{12}CO emission across a cut passing through the centre of nebula at an angle of -5° as shown in Fig. 3.11.

away from the bulk emission from the cloud. Arce et al. (2011) has also found similar high velocity shells in the Perseus cloud, a site of low- or intermediate-mass stars.

The position of the shells obtained on blue-shifted velocities are marked as B1, B2, B3, B4, B5, B6, B7 and on red-shifted as R1, R2, R3, R4. Different peaks in PV plot correspond to the high velocity components of ^{12}CO gas and are identified as multiple "shells" present around the star. The first red shifted peak, R1 is located on extreme eastern side of central star at a distance ~ -0.19 pc from HD 200775. It can be understood by looking at the channel maps from 4 to 5 km s^{-1}. The peak B1 extending till -0.5 km s^{-1}is lying adjacent to R1 on the eastern side of central star (Fig. 6.4 (b). The distance of B1 is -0.17 pc from central star. The peak, R2 is closer to HD200775 at a distance of 0.12 pc and located towards the front edge of the arc-like emission in the channel map. The maximum red-shifted velocity was found at the position of R6 which shows a localised emission in channel map having velocities in the range of +5 to +7.5 km s^{-1}. There is evidence of more blue-shifted high velocity ^{12}CO gas (shells) as compared to red-shifted emission on the western side of the central star. The peaks B3 and B4 at a distance of -0.01 pc and 0.03 pc are closest to HD 200775. The projected emission corresponding to these peaks can be clearly seen in the channel maps from -2.5 to 0 km s^{-1}. R4 is well extended towards the extreme west side starting from a distance of 0.13 pc. The diffuse extended emission can be seen in channel map 3 to 4 km s^{-1}where it is surrounding the cavity region. The high velocity peaks systematically increases from B1 to B6 with the maximum difference of the velocity as ~ 4.7 km s^{-1}from the high velocity components.

3.4.2 Properties of cores (clumps) around HD200775

Fig. 6.3 (right panel) shows the distribution of different cores extracted using *Astrodendro* algorithm. All the cores C1-C10 except C8 are located around the central star HD 200775 with their central positions lying on the filaments. Filament F4a hosts the maximum number, three cores C4-C6 as compared to any other filament along its length. We calculated the gas and the dust parameters of these cores which are within three velocity channels and extends over thrice the pixel grid of column density map. Table 6.1 shows the derived properties of the cores. The column (2) and (3) are Right Ascension and Declination of the cores that we obtained from the Astrodendro algorithm. Column 4 shows the size of all the cores in parsec which was obtained by fitting an ellipse to the closed contour around the peak of core. The effective radius is defined as FWHM of geometric mean of major and minor axis derived from *Astrodendro* method.

The centroid velocity (V_{lsr}) and velocity dispersion (σ) are the average values over pixels chosen for calculating the LTE parameters. We fitted a single Gaussian function to all the spectral profiles of C^{18}O line assuming that there exists a single cloud component lying along the line-of-sight.

The column density of C^{18}O gas was calculated using the LTE calculation described in the previous section. Using column density values of each pixel around the core, the total gas mass of the

Table 3.2: Properties of core derived using Astrodendro algorithm.

Core Name	RA (°)	Dec (°)	R_{eff} (pc)	V_{lsr} km s^{-1}	M_{LTE} M⊙	M_{dust} M⊙	M_{vir} M⊙
(1)	(2)	(3)	(4)	(5)	(6)	(7)	(8)
C1	315.257119	68.092265	0.05	2.38	2.62	0.54	5.58
C2	315.371563	68.117479	0.11	2.38	11.06	3.16	11.60
C3	315.101556	68.123647	0.10	2.31	8.47	1.84	10.29
C4	315.587862	68.162606	0.13	2.58	22.66	6.59	12.20
C5	315.698927	68.189416	0.08	2.53	9.10	1.89	6.79
C6	315.846812	68.195265	0.16	2.56	20.61	9.68	10.87
C7	315.417029	68.203120	0.21	2.63	45.87	18.89	20.44
C8	315.579568	68.216519	0.06	2.52	3.68	0.79	6.90
C9	315.223645	68.251635	0.16	2.77	13.45	6.21	9.60
C10	315.230815	68.294893	0.13	2.76	8.75	3.89	9.57

whole core is calculated as

$$M_{LTE} = \sum_i \mu_H m_H N_i(H_2) A_i$$

where μ_H is mean molecular mass of the cloud, m_H is hydrogen mass and N_i (H_2) is hydrogen column density from gas emission of each pixel A_i is area of each pixel of size $20''$. We considered emission from all those pixels which are falling within twice the extent of each core. The basic condition of each core to collapse is that it should be gravitationally bound, i.e. the gas mass should be higher than the virial mass. Assuming that if the density profile is not spherical, the virial mass can be obtained by the following expression (MacLaren et al., 1988):

$$M_{vir} = 126 \times \Delta v^2 \times R, \tag{3.5}$$

where Δv is the total FWHM value of the line and R is the FWHM size of the source in pc. The velocity dispersion of the line used in the above expression is a combination of thermal and non-thermal components of the molecular gas.

The range of the LTE masses is from 2.6 to 46 M⊙ with the C1 being the least massive and the C7 being the most massive core. C1 and C8 are the smallest in sizes. These two cores are not virialised and hence may disperse. The mass of the cores obtained from gas analysis is higher than that of mass obtained from dust analysis. Although we expect that the Hydrogen column density from $C^{18}O$ observations will vary by a factor of few due to abundance variations and metallicity factors (Bolatto et al., 2013). However, in our results, the mass obtained from dust emission is lower the

mass in gas emission. We note that the estimation of dust column density using Spectral Energy Distribution is based on the assumption that the dust is isothermal along the line-of-sight. So any variation in the dust temperature layers makes the estimation highly uncertain. Hence, underestimating or overestimating the dust temperature will effect the the Planck function by a factor of 2 or 3 and consequently the dust mass (Stamatellos & Whitworth, 2005; Stamatellos et al., 2007). In this case, the regions around the central star is possibly heated up by the radiation from central star so the isothermal case is not completely valid. The contribution of uncertainty from distance is only 1%. Also, the excitation temperature calculated is the upper limit here as we have used the peak antenna temperature from the ^{12}CO line assuming the excitation temperature for both the tracers is same.

The mean centroid velocity changes from 2.4 to 2.8 km s^{-1}with the eastern and southern clumps with blue shifted velocity as compared to C7, C9 and C10. This could be because of the systematic movement of the material in the clumps on the eastern and north-western clumps. This implies that the gas is in asymmetric motion with the upper eastern part is predominantly coming nearer and western part is moving away along the line-of-sight. The spectral profile features show multiple components indicative of bulk motions.

The analysis of the molecular line profiles may help us to investigate the kinematic signatures associated with different dynamic processes in the interiors of the cloud such as infall, expansion and outflows. Examining the shape of profiles at core position and in its environment will give an important clue about the effect of radiation on the high density regions. The critical density of $C^{18}O$ 2.7 mm (J=1-0) line is 1.9×10^3 cm^{-3} which is optically thin. The critical density of optically thick CS (2-1) 3.0 mm line is 5.8×10^5 cm^{-3} and of optically thin N_2H^+ emission is $\sim 10^6$ cm^{-3}. Comparison of optically thick ^{12}CO and optically thin $C^{18}O$ line can be used to trace infall motions. Since N_2H^+ emission is not detected everywhere at the emission of CS line, we show $C^{18}O$ and CS profiles in further sections so that we can trace regions of different density and structure. However, it may be complicated due to the variation in the abundance and optical depth and molecular freeze-out on dust grains.

The blue asymmetry occurs where blue peak in the double peak is brighter than the red peak as suggested by the models (Myers et al., 1996). The self-absorbed feature in the optically thick line is caused by the inward motions of the gas which is collapsing. Many observational studies have supported the model by studying the line profiles in various star forming regions undergoing collapse (Lee et al., 2004; Stahler & Yen, 2010; Tsamis et al., 2008).

Fig. 3.13 shows the average profile of each core where the average was taken within the extent of the ellipse derived using source extraction method. There are diverse profiles exhibited by the extracted cores. The clumps C1, C2, C3, C4, C7 and C8 which are in the proximity of HD 200775 show less $C^{18}O$ intensity and broader profiles. While the clumps lying on the tails of the filaments show high intensity and narrower profiles. The $C^{18}O$ emission is more turbulent in the clumps facing the central star. C5 and C6 exhibit red-blue and blue-red asymmetry respectively which suggests the signatures of expansion and infall of material. The line profiles towards C1, C2 and C4 resemble red-skewed profiles. This could be as a result of the global expansion as the stellar winds from HD

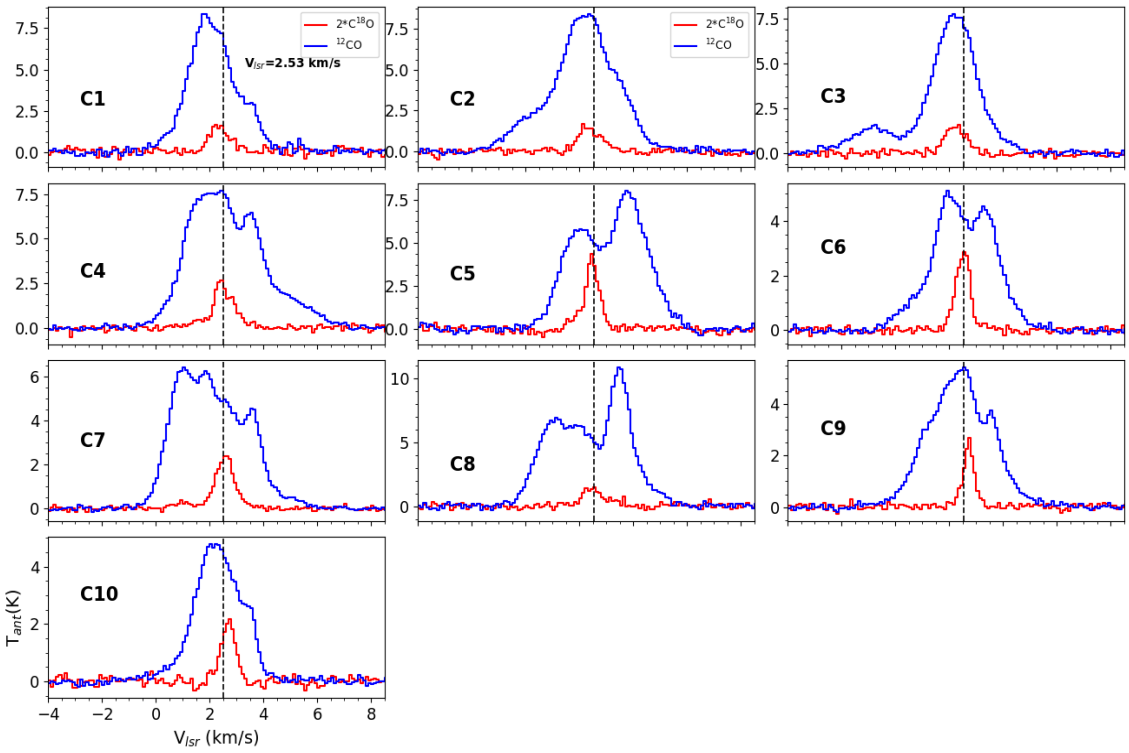

Figure 3.13: Average profiles of all the clumps C1-C10. The dashed line in each figure represents the systematic velocity of the cloud. $C^{18}O$ profile is scaled up by two times the antenna temperature (T_{ant}).

200775 will affect the cloud material. Yuan et al. (2013) has studied the region around L1174 cloud using higher transitions of ^{12}CO and ^{13}CO line and found the similar shaped profiles. All the cores distributed around HD200775 differ significantly in terms of their chemical abundance and kinematic properties. In next section, we will discuss the spectral profiles around HD200775 where the high density structures (cores and filaments) are lying.

3.4.3 LDN 1174 core

This core resolves into two peaks as seen in the dust column density map. Though Astrodendro algorithm filters out these peaks based on the minimum number of pixels contained in a core, the core is a real structure.

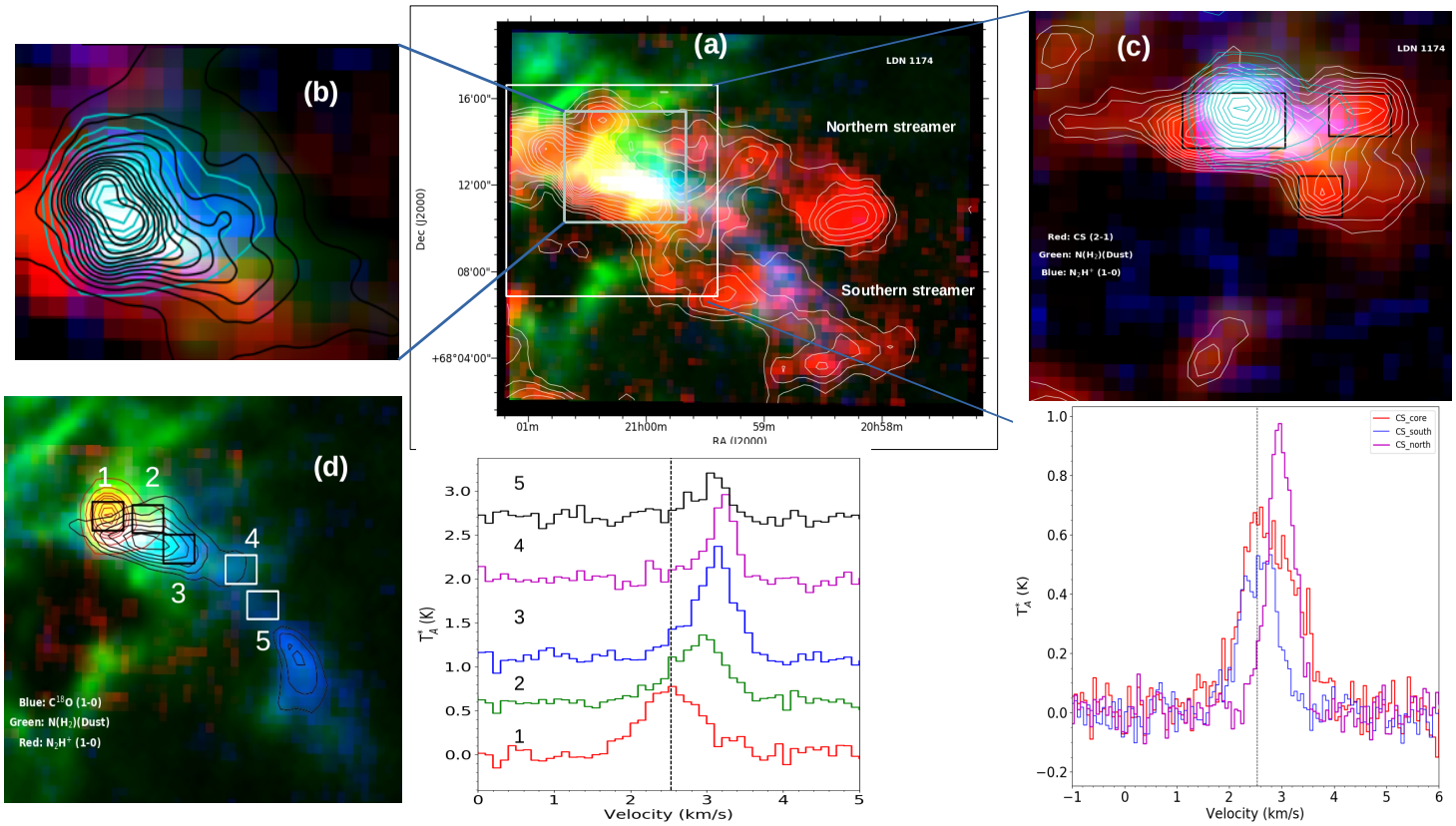

Figure 3.14: **(a):** Color-composite image around region of L1174 cloud, red is the channel map of ^{12}CO line in the velocity range 4.0 to 5.0 km s^{-1}, green is the dust column density map and blue is the channel map of C^{18}O emission in 3.0 to 3.3 km s^{-1}. **(b):** Color-composite image of square region where red is ^{12}CO emission in 3 to 4 km s^{-1}, green is dust column density and blue is N_2H^+ emission. **(c)**: Color composite map of the same region where red is CS (2-1) emission, green is column density map and blue is N_2H^+ (1-0) emission. Black contours marks the emission from dust column density where the levels are in the range 0.8-2.4 $\times$ 10^{22} cm^{-2}. **(d):** Color-composite image of same region with red is N_2H^+ integrated emission, green is column density and blue is C^{18}O emission in high velocities range 3.0-3.2 km s^{-1}.

Fig. 3.14 (a) shows the color-composite image around L1174 where red is the channel map of ^{12}CO line in the velocity range 4.0 to 5.0 km s^{-1}, green is the dust column density map and blue is the channel map of C^{18}O emission in 3.0 to 3.3 km s^{-1}. The white peak at the centre represents the peak position of the core where all the gas and dust emissions are equally present. There are two streamers in the ^{12}CO emission, identified as *Northern streamer* and *Southern streamer* which show two peak at their extreme edges as shown by the white contours. The C^{18}O emission extends out in between the high velocity gas of ^{12}CO emission.

Panel (b) shows the color-composite map around high density peak region of L1174 where red is ^{12}CO emission in 3 to 4 km s^{-1}, green is the dust column density and blue is N_2H^+ emission. The peak of the dust emission correlates with N_2H^+ emission although we find two very high density peaks. There is a spatial extension seen in the morphology of dust and N_2H^+ emission towards the west direction. The high velocity low density gas lies at the edge of gas emission which might have a significant effect on the motion of the gas present around the core. To quantify the effect of high velocity on the dense material around the core, we studied the shape of line-profiles also in different tracers around this region.

The N_2H^+ line, being a tracer of high density gas in a core, shows seven hyperfine components. We fitted all the seven components using CLASS-GILDAS software and averaged the N_2H^+ profiles around the peak intensity of N_2H^+ line. The V_{lsr} of this core is calculated as 2.5 km s^{-1}.

Panel (c) shows the color-composite image of the zoomed region (size $10' \times 10'$) where red is integrated intensity CS (1-0) emission in 3.0-3.2 km s^{-1}, green is dust column density and blue is total integrated N_2H^+ emission around core. As shown by contours of CS (2-1) emission shown in white color, the morphology is extended towards western side with a bifurcation present. There are two peaks present towards extension of CS emission. Although the spatial distribution of intensity looks similar in both the blobs, there is a difference in the velocity structure of both the arms.

The south-west arm is blue-shifted with respect to V_{lsr} velocity ($\sim$ 2.55 km s^{-1}). The profile at the south-west blob shows peak at 2.2 km s^{-1}. We plotted average spectra of CS line at the identified positions. The CS profile at the peak position of core is shown in red color. The antenna temperature is 0.6 K and the profile is skewed towards red-shifted velocities. The north-west peak is agreeing well with the extension of N_2H^+ emission towards west and the peak is red-shifted at the velocity $\sim$ 3.2 km s^{-1}.

We show color-composite image in panel (d) where red is velocity integrated N_2H^+ (1-0) emission, green is dust column density, and blue is C^{18}O emission in the velocity range 3.0-3.2 km s^{-1}. Since C^{18}O line is an optical thin tracer and has lower critical density threshold for excitation in comparison with N_2H^+ line, the C^{18}O emission is more distributed around the core peak. But again there is an elongated morphology of the core in the same direction as N_2H^+ core emission. The representative C^{18}O line profiles at some selected positions from 1-5 (identified in the panel (b)) are shown by the average spectra. The black dashed line shows the systematic velocity of the cloud, $\sim$ 2.55 km s^{-1}. The peak velocity of C^{18}O line at the core position is shown in red color which is at 2.55 km s^{-1}. As we go away from the peak emission of the core, there is a decrease in the C^{18}O antenna temperature

and a shift in the peak velocity of $C^{18}O$ line. The peak velocity at the core in $C^{18}O$ line is ~ 2.5 km $s^{-1}$and it shifts to ~ 3.2 km s^{-1}towards the tail region of the $C^{18}O$ emission.

Overall, the region around L1174 is spatially extended towards west in projection and kinematically shifted towards the higher velocities. We consider the emission of the gas at the velocity greater than 3.0 km s^{-1}as high-velocity emission. The spectral signatures shows that the core has been peeled off along the direction of streamer. We calculated the mass of high velocity gas in the $C^{18}O$ emission in velocity range 3.0-3.2 km s^{-1}at only those pixels where the integrated intensity is greater than 3σ emission. The mass is calculated as 10 M⊙. Using LTE parameters, we calculated the mass of the core as 12 M⊙ and virial mass is 13 M⊙. The total velocity dispersion of the core including thermal and non-thermal component is found out as 0.26 km s^{-1}.

3.4.4 F4b region

Fig. 3.15 shows the color-composite image (left) of the region located towards northern region of HD 200775, identified as core 7 in Fig. 6.5 red is N_2H^+ emission, green is dust column density and blue is CS (2-1) emission. The morphology of core C5 in CS and $C^{18}O$ emission are elongated in different directions. The $C^{18}O$ (green) is in north-east direction whereas CS is oriented along northern and western side. We found that there are tails in CS emission which joins with the F6 filament. The velocity integrated intensity contours of N_2H^+ are shown in black dotted lines. The peak of N_2H^+ and CS emission are displaced by three pixels along the direction of F4b.

Right panel shows the color-composite map of the same region where red represents total integrated emission of CS (1-0) emission from 1.5 to 3.8 km s^{-1}, green is the dust column density map, blue is moment 0 map of $C^{18}O$ emission. The dust emission and gas emission seen in $C^{18}O$ integrated intensity map is well correlated and oriented in the direction of filament F4b. Since the front edge of this region coincides with the high velocity gas passing through the gap, the gas and dust are significantly affected by the radiation from the star. The variation of properties of filament F4b also shows that the front edge has the maximum temperature of 28 K which steeply decreases down to the temperature of high density material ~ 12 K.

We averaged the N_2H^+ profiles within the half-maximum contours. The V_{lsr} of the core as shown by N_2H^+ average spectra is ~ 2.5 km s^{-1}. The N_2H^+ line, being a tracer of high density gas in core, shows seven hyperfine components. We fitted all the seven components using CLASS-GILDAS software. The V_{lsr} of this core is calculated as 2.5 km s^{-1}. Fig. 3.16 shows the average profiles of $C^{18}O$ and CS emission within the half-maximum contour of the $C^{18}O$ emission. The CS emission is broader and less intense than the corresponding $C^{18}O$ emission. The average line velocity from CS and $C^{18}O$ emission is 2.5 km s^{-1}. We show the average profiles of $C^{18}O$ and CS lines at some selected positions identified by squares marked. To examine whether there is systematic velocity shift in the line profiles, we compared the average profiles of $C^{18}O$ and CS profiles along the direction of F4b. Left most panel shows that there is no change in the peak velocity as we move away from the central star. Similarly, the CS profiles do not show any change in the peak velocity. Clump C7 lies at

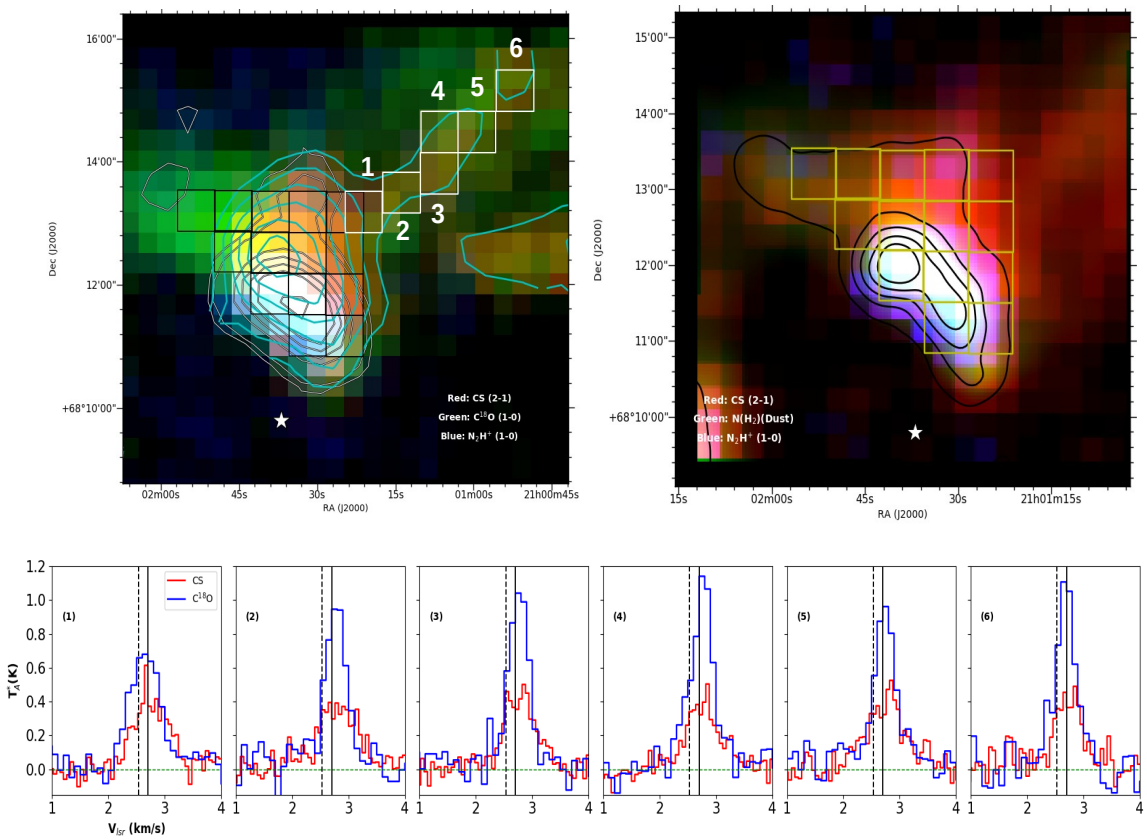

Figure 3.15: Color-composite image around F5 region, where red is CS (2-1) emission, green is dust column density map and blue is $C^{18}O$ emission. White star marks the position of HD 200775. **right panel**: Color composite map of the same region where red is CS (2-1) emission, green is column density map and blue is N_2H^+ (1-0) emission. Black contours marks the emission from dust column density where the levels are in the range 0.8-2.4 $\times$ 10^{22} cm^{-2}.

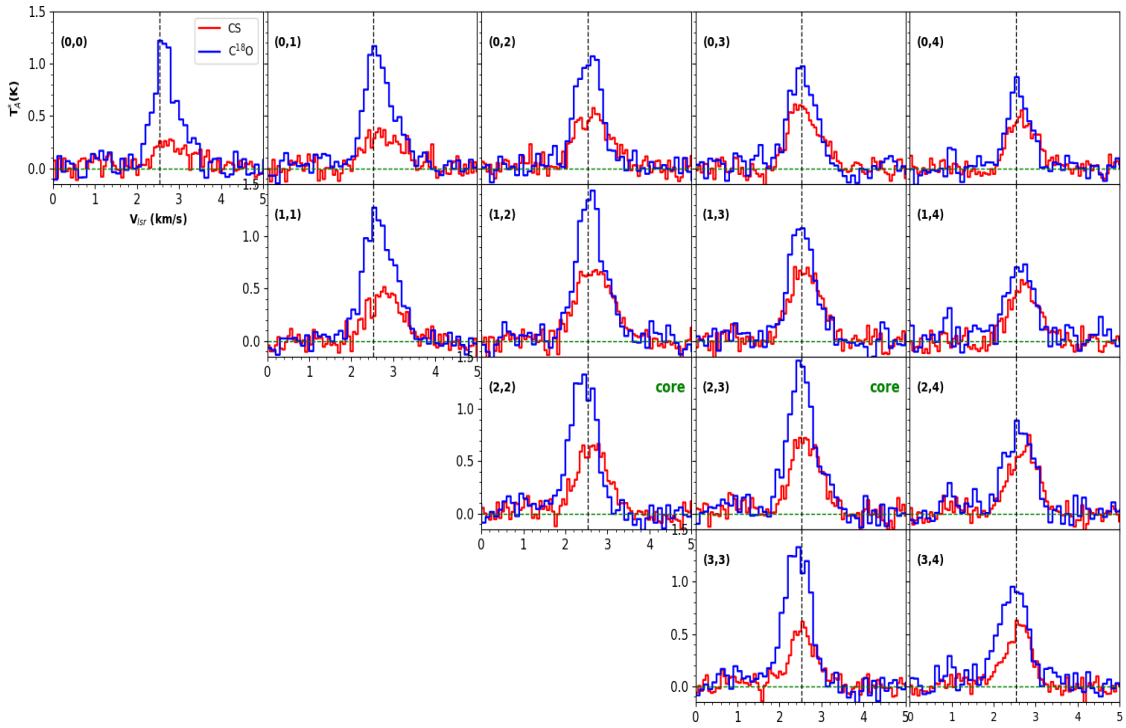

Figure 3.16: Spectra of CS and $C^{18}O$ emission at the squares marked in fig. 3.15. Red spectrum represents CS (2-1) line and blue is $C^{18}O$ line. The intensity is plotted in units of antenna temperature (K). The vertical dotted in each plot shows the V_{lsr} velocity of the cloud, $\sim$ 2.5 km s^{-1}. The positions (2,3) and (2,4) marks the position of high density core C7.

the peak of N_2H^+ emission with a peak column density of 1.5×10^{22} cm^{-2}. The mass of this core using LTE parameters is calculated as ~ 28 M$\odot$.

Asymmetric double peaked profiles with blue stronger than red or red stronger than blue are always considered as the effective tracers of kinematics in the star-forming cores. The blue-red profiles are linked with the inward motions in cores (Zhou et al., 1993) and red profiles with the outflows or expansion. All lines in this region are mostly red-skewed profiles where dip is caused by the self-absorption of the cloud in motions. The red-skewed spectra are mostly dominant in the regions having expansion or energetic outflows. There is decrease in the intensity of $C^{18}O$ profiles from east to west side. The CS profiles have higher intensities around the position of core (2,2) and (2,3). Some CS profiles at positions (2,2) and (1,1) show red-blue asymmetry whereas $C^{18}O$ is gaussian at the systematic velocity with a high velocity component on red-shifted velocity. This indicates that there can be infall motion currently occurring in the core centre. The positions (3,4) and (2,4) exhibit blue-skewed asymmetric profiles.

Banda-Barragán et al. (2016) proposed that the formation of filaments takes place during wind-cloud interaction and tail-like structures will form as the cloud is disrupted. The formation of this tail could be because of the mixing of high velocity material and density from the envelope part of the filament. Around this region, we found that almost all the profiles are red-skewed which implies the stripping of gas away from the high density central core region. As mentioned before, we find that there is tail-like structure also originating from filament F4b towards north-west in CS and $C^{18}O$ emission. The spectral profiles at this region are shown by marked squares from 1 to 6. Except position 1, all the profiles are showing red-blue asymmetry in the CS line and the peak of optically thin $C^{18}O$ line lies at the dip of optically thick line. That implies that the there is a global expansion present in the F4a region.

3.4.5 F4a-C2 region

Fig. 3.17 shows the color-composite image of F4a region where red is CS (2-1) emission, green is column density map and blue is $C^{18}O$ emission. The $C^{18}O$ emission is well correlated with dust emission towards the edge of F4a filament hosting a clump, C3. The peak of intensity in $C^{18}O$ emission is consistent with the peak in CS emission where the extension of CS emission along the filament does not match with the $C^{18}O$ emission. There is a steep increase in the intensity of $C^{18}O$ and CS contours which implies that the material around this region has been significantly affected by the strong winds from the central star HD 200775. That can be also be understood from the variation of filament properties as a function of distance from the star. The closer points show higher Mach number in the range 1-2 which suggests that the material around is highly turbulent. The spectra at the marked squares are showed on right side where red spectrum shows CS and blue shows $C^{18}O$ emission. We noticed that there is a diversity of profiles along the filament. The antenna temperature towards 1 and 2 positions show asymmetric profiles and $C^{18}O$ lines appear saturated at the position of V_{lsr} of the cloud. The systematic velocity of the cloud is marked by the black dotted line which is at

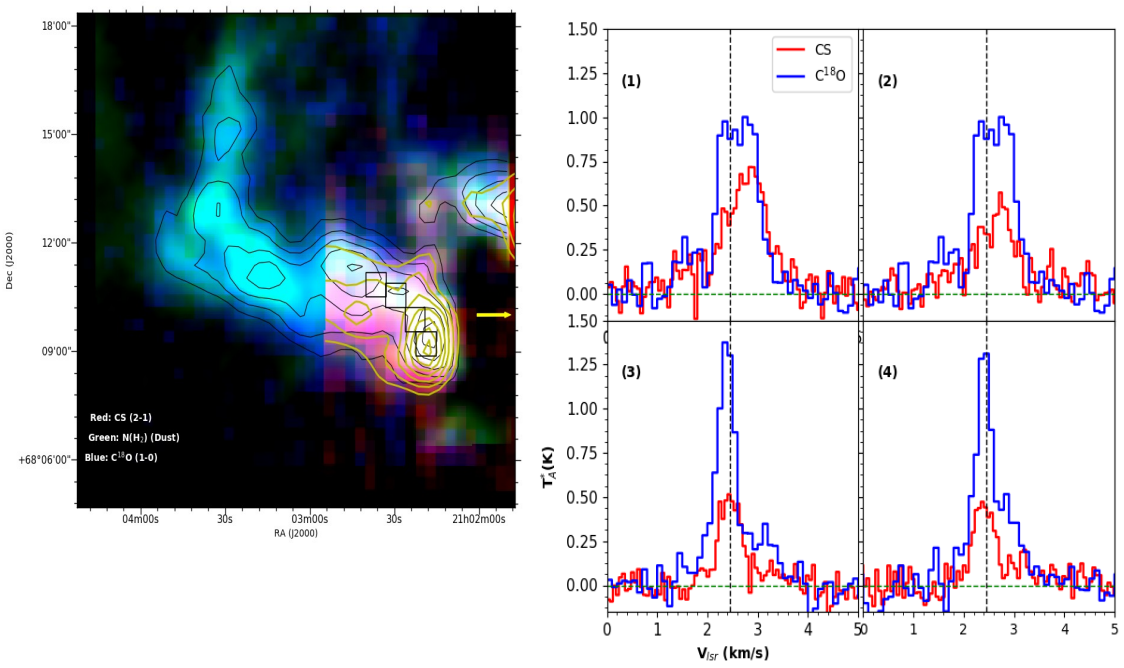

Figure 3.17: Color-composite image of F4a region towards eastern side of HD200775. Red represents CS (2-1) emission, green is column density map and blue is $C^{18}O$ emission. The yellow arrow marks the direction of central star. Velocity integrated contours of $C^{18}O$ emission in the range 1.5-3.6 km $s^{-1}$are shown in black color and of CS emission in yellow color. The levels range from The black square boxes show the representative subregions labelled from 1-4. *Right panel:* The CS and $C^{18}O$ profiles at the white boxes. The positions are marked in the plot.

$\sim$ 2.5 km s^{-1}. The CS lines shows red-blue asymmetry in 1 and 2 regions with an intensity dip at the V_{lsr} of the cloud. It can happen when there is a centrally concentrated system is expanding outward. The intensity in both the lines are decreasing at the same velocity which shows that the gas is expanding at the same velocity. In contrast to these, the regions 3 and 4 shows highly peaked narrow profiles with red-asymmetry. The CS lines are less in intensity and exhibit a broad Gaussian component. The reason for the high velocity component in $C^{18}O$ emission could be because of the effect of high velocity low density gas present around the periphery of the region. The stellar wind and the energetic photons from HD 200775 could have had significant effect on the region and might have compressed the material which results in the observed kinematical behaviour of the bulk material. Simulations carried out by Dale et al. (2005); Miao et al. (2006) pointed out the effect of the radiation on the clumpy structures. The spherical uniform cloud structure evolves to cometary or triggered star formation under the influence of strong ultraviolet radiation from nearby ionizing star.

3.4.6 F2-C1 and F3-C10 region

The regions towards the south and south-west which are identified by F2 and F3 filaments respectively also seems to have affected by the stellar winds from the star. The orientation of F3 is oriented towards the south-west side of the star and delineating the outer parts of the cavity. On the other hand, F2 is oriented along the direction perpendicular to F3. The cores hosting by these filaments, C1 and C10 show diverse profiles. Fig. 3.18 shows the color composite image where red is the moment 0 emission of CS (2-1) line, green is dust column density and blue is $C^{18}O$ line emission. The integrated intensity contours in white color shows a clumpy and elongated structure towards the southern direction. The peak positions of $C^{18}O$ emission towards core C1 and and C10 are well matched with the corresponding CS (2-1) emission. The profiles of CS (2-1) (in red) and $C^{18}O$ (1-0) (in blue) at the grid map shown in color-composite image are shown on right panel. All the profiles in CS and $C^{18}O$ emission are almost of same intensity and same shape which implies that the same layer of molecular gas is being traced by both the lines. Position (0,1) shows profiles at the region closest to the star radiation from HD 200775 directly. The $C^{18}O$ line peaks at V_{lsr} velocity with high velocity wings on both the side whereas CS line is shifted towards bluer side with skewness in red shifted velocities. The next two rows trace the regions within the core showing spherical morphology. We notice that there are infall signatures in the profiles which are clearly seen at positions (1,0), (1,2), (2,0) and (2,1) where the line profiles exhibit blue-red asymmetry. There are two peaks observed with bluer component higher than the red peak and the dip in the intensity lies at the systematic velocity of the cloud $\sim$ 2.55 km s^{-1}. The CS and $C^{18}O$ lines show maximum antenna temperature at (1,0) and (1,1) positions with a value of 0.6 K.

The region around filament F3 labelled as C in color-composite image is shown on bottom-left. We averaged four profiles in each square box. The position 1 shows the peak intensity of $C^{18}O$ line at the position of the core which is around $\sim$ 1 km s^{-1}. However, CS line intensity is not very high at the core position rather shows multiple peaks with a blue-skewed profile. Both the lines are blue-shifted

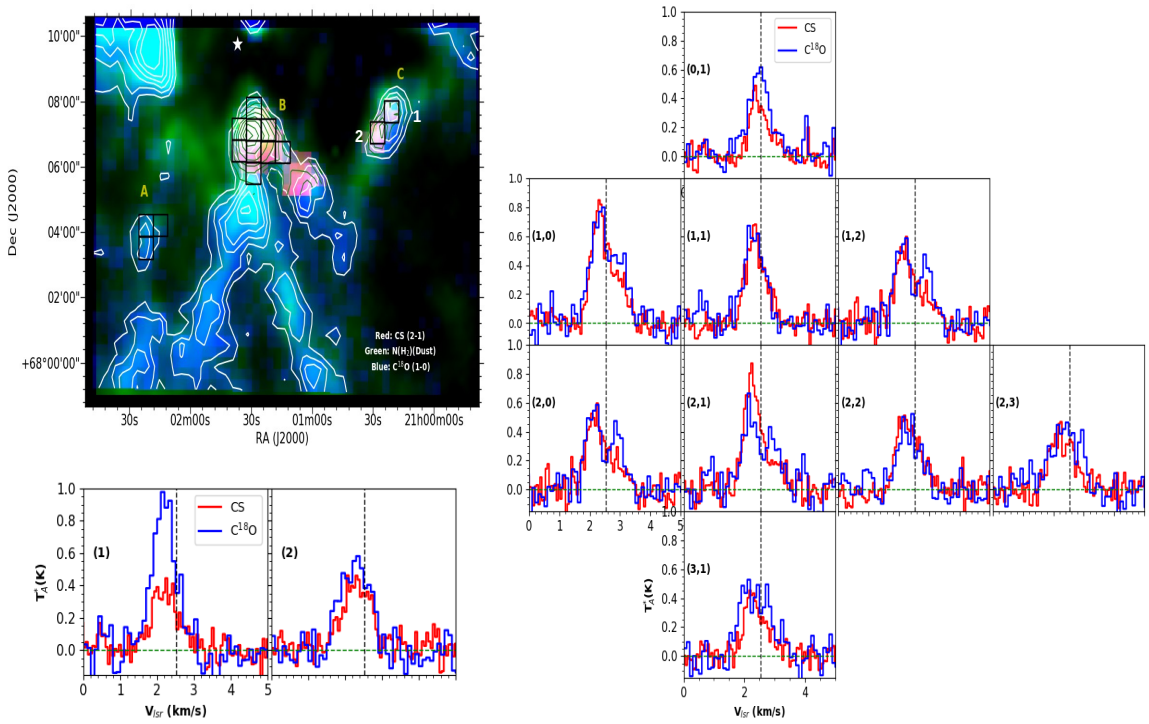

Figure 3.18: Color-composite image of region around F2 and F3 filaments towards eastern side of HD200775. Red represents CS (2-1) emission, green is column density map and blue is $C^{18}O$ emission. The yellow arrow marks the direction of central star. Velocity integrated contours of $C^{18}O$ emission in the range 1.5-3.6 km $s^{-1}$are shown in black color and of CS emission in yellow color. The subregions are labelled as A, B and C. *Right panel:* The CS and $C^{18}O$ profiles at the square boxes shown in region B. The positions are marked in the each plot of profile. *bottom-left:* Profiles of CS (2-1) and $C^{18}O$ lines at positions 1 and 2 identified in the color composite images. The x-axis is in the units of velocity and y-axis is in the units of antenna temperature (T_A^*).

with the peak at ~ 2.2 km s^{-1}. Position 2 shows the profiles towards the southern part of F3. The peak antenna temperature is ~ 0.4 K. Both the lines are broader having the same intensity variations.

Numerical simulations carried out by Banda-Barragán et al. (2016) showed that the wind swept clouds can produce the tail-shaped structures as the winds interact with the main clouds and the surrounding inhomogenities. The formation of filaments will commence during the stripping phase of the cloud disruption. The wind carries away the material stripped in downstream as the created instabilities remove material from the surface layers of the cloud. In our result, we find that there are layers of high velocity gas present around the high density structures. The kinematic signatures of spectral profiles which is blue or red skewed profile show that the high velocity low density gas is stripping away the material. The regions discussed above are under the influence of the stellar winds as suggested by the high velocity gas escaping through the gaps.

3.4.7 Properties of the gas along filaments

To investigate the effect of the central star on the high density structures of the gas and dust along the crest of filaments identified in Fig. 3.3, we plotted gas and dust properties as a function of distance from HD200775 in Fig. 3.19. We regridded the dust column density map at 3″ to 20″ pixel grid to correlate the dust column with the $C^{18}O$ gas. We derived the peak line temperature, centroid velocity and velocity dispersion using Gaussian fitting to $C^{18}O$ spectra. We show the properties of those filaments which are derived using threshold of 3σ, where $\sigma \sim 0.7 \times 10^{21}$ cm^{-2}.

The left panel shows the dust and gas properties for filaments F1, F6, F9 whereas the right panel shows the same for F2, F4a, F4b, F5. The reference point of distance is taken from the position of HD 200775 so that we can understand the effect on gas with respect to the distance from star. The first row shows the dust column density distribution along the filaments F1, F6 and F9. The column density varies from 0.9 to 4.3×10^{21} cm^{-2}. On right panel, the dust column density varies from 9.0×10^{21} to 2×10^{22} cm^{-2}. Filament 5 shows the highest column density of 2×10^{22} cm^{-2} and the position matches with the position of the cloud L1174 whereas the filament 4 show the least column density. The extreme end of all the filaments closest to HD 200775 has higher column density as compared to the points at larger distances from the central star. Points at shorter distance values are closest to the star position. Filament F4b exhibits a peak column density of 1.5×10^{22} cm^{-2} and shows a decrease in the column density as it goes away from the star. Panel (b) shows the temperature distribution of all the filaments as a function of distance from the star. As in the case of column density values, the dust temperature also shows similar variations with a higher value for the points closest to HD 200775. The extreme end of F4b is the closest region out of all the filaments and shows the maximum dust temperature of 27 K. All the filaments shows a decrease in temperature for the regions away from the star.

We plotted the V_{lsr} at every point of the respective filaments. We fitted a single Gaussian profile at every point to the $C^{18}O$ profiles and obtained the peak velocities. The peak velocity changes from 2.3 to 3.6 km s^{-1}. The velocity field of F2 is overall blue-shifted with respect to the systematic velocity

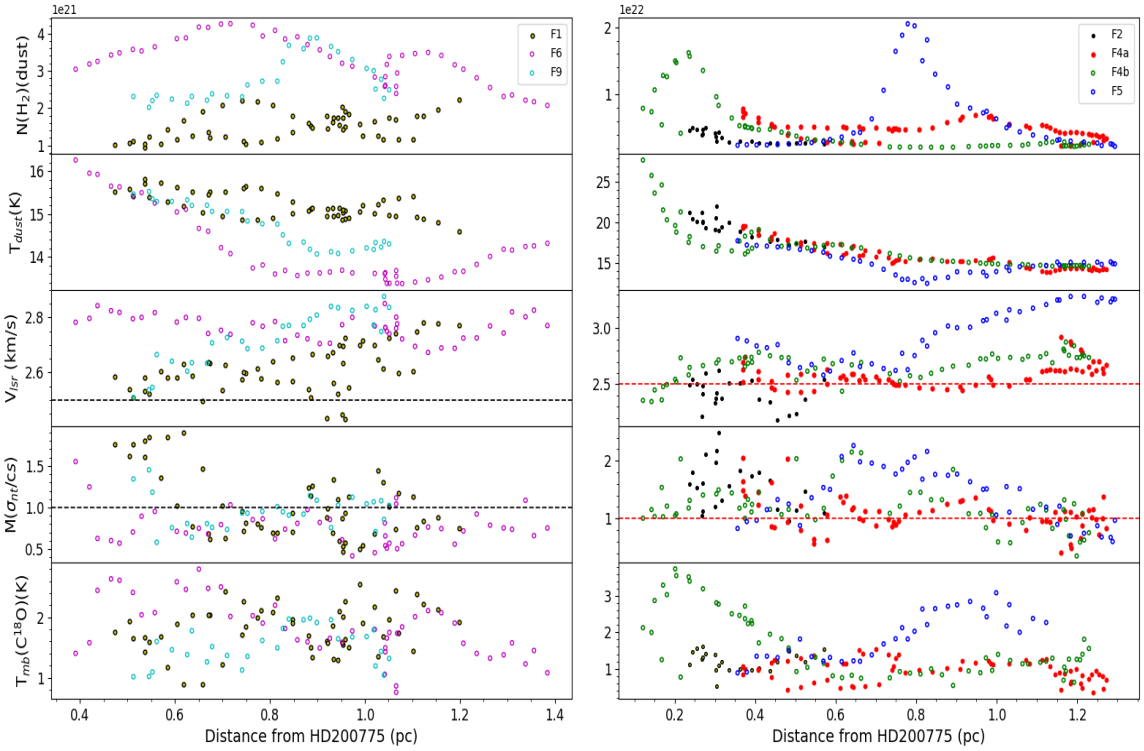

Figure 3.19: Results of $C^{18}O$ (1-0) and dust emission analysis of the derived filaments as a function of distance from HD 200775 in units of pc. Left column shows the properties of filaments F1, F6, F9 whereas right column shows the properties of F2, F4a, F4b, F5. Hydrogen column density derived using Herschel PACS and SPIRE images. **(b)** Dust temperatures. **(c)** Centroid velocity of $C^{18}O$ obtained from Gaussian fitting of profiles. The horizontal line at 2.7 km s^{-1}shows the V_{lsr} of the cloud. **(e)** Main beam brightness temperature using $C^{18}O$ lines.

of the cloud ($\sim$ 2.7 km s^{-1}). The values near the star are more closer to V_{lsr} as compared to the points at the extreme ends of the filament. There is a velocity gradient between the two ends of the filament. Similar to this, the filament 4a also appears to be at velocity less than systematic velocity of the cloud except the extreme end of the filament where it changes from 2.5 to 2.9 km s^{-1}. The dispersion in the centroid velocities is calculated as 0.1 km s^{-1}which is within the spectral resolution of the data. Overall, F4a is velocity coherent as the centroid velocity is not changing over its length. On contrary to this, the velocity field of F4b shows a gradual change from 2.4 km s^{-1}to 2.9 km s^{-1}with a dispersion of 0.11 km s^{-1}. Filament 5 exhibits a sharp velocity gradient of 1.3 km s^{-1}pc^{-1} at the point where the column density starts rising at a distance of 0.8 pc from central star. The variations of the centroid velocity along F1, F6, F9 (left panel) are within shorter range as compared to the right panel. Filament F6 exhibits a sharp rise in velocity from 2.45 to 2.85 km s^{-1}. The variation of the centroid velocity along F9 is mostly around systematic velocity of the cloud ranging from 2.5 to 2.9 km s^{-1}.

The linewidth of a spectral line is a combination of thermal and non-thermal motions (Myers, 1983). Non-thermal motions are generally arising from turbulence in cloud or core scale mechanisms. We have separated out the thermal component from the observed line-width obtained from the Gaussian fitting analysis with the assumption that the two components are independent of each other. The non-thermal component is calculated as

$$\sigma_{nt} = \sqrt{(\sigma^{obs})^2 - (\sigma^{th})^2}$$

where σ^{th} is $\sqrt{kT/\mu m_{obs}}$, thermal velocity dispersion, μ is the molecular weight of the observed $C^{18}O$ molecule, T is the gas temperature and k is the Boltzmann constant. The Mach number (M) is defined as the ratio of non-thermal component (σ_{nt}) and isothermal sound speed (c_s) shown in the panel (d).

The variation shows the extent of non-thermal motions distributed as a function of distance from the star. We find that much of the gas in the filament is supersonic as $M > 1$. The main beam temperature (T_{mb}) of $C^{18}O$ line shows diverse variations for all the filaments. The maximum values of F2 has T_{mb} in the range of 0.7 - 1.5 K. F4b shows the maximum T_{mb} as 3.2 K in the close proximity of HD200775 at a distance of 0.2 pc.

The NGC 7023 nebula and associated cloud, L1174 provides a good example for showing the effects of massive nearby star on the core properties. As we found in the previous section of filaments and cores, the decrease of dust temperature and T_{mb} along the projected distance from the central star suggests that the star has a significant effect on the nearby structures.

3.4.8 Magnetic field effects on all the cores

As discussed in sec. 3, the orientation of the B-field as inferred from the optical and the Planck polarization measurements show a well defined pattern with respect to the high density structures around HD 200775. Fig. 3.8 shows the dust column density map in color-scale with overplotted

optical in white and Planck polarization vectors in yellow color. We notice a significant difference in the angle between east and west. The B-field is perpendicular to the filaments on the east while it is parallel to the filaments towards west. Considering the fact that the filaments are aligned with global B-field, this implies that it plays an important role here in shaping the morphology and governing the dynamics of the cloud. Previous studies have shown that the relative orientation between the B-field and elongated structures changes from parallel to perpendicular as the density transitions from $\sim 10^{21.7}$ to higher than $\geq 10^{21.7}$ cm^{-2} (Planck Collaboration et al., 2016a; Soler et al., 2016).

As mentioned earlier, this region represents a system showing interaction of stellar winds and the high density filament material. Köhler et al. (2014) pointed out from the Herschel observations using higher transitions that they could be primordial filaments already present prior to star formation. Our observations of gas around HD 200775 shows signatures of wind and cloud interactions as shown by the spectral profiles either expansion/contraction. The properties of filaments and cores in this region is highly affected by the stellar wind-cloud interaction. The morphological appearance of filaments suggest that if they were present prior to star formation, their evolution might have taken place in terms of filamentary tails. The kinematics of various regions around HD 200775 (F4a, F4b, F7) tells us about the signatures of effects of high velocity low density gas on the high density material present. The front edges of the regions F4a, F5 and F7 tells us that the material has been illuminated by the ionized radiation of from the nearby massive star. Based on the 3D radiation-magnetohydrodynamical studies of pillars and globules by Mackey & Lim (2011), it was shown that the magnetic fields are important in the evolution of cometary globules.

The regions that we studied above show filamentary structures which are either tail shaped or small globules. It might be possible that these structures basically are like pillars which fragment into small globules under the effect of UV radiation from the massive star. The radial profiles and spectral index values obtained imply that out of all the structures, only three filaments are well defined with column density higher than Av ≥ 5. Eventually, some of the pre-existing density structures embedded in the filaments would collapse to form stars. The other view could be that the large scale compression of HII region to the surface of molecular cloud has created pillars which turn into globules. The scenario of *Radiation driven implosion* in the formation of globules involves illuminating the pre-existing clump dense gas by UV radiation and photoevaporating the low density gas leaving only dense structures that may form stars (Miao et al., 2006, 2009). The creation of bright rimmed clouds occurs by the instabilities at the interface of molecular cloud and HII regions. The turbulent structures at the edges of the filaments and the decay of temperature along the length suggest that the extent of interaction is high. Observational studies by various authors (Fukuda et al., 2013; Morgan et al., 2009; Urquhart et al., 2009) have also confirmed the interaction of HII regions with the clumpy structures.

Considering the kinematic features of ^{12}CO lines obtained at the edges of the regions in vicinity of star reveals that there is an interaction of explanding HII regions with the cloud. This does not mean that the star formation will happen only at the edge of these structures. The cores distributed along the length suggests that there are compressed material along the filaments in the tail like structures.

We present the detailed mapping study of the region surrounding the central star HD 200775 using CO isotopologues, ^{12}CO and $C^{18}O$ and high density tracers CS (2-1) and N_2H^+ (1-0) lines. The summary of the results are described below:

- We extracted 10 filaments using *Filfinder* algorithm around HD200775. The radial profile structure of three filaments have been found out with spectral index in the range 2.5-3.5 and mean flattening radius as 0.06.
- Twelve molecular clumps were identified in the vicinity of HD 200775. We studied dust and kinematical properties of the filaments and clumps using ^{12}CO and $C^{18}O$ (1-0) lines. Various properties of filaments like dust column density and turbulent structure using Mach number show that the properties are in the effect of high energy radiation from HD 200775.
- Kinematical signature of red-skewed profiles are present towards the filaments on the eastern side and the northern part of HD 200775 which suggests the presence of global expansion of the cloud. The extracted filaments exhibit a turbulent velocity structure at the edges facing HD 200775 with tail shaped morphology.

Chapter 4

Interplay of magnetic field and gas dynamics in LDN 1172

4.1 Introduction

In the previous chapter, we studied the effect of the Herbig Be star, HD 200775, on the dynamics of gas around it using dust continuum and large-scale molecular line observations. The kinematics of filaments and cores around the reflection nebula has been characterized with respect to the radiation field from the star. In this chapter, we discuss the tail region of the complex, which is $\sim$ 10 pc in length as seen in the images obtained with the *Herschel* and extends towards the southern part of the nebula.

The origin of filamentary structure is still unclear despite the universality of filaments at all scales that is established by the observations of the *Herschel* Space observatory (André et al., 2010; Men'shchikov et al., 2010). The hub-filament structure is one of the common morphological features seen in the ISM. Myers (2009) has pointed that a significant number of the nearest young stellar groups are associated with the "hubs" having column density higher than of the order of 10^{22} cm^{-2}. The filaments extend out from these hubs with lower column density and having low star formation activity. The filaments are thought to provide the material required for the cores to build-up, most likely, through accretion.

The morphology of these filaments could possibly be created by stagnant gas due to either large-scale compression flows (Peretto et al., 2012) or due to the support from helical magnetic fields (hereafter B-field) (Fiege & Pudritz, 2000b). Alternatively, they can be described as isothermal self-gravitating cylinders in pressure equilibrium with the external medium (Fischera & Martin, 2012; Heitsch, 2013). It is postulated that the orientation of the B-field with respect to the gas motions and the dense filamentary structures will give insight into whether (a) B-field channels the gas flow as for the strong B-fields, or (b) whether the magnetic field is dragged along with the flow as would be the case with the weaker strength case (Hull et al., 2014). Results from numerical simulations

made by Gómez et al. (2018) show that filaments are basically loci of the colliding turbulent flows and B-field structures in these self-gravitating filaments are found to be perpendicular to the dense structures. Soler & Hennebelle (2017) suggested that the transition from parallel to perpendicular alignment is an outcome of the gravitational collapse or converging flows.

Correlated B-fields on scales of 1-10 pc have been observed in interstellar clouds (e.g., Chapman et al., 2011; Clemens et al., 2018; Goodman et al., 1992; Heyer et al., 1987; McCutcheon et al., 1986; Pereyra & Magalhães, 2004; Soam et al., 2017, 2015; Vrba et al., 1976; Wang et al., 2017). The B-fields may play an important role in regulating these flows. The relative role played by the magnetic fields, turbulence, and self-gravity in the formation of filaments and their evolution to the cores is still not completely understood.

LDN 1172 (hereafter L1172), a dark nebula, lies in the tail part of the cometary shaped complex. It appeared first time as an extended emission in 100 μm and 160 μm continuum maps (Ladd & Hodapp, 1997). Fig. 4.1 shows the dust column density map of the whole complex. The reflection nebula, NGC 7023 and L1174 which are discussed in the previous chapter, are identified and labelled. The dark nebula, L1172 is also identified and labelled. There is one more dark cloud, LDN 1173 (hereafter L1173), lying to the east of L1172 is also identified and marked in the figure.

L1172 harbors an young source IRAS 21017+6742 (Clark, 1991) with the presence of outflow (Wu et al., 1996). Kauffmann et al. (2008) studied the dust properties of L1172 using 1.2 mm thermal dust emission using MAMBO bolometer array. Multiple line observations covering the high density core, L1172, using CS (2-1), NH_3 (Zhou et al., 1989) have been carried out. The $H^{13}CO^+$ line kinematics was also studied by Mardones et al. (1997). The peak emission in N_2H^+ line matches with HCO^+ self-absorption dip. Previous line observations were made using frequency switching observations technique. Gregersen et al. (2000) carried out $H^{13}CO^+$ (3-2) observations using 10.4 m telescope of the Caltech Submillimeter Observatory (CSO) at Mauna Kea, Hawaii. They found out double-peaked profiles with the absorption of $H^{12}CO^+$ emission at peak of $H^{13}CO^+$ peak emission. B-field geometry of the entire complex was derived by Piyali et al. 2020 (submitted) using R-band polarimetry of the background stars.

To understand the physical processes involved in the filament formation and their evolution, it is important to study their morphology, density structures, B-field geometry, and kinematics of gas molecules of the complex as a whole. The role of the B-fields in the formation of filaments and their evolution is likely to be important as it makes the flow to survive longer where velocity field and B-field are preferentially aligned parallel to each other (Matthaeus et al., 2008). In this chapter, we investigated the kinematics of the gas lying in the tail part of L1172/1174 complex by making molecular line observations. The main goals of the study are (a) to examine the properties of the filaments associated with the tail, (b) to examine the properties of the clumps identified, and (c) to examine the properties of the filaments with respect to the B-field geometry. The results from this study are expected to provide useful insight into the formation of the "hub-filament" structure seen in L1172/1174.

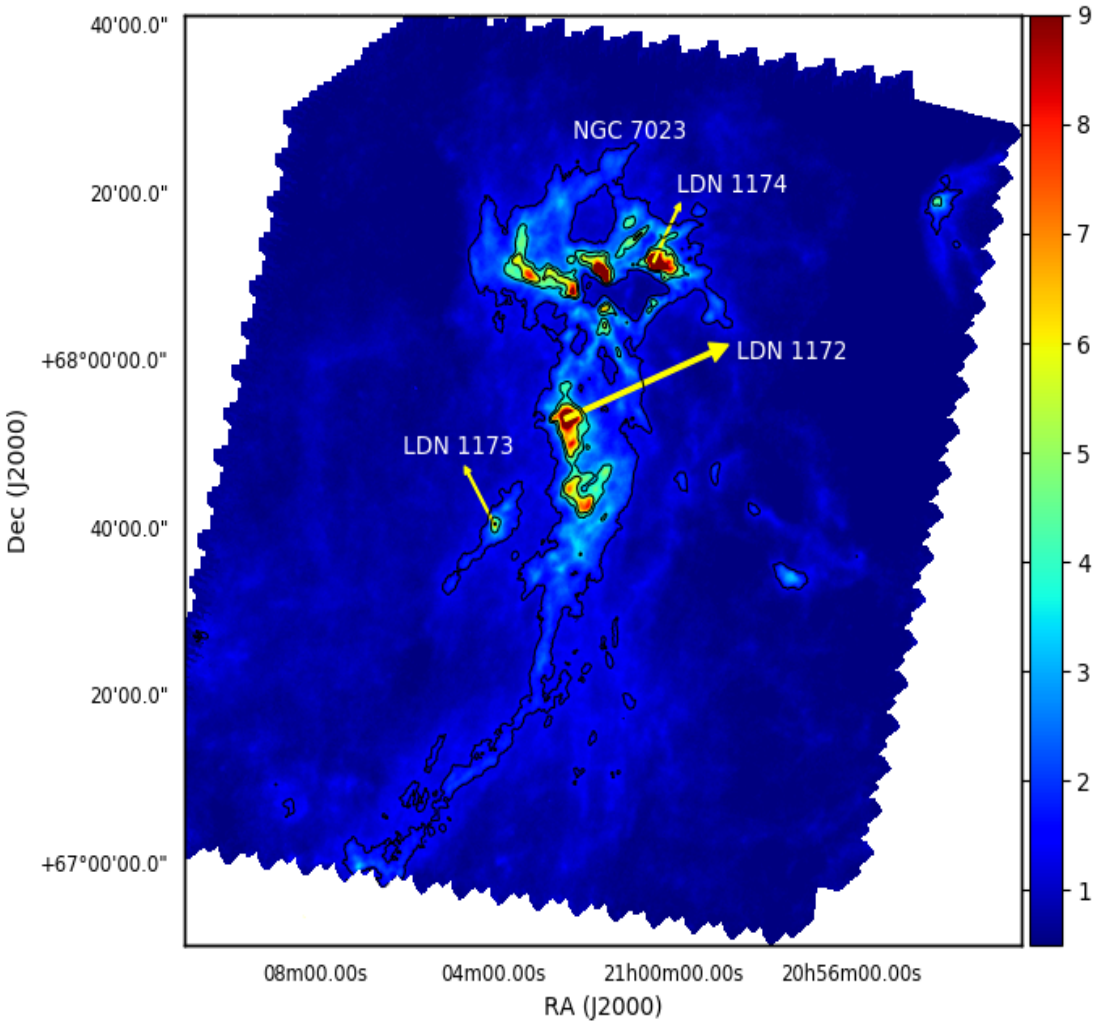

Figure 4.1: Distribution of clouds over the full complex L1172/L1174. The dark nebulae L1174, L1173, L1172 are labelled with NGC 7023 reflection nebulae. Black contours represent column density contours in the range 1-3 $\times$ 10^{21} cm^{-2} in steps of 1 $\times$ 10^{21} cm^{-2}.

4.2 Observations and data reduction

4.2.1 Molecular line observations

We have carried out On-The-Fly (OTF) mapping of the region of the cloud L1172/L1174 with the 14 m diameter single-dish telescope of Taedeuk Radio Astronomy Observatory in Daejeon, South Korea between November 16-28, 2018. The basic information for each line observed is given in the Chapter 3. We have used dust continuum data and extracted Planck polarization maps to study B-field structure of the tail region. Since it is a part of the full complex like molecular line observations, the details have already been discussed in the Chapter 3. The regions numbered as 3 and 4 in the Chapter 3 (Fig. 3.1) will be discussed in detail in this chapter.

4.3 Results and Analysis

4.3.1 Identification of the filaments and Clumps

Using the *Herschel* images taken at wavelengths from 160 μm to 500 μm with the PACS and the SPIRE instruments, a dust temperature (T_d) map and a column density (N_{H_2}) map of the entire L1172/1174 complex were produced by (Di Francesco et al., 2020). The maps are produced at a spatial resolution of $36''$ with a pixel grid of $3''$. The modified blackbody used in the spectral energy distributions (SEDs) fitting of each pixel includes a dust opacity, $\tau = 0.144$ cm^2 g^{-1} at 250 μm (incorporating a dust-to-gas ratio of 100) with a power-law dependence with wavelength of index, $\beta = 2.0$ Hildebrand (1983). In addition, the mean molecular weight per H_2 molecule of $\mu = 2.8$ is assumed here (Kauffmann et al., 2008) to convert gas surface density into H_2 column density.

To trace the high density structures in the cloud, we used publicly available package *Filfinder* (Koch & Rosolowsky, 2015) on the dust column density map at the resolution of $36''$. We used a flattening percentile of 99 to suppress the presence of high density peaks or clumps present in the data. A global threshold of 1.55×10^{21} cm^{-2} is applied which is two times the mode of column density distribution to derive a mask. We used an adaptive threshold of 0.2 pc (twice the expected filament width (Arzoumanian et al., 2011)). The size threshold corresponds to an area of ellipse with a width of 0.1 pc and an aspect ratio of 5. The "skeleton" is the medial line of a filament which is used in further analysis. We have pruned the extracted filaments by putting a branch threshold of 10 pixels. The distribution of filaments extracted using the *Filfinder* algorithm are shown in solid black curves in Fig. 6.3 (left panel). The filament extending in the north-south direction has a maximum length of 10 pc with an orientation of 162° and a curvature of 46° with respect to the north increasing eastward. The morphology of the longest filament (F_l) is not straight but exhibits a loop like structure towards the western side which will be discussed further in the channel maps. In addition to this, there are fainter filaments also identified which are shorter in length. We will also discuss about a filament F_m which is on the eastern side of the longest filament.

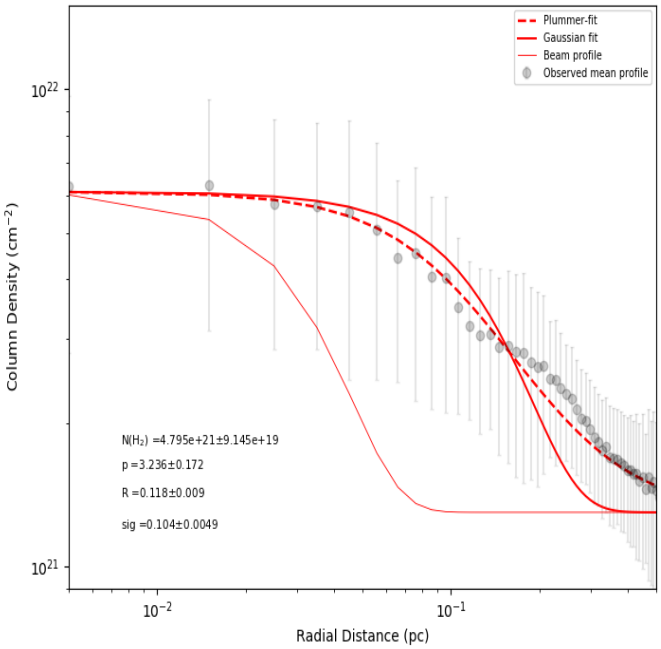

Figure 4.2: Mean radial column density profile of the filament, F_l (gray points) measured perpendicular to the crest of filament. The gray error bars mark the $\pm 1\sigma$ dispersion. The solid red curve shows the best-fit Plummer model fitted on the mean radial profile. The red dashed curve represents the best-fit Gaussian function to the range of inner radius in the filament. The thin solid red curve represents the Gaussian profile of the beam.

We derived the radial profile of the filament containing cloud L1172 extending from north to south direction. The background column density is a local property of every filament and varied through the full column density map. We fitted a Plummer-like function (Nutter et al., 2008) and a Gaussian function to the average column density profiles on three filaments which are shown with red color curve overlapped on black color filaments in Fig. 6.3. The resulting radial profiles are shown in Fig. 4.2. The fitting radius was taken as 0.5 pc and the local background density was taken as 1.3× 10^{21} cm^{-2}. We then sampled the radial profile with cuts perpendicular to the crest. The positions of the cuts along the crest were separated by 20 pixels to ensure that the profiles at the crest position are not correlated. The presence of high density peaks of the cores along the length of the filament may effect the estimation of the filament properties and hence needs to be removed. We used only negative side of the radial profile so that the local background is not affected by the neighbouring high density peaks. A zeroth-order polynomial fit was applied to the background subtraction before we made the fits to the profile. The diameter of the flat inner plateau is found to be $2R_{flat}$ = 0.172±0.005 pc. The power-law index of the best-fit Plummer model is p = 2.6±0.1, while the mean deconvolved width of the best-fit Gaussian model is FWHM = 0.23 pc. The peak column density value from the best-fit is found to be ≈ 4.9±0.06 × 10^{21} cm^{-2}.

We also used *Astrodendrogram*, a Python based package to extract the clumps from L1172/L1174 using dust column density map. The following parameters were set: minimum threshold ~ 2.8 , min_delta ~ 0.7 , min_pix ~ 5. The minimum number of pixels were taken as 5 to consider any clump as an independent parameter. More details on its methodology are given in chapter 2.

A total of 24 clumps were extracted from the algorithm where the ones which lie on the edges of map were removed. The area subtended by each clump should be larger than the area of beam, 36″. This condition removes two high density cores from the sample as the core has been resolved into two. These cores are on the eastern side of L1174 nebula and coincides with the position of L1174 high density core within 20″ of the positions of the clumps. We will consider the properties of these clumps separately in section 5.4. In this chapter, we will discuss about the properties of the clumps which lie only on the filament.

4.3.2 Large scale distribution of gas

- **^{12}CO (1-0) and C^{18}O (1-0) emission**

  As already mentioned in chapter 3 (section 2), the tail region shows only one velocity component in the resulting averaged spectrum. That implies the presence of only one cloud component along the line-of-sight. The velocity component is well fitted with a single Gaussian function. We obtained a peak velocity of 2.82 km s^{-1}based on the Gaussian fit to the ^{12}CO (1-0) line. The averaged spectrum of C^{18}O also shows a single peak at 2.78 km s^{-1}. The line width of ^{12}CO is found to be ~2.3 km s^{-1}while C^{18}O is relatively narrower with a line width of ~0.84 km s^{-1}. The Gaussian fit to ^{12}CO line shows deviation at higher velocities from 4 to 6 km

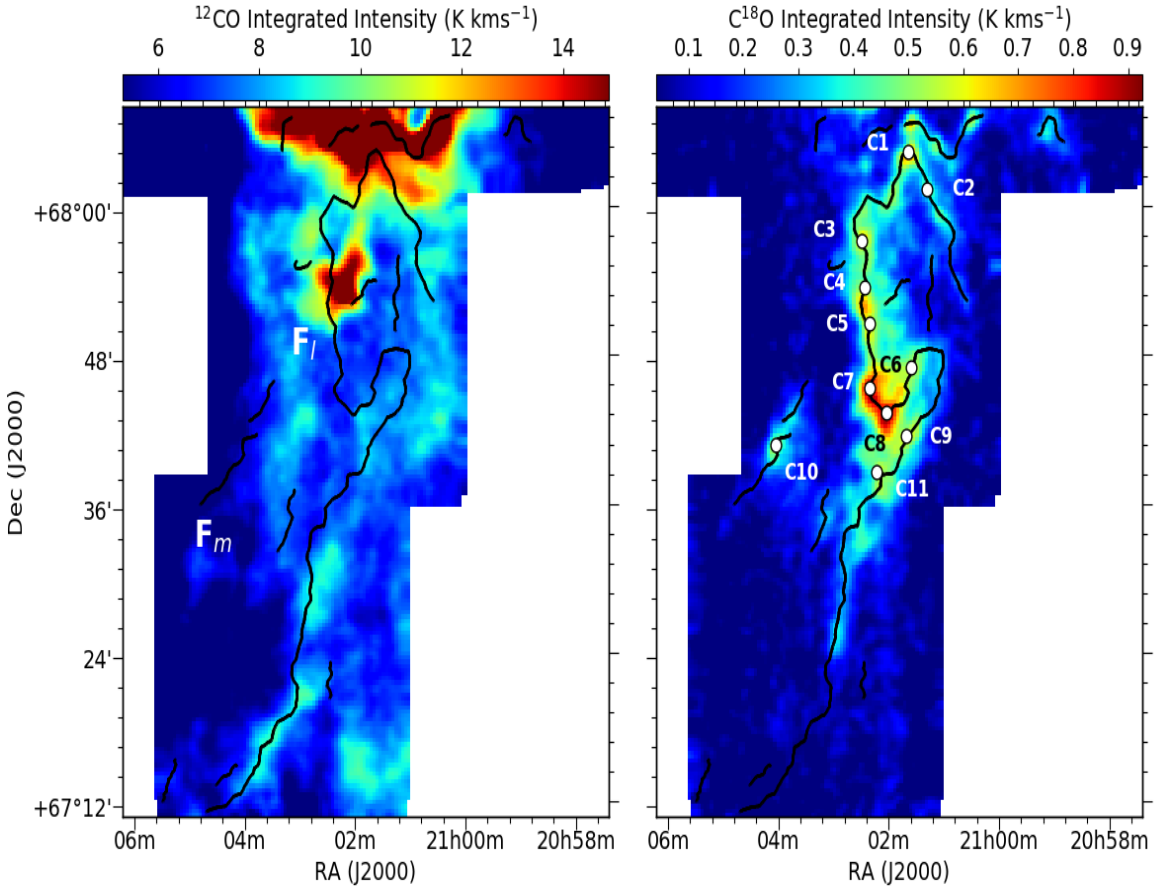

Figure 4.3: Integrated intensity contours of ^{12}CO (left) and the C^{18}O (right) gas emission. The extracted filaments are shown in left panel by black curves. The white circles in right panel (numbered from 1-11) shows extracted clumps using Astrodendrogram algorithm.

$s^{-1}$and from 1 to 0 km s^{-1}. The detailed analysis of the high velocity components will be explained using channel maps in further sections.

Fig. 6.3 shows the distribution of ^{12}CO and C^{18}O gas for the filamentary region. The moment maps for ^{12}CO and C^{18}O are created by using those channels having temperature values exceeding 0.3 K and 0.1 K (approximately 3 times the rms level per channel) respectively. The integrated intensity distribution of ^{12}CO is shown in Fig. 6.3 (left panel). The ^{12}CO is integrated over a velocity range of -4.5 to 7.5 km s^{-1}. The distribution of ^{12}CO line is quite diffuse and prevalent over the whole mapped region. The intensity of the emission is selectively higher towards the western side of the longest filament as compared to that of the eastern part. The distribution of C^{18}O (1-0) emission is shown in Fig. 6.3 (right) in units of K kms^{-1}. The intensity levels are taken from 0.1-1.3 K kms^{-1} in steps of 3σ= 0.1 K kms^{-1}. The velocity channels used for the summation are in the range of 1.9-3.6 km s^{-1}. The C^{18}O emission does not appear to correlate very well with the longest filament obtained from the dust column density map shown in Fig. 6.3. The southern most part of the filament does not show the C^{18}O emission greater than 3σ value. The spatial extent of C^{18}O is found to be less when compared to the ^{12}CO emission (greater than 3σ). The longest filament derived from the dust emission does not correlate well with the C^{18}O emission. All the filaments other than F_l and F_m do not have emission greater than 3σ in C^{18}O emission, therefore we will not consider them in our kinematical analysis. The clumps are identified on the intensity image of C^{18}O line where except C1, all the clumps lie on the filament F_l.

Fig. 6.4 shows the channel maps of ^{12}CO line over the velocity range from -4.1 to 7.5 km s^{-1}. The distribution of ^{12}CO emission is quite diffuse over the full velocity range. However, most of the structures are seen in the velocity range of 2.0 <v≤ 3.0 km s^{-1}, Fig. 6.4 (d). There are low density striations seen around the filaments F_l and F_m which are oriented parallel to the direction of the southern part of longest filament. The gas motion in blue- and red-shifted velocities is preferentially seen towards eastern and western side of filament. In panel (g), we notice that there is an enhanced emission towards the extreme south of the mapped region. The detailed study of high velocity components present along the line-of-sight will be analysed by examining individual line profiles.

Fig. 6.5 shows the channel maps of C^{18}O emission towards the filamentary structure. Each channel map is obtained by integrating the emission over 0.3 km s^{-1} velocity intervals. These channel maps help us to examine the gas distribution in the filament for a given velocity interval. The extreme ends of the filament F_l start appearing prominently in panel (b). The longest filament is predominantly distributed over two velocity channels in panel (c) and (d). The emission towards the loop structure in F_l is the highest in panel (d) with intensity ∼1 K km $s^{-1}$and disappears in velocity range from 3.2 to 3.5 km s^{-1}.

- **Gas kinematics of the filaments**

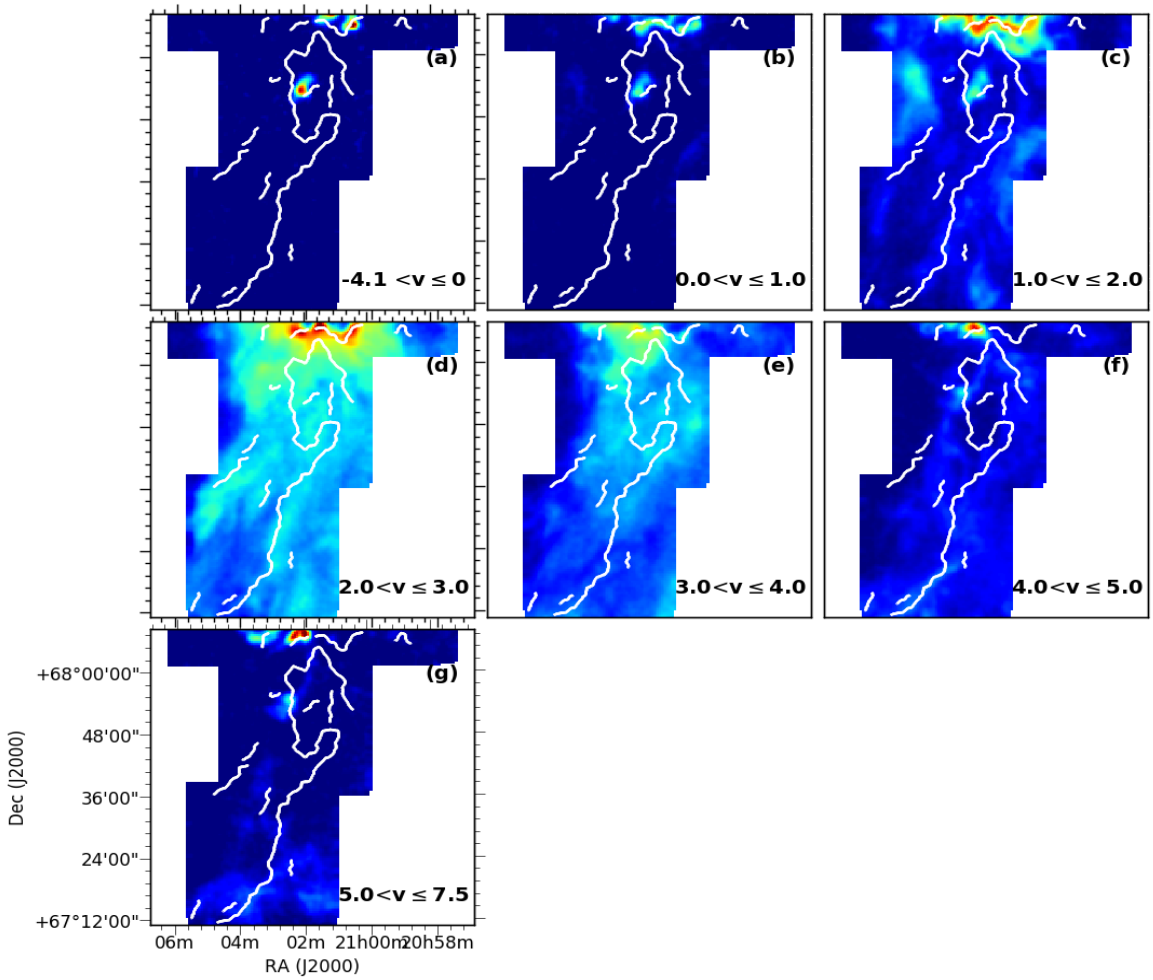

Figure 4.4: Channel maps for ^{12}CO lines. Each channel shows the velocity range used for the integrated emission. The intensity is in the units of K km s^{-1}. Each panel shows emission higher than the threshold of the map.

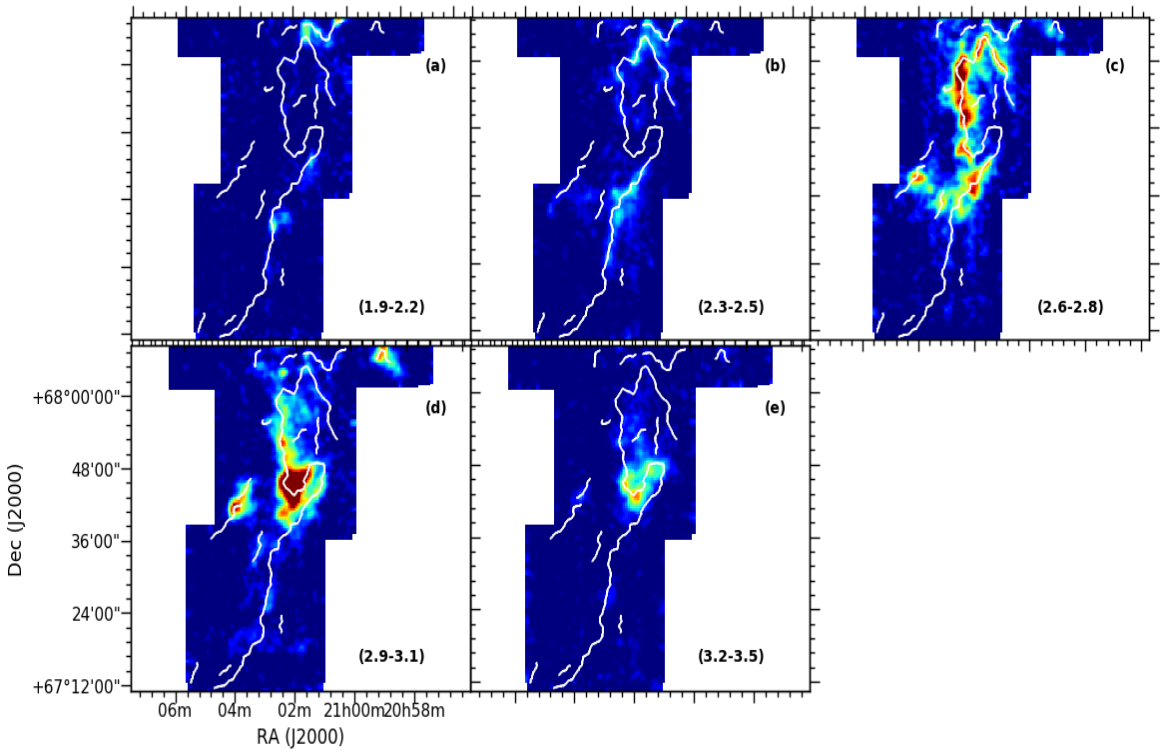

Figure 4.5: Channel maps for $C^{18}O$ lines. Each channel shows the velocity range used for the integrated emission. The intensity is in the units of K km s^{-1}. The background intensity is 0.02 K km s^{-1}. The white lines in each panel shows the crest of derived filaments.

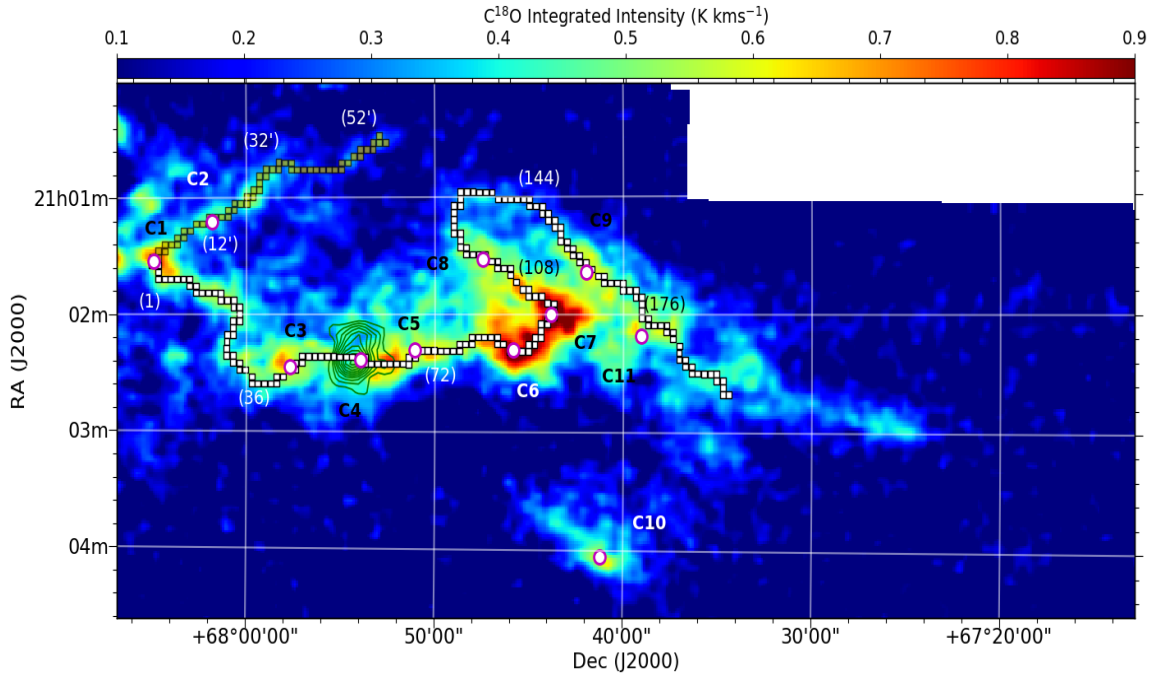

Figure 4.6: Integrated intensity image of $C^{18}O$ emission over the range 2.0-3.5 km s^{-1}. The image is rotated by 90 degrees and the vertical axis shows right ascension. The magenta circles marks the position of clumps extracted. The white boxes show the positions of skeleton of filament along north-south direction. The numbers are identified to show the representative positions along the filament. Green contours show the integrated emission of N_2H^+ (1-0) emission.

Characterising the gas motion inside the filaments requires the study of velocity structure. We investigate the radial velocity fields of the derived filaments along their major axes and compare our results with the existing filament and core formation models. We extracted 10 filaments in the tail region of this complex. The filaments where the integrated intensity is less than 3σ were not considered in the characterisation of the gas motions along their length. Since the main filaments, F_l and F_m show the intensity greater than 3σ in $C^{18}O$ line map, we focused mainly on the analysis of these two filaments. In this section, we studied the kinematical properties with the special focus on the line shape properties and velocity gradients.

From the channel maps (Fig.6.5), we noticed that the longest filament identified using Filfinder is not traced in a single velocity channel around the ambient velocity but the parts of it are distributed over a velocity range from 1.9 to 3.5 km s^{-1}. Therefore, we looked into the detailed velocity structure by examining the line profiles over the filament length starting from the southern part of the HD 200775. Fig.4.6 shows the integrated intensity map for $C^{18}O$ emission over the tail part of the complex. The skeleton of F_l is shown by small white boxes of size $20'' \times 20''$ each. There are 244 extracted set of spectra along the filament. White circles represent the position of extracted clumps. The green contours are the integrated intensity

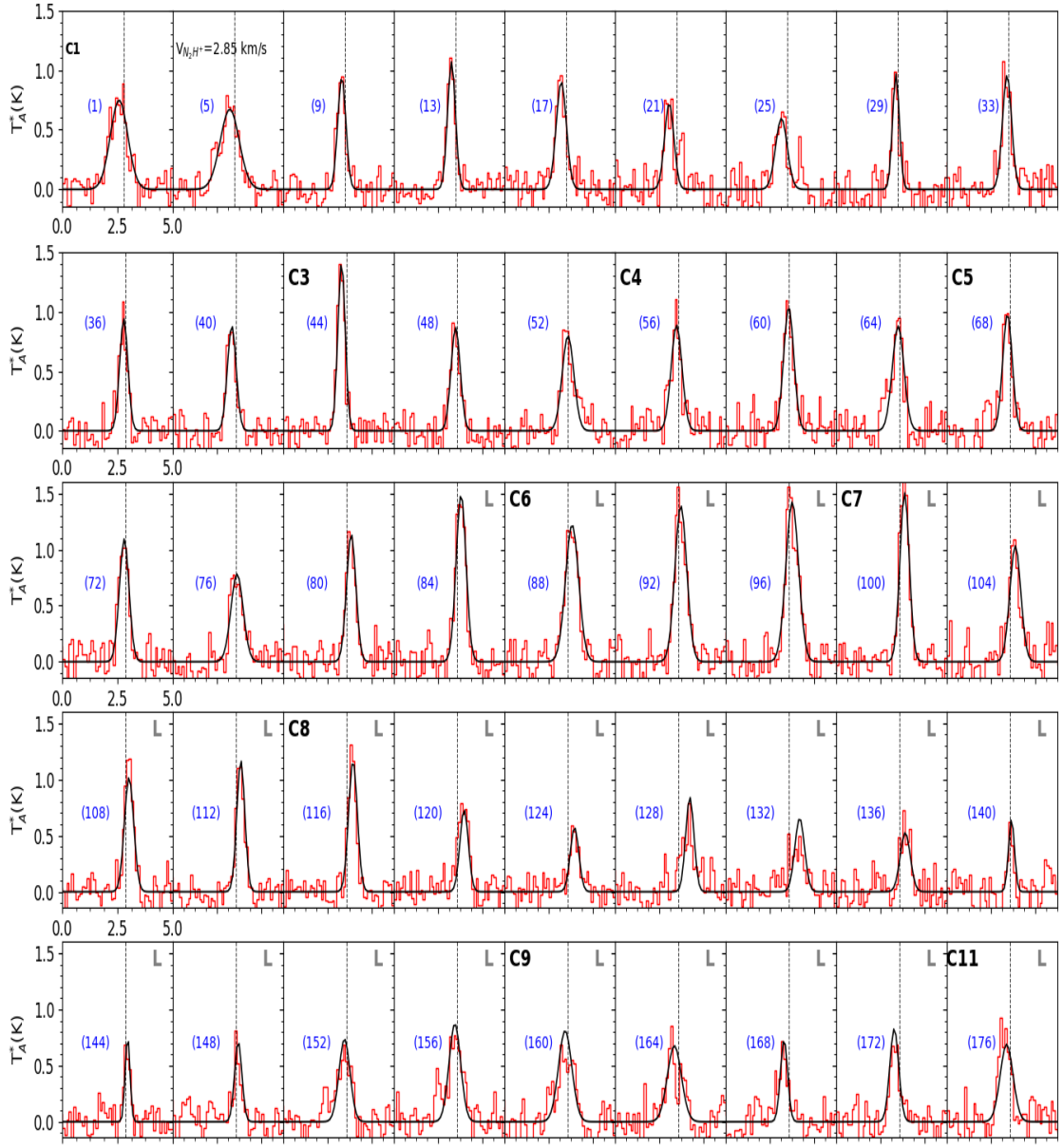

Figure 4.7: Profiles of $C^{18}O$ lines over the longest filament, F_l. Each panel represents the $C^{18}O$ emission at each pixel identified in Fig. 4.6. The black boxes represent positions of high density skeletons derived from *Filfinder*. The black solid line shows the fitted gaussian function to the profile. Each box is labelled starting from 1-176 in steps of 4 spectra along the length. The V_{lsr} of the cloud, 2.85 km $s^{-1}$is shown with dashed black line. The spectrum with at the positions of the cores are labelled from C1-C11 and the letter "L" at top right corner of spectra shows the profiles along the loop structure.

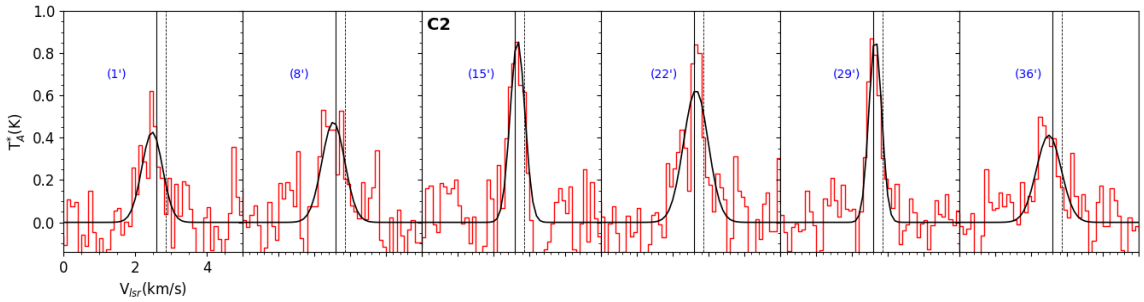

Figure 4.8: Profiles of $C^{18}O$ lines over the western part of the filament, F_l which is denoted by 12', 32' and 52' in Fig. 4.6.

emission for N_2H^+ line. But only some of the representative positions along the length are shown in Fig.4.7.

The $C^{18}O$ lines are displayed as a step function in red with a Gaussian fitting to each using the black solid lines in Fig.4.7. All along the filament, the $C^{18}O$ show emission characterized by a single peak implying the presence of only one cloud component along the line-of-sight. There is a variation in the centroid velocity and velocity dispersion all over the position of the filament. The regions nearer to the hub harbouring clumps C1 and C2 show broader line profiles with low $C^{18}O$ intensity and with higher velocity width. The profiles are shown at every fifth spectrum along the crest of filament. The maximum intensity is obtained around the loop structure (in sec 4.4.3) of the order of 5 K. The extreme end of the filament towards south shows an asymmetric emission on the blue shifted velocities. The western side of the main filament shows a branch of length 1.8 pc with numbers from 12, 32' and 52'. We plotted spectral profiles at some selected positions as shown in Fig. 4.8. The spectrum 22' shows two components in $C^{18}O$ profiles. The solid black line shows the peak value of the $C^{18}O$ emission in this branch, 2.6 km s^{-1}which is different from the V_{lsr} of the cloud (dottted line, 2.85 km s^{-1}). In such cases, we specifically fitted a single Gaussian component to the profile which is closer to the systematic velocity. The spectrum 15' shows the position of core C2 where the profile exhibits a single Gaussian function with temperature as 0.75 K.

As the Fig.4.6 suggested, we find that the $C^{18}O$ intensity is very high towards the southern part of the filament that harbours two clumps, C6 and C7. Correspondingly, the profiles at these positions are highly peaked at the intensity value of 1.2 K and show quite narrower width.

Most of the positions along the filament F_l show a relatively simple velocity structure with one velocity component. In order to have a complete image of the kinematical profiles of the filaments, we extracted a number of ^{12}CO and $C^{18}O$ spectra along the filament skeletons. In $C^{18}O$ lines, we fitted single Gaussian function to all the lines where signal-to-noise (S/N) is greater than 3. We obtained the optimum fitting parameters, such as; peak temperature (T_{peak}), centroid velocity (V_{lsr}) and velocity dispersion (σ). In addition to the kinematic properties,

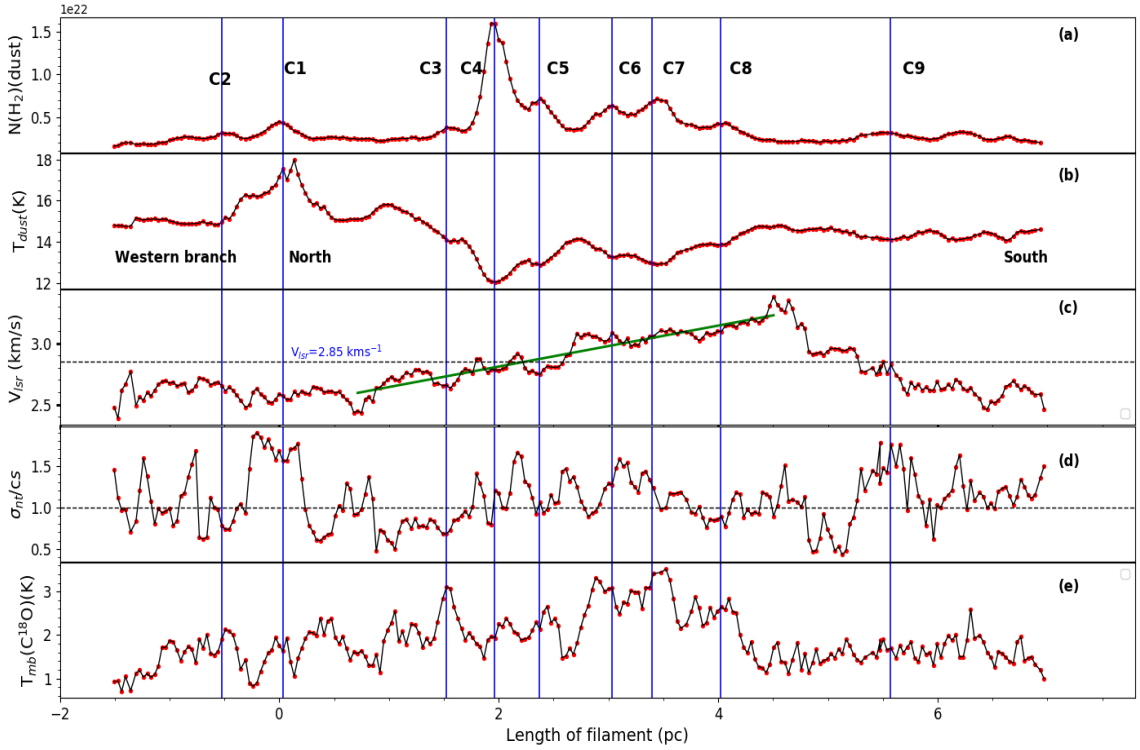

Figure 4.9: Variation of dust column and gas along the length of filament. The northern most point is taken as the reference for the distance axis. The western side branch is shown with negative value of distances.

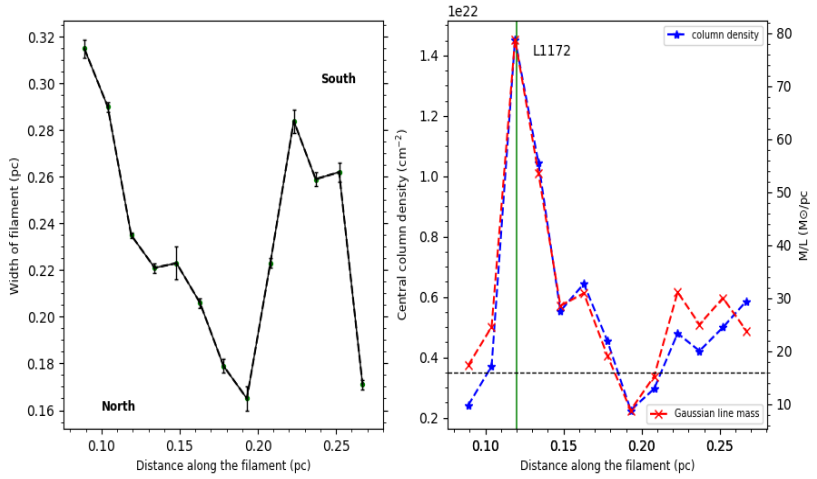

Figure 4.10: **Left panel:** Deconvolved Gaussian FWHM of the filament as a function of position along the crest of F_l (starting from Northern part towards the core). **Right panel:** The dashed blue line shows the central column density along the skeleton of the filament obtained from the best-fit Plummer model. Dashed red line shows the background-subtracted mass-per-unit length calculated from the Gaussian fit (dashed red line). The dashed gray horizontal line indicates the critical mass-per-unit length of an isothermal filament in equilibrium as $2c_s^2/G \sim 16\ M_\odot\ pc^{-1}$ at 10 K.

the comparison of the distribution of the dust with the gas along the filament is also made as it is useful to understand the overall structure and the kinematics of the different parts of the filament. We show the gas and dust the properties of F_l in Fig.4.9.

We regridded the pixel grid of dust column density and temperature map at 3″ with respect to the 20″ which is pixel grid of $C^{18}O$ emission map. The northern most part of F_l filament is chosen as the origin for the distance along the filament. The top panel (a) shows the variation of the dust column density as a function of distance along the filament. The filament F_l shows the column density in the range 2.4-16 $\times\ 10^{21}$ cm^{-2}. The maximum value of the column density is 1.6 $\times\ 10^{22}$ cm^{-2} which is at the position of L1172 (C4). The variation along the filament skeleton shows multiple peaks along the length which correspond to the clump positions identified in the figure. The positions of the clumps are identified using vertical lines drawn in violet. Panel (b) shows the variation of the dust temperature as a function of distance from the northern part. The starting point at 0.034 pc distance shows the maximum temperature around of 17.5 K which coincides with the position of core C1. This position is directly being affected from the radiation from the central star which has heated up the surrounding gas and thereby, C1 possesses a higher temperature. The dust temperature varies from 12 to 18 K. There is a temperature gradient from north towards L1172 core and then rises up gradually till 14 K.

The mass per unit length decides whether a filament is unstable to the gravitational collapse radially and fragmentation along the length of filament. For the filament which is non-magnetized and isothermal, the critical line mass, M_{line}(crit) is approximately 15-20 M$\odot$ pc^{-1} for the typical temperatures of molecular gas $\sim$ 10-12 K (Inutsuka & Miyama, 1997). The column density emission was used to constrain the radial profile structure of the density of the filament and estimated its mass-per-unit length (M_{line}) as a function of position along the main axis. Fig. 4.10 shows the variation of M_{line} with the distance along the filament. The variation of M/L along the crest of the filament shows that the filament is marginally supercritical. We define filament width to be the FWHM value deconvolved by the beam-width as described by (Arzoumanian et al., 2011). The mean FWHM of the derived filament skeleton is $\sim$ 0.2 pc and spectral power index is 2.6.

Panel (c) of Fig. 4.9 shows the variation of centroid velocity (V_{lsr}) along the filament as a function of length from the north to the south direction. The velocity structure of the filament F_l is characterized by continuous and unique velocity component. At large scales, the filament F_l presents a longitudinal and smooth velocity gradient along the length of filament towards the core C4 till C8 and the value is calculated as 0.2 km s^{-1}pc^{-1}.

Although the average spectrum of the mapped region shows a single velocity component, most of the positions along F_l show narrow lines in C^{18}O emission. We parameterized the kinematic information present in ^{12}CO and C^{18}O data by fitting Gaussian profiles to all the spectra after examining individual spectrum.

The centroid velocity ranges from 2.4-3.4 km s^{-1}. The mean value is 2.8 $\pm$ 0.2 km s^{-1}. There is evidence of smooth velocity gradient over 1 pc towards the C4 starting from 0.7 to 2.7 pc. The systematic velocity of the L1172 cloud is found to be 2.85$\pm$0.02 km s^{-1}. The dispersion in the values is 0.08 km s^{-1}which is slightly higher than the spectral resolution of the data.

The filament has line-widths in the range of 0.23-1.0 km s^{-1}for C^{18}O spectral profiles. Finally, we studied the variation of mach number (M) in the fourth panel (d). As explained and used in previous chapter also, the Mach number is σ/c$_s$(T$_k$) a ratio of non-thermal velocity dispersion and isothermal sound speed. The total velocity dispersion is a combination of thermal and non-thermal components in the spectral lines. The non-thermal component σ_{NT} can be determined as,

$$\sigma_{nt} = \sqrt{(\sigma^{obs})^2 - (\sigma^{th})^2}$$

where σ^{th} is given as $\sqrt{k_B T_k/\mu_{obs} m_H}$ which is the thermal velocity dispersion, $\mu_{obs} \sim 30$ is the mean molecular weight of the observed C^{18}O molecule, T$_k$ is the gas kinetic temperature and k$_B$ is the Boltzmann constant, m$_H$ is the mass of hydrogen.

We use gas kinetic temperature as excitation temperature derived from the LTE analysis. The isothermal sound speed, c$_s$(T$_k$) $\approx$ $\sqrt{k_B T_k/\mu_{gas} m_H}$ is calculated assuming average molecular

mass as 2.3 and m(H_2) is the mass of hydrogen. The dashed horizontal line marks the value of M as 1. The value of Mach number varies from 0.8 to 2. The extreme points of the variation shows the maximum values which are in the vicinity of the star, that hosts the hub. The gas along the length of filament are either subsonic (≤ 1) or transonic (~ 1) on an average. Overall, the filament can be considered as subsonic to transonic.

The bottom most panel of Fig. 4.9 shows the variation of main beam temperature along the length of filament. The main beam temperature lies in the range 1.0-3.4 K. The main beam temperature is 0.8 K at the position of C4. However, the maximum value of T_{mb} approaches higher value around C6 and C7 positions. The absence of a well defined peak around L1172 core could be because of the depletion of carbon based molecules.

4.3.3 Kinematics of L1173 filament

We derived properties of the filament identified along L1173, identified as F_m using the dust continuum and $C^{18}O$ line emission. The pixels along the skeleton of L1173 filament which do not exhibit $C^{18}O$ emission greater than 3σ ($\approx$ 0.3 K km s^{-1}) were not considered in the analysis.

Fig. 4.11 shows the comparison of gas and dust properties along the filament, L1173. It hosts a core named as C10 identified by red solid line at a length of 0.8 pc. The reference point is taken from the southern part of the filament. Panel (a) shows the dust column density as a function of distance towards the west along its length. There are two filaments around this region as evident from Fig.6.3 (left panel). The peak column density is 4×10^{21} cm^{-2} and the values varies from 2-4 $\times$ 10^{21} cm^{-2}. The dust temperature value shown in panel (b) ranges from 13.5 to 15.5 K. The average dust temperature is 14.6±0.5 K. The two extreme ends of the filament shows higher dust temperature of the order 15.5 K.

Panel (c) shows the variation of the centroid velocity as a function of the distance. The centroid velocity ranges from 2.5 to 3.1 km s^{-1}. We calculated mean centroid velocity as 2.85 km $s^{-1}$with a dispersion of 0.19 km s^{-1}. The peak line velocity shows a unidirectional shift from blue-shifted to red-shifted velocities occurring almost at the location of the core C10.

The Mach number (in panel (d)) shows that the motions over the filament is overall subsonic. The value of Mach number ranges from 0.4 to 1.1 with a mean value as 0.7. The non-thermal motions were calculated adopting the same procedure as we used in the case of F_l filament. To calculate the non-thermal velocity, we used T_x excitation temperature obtained at each pixel which is the mean value obtained along the filament. The points around southern edge and at distance 0.22 pc, the filament shows almost transonic motion where it is slightly higher than 1. Otherwise, the filament as a whole is found to be quiescent. Panel (e) shows the variation of main beam brightness temperature, T_{mb} which shows a positive increase from reference to

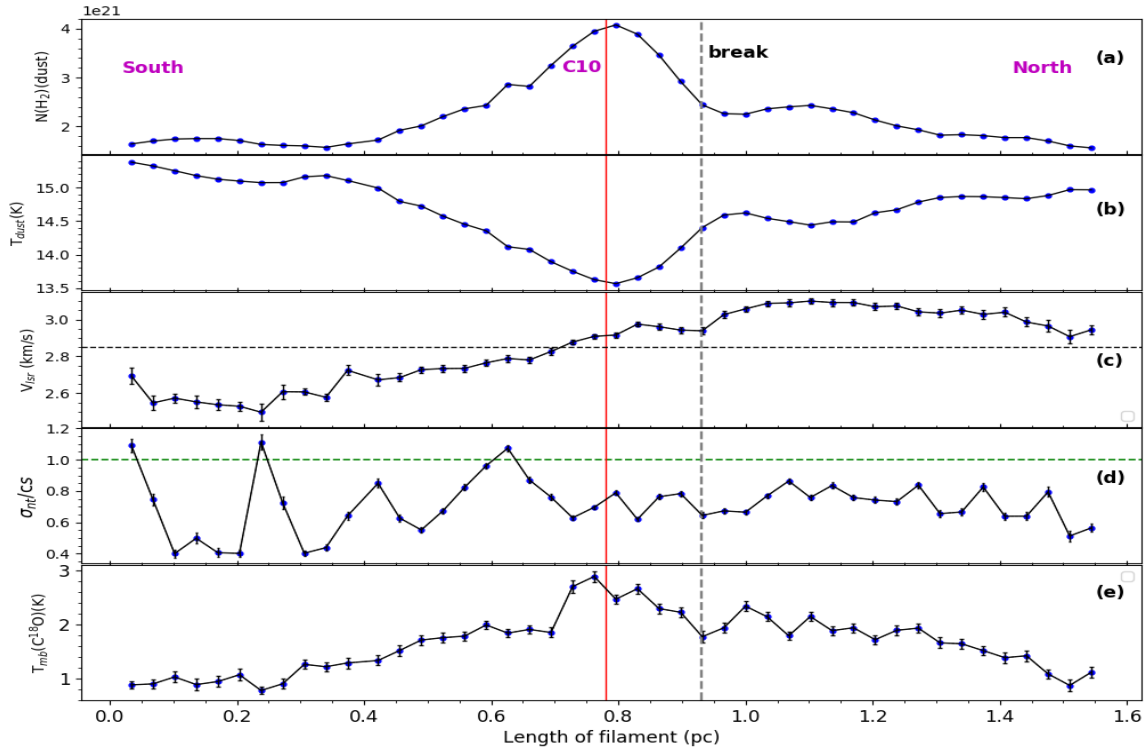

Figure 4.11: Variation of gas and dust properties along L1173 filament. Panels a,b,c,d,e are similar like long filament, F_l. Red solid line represents the core position, C10. The reference point is taken from southern edge of F_m filament.

Table 4.1: Properties of core derived using Astrodendro algorithm.

Core Name	RA (°)	Dec (°)	R (pc)	V_{lsr} km s^{-1}	M_{LTE} M⊙	M_{dust} M⊙	M_{vir} M⊙
(1)	(2)	(3)	(4)	(5)	(6)	(7)	(8)
C1	315.386505	68.081868	0.11	2.48	8.68	3.17	10.72
C2	315.300464	68.030586	0.08	2.65	3.11	1.48	4.98
C3	315.611498	67.961671	0.08	2.69	3.43	1.61	3.95
C4	315.597106	67.898789	0.17	2.81	10.62	18.12	9.69
C5	315.575089	67.850899	0.07	2.78	2.24	2.62	3.38
C6	315.381389	67.791299	0.09	3.11	2.90	1.90	4.17
C7	315.574748	67.764050	0.11	3.02	7.55	4.29	7.14
C8	315.499076	67.731148	0.13	3.06	10.74	6.79	7.77
C9	315.409814	67.699787	0.14	2.84	7.51	4.24	11.19
C10	316.011956	67.687017	0.12	2.91	4.34	3.28	4.75
C11	315.544369	67.651196	0.17	2.77	9.91	6.06	10.75

the middle point of the filament. The core position shows the maximum value of $T_{mb} \sim 2.9$ K. The position of $C^{18}O$ peak matches well with the dust column density peak in panel (a) which suggests that core is evolving. The value ranges from 0.7 to 2.8 K with lower temperature on both the edges of filament. The mean and dispersion of T_{mb} is 1.6 K and 0.53 K.

4.3.4 Properties of the Clumps identified

Fig. 6.3 (right) shows the distribution of clumps derived using the *Astrodendro* algorithm in the tail region of L1172/L1174 complex. Assuming a single cloud component along the line-of-sight, we fitted a single Gaussian function to all the $C^{18}O$ profiles. We derived the best fit parameters such as the peak temperature T_{peak}, the centroid velocity (V_{lsr}) and the velocity dispersion (σ). Table 6.1 shows the physical properties derived for all the clumps. The clumps are distributed throughout the length of the tail region of L1172/L1174 complex. The range of the estimated effective radius is from 0.07 to 0.18 pc which is the geometric mean of the FWHM of the major and the minor axes.

– Core C1: C1 lies at the extreme northern edge of the filament F_m where the effect of the radiation from HD 200775 is possibly the maximum. The top left panel of Fig. 4.12 shows the average profile around the clump C1. The ^{12}CO profiles shows high velocity

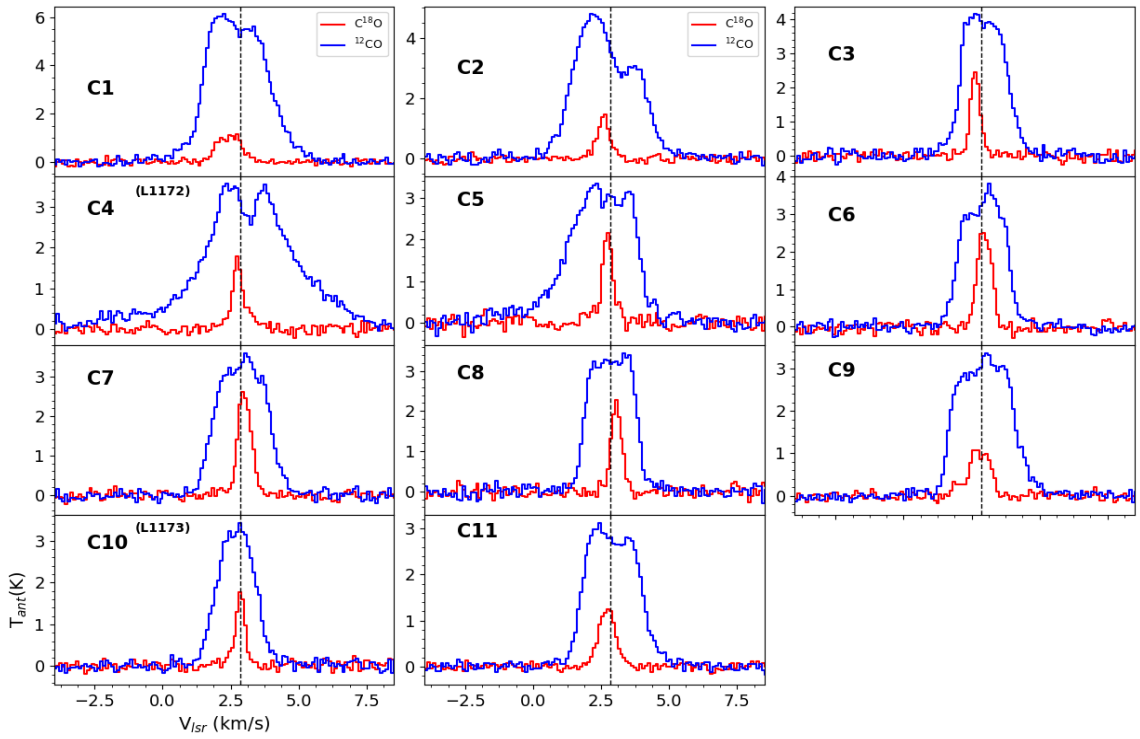

Figure 4.12: Average profiles of each core where red is $C^{18}O$ line scaled by a factor of 2 and profile in each panel is ^{12}CO emission. The dashed line shows the v_{lsr} of the cloud ~ 2.85 km s^{-1}using N_2H^+ lines.

component on red-shifted velocities. The peak of $C^{18}O$ line is 2.5 km s^{-1}. The dashed line in black color shows the systematic velocity of the cloud ~ 2.85 km s^{-1}. The line is broader and the presence of high velocity wings in ^{12}CO emission is evident.

- Core C2: This core lies at the western branch of F_l. The average profile of ^{12}CO line shows again high velocity wings and multiple components. The blue shifted peak is brighter than the red-shifted peak but this cannot be attributed to the infall asymmetry since the single peaked $C^{18}O$ line does not coincides with the dip in the ^{12}CO line.

- Core C3: C3 lies at the middle part of the filament F_l with mean velocity as 2.7 km s^{-1}. The average $C^{18}O$ emission is single peaked but higher than the C1 and the C2. Both the lines are narrower which suggests that the gas is mostly quiescent around this core.

- L1172 (C4): The kinematical properties of this core also called L1172 which is gravitationally bound and harbours a protostar, IRAS 21017+6742 (Clark, 1991). Using N_2H^+ hyperfine fitting, we derived the V_{lsr} velocity as 2.85 km s^{-1}. The ^{12}CO line very well traces the outflow as the low-intensity high velocity wings of outflow are detected because of its high abundance. The core has a peak dust column density of 2 $\times$ 10^{22} cm^{-2} and the dust temperature as 12 K. The systematic velocity is derived as 2.8 $\pm$ 0.02 km s^{-1}using $C^{18}O$ lines. The morphology of the $C^{18}O$ emission is not well concentrated around the core centre. The value of the average FWHM velocity of the gas was calculated as 0.6 km s^{-1}. With these values, the virial mass is calculated as 10 M$\odot$. The gas mass is calculated as 11 M$\odot$.

- C5: This core lies next to the L1172 core but not having larger mass. The size is smallest of all the derived cores which is derived as 0.07 pc. There are signatures of high velocity wings on blue-shifted velocity of ^{12}CO profile but narrower $C^{18}O$ emission. It shares a similar mean velocity of 2.8 km s^{-1}just like C4.

- C6,C7: Both these two cores show similar shapes of average profiles in ^{12}CO and $C^{18}O$ emission. The mean centroid velocity is also similar ~ 3.1 km s^{-1}.

- C8, C9: These two cores are of same size ~ 0.14 pc. The profile of the ^{12}CO line in C8 is broader with no high velocity wings and the profile of $C^{18}O$ line shows the highest temperature of all but narrower. C9 shows less $C^{18}O$ emission with an extra emission towards blue-shifted velocities. The high temperature at the position of C8 implies that the column density of $C^{18}O$ line is very high.

- L1173 (C10): The mean value of the peak velocity obtained using the $C^{18}O$ lines is 2.9 km s^{-1}. The gas mass of this core is almost equal to virial mass given the uncertainty which implies that the core is on the verge of being gravitationally bound. The lines are narrower in ^{12}CO and $C^{18}O$ averaged emission.

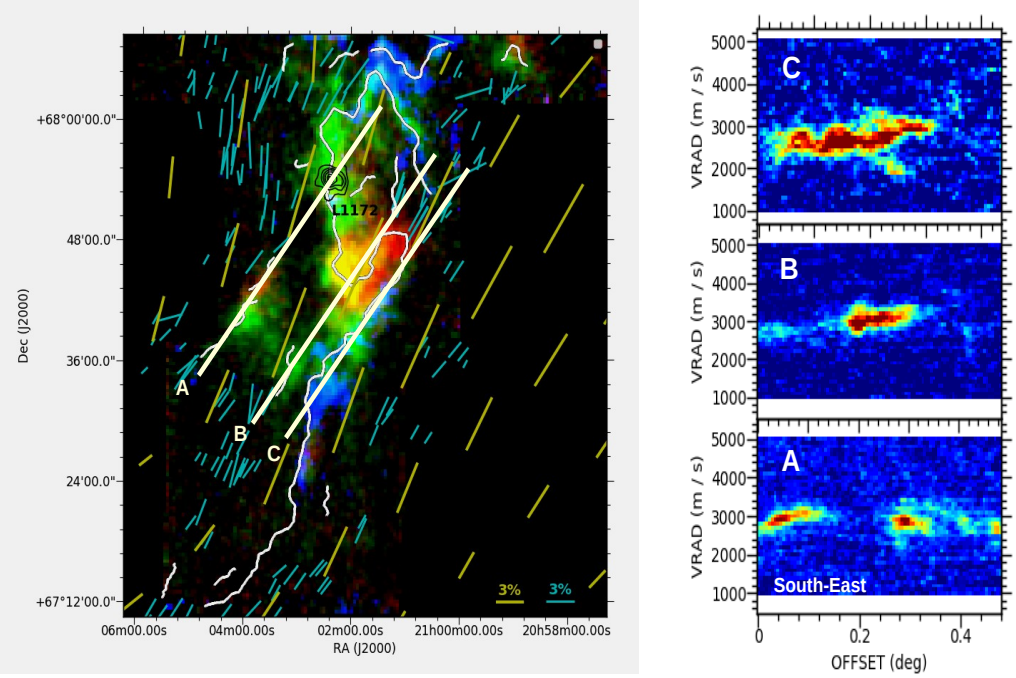

Figure 4.13: **Left:** Color-composite image of tail region of L1172/L1174 complex. The R-band optical and Planck polarization vectors overplotted on color-scale dust column distribution of L1172-L1174 complex. **Right:** Position velocity diagrams of the respective cuts shown in left panel.

– Core C11 shows an asymmetric profile of ^{12}CO line with blue peak brighter than red shifted peak. The red-shifted part of the line are more broader than the bluer side velocities.

4.3.5 Polarization measurements

Fig. 4.13 shows the results of optical polarization measurements in R-band and Planck polarization measurements in red color. The polarization vectors are overplotted on the dust column density map for the tail region of L1172/L1174 complex. The angles are converted from the equatorial to the galactic coordinate systems and are measured from the Galactic north increasing towards the east. The P(%) values are found to range from 0.4% to 4% and θ from 145°- 223°. The average values of P(%) and θ are 2.1±0.8% and 195°±12% respectively.

The Loop structure: The integrated intensity map of C^{18}O line shows maximum intensity ~ 1K km s^{-1}towards the western side of F_l as shown in Fig. 4.7. It appears like a loop which is oriented towards the north-west direction. The orientation of the loop matches with the orientation of the

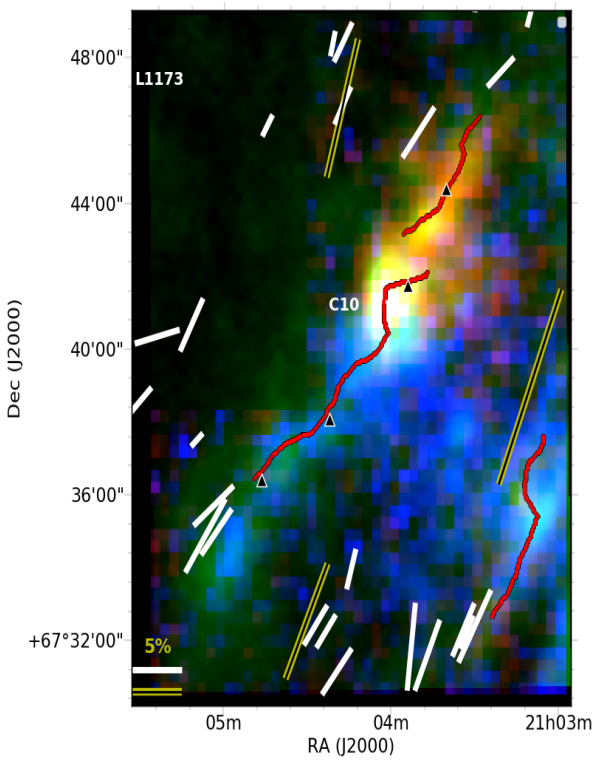

Figure 4.14: **Left:** Color composite image of F_m filament. Red shows the velocity range from 2.9-3.2 km s^{-1}, green shows the dust column density *Herschel* image and blue shows the channel map integrated from velocity range 1.9-2.8 km s^{-1}. Yellow lines show the Planck polarization vectors and white lines show the R-band optical polarization vectors. The scale of 5% is shown for reference. Red solid curve shows the extracted skeleton of F_m.

L1173 filament also. The orientation of the B-field as inferred from *Planck* and R-band polarization is shaping the loop structure as shown in Fig. 4.13. The angle of polarization is 135° for the southern part of filament derived from both the polarization observations. We notice that there are hair-like faint striations in between F_m (L1173) filament and the loop structure which are also oriented parallel to the B-field. The orientation of L1173 filament, striations and the loop structure are all aligned roughly in the same direction. To understand the velocity field along these directions, we made the Position velocity diagrams along three cuts as shown in Fig. 4.13. The analysis of velocity field along the L1173 filament, striations, and the loop structure shows a smooth velocity shift towards the north-west direction. The right panel of Fig. 4.13 shows the position velocity cuts at an angle of 135°from north towards east. We find a difference of 1 km s^{-1}between two extreme ends of the cut.

Fig. 4.14 shows the color composite image of the filament F_m containing L1173 core. The orientation of the filament is towards the north-western side. As discussed earlier, there is a change in the velocity from the south to the extreme northern edge of the filament from a blue- to red-shifted velocities. The B-field inferred using the R-band and the Planck polarization measurements is parallel to the direction of the change in the velocity and the orientation of the filament. This suggests that the

B-field may be playing a decisive role in the formation of this filament and shaping the morphology of the cloud. The clump, C10 is at one edge of the filament with the well defined peak of $C^{18}O$ ($T_{mb} \sim 3$ K) implies that the filament has already fragmented but the core is not yet virialised. This scenario agrees well with the magnetohydrodynamical studies where the colliding flows channelised by the B-fields are believed to be responsible for the formation of cores.

Although the orientation of the filament is 162°, there is a curvature of 48°in the shape of F_l. The B-field has a different direction from the loop structure to the northern parts which matches well with the filament orientation. The good agreement between the orientation of the structure and the field lines suggests that the large scale B-field is well coupled with the diffuse and high density material present in the filament. In addition, the loop shaped structure is actually the region where the B-fields change their orientation.

4.4 Discussion

The results presented in this chapter reveal the detailed velocity, temperature and density structure of the material distributed in the L1172/1174 cloud complex in the form of filaments and in the clumps that these filaments harbour. Of the two main filaments, F_l and F_m, F_l filament is the main one that physically originates from the hub hosting intermediate mass star, HD 200775 and the F_m is the one that is located towards the eastern side of F_l and runs parallel to it. There is no evidence of any velocity gradient in F_l towards the hub. On the contrary, a gradient in the velocity is seen towards the C4 clump, the sole region where current star formation is happening in the filament. It is possible that in the past, the filament might have channelled the material to form the core which produced the star HD 200775. But as the star evolved, the radiation from it might have terminated the accretion of the material through the filament. This is supported by the fact that HD 200775 is situated in a cavity cleared as a result of a possible outflow activity sometime in the past (Watt et al., 1986). The column density of the material shows a systematic drop and the temperature shows a systematic rise as we approach towards HD 200775 which support the above arguments.

The shape of the mean column density profile derived for the F_l filament shows a well defined power law regime at larger radii (see Fig. 4.2). The spectral index, $p \sim 2.6$ obtained for F_l matches well with the range of values in other filamentary complexes (Hacar & Tafalla, 2011; Kainulainen et al., 2016; Tafalla & Hacar, 2015). We fitted the radial profile over the length where the density contrast is higher than 5 times the background threshold column density. The variation of the mass-per-unit length along its length suggests that the filament is thermally supercritical as the value is higher than the isothermal self-gravitating case (16 $M_\odot$ pc^{-1}) except at the of distance 0.2 pc. This region lies in between the L1172 core and other cores C7, C8 and possesses less dust column density. This is the region where the B-field also shows a curvature. We also presented the kinematical state of each derived clumps located in the tail region of the complex (see section 4.3.4). The presence of several clumps along the length suggests that the filament is already fragmented. The velocity structures of

these clumps suggest that except for L1172 (C4) clump, all other clumps are not yet virialised. The presence of L1172, which is already undergoing collapse (as it harbours a protostar), has a striking effect on the surroundings of the filament in the longitudinal direction.

The velocity field in the filament from the core C1 towards the extended tail (panel (c) in Fig 4.9) shows a change from blue-shifted to red-shifted velocity with respect to the systematic velocity of the cloud which is 2.85 km s^{-1}. It varies from 2.5 to 3.3 km s^{-1}along the length. We calculated a unidirectional gradient of $\sim$ 0.2 km $s^{-1}pc^{-1}$ by calculating slope in the region where a fitted straight line is shown in green color in Fig 4.9 (c). The southern part of HD200775 which is emerging like a tail towards south is not physically associated with the hub as seen in the *Herschel* emission. Therefore, there are less chances of movement of material towards the hub from the filament F_l. L1172-L1174 is one of the hub-filament system which is having a single filamentary branch emanating from it (Myers, 2009). Since the highly evolved core L1172 is currently forming star within the filament, this longitudinal velocity gradient can be attributed to the accretion of material towards core and within 2 pc of the distance from the core shows that there is bulk gas motion towards the dense core. The overall filament is transonic as the mach number is between 1 and 2. The non-thermal pressure gradient between the core and environment is not very high that facilitates the inward motion. Previous studies of the filaments in both low- and high-mass star forming regions have shown the presence of systematic velocity gradients perpendicular or parallel to the filaments (Dhabal et al., 2018). Such velocity gradients across the filaments can be explained by the accretion of material towards the filament axes or the rotation of the filaments. The total mass of the core is found to be 10.6 M$\odot$ and virial mass is 9.6 M$\odot$. The core is already virialised and has collapsed to form a protostar. This core is chemically evolved since the $C^{18}O$ is already depleted and N_2H^+ total intensity is 1.7 K km s^{-1}. The mass per unit length of the filament is greater than 16 M$\odot$ pc^{-1} which means that the filament is supercritical and still accreting mass.

The position angle of the filament, F_l is 162° with respect to North as derived from the Filfinder. The mean value of B-field orientation using the Planck as well as the R-band polarization is ~148° with respect to the North increasing towards the East. The almost parallel orientation of the filament with the optical and the Planck polarization lines suggests that the B-field had played an important role in shaping the morphology of the filamentary structure of the cloud. Also, the Planck and optical vectors are well correlated with each other. Soler et al. (2016) found a similar agreement in the B-field orientation inferred using extinction and thermal dust emission in four nearby filamentary clouds Taurus, Pipe, Musca and Lupus clouds (Planck Collaboration et al., 2016b). Previous studies towards the filamentary clouds like Ophiuchus have shown the parallel orientations of filament with the B-field (Soler, 2019).

The M/L for the filament F_l suggests that the filament is thermally supercritical and self-gravity is have started dominating in northern part of the filament as suggested by radial profile structure. Although gravity is playing role in the dynamics but the B-field as suggested by the polarization observations are expected to modify the material flow (Cox et al., 2016; Li et al., 2014; Planck Collaboration et al., 2016a,b). The filament width is found to be ~0.2 pc and any argument about

the transverse velocity gradient is beyond the scope of these observations with spatial resolution of observations ~0.07 pc. Although there is a gradient constantly increasing along the length till ~4.5 pc, there is a sharp change at 4.8 pc is at 2.9 km s^{-1}. If gradient along is part of one filament then the positive or negative change should be a continuous function of distance.

One possible caveat or uncertainty in the implication is the inclination angle of the filaments. If the filament is inclined, then the velocity gradients we observe will include the projected effects of the filament that might be responsible for the sharp rise (Dhabal et al., 2018).

The regions towards the southern part of the filament appears more intense in the velocity channel 2.9-3.2 km s^{-1}. Considering the direction of B-field and velocity cuts along the same direction suggests that this might be an acceleration of material towards the north-west which is responsible for the higher velocities over there. This filament fragmentation matches well with the magnetically-regulated scenario with a transonic motion along the length.

Based on numerical models proposed by Gómez et al. (2018), it is suggested that a filament that is collapsing can drag the B-field lines initially along a direction parallel to the filament. This embedded B-field can further stabilise the cloud radially against the self-gravity but further support the collapse and fragmentation along the axis of filament once the mass-per-unit length (M/L) has reached the critical stage. Both the turbulence and the B-field can facilitate the fragmentation and in the formation of pre-stellar cores. But Chen et al. (2017) suggested that there are filamentary scenarios where the B-field will not become perpendicular to the filamentary dense structures. The flip in the orientation in the projected 2-D maps happens at typical column density of $\sim 10^{21-21.5}$ cm^{-2}.

We find that near the loop structures identified in Fig. 4.13 and the parallel striations and the filament L1173 are all parallel to the B-field orientations whereas the initial part of filament which is dense enough and well defined filament is found to be parallel to the large-scale B-field inferred from Planck polarization. We do not find a flip in the B-field lines projected on the plane of sky over the dense filament. The lines appears to drag the material towards the north-western side. The mean position angle of the filament is 164°increasing towards north towards east with a general variation along its length. The polarization vectors from Planck as well as R-band optical polarization data show that B-field orientation is parallel to the filament. In terms of integrated intensity of $C^{18}O$ emission and dust emission, F_m filament, although smaller but possesses faint emission. The B-field orientation is found to oriented along both the filaments, F_l and F_m morphologies.

The morphological appearance of the filament with no low density striations parallel to the B-field lines from the east direction suggests that the distribution of material around the filament does not follow similar mechanism like other nearby filaments like Taurus, Musca and Pipe Nebula. It suggests that the high density material is being dragged towards west along the B-field lines. This is in contrary to the theoretical models by Chen et al. (2017) where the material is being accreted to high density filaments along B-field lines through low density striations.

With all these findings, we suggest that dynamics in this filament is not consistent with the mechanism of hub-filament systems.

4.5 Conclusions

We studied the kinematics and the magnetic field structure of the tail region of L1172/L1174 complex which is about 7 pc in length in *Herschel* dust emission. The main conclusions from this study are as follows:

- We extracted 11 filaments and 11 cores in the tail region of L1172/L1174 complex. However, only two filaments F_l and F_m containing L1172 and L1173 core respectively, were studied in detail for its kinematics due to high SNR in $C^{18}O$ emission.
- We derived the radial column density structure of the filament, F_l which shows a shallow profile with p $\sim$ 2.6 but higher width of 0.2 pc. We studied the stability of the filament by determining the M/L and comparing with critical line mass of an isothermal self-gravitating filament. The derived line mass is 42 M$\odot$ pc^{-1}, thereby thermally super-critical.
- The kinematical properties of the filaments and clumps were established using ^{12}CO and $C^{18}O$ (1-0) line tracers by examining centroid velocities and line-widths along them. The longest filament containing L1172 shows mostly transonic non-thermal motions except the northern part of filament. The radiation from HD 200775 is responsible for higher Mach number. The V_{lsr} of the cloud was found as 2.85±0.05 km s^{-1} using hyperfine fitting of N_2H^+ lines. The kinematics of the filament, F_l suggests that there is an accretion of material towards L1172 core which has already collapsed with a gradient of $\sim$ 0.2 km s^{-1}pc^{-1}.
- We calculated a positive velocity gradient of 1 km s^{-1}towards north-west direction with an alignment with B-field lines. We found a peculiar loop structure towards the southern western part of complex which show maximum $C^{18}O$ emission.
- We found that the B-field structure is aligned along the orientation of the filaments F_l and F_m which suggests that the B-field is important in the dynamical stability of the filament present in this complex.

Chapter 5

Distance, magnetic field and kinematics of a filamentary cloud LDN 1157

5.1 Introduction

In the previous chapters, we studied the physical structure and gas kinematics of L1172/L1174 complex where the complex presents a hub-filament morphology having active star formation currently going on in the hub and in the filament part.

In this chapter, we present results of a study conducted on an isolated star forming molecular cloud LDN 1157 (L1157). The cloud is located in the Cepheus flare region and is spatially (Dutra & Bica, 2002; Lynds, 1962) and kinematically (Yonekura et al., 1997) associated with a complex containing a number of clouds namely, LDN 1147/1148/1152/1155/1157/1158 (hereafter L1147/1158 complex). This complex is around 1.5° away from the complex L1172/L1174. There is an ambiguity in the adopted distance of the cloud. The most widely quoted distance of L1147/1158 is 325±13 pc (Straizys et al., 1992). However, in several studies, 250 pc (e.g., Looney et al., 2007; Podio et al., 2016) and 440 pc (e.g., Avery & Chiao, 1996; Gueth et al., 1996) distances are also used.

Fig. 5.1 shows the full complex L1147/L1158 complex. The L1157 complex is shown with white rectangle of $12' \times 12'$. We studied this kinematics of the region using ^{12}CO , C^{18}O (1-0) lines with N_2H^+ (1-0) lines to trace the high density region.

The L1157 harbours a cold, extremely red object, IRAS 20386+6751 (hereafter L1157-mm), classified as a Class 0 source (Andre, 1996; Andre et al., 1993) having a bolometric luminosity of 11 $L_\odot$ and bolometric temperature between 60-70 K (Gueth et al., 1997). The source shows a well collimated bipolar outflow of $\sim 5'$ spatial size (Bachiller et al., 2001) and a $\sim 2'$ flattened envelope perpendicular to it (Looney et al., 2007). The position angle of

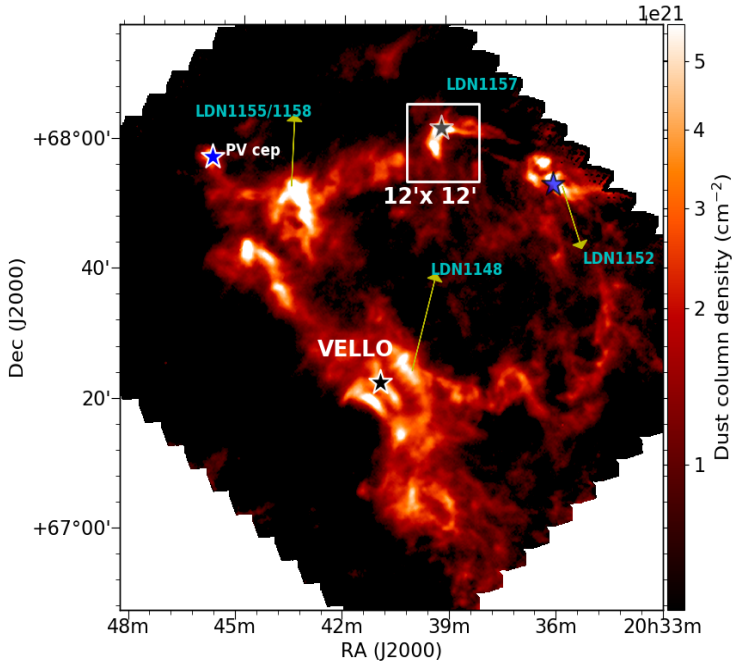

Figure 5.1: Dust column density distribution of L1147/L1158 complex. The dark clouds L1155/1158, LDN 1157, LDN 1152 and LDN 1148 are labelled. Marked stars show the positions of the young stellar objects present in the region. The white square shows the region mapped in molecular line observations for LDN 1157 cloud.

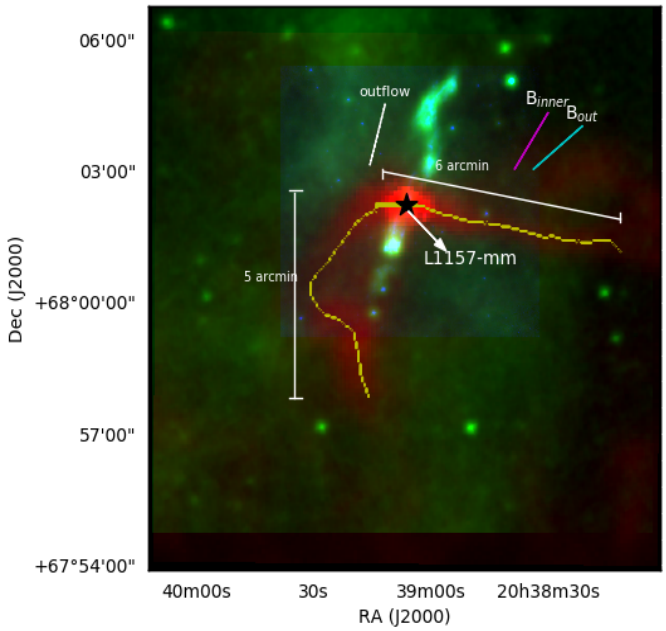

Figure 5.2: Color composite image of the filamentary cloud L1157 made using *Herschel* 250 μm (red), WISE 12 μm (green) and Spitzer 8 μm emission (blue). A filament structure in yellow color based on the dust column density ($N(H_2)$) distribution extracted using the *Filfind* algorithm is also shown. White segment shows orientation of the outflow, magenta and cyan segments represent the orientation of inner (traced for submm polarization emission measurements) and outer magnetic fields (traced for the optical polarization measurements of background stars), respectively.

the outflow measured counterclockwise from the north is 161° (Bachiller et al., 2001) with an inclination angle of ∼10° (Gueth et al., 1996). The magnetic field orientation inferred from 1.3 mm polarization measurements shows an hourglass morphology with the central vectors showing a position angle of ∼ 148° measured counterclockwise from north (Stephens et al., 2013).

Using the column density map produced from the *Herschel* images, we traced a single filament which runs almost in the east-west direction and then changes its direction towards the south. The filament is traced using the *Filfind* algorithm (described in section 5.3.2). Both the east-west and the north-south segments of the filament are found to be ∼ 5′ in length. In Fig. 5.2, we show a colour composite image of the region containing the cloud L1157 produced using the *Herschel* 250 μm (red), *WISE* 12 μm (green) and *Spitzer* 8 μm (blue) emission. Emission from the protostar (identified using black star symbol), the bipolar outflow originating from it and a well defined filament structure extending to the west of the protostar is conspicuous in Fig. 5.2. The age estimates of L1157-mm, ∼ 150 kyr (Arce et al., 2008; Bachiller et al., 2001; Froebrich, 2005), suggest that the star formation has just recently

got initiated in L1157 and hence the conditions that led this cloud to form star(s) may still be preserved. Additionally, absence of any active high mass star formation in the vicinity of L1157 (Kun et al., 2009) presents a simple case of isolated low mass star formation occurring in a quiescent environment.

5.2 Observations and Data Reduction

5.2.1 Optical Polarimetry

The polarimetric observations presented here were carried out over several nights in November 2015 at the Cassegrain focus of the 104-cm Sampurnanand Telescope, Nainital, India. We used the Aries IMaging POLarimeter (AIMPOL) which incorporates an achromatic rotatable half wave plate (HWP) as modulator and a Wollaston prism beam splitter as the analyzer. Standard Johnson R_{kc} filter with λ_{eff} as 0.76 μm was used for polarimetric observations. The spatial resolution (FWHM) corresponds to 2-3 pixels on CCD. The data reductions are carried out using software developed in Python to identify the ordinary and corresponding extraordinary images of each object in the field of view. The photometry is carried out using aperture photometry provided by the Image Reduction & Analysis Facility (IRAF) package. The details of the reduction of polarimetric data is found in chapter 2.

5.2.2 Radio Observations

The molecular chemistry is different at various layers of the molecular cloud which makes it difficult to discuss the kinematics with a single molecular tracer. We have chosen a set of molecules ^{12}CO (J = 1 – 0), C^{18}O (J = 1 – 0), N_2H^+ (J = 1 – 0) to be observed with the same telescope to constitute a homogeneous set of same calibration. Because of high difference in dipole moment of N_2H^+ and ^{12}CO molecules, this data is sensitive to low as well as high density regions. The filamentary structure of L1157 cloud has been mapped with these tracers using 13.7 m diameter single dish radio facility at Taeudek Radio Astronomy Observatory (TRAO) which is located at Korea Astronomy and Space Science Institute (KASI). We mapped the region using On-The-Fly (OTF) mapping technique, with a size of $12^{'} \times 12^{'}$ for ^{12}CO, C^{18}O and $8^{'} \times 8^{'}$ region for N_2H^+ in J = 1 – 0 transition. The center of the maps was 20h39m06.19s +68°02′15.09″. The signal-to-noise ratio (SNR) for ^{12}CO line at the position 20h39m12.837s +68°01′06″ is found to be ∼ 18 with the peak $T_A{}^*$ as 3.87 K and rms as 0.22 K at velocity resolution 0.06 km s^{-1}. The resulting 1σ rms noise levels in $T_A{}^*$ scale are ∼ 0.3 K for ^{12}CO (1-0) and 0.1 K for C^{18}O line, respectively. The final data cubes have cell size of 22″ and 0.06 km s^{-1}velocity channel width.

5.3 RESULTS

5.3.1 Polarization results

We made optical polarization measurements of 62 stars that are projected on an area of 0.3°× 0.3°around the protostar, L1157-mm. We show the measured degree of polarization (P%) and polarization position angles (θ_P) in Fig. 5.3 using open circles. The polarization measurements for which the ratio of P% and its corresponding error is greater than 3 are plotted. For the majority of the sources, P% ranges between $\sim 1-2\%$ and the θ_P ranges between $\sim 110° - 140°$. The mean values of P% and θ_P of the sources showing P%$\geqslant 1$ are 2.1 and 129°, respectively and the corresponding standard deviation values are 0.6 and 11°, respectively. Also shown are the polarization values of 16 sources selected from a circular area of 5° radius about the protostar. Though there are 18 sources present within our search radius, we rejected two sources, namely, HD 200775 and HD 193533. The HD 200775 is an intermediate mass Herbig Be star causing a reflection nebulosity, NGC 7023. The HD 200775 is situated at a distance of 357±6 pc (Bailer-Jones et al., 2018) and the P% and θ_P values given in the (Heiles, 2000) catalog is $\sim 0.8\pm0.2$ and $\sim 92° \pm 7°$. It is highly likely that the polarization measurements are affected by the presence of the intense emission from the nebulosity surrounding the star due to scattering. The second star, HD 193533 is an M3III and classified as a variable star in the Simbad database. The distance, P% and θ_P values for this star are 301±5 pc, 0.3±0.05 and $142° \pm 4°$, respectively.

5.3.2 Identification of Filaments and Clumps

The whole L1147/1158 complex was observed by the *Herschel* telescope. The PACS (Poglitsch et al., 2010) and SPIRE (Griffin et al., 2010) instruments were used to observe the region simultaneously at 70 μm, 160 μm, 250 μm, 350 μm and 500 μm wavelengths as a part of the Gould Belt Survey (André et al., 2010). The 160-500 μm *Herschel* images were used to construct an H_2 column density map and a dust temperature map of the entire complex at the spatial resolution of $36''$. The units of SPIRE images which is in MJysr^{-1} were changed to Jy pixel^{-1} using *convertImageunit* task in Herschel Interactive Processing Environment (HIPE). For the SED fitting on pixel-to-pixel basis, all the maps (PACS 160 μm, SPIRE 250 μm, 350 μm, 500 μm) were convolved to the 500 μm image using the kernels from Aniano et al. (2011) and regridded to a pixel scale of $14''$. The background flux density (I_{bg}) was determined using values from the pixels in a relatively darker patch in the sky. The emission

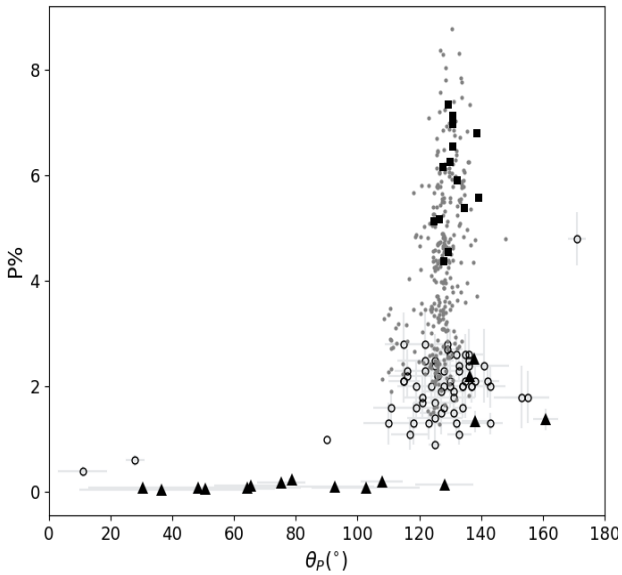

Figure 5.3: The P% vs. θ_P for the 62 sources (open circles) projected over 0.3°×0.3°area around the protostar, L1157-mm. The measurements are made in R_{kc} filter. The *Planck* polarization results (see sec 5.4.2) from within 1°region around L1157 cloud are shown using filled circles in grey. The *Planck* results from the region where we carried out the optical polarization observations are shown using the squares in black. Also shown are the polarization values (filled triangles) of the sources distributed in a circular region of 5° radius about the protostar obtained from the (Heiles, 2000) catalog.

of every pixel is assumed to be represented by modified blackbody emission:

$$S_\nu(\nu) = \Omega(1 - \exp(-\tau_\nu))B_\nu(\nu, T_d), \tag{5.1}$$

with

$$\tau_\nu = 0.1 \mu m_H \kappa_\nu N_{H_2}, \tag{5.2}$$

where $S_\nu(\nu)$ is the observed flux density for a given frequency ν and solid angle Ω, $\tau(\nu)$ is the optical depth , $B(\nu)$ is the Planck function, T_d is the dust temperature, m_H is mass of hydrogen, μ_{m_H} is the mean molecular weight taken as 2.8 (Kauffmann et al., 2008), N_{H_2} is the column density for hydrogen. All the fluxes have been normalized to Jy pixel^{-1}. For opacity, we assumed a functional form of $\kappa_\nu = 0.1\ (\frac{\nu}{1000GHz})^\beta$ where β is the spectral emissivity index and the value is taken as 2 (Schnee et al., 2010). The derived column density and dust temperature maps were regridded using Astronomical Image Processing System (AIPS) to 3″. Because we are modelling the cold dust emission longward of 160 μm, the fit was relatively poorer near the protostar where contribution from warm dust would also be present. Hence, a single blackbody model cannot be used.

To characterize the filament properties, we used *FilFinder* algorithm to extract the filaments from the column density map. The *FilFinder* algorithm was developed to extract filamentary structures in clouds observed by the *Herschel* (André et al., 2010). The extraction is performed by reducing the regions of interest to topological skeletons based on specified threshold intensities. Each element of the skeletons therefore represents the medial position within the extents of the required region (Koch & Rosolowsky, 2015). The emission structures in L1157 was flattened to a percentile of 99 to smooth the bright features in the image. While creating masks, the global threshold was taken as $\sim 2.1 \times 10^{21}$ cm^{-2} (3σ above the background, $\sigma \sim 7.0\times 10^{20}$ cm^{-2}) with size threshold as 300 pix^2. The masks were reduced to skeletons using medial axis transform which extracts one single filament. A single filament of ~1.2 pc in length that runs all along the coma-structure of the cloud is traced. For the purpose of analysis, we divided the filament into east-west and north-south segments. The orientation of the east-west segment is found to be 77° and a curvature of 76° with respect to the north increasing eastward. The extracted filament is shown in Fig. 5.2 and Fig 5.4.

We used the well-known *Clumpfind* (Williams et al., 1994) routine to identify high density regions on the filament from the column density map. Based on the *Clumpfind* routine, we obtained two clumps: C1 and C2 which are lying on the filament (Fig. 5.4). The centers of these clumps are 20h39m06.79s +68°02′12.27″ and 20h39m20.349s +67°59′03.74″ respectively with a typical uncertainty in the positions of ~ 10″ (Fehér et al., 2017). While the clump C1, located on the east-west segment where the protostar L1157-mm is currently

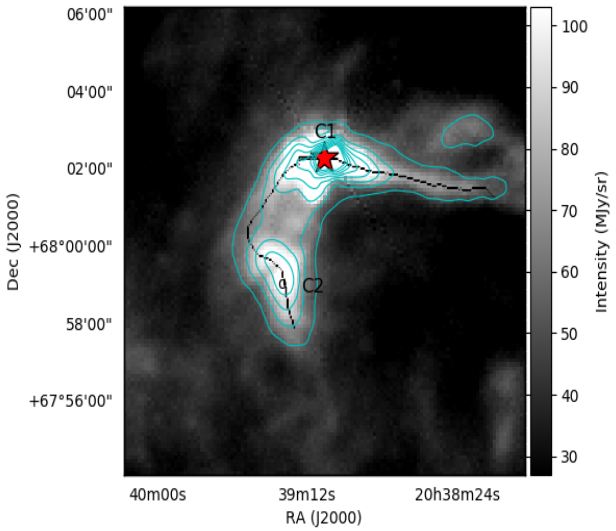

Figure 5.4: Contours of column density, N(H_2), in cyan color overlayed on the *Herschel* 250 μm grey scale emission. The star symbol in red and the small circle in black identify the position of the clump C1 which harbours the protostar L1157-mm and the clump C2, respectively. The contours are shown from the levels of 3-20σ ($\sigma \approx 7\times 10^{20}$ cm^{-2}).

forming, the clump C2 is found to be located on the north-south segment of the filament. Based on the absence of any 70 μm source associated with the C2, we classify it as starless. We noted that if we use 250 μm emission map instead of the column density map, the *Clumpfind* algorithm resolves C2 into two separate clumps. This may be due to the high spatial resolution of the 250 μm emission map compared to the column density map. Because our molecular line observations are also finding a single density peak at the position of C2 due to relatively coarse spatial resolution, we considered C2 as a single clump in our study.

Radial profiles and widths of the filaments are two of the most important properties of prime interest to understand the dominant physics (gravity, turbulence, magnetic field orientation) involved in their formation. We constructed the column density profiles of the filament identified in L1157 using the publicly available package, *Radfil* (Zucker & Chen, 2018). The derived filament mask and the spine of the column density map derived from *Filfind* were supplied as an input. The spine was smoothed to get a continuous distribution in column density. The crest of the filament was sampled at an interval of 40 pixels (0.18 pc) which corresponds to three times the beam width (0.061 pc at 340 pc). Therefore, the mean profile was constructed by averaging the profiles of the perpendicular cuts made at nine positions along the filament and setting the *Fold = True* in the *Radfil* to add all the profiles towards positive radial distance. We fixed the fit distance from 0.0 to 0.5 pc and evaluated the background at a distance of 0.5-0.6 pc from the filament crest (out of all possible trials conducted using the *Radfil*, the minimum value of the background column

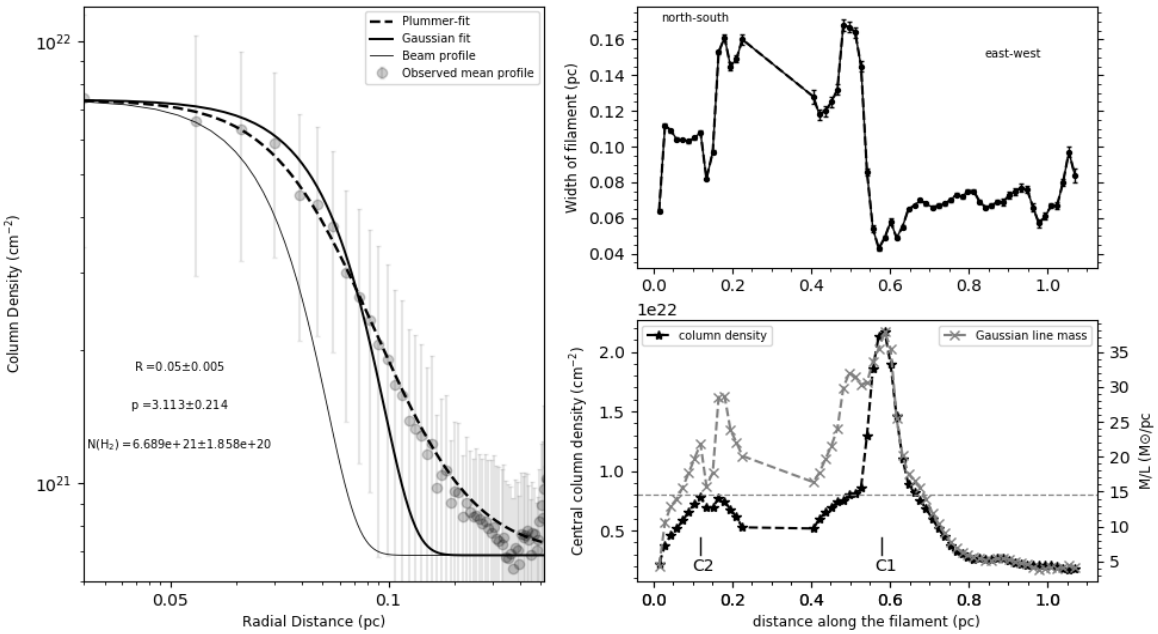

Figure 5.5: **Left:** Mean radial column density profile of the L1157 filament (in grey points) measured perpendicular to the crest of filament shown in Fig. 5.2. The grey error bars mark the $\pm 1\sigma$ dispersion of the distribution of radial profiles along the spine of filament. The black dashed curve shows the best-fit Plummer model fitted on the mean radial profile. The solid black curve marks the best-fit Gaussian function to the inner radius of the profile. **Right upper panel:** Deconvolved Gaussian FWHM of the L1157 filament as a function of position along the crest of filament (starting from southern core towards central protostar). **Right lower panel:** The central column density along the crest of the filament obtained from the best-fit Plummer model in black dashed line. Background-subtracted mass-per-unit length calculated from the Gaussian fit (in grey dashed line). The grey dashed horizontal line indicates the critical mass-per-unit length or line mass of an isothermal filament in equilibrium as $2c_s^2/G \sim 15\ M_\odot\ pc^{-1}$ at 10 K.

density is estimated from this distance range). A zeroth-order polynomial fit was applied to the background subtraction before making the fits to the profile. The diameter of the flat inner plateau is found to be $2R_{flat}$ = 0.126±0.003 pc. The observed mean column density profile was fit by a Gaussian model over the inner radius of 0.05 pc. The power-law index of the best-fit Plummer model is p = 3.1±0.2 while the mean deconvolved width of the best-fit Gaussian model is FWHM = 0.09 pc.

An elongated structure showing minimum values of both aspect ratio and column density contrast with respect to the background value is normally identified as a filament (Arzoumanian et al., 2019). The aspect ratio, defined as l_{fil}/W_{fil}, of the sole filament identified in L1157 is 1.2/0.09≈ 14. The intrinsic column density contrast, $N^{o}_{H_2}/N^{bg}_{H_2}$, of the filament is estimated to be ≈ 8, where $N^{o}_{H_2}$ (= $N^{fil}_{H_2}$-$N^{bg}_{H_2}$), is the column density amplitude of the filament. The column densities of the pixels that form the extracted filament structure are averaged to get a representative value for the whole filament. One of the important consequences of obtaining column density profile is to calculate the mass per unit length. We derived the mass per unit length (M_{line}) for each position along the filament using the best fit Gaussian parameters: central column density (N_{H_2}) and standard deviation (σ). The right lower panel of Fig. 5.5 shows the distribution of the background subtracted Gaussian mass-per-unit length along the crest of filament at every cut which was taken at an interval of 3 pixels (∼ 0.015 pc). The dashed horizontal line marks the critical mass-per-unit length which characterises an isothermal cylindrical filament in equilibrium. The extreme end of the north-south segment of the filament (20h39m17s +67d57m56s) was taken as the starting point of the filament. The right upper panel in Fig. 5.5 shows the deconvolved FWHM derived from the Gaussian fitting of the mean column density radial profile as a function of distance along the filament crest. Although the cloud reflects as a single filament derived from the *Filfind* algorithm, differences are found in the inner widths of the north-south and the east-west branches. The characteristic width of the east-west branch is more well-defined and constrained as compared to that of the north-south branch. The positions where we could not fit the radial profile with a well-defined Gaussian function are not included in the plot. The small dip near the C2 corresponds to the region between the two peaks seen in 250 μm *Herschel* map (FWHM ∼ 18″) but barely noticeable in the column density map (FWHM ∼ 36″).

5.3.3 Molecular line analysis

The CO isotopologues are commonly used to probe the gas at different densities. While the most abundant isotopologue, ^{12}CO is considered to trace the most diffuse and external gas of molecular clouds, its rarer counterpart, C^{18}O (J = 1 – 0) line having a critical density of 2.4

$\times 10^4$ cm^{-3}, is one of the best tracers of high column- and volume- densities without getting saturated. However, $C^{18}O$ is found to disappear from the gas phase in high, chemically evolved regions due to its condensation onto the surface of the dust grains (Bergin et al., 2002; Caselli et al., 1999; Cazaux et al., 2017). The N_2H^+ molecular line, on the other hand, is considered to be the most efficient tracer of dense cores in clouds because the abundance of this molecule gets enhanced when CO condenses onto the dust grains (Bergin & Tafalla, 2007).

The kinematic information from the observed molecular lines is extracted by fitting Gaussian profiles to all our spectra using programs developed in Python. We examined individual spectrum and fitted independently using one single component at each individual position in $C^{18}O$ lines. We obtained a total of 1089 spectra in ^{12}CO, $C^{18}O$ and 306 spectra in N_2H^+ lines from the field containing the cloud L1157.

Various fundamental properties of the cloud like excitation temperature, optical depth, and the number density are derived using spectral data obtained at different positions of the cloud. The local thermodynamical equilibrium analysis was used to calculate the parameters. The details are already explained in chapter 3.

But all the lines are not fitted to a perfect Gaussian. Thus the chi-square minimization has been done to determine the goodness-of-fit. We obtained integrated intensity (moment 0) maps of ^{12}CO, $C^{18}O$ using spectral data cubes with position-position velocity information. The values below 3σ were not considered to obtain summation over the channels. The rms value of each line map was calculated as $\sim \sqrt{N}\delta v T_{rms}$, where N is the number of channels used for integrating the emission, δv is the velocity resolution and T_{rms} is the noise of the line profile.

The characteristic shape of the observed line profiles is a critical factor in determining the physical state of molecular gas in a region. Fig. 5.6 on left-hand panel shows ^{12}CO (white) and $C^{18}O$ (1-0) (red) line profiles plotted together at different positions on the cloud and on the right-hand panel, the average ^{12}CO , $C^{18}O$ and N_2H^+ (isolated component) profiles over the half-maximum contour of the intensity map of N_2H^+ emission. The ^{12}CO emission is detected from all over the observed region and conspicuously, shows diverse line profiles with asymmetric structure detected in a large area. The ^{12}CO lines show wide line-width and two velocity components especially on the cloud. This could be either due to the self-absorption by the optically thick material at the systematic velocity of the cloud, if there is only a single cloud component, or due to the presence of additional velocity components along the line-of-sight. The significant emission of $C^{18}O$ line ($\geq 3\sigma$) is obtained towards the high column density region seen in the *Herschel* dust map as shown in Fig. 5.4. The $C^{18}O$ line profiles show an optically thin feature i.e., a single Gaussian component. The absorption

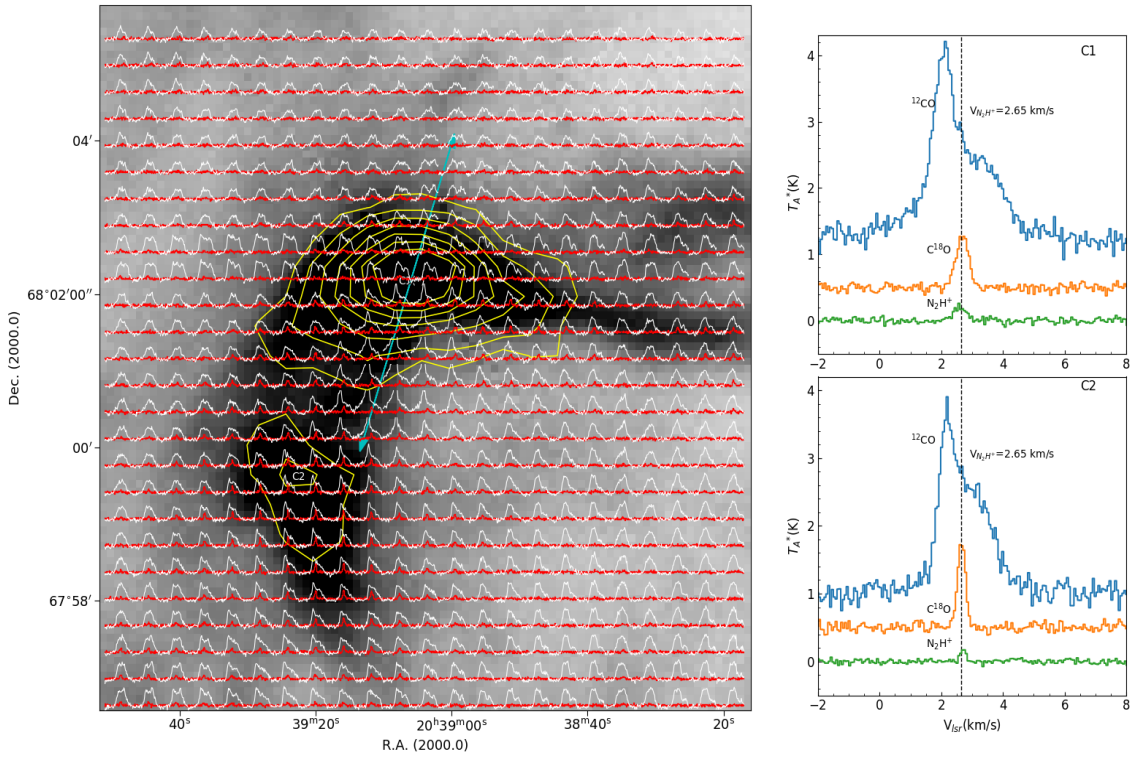

Figure 5.6: The distribution of ^{12}CO (white) and $C^{18}O$ (red) profiles over the $9' \times 9'$ region. On the left-hand panel, the background image is *Herschel* 250 μm emission for L1157 cloud where contours of N_2H^+ (1-0) line overlayed in yellow color. The position of core C1 and clump C2 are marked in white color. The extent of outflow is marked by the arrow in cyan. Contour levels start from 4σ in steps of 3σ where $\sigma \sim 0.05$ K km s^{-1}. The small windows on the right-hand panel shows the average spectra of ^{12}CO , $C^{18}O$, N_2H^+ (1-0) (isolated component) lines for C1 (top) and C2 (bottom). The average was taken over the half-maximum contour of the intensity map of N_2H^+ emission for C1 and C2. The dashed line indicates the velocity of N_2H^+ obtained from the Gaussian hyperfine fitting of its seven hyperfine components.

of double peaked profiles of ^{12}CO lines coincides with the single peak of C^{18}O emission confirming the existence of only a single cloud component along the line of sight.

The C^{18}O line width is found to be much narrower than that of ^{12}CO. The presence of well studied outflow (Umemoto et al., 1992) is evident as broad high velocity wings on both sides of the ^{12}CO line profiles when compared visually with the shape of C^{18}O Gaussian component. Interestingly many positions along the filament and surrounding regions around C1 and C2, the profiles show blue-red asymmetry (section 5.4.5). The N_2H^+ emission is detected towards both C1 and C2 (contours shown in yellow color).

5.4 Discussion

5.4.1 Distance of L1148/1157 complex

One of the most direct methods of finding distances to molecular clouds is to estimate distances of the YSOs that are associated with the cloud (e.g., Loinard et al., 2007; Ortiz-León et al., 2018). The stellar parallax measurements obtained for these YSOs from the *Gaia* DR2 (Lindegren et al., 2018) offer an unprecedented opportunity to estimate distances to molecular clouds with improved accuracy and precision. A total of 6 YSO candidates have been identified so far toward the direction of L1148/1157 (Kirk et al., 2009; Kun, 1998). We found a *Gaia* counterpart for 3 of the 6 YSO candidates well within a search radius of 1″. We obtained their distances from the (Bailer-Jones et al., 2018) catalog and proper motion values in right ascension ($\mu_{\alpha\star} = \mu_\alpha \cos\delta$) and in declination ($\mu_\delta$) from the (Gaia Collaboration et al., 2018) catalog. Within the L1147/1158 complex (Yonekura et al., 1997), the dark cloud, L1155, harbours two YSOs, namely, 2MASSJ20361165+6757093 and IRAS 20359+6745 and in cloud L1158, at its north-east edge, an another YSO candidate, PV Cephei, is located. Presence of a bright nebulosity associated with IRAS 20359+6745 (Magakian, 2003) and the PV Cephei (Scarrott et al., 1991) are a clear evidence of their association with their respective clouds. No detection was found in the *Gaia* DR2 database for the other three YSO candidates, namely L1148-IRS, which is associated with L1148 (Kun, 1998), IRAS 20353+6742 which is associated with L1152 (Benson et al., 1988) and L1157-mm in L1157. The mean value of the distance calculated from the three YSOs is 340 pc with a dispersion of 3 pc. The mean (standard deviation) values of the $\mu_{\alpha\star}$ and μ_δ for them are 7.806 (0.326) mas/yr and -1.653 (0.229) mas/yr respectively. Similar distance and proper motion values shown by all the three YSOs indicate that they are spatially and kinematically associated with each other and that the complex is also located at a distance of 340 ± 3 pc from us. Similar values of V_{lsr} (≈ 2.6 km s^{-1}) shared by the individual clouds of the complex (Harjunpaa et al., 1991; Suzuki et al.,

2014; Yonekura et al., 1997) also supports the above argument. Straizys et al. (1992), based on Vilnius photometry which gives two dimensional classification and extinction suffered by stars, estimated distances to the L1147/1158 cloud complex. Using 10 reddened stars in the direction of L1147/1158 they estimated a distance of 325±13 pc to the cloud.

The degree of P% measured in the optical wavelengths made using the pencil-beam of a starlight passing through the interstellar medium is often found to correlate with the extinction (A_V) measured to that line of sight upto at least an A_V of ~ 3 magnitudes (Guetter & Vrba, 1989; Harjunpää et al., 1999). Therefore as the distance to the observed stars increases, the column of the dust grains present along the pencil-beam also increases leading to a gradual increase in the P% provided no significant depolarization is occurring along the path. When the starlight passes through a molecular cloud, the measured P% will have an additional contribution from the dust grains present in it. This will lead to a sudden increase in the values of P% for the stars background to the cloud while the foreground stars will show P% due to the contribution from the foreground ISM alone. Therefore, the presence of a molecular cloud can be inferred from the measured polarization of the foreground and the background stars (e.g., Alves & Franco, 2007; Arnal et al., 1993; Cernis, 1987; Guetter & Vrba, 1989; Neha et al., 2016; Rizzo et al., 1998).

In Fig. 5.7 we show P% for the 62 stars, observed by us, as a function of their distances that are obtained from the (Bailer-Jones et al., 2018) catalog by making a search for the *Gaia* counterparts within a search radius of 1″. For all the sources, we found a counterpart well within 1″ from our input coordinates. The sources selected from the (Heiles, 2000) catalog are shown using black triangles. The distances for these stars are also obtained from the (Bailer-Jones et al., 2018) catalog. Up to a distance of ~ 340 pc, the P% of sources obtained from the (Heiles, 2000) catalog shows very low values. The weighted mean values of P% and θ_P for the sources located at distances $\leqslant 340$ pc are 0.1±0.05 and 65°±29°, respectively. For the four sources located beyond 340 pc, the weighted mean values of P% and θ_P are found to be 1.6±0.4 and 148°±11°, respectively. The θ_P of the sources from the (Heiles, 2000) catalog are found to show a systematic change from $\sim 25°$ to $\sim 125°$ with the distance till about 340 pc. Beyond this distance, sources are found to show θ_P similar to those obtained for our target sources. Among the sources observed by us, only two sources are having distances less that 340 pc. The weighted mean value of P% and θ_P of these two sources are 0.5±0.1 and 16° ± 8°, respectively. For the sources observed by us and located at or beyond 340 pc, the weighted mean value of P% and θ_P are found to be 2.1±0.6 and 129° ± 11°, respectively. The distribution of P% and θ_P as seen in Fig. 5.7 further supports the 340 pc distance estimated for the L1148/1157 cloud complex.

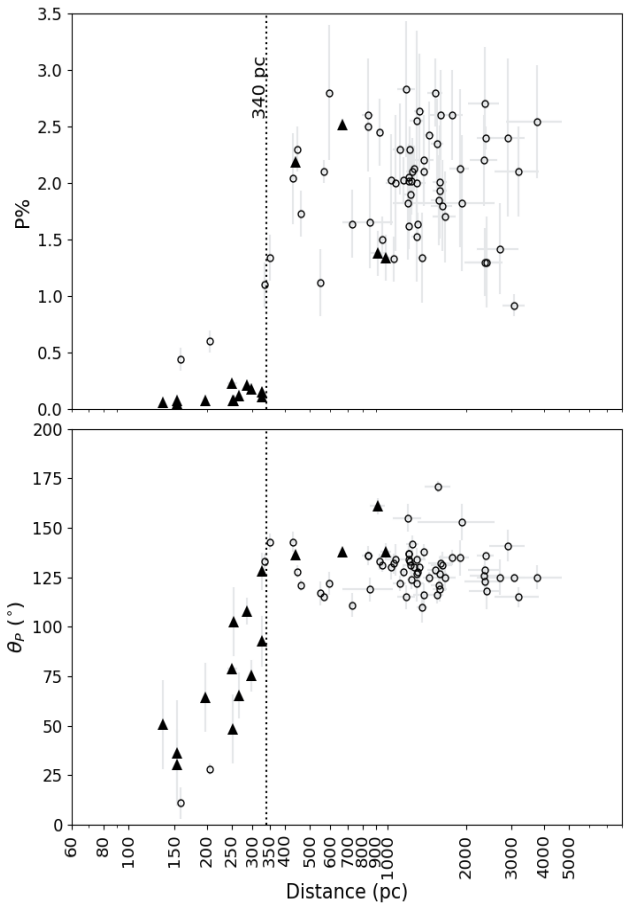

Figure 5.7: **Upper panel:** The P% vs. distance of the sources for which we made polarization measurements (open circles in black). The distances are obtained from (Bailer-Jones et al., 2018) catalog. Polarization measurements of the field stars (filled triangles) are obtained from the (Heiles, 2000) catalog. The vertical line is drawn at 340 pc. **Lower panel:** The variation of polarization position angles of stars as a function of their distances.

5.4.2 Magnetic field geometry in L1157

The dynamics of interstellar dust grains can be affected by the presence of magnetic field. It was shown that a rotating non-spherical dust grains would tend to align with their long axis perpendicular to the interstellar magnetic field (Crutcher, 2012; Davis & Greenstein, 1951; Jones & Spitzer, 1967; Lazarian, 1995; Purcell, 1979). When an unpolarized starlight from a background star passed through regions of such aligned dust grains, they polarize the starlight by selectively absorbing the component parallel to the long axis of the grains. Thus the polarization position angles provide a sense of the plane-of-sky component of the magnetic field. As it is evident that most of the stars observed by us towards L1157 are background, the measured values of θ_P represent the magnetic field geometry of the cloud. The two stars in our sample which are foreground show higher P% values when compared to those from the (Heiles, 2000) catalog. We subtracted the mean P% and θ_p values of these two foreground sources from the rest of the sources vectorially and found the values to be 2.3±0.8 and 127° ± 12°. Therefore, 127° ± 12° is taken as the orientation of magnetic field in L1157 inferred through optical polarization. The magnetic field orientations thus obtained are overplotted (using vectors in red) on the DSS image as shown in Fig. 5.8 (a). The position of the protostar L1157-mm is shown using a star symbol in red. The length of the vectors corresponds to the P% values and the orientations correspond to the θ_P values measured from the north increasing towards the east. The polarization measurements using background starlight in the optical wavelengths typically works only for the regions of low A_V ($\lesssim 5$). This is because, the dust grains present deep inside the molecular clouds though are efficient in diminishing background starlight, are believed to be not much efficient in polarizing the light in optical wavelengths (Crutcher, 2012; Goodman et al., 1995). Therefore the optical polarization vectors shown in the Fig. 5.8 (a) basically trace the orientation of the magnetic fields at the envelope (low-density regions) of L1157. The magnetic field orientation found to be well ordered at $\sim 0.2-2$ pc scales which suggests that the inter cloud magnetic field (ICMF) might have played an important role at least in the initial building up of the cloud.

The magnetic field orientation of a region can also be inferred through the observations of polarized thermal emission from the dust grains (Goodman, 1995; Greaves et al., 1999; Hildebrand et al., 1984). Far-infrared and submillimeter polarimetric observations made by the *Planck* have been used not only to infer the direction of the Galactic magnetic field but also to put new constraints on the properties of dust (Planck Collaboration et al., 2016a, 2015b, 2016b).[1] We used the 353 GHz (850 μm) data, which is the highest-frequency

[1]The entire sky was surveyed by the *Planck* in nine frequency bands, from 30 GHz to 857 GHz with unprecedented sensitivity and angular resolutions varying from 30′ at 30 GHz to 4.8′ at 857 GHz. Of the nine, seven bands were sensitive to the polarized thermal emission from the Galactic dust.

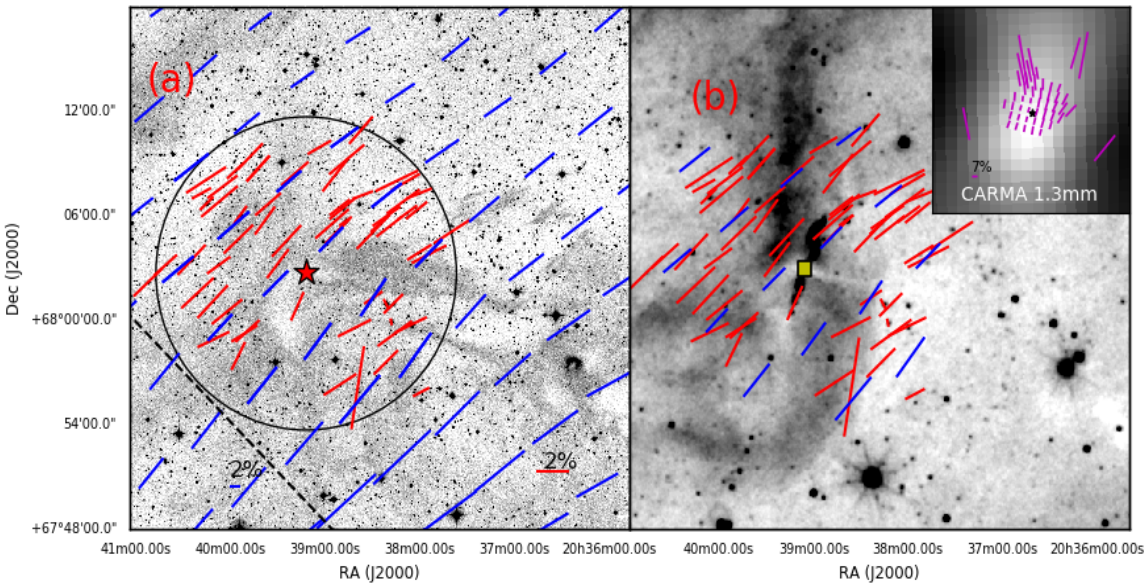

Figure 5.8: **(a):** Optical polarization vectors (in red color) over plotted on image of 0.5° × 0.5° DSS image. The dashed line shows the direction of galactic plane. The circle shows the region of optical polarization observations. *Planck* polarization vectors are shown in blue color (inside and outside the circle). **(b):** *WISE* 12 μm image for the same region in inverted scale. Optical (in red) and Planck (in blue) polarization vectors are overlayed. The box in yellow color around the location of protostar marks the region of submillimetre polarization observations observed in wavelength 1.3 mm using CARMA (Hull et al., 2013) and the vectors are shown in inset (upper-right) by magenta color. The location of protostar in the inset is identified by black star symbol.

polarization-sensitive channel of the *Planck*, to produce the structure of the Galactic magnetic field in the vicinity of L1157. We selected a ~1°diameter image centered around the cloud and smoothed it down to the 8′ resolution to obtain good SNR. The results are shown in Fig. 5.3 using dots in grey. The P values range from ~2%-8% with a mean value of 4.4% and a standard deviation of 1.6%. The polarization position angles (added 90°to infer the projected magnetic field) show a highly regular distribution with a mean value of 127°and a standard deviation of 6°. The polarization vectors (magenta) are presented on the 0.5° × 0.5° DSS image as shown in Fig. 5.8 (a). The vectors in blue are those from a 0.3° × 0.3° circular region similar to where we carried out optical polarization observations. These results are shown using filled squares in black in Fig. 5.3. It is noted that the positions showing relatively higher values of P show relatively less dispersion in θ_P. The mean and the standard deviation of the source with P⩾4% are 129°and 4°, respectively. The projected magnetic field geometry inferred from the optical and the *Planck* polarimetry are in good agreement with each other. Such an agreement between the magnetic field directions inferred from the optical and the *Planck* are seen towards a number of clouds belonging to the Gould Belt (Gu & Li, 2019; Soler et al., 2016).

5.4.3 Magnetic field strength

The strength of the plane-of-the-sky magnetic field toward the envelope of L1157 is estimated using the Chandrashekhar & Fermi (C-F) method (Chandrasekhar & Fermi, 1953; Davis, 1951). The following formula is used to calculate the strength of plane of the sky component of the magnetic field:

$$B_{pos} = 9.3 \times \sqrt{\frac{n_{H_2}}{cm^{-3}}} \times \frac{\Delta \mathrm{v}}{kms^{-1}} \times (\frac{\Delta\phi}{1^\circ})^{-1}, \tag{5.3}$$

where Δv is the FWHM obtained from the Gaussian fitting to the ^{12}CO spectra and the value is ~1.8 ± 0.1 km s^{-1}. We used the area in ^{12}CO emission map where profiles are can be single Gaussian and matches with the positions of observed background stars. The volume density of the hydrogen gas (n_{H_2}) associated with the optical polarization is estimated as ~1000 cm^{-3}. We considered the extent of column of the cloud material lying along the line-of-sight as 0.3 pc (three times the width of the filament) and the column density with value 8.0 × 10^{20} cm^{-2} was converted into volume density. We calculated the average of column density values at the positions of observed background stars. The dispersion in the polarization angles is taken as 11°. With these values, the strength of magnetic field was calculated as ~ 50 μG. By taking into account the uncertainties in θ and velocity dispersion, the typical uncertainty in the magnetic field strength is calculated to be ≈0.5B$_{pos}$. The

strength of magnetic field towards the high density regions calculated using 1.3 mm dust continuum emission is found to be 1.3 - 3.5 mG (Stephens et al., 2013).

5.4.4 Correlations between magnetic field, filament and outflow directions in L1157

Star formation process begins with the accumulation of matter from inter-cloud medium. In models where magnetic fields are dynamically important compared to the turbulence (e.g., Allen et al., 2003a,b; Galli & Shu, 1993a,b; Shu et al., 1987; Tomisaka, 1998), the accumulation of matter is controlled by the ICMF. The gas slides along the field lines (Ballesteros-Paredes et al., 1999; Van Loo et al., 2014) forming filamentary structures aligned perpendicular to the ICMF. It is in these filaments that cores are found to be forming (Könyves et al., 2015; Polychroni et al., 2013). For the reason that the assembly of the matter is guided by the magnetic fields, the ICMF direction is expected to get preserved deep inside the cores (Hull et al., 2014; Li et al., 2009, 2015) predicting the ICMF to become parallel to the core magnetic field (CMF). The local CMF within individual cores (subcritical) provides support against gravity preventing them from collapse and thus account for the low efficiency of the star formation process (e.g., Mouschovias, 2001). The neutral particles, coupled weakly to the ions and hence to the magnetic fields, can drift towards the center of the core enabling it to amass more material. The increasing central mass gradually increases the mass-to-magnetic flux ratio leading the core to become supercritical and driving it to collapse under gravity. Under the influence of gravity, the initial uniform magnetic field is expected to get dragged toward the center of the core forming an hourglass-shaped morphology (Galli & Shu, 1993a,b). As the collapse progresses, a pseudo-disk is expected to form at the central region with the symmetry axis of the pinching to become perpendicular to it. The protostellar object embedded deep inside the cores, continues to build up mass through accretion and simultaneously develops a bipolar outflow. As the initial cloud angular momentum is expected to get hierarchically transferred to the cores and eventually to the protostar, the rotation axis (of the core/accretion disk) is expected to become parallel to the ICMF and CMF (Machida et al., 2006; Matsumoto et al., 2006) and perpendicular to the core minor axis and the filament structure.

In the above framework of magnetic field mediated star formation, a number of observational signatures that can manifest the role played by the magnetic fields are recommended (e.g., Hull et al., 2014; Li et al., 2009, 2015). Some of these are (i) the relative orientations between (a) the ISMF and the CMF, (b) the ISMF and the long axis of the filament, (c) the ISMF, CMF and bipolar outflows, (d) the filament and the outflows, and (ii) an hour-glass

morphology of the magnetic field at the core scale with the symmetry axis perpendicular to the major axis of flattened pseudodisk. We examined these relationships in L1157 which is not only successful in forming a star but is also at its earliest stages of star formation therefore the initial conditions that led this cloud to form star may still be conserved.

The polarisation measurements of the region surrounding L1157-mm were carried out at 1.3 mm (resolution 1.2″-4.5″) and 350 μm (10″) (Chapman et al., 2013; Stephens et al., 2013) with the aim to trace the magnetic field orientation at the inner regions of the core (Goodman, 1995; Greaves et al., 1999; Hildebrand et al., 1984). The SHARP and the CARMA vectors with their standard deviation have been quoted as P = 0.7% ±0.2%, θ =142°±9°and P = 3.8% ±0.1%, θ =147.8°±0.8°, respectively. We adopted an orientation of 145°±9°for the CMF which is the mean value of the magnetic field directions inferred from the SHARP and the CARMA results. The magnetic field inferred from the 1.3 mm polarization measurements is shown in the inset in Fig. 5.8 (b) by overplotting the vectors on the WISE 12 μm image. The CARMA and SHARP polarization measurements were carried out at the scales of $\sim 400-1500$ au and ~ 3500 au (using the distance of 340 pc), respectively thus representing the CMF. The offset between the relative orientations of the ICMF inferred from the optical (and the *Planck*) polarimetry and the CMF obtained from the SHARP and CARMA is ∼18°±14°. The nearly parallel orientations of ICMF and CMF suggest that the CMF is anchored to the ICMF in L1157. The near parallel magnetic field geometry from large to core scales indicates that the fields have not been disturbed by turbulent motions resulting from the collapse of material during the star formation process in L1157.

The orientation of the magnetic field towards L1157-IRS was found to exhibit an hour glass morphology (Stephens et al., 2013). The symmetry axis of the hourglass morphology is found to be perpendicular to a flattered structure ($\sim 0.1-0.2$ pc) seen in absorption against a bright emission possibly due to the polycyclic aromatic hydrocarbons from the diffuse interstellar medium in the background (Looney et al., 2007). The N_2H^+ emission, having a spatial extent of $\sim 30,000$ au and oriented 75° with respect to the north to east (elongated perpendicular to the outflow; Chiang et al., 2010), is found to coincide with the absorption feature. These structures extend further, at least, to the western side of L1157-mm coinciding with the east-west segment of the filament to upto a length of ~ 0.5 pc. From the *Filfind* algorithm, the east-west segment of the filament is oriented at an angle of 79° (consistent with the orientation of N_2H^+ emission) is making an offset of 48° with respect to the ICMF and 66° with respect to the CMF direction. The offset of 66° of CMF with respect to the east-west segment of the filament suggests that the star formation in L1157 supports a scenario where the magnetic field is sufficiently strong enough to have influenced the formation of at least the east-west segment of the filament structure (Planck Collaboration et al., 2016b; Soler

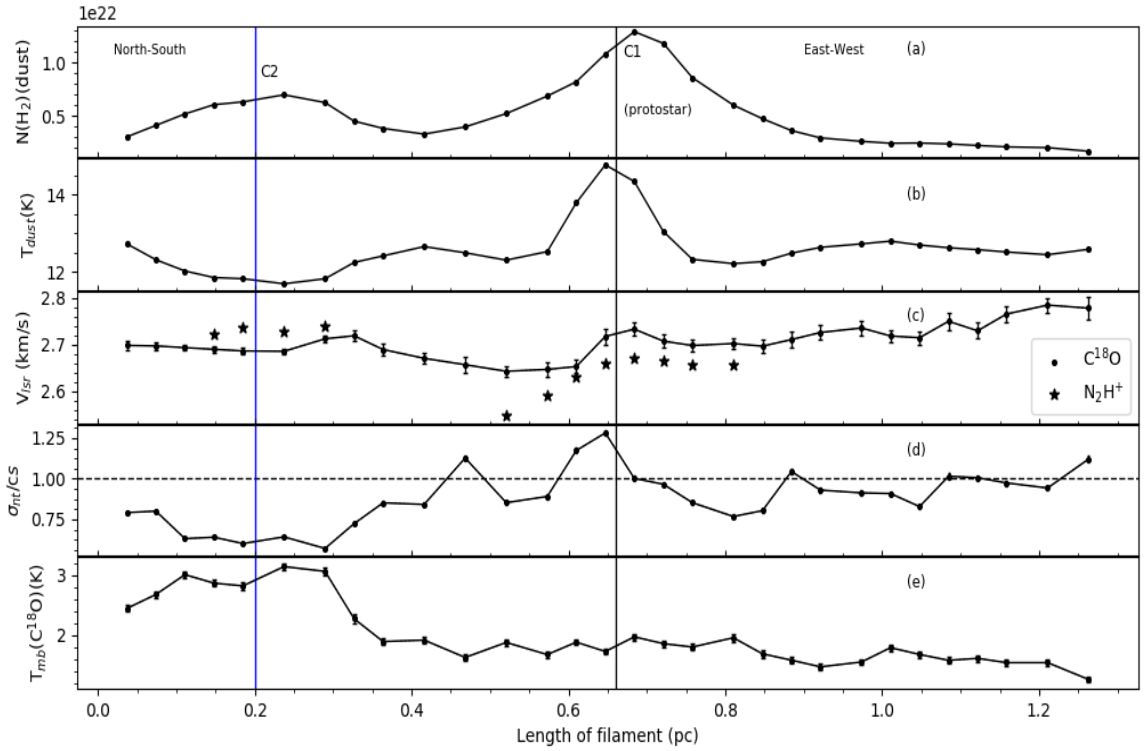

Figure 5.9: Results of $C^{18}O$ (1-0) and dust emission analysis along the cloud filament length. **(a)** Hydrogen column density derived using Herschel PACS and SPIRE images. **(b)** Dust temperatures. **(c)** Centroid velocity of $C^{18}O$ obtained from Gaussian fitting of profiles (filled dots). The centroid velocities obtained using hyperfine fitting of N_2H^+ (1-0) line coinciding with the positions along the filament are marked by filled stars. **(d)** Mach number which is the ratio of non-thermal velocity dispersion (σ_{nt}) along the line-of-sight and isothermal sound speed (c_s) at 10 K ($\sim$ 0.19 km s^{-1}). Blue line around 0.2 pc and black line 0.65 pc shows the position of clump C2 and class 0 protostar L1157-mm respectively. **(e)** Main beam brightness temperature using $C^{18}O$ lines.

et al., 2013). The north-south segment of the filament, however, is found to be almost parallel to both the ICMF and CMF.

The relative orientation of the bipolar outflow and the filament (the absorption feature and the N_2H^+ emission) in L1157 is found to be 82°±10°(assuming an uncertainty of 10°*inthedeterminationoftheoutflowpositionangles*,*e.g.*, *Soamet al.*, 2015) which is almost perpendicular to each other. If we consider the outflow direction as a proxy to the rotation axis, then the orientation of outflow with respect to the filament provides evidence for the manner in which matter got accumulated prior to the initiation of the star formation. In L1157, the material might have got accumulated first onto the filament channeled by the magnetic field lines aligned perpendicular to it and then as the density increased, the flow pattern changed its direction and might have flown along the filament towards the core. In such a scenario, one would expect the rotation of the protostar to be perpendicular to the filament since the local spin motion depends on the flow direction (Clarke et al., 2017; Stephens et al., 2017).

The offsets between ICMF and the outflow direction and between CMF and the outflow direction is 34°±16° and 16°±14° (see also Stephens et al., 2013), respectively which suggest that CMF is relatively more aligned with the outflow than the ICMF. Examples of both, alignment and misalignment or random alignment of outflows and magnetic field exist in the literature. Though the studies have shown that the outflows are preferentially misaligned or are randomly aligned with the magnetic fields, L1157-mm shows a good alignment especially between the outflow and CMF directions (see also Hull et al., 2013). Misalignment between magnetic fields and outflows are suggested as an essential condition to allow the formation of circumstellar disk (Krumholz et al., 2013).

5.4.5 Properties of the matter along the filament

To study the dust properties and large scale velocity field of the gas lying along the spine of the filament identified towards L1157, we derived peak line temperature, velocity centroids and velocity dispersion by making Gaussian fits to all $C^{18}O$ spectra having a S/N⩾3. The results are presented in Fig. 5.9 as a function of the positions along the main axis of the filament. The southern end of the north-south segment of the filament is taken as the starting point. The positions of the two condensations C1, C2 identified using the *Clumpfind* routine are marked. To compare the properties of dust and gas emission in the cloud, we convolved and regridded the dust column density map at ∼36″ grid using the beam size of TRAO (∼ 49″ at 110.20 GHz) (Jeong et al., 2019). The advantage of this approach is that the comparison is made over the same area on the source, but the disadvantage is that all the spatial structures smaller than this beam size get smoothed out.

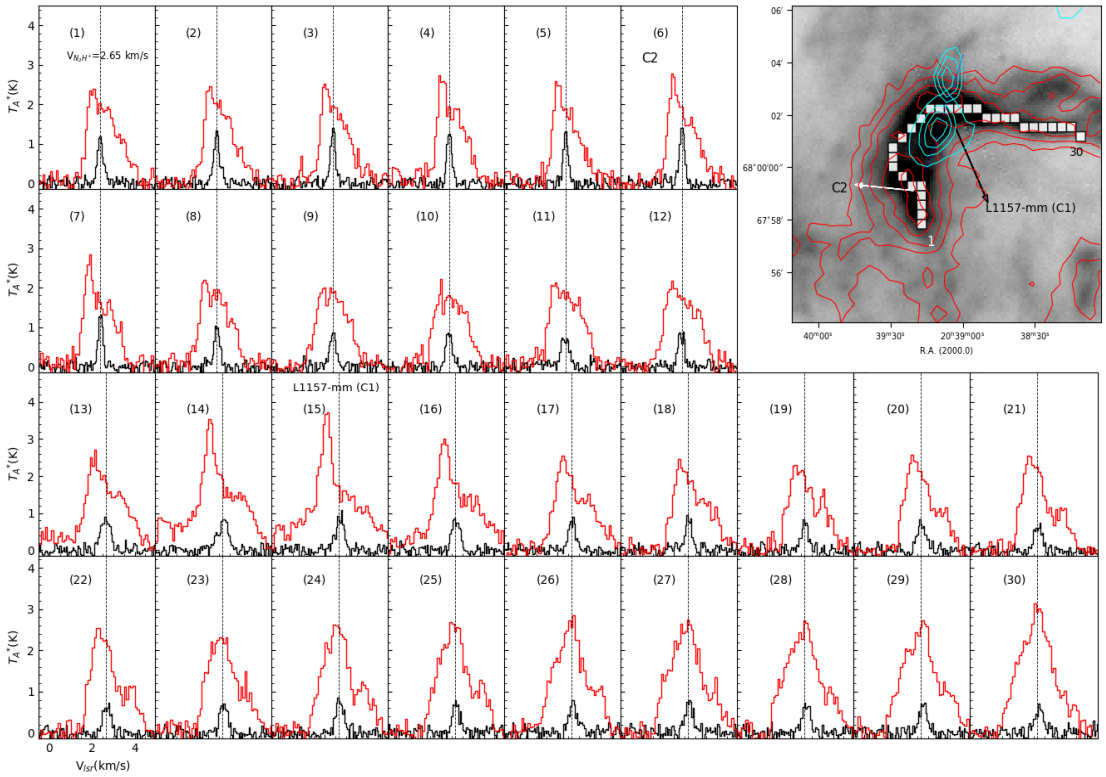

Figure 5.10: Distribution of $C^{18}O$ (black) and ^{12}CO (red) (1-0) line along the positions of *Filfind* skeleton. The dotted line shows the v_{lsr} of the cloud which is adopted from N_2H^+ peak velocity. The spatial positions of profiles are shown with filled white boxes on 250 μm *Herschel* image (upper-right) from 1-30 starting from extreme south towards west along the filament. The protostar L1157-mm and clump C2 are marked by black and white arrows, respectively. Integrated intensity contours of $C^{18}O$ (1-0) shown in red colour are obtained by summing flux over the velocity intervals from 2.2-3.0 km s^{-1}. The contours start from 6σ with intervals of 4σ where $\sigma \sim 0.019$ K km s^{-1}. The contours in cyan show the blue-shifted (towards north) and red-shifted lobe (towards south) of bipolar outflow. The levels for blue-shifted lobe range from 0.12-0.5 in steps of 0.08 K km $s^{-1}$and red-shifted lobe in range of 3.9-6.9 K km s^{-1}in intervals of 1 K km s^{-1}. The ^{12}CO line was integrated from -2.2 to +2.3 km $s^{-1}$for high velocity wings in southern lobe and 3.0 to 3.9 km s^{-1}in northern lobe.

In the panels (a) and (b) of Fig. 5.9, we show the derived dust column density and the dust temperature calculated using the *Herschel* data along the filament. The column density ranges from 1.7× 10^{21} to 1.3× 10^{22} cm^{-2}. The average dust column density of the filament is ∼ 5× 10^{21} cm^{-2}. The dust temperature range from 12 to 15 K with an average temperature of 13 K. The column density and the dust temperature both peak at the position of L1157-mm (identified using thick line in black). However, the values remain nearly constant on both north-south and east-west segments of the filament. The peak value of the dust column density on the filament, 1.3× 10^{22} cm^{-2}, is found at the position of C1 where L1157-mm is embedded. The mass-per-unit length values along the length of the filament were derived using the radial profile analysis as shown in Fig. 5.5 (right lower panel). Ostriker (1964) considered the mass-per-unit length or line mass of an isothermal filament in equilibrium as $2c_s^2/G \sim 15$ $M_\odot$ pc^{-1} at 10 K. The mass-per-unit length along the filament in L1157 ranges from 4-38 $M_\odot$ pc^{-1}. The line mass around C1 and C2 are larger than the equilibrium value which implies that these parts of the filament are supercritical. The values obtained around C1 and C2 are consistent with those found towards the Taurus molecular cloud (Palmeirim et al., 2013).

The mean column density profile of L1157 cloud is described with a Plummer-like function with a power law index of p∼3 (See 5.3.2). The value falls in a range of the typical values of p (∼ 1.5 – 3) obtained in the case of several filaments such as p∼ 2.7 – 3.4 in L1517 (Hacar & Tafalla, 2011), and p = 3 in L1495 (Tafalla & Hacar, 2015). The radial equilibrium of the filamentary clouds can be explained by considering them as isothermal cylinders using pure hydrostatic models (Ostriker, 1964) or magnetohydrostatic models (Fiege & Pudritz, 2000a). The former models can lead to density profiles as $\rho \sim r^{-4}$ and the latter ones to $\rho \sim r^{-2}$. Our results with power-law index, p∼3 suggest that the filament column density profile supports a theoretical model with magnetic fields. The results of magnetic field studies presented here support the fact that the magnetic field has played an important role in the dynamical evolution of L1157.

The $C^{18}O$ is detected at points all along the ∼1.22 pc length of the filament and correlates well with the dust emission. The distribution of ^{12}CO (in red) and $C^{18}O$ (in black) profiles all along the spine of the filament is shown in Fig. 5.10. Position 1 corresponds to the southern end of the north-west segment and position 30 corresponds to the western end of the east-west segment of the filament. There is a strong tendency that blue asymmetry in ^{12}CO line profile is seen at high column density region while no clear asymmetry in those lines is seen at low column density region. The ^{12}CO line profiles at positions 1-3 in the north-south segment of the filament show a blue asymmetry. As we approach towards the C2 (positions 4-7), the ^{12}CO profile becomes blue-red asymmetry with the blue peak brighter

than the red peak. Then the line profile becomes more of a symmetric one till the position 12. The profile becomes blue-red asymmetry again as we approach C1 and continues till the position 17. The $C^{18}O$, which is an optically thin tracer, peaks at the velocity of the self-absorption, suggesting that the double-peaked profiles of ^{12}CO (Fig. 5.10) in the panels 4-7 and 13-17 are most likely due to inward motions assuming that the gas in the inner parts of the C1 and C2 has a warmer excitation temperature than that towards the envelope. The inward motions seen here could be interpreted as due to collapse or infall motion (Lee et al., 1999, 2001; Tafalla et al., 1998). The linear extent of the infall motion is around ~ 0.15 pc. The $C^{18}O$ lines are well fitted with a Gaussian profile throughout the filament. The $C^{18}O$ line-width around the clump C2 is found to be narrower than that found around the core C1. The ^{12}CO lines at positions 23-30 peaks at the systemic velocity of the cloud with an additional red component which is most likely caused due to the effect of the red lobe of the outflow.

The values of the observed line-width (full-width at half maximum) of $C^{18}O$ profiles range from ~ 0.3 to 0.6 km s^{-1}. We fitted a single Gaussian profile to all the $C^{18}O$ profiles and obtained the peak velocites. The mean value of V_{lsr} of the full L1157 filament was found to be 2.65 ± 0.05 km s^{-1}. The systematic velocity of the cloud was estimated by taking an average of the velocities at positions where significant emission in the N_2H^+ line was detected. The variation in the centroid velocity (V_{lsr}) all along the spine of the filament is shown in Fig. 5.9 (c). The peak velocity changes from 2.64 to 2.78 km s^{-1} (2-3 velocity channels). The filament appears to be velocity coherent as there is no significant change in the peak velocity. This is consistent with the previous studies of nearby filaments forming low mass stars (Hacar & Tafalla, 2011). The mean dispersion in the centroid velocities obtained from the Gaussian fit is found to be ~ 0.03 km s^{-1}. To the west of the C1, the east-west segment of the filament shows almost a constant value of V_{lsr} (≈ 2.7 km s^{-1}). Compared to this, the velocity structure of the north-south branch shows discernible variation. No notable variation in the values of V_{lsr} obtained from $C^{18}O$ lines is seen along the filament except at the position where the north-west segment of the filament changes its direction towards the east-west segment.

The N_2H^+ (1-0) line emission was detected towards both C1 and C2 with emission being prominent in regions around C1. The seven components in N_2H^+ (1-0) spectra were simultaneously fitted with seven Gaussian forms at once with their line parameters given by Caselli et al. (1995). We obtained V_{lsr} of the cloud, line-width, total optical depth of all the components using fitting results. The peak velocity in N_2H^+ lines varies from 2.54-2.74 km s^{-1}. The peak velocities obtained from the N_2H^+ line towards C1 and C2 along the filament spine are shown in Fig. 5.9 (c) using star symbols. The V_{lsr} of the C1 and C2 was estimated

as 2.62 km $s^{-1}$and for 2.72 km s^{-1}respectively. The N_2H^+ line shows a systematic change in the velocity across the position of L1157-mm. The velocity gradient estimated using N_2H^+ emission is found to be 0.37 km $s^{-1}pc^{-1}$. Chiang et al. (2012) detected N_2H^+ emission across an elongated region of $\sim 30,000$ au (considering a distance of 340 pc) which is consistent with the flattened structure seen by (Looney et al., 2007). Systematic variations in the velocity are seen in N_2H^+ emission across the flattened envelope at $\sim 30,000$ au (Chiang et al., 2012), similar to the variations noticed by us at ~ 0.1 pc scale. This suggests that the variations in the velocity observed at different scales (Chiang et al., 2012; Kwon et al., 2015) are most likely inherited from the bulk motion of the gas at the cloud scale.

The linewidth of a spectral line is a combination of thermal and non-thermal motions (Myers, 1983). Non thermal motions are generally arising from turbulence in cloud or core scale mechanisms. We have separated out the thermal component from the observed line-width obtained from the Gaussian fitting analysis with the assumption that the two components are independent of each other. The non-thermal component is calculated as

$$\sigma_{nt} = \sqrt{(\sigma^{obs})^2 - (\sigma^{th})^2}$$

where σ^{th} is $\sqrt{kT/\mu m_{obs}}$, thermal velocity dispersion, μ is the molecular weight of the observed $C^{18}O$ molecule, T is the gas temperature and k is the Boltzmann constant. The mach number (M) is defined as the ratio of non-thermal component (σ_{nt}) and isothermal sound speed (c_s) shown in the panel (d) of Fig. 5.9. The variation shows the extent of non-thermal motions distributed along the positions of the filament. We find that much of the gas in the filament is subsonic as $M \leq 1$. Only the region around the protostar shows the signature of turbulent motions as the $\sigma_{nt} \geq c_s$. The $C^{18}O$ peak line temperature is plotted as a function of position in the panel (e) of Fig. 5.9. The intensity peak observed in $C^{18}O$ towards the C1 is found to be shifted from the peak intensity in dust emission. We believe that this could be because of the depletion of the $C^{18}O$ molecules from the gas phase at the high density regions. On the other hand, the $C^{18}O$ line intensity peaks in the vicinity of C2 ($T_{mb} \approx 3.0$ K) and remains roughly constant at T_{mb} of $1.0 - 3.0$ K all along the parts of the filament. The $C^{18}O$ emission is lesser at the position of C1 where dust emission is the brightest and $C^{18}O$ is comparable to other positions along the east-west branch. Contrary to this, $C^{18}O$ emission is the strongest at the position of C2 where dust emission is second brightest. It might happen that $C^{18}O$ is highly depleted or photo-dissociated at region around C1. However, C2 clump seems less depleted in comparison with C1 core. This suggests that the C2 is chemically younger core than C1. Overall the L1157 is velocity-coherent and

mostly subsonic throughout its length though having internal dynamics around core C1 and C2.

We derived total mass of the cloud by summing up all the N(H_2) values falling within the half-maximum contour level in the intensity map of $C^{18}O$ as shown in Fig.5.10 where it covers the high density region of the cloud. The corresponding pixels in the dust column density map were used to calculate the mass of cloud by dust emission. The mass of the L1157 cloud by gas emission was estimated as ~ 8 $M_\odot$ whereas the mass of the cloud by dust emission was calculated as 16 $M_\odot$. There is a difference by a factor of more than 2 between mass (M(H_2)) calculated from $C^{18}O$ observations and *Herschel* dust emission map. We expect the coupling of gas and dust in the interstellar matter at the volume densities of $\sim 10^5$ cm^{-3} which do not correspond to the critical density of $C^{18}O$ molecules (Goldsmith, 2001). The typical uncertainty in the estimation of the M(H_2) value using dust emission is a factor of 2. The dominant factor contributing to the error in the mass estimation is the uncertainty in the opacity law. This value is an upper limit as we lack information on the inclination of the filament. The difference between the M(H_2) values derived from gas and dust can be attributed to various factors. The $C^{18}O$ molecules can deplete and freeze out on dust grains in high density regions ($n_{H_2} \geq 10^5$ cm^{-3}) and low temperatures (T $\leq$ 20 K). In addition, *Herschel* is capable of tracing the dust column where the temperatures are higher but $C^{18}O$ line might get affected by the interstellar radiation field (ISRF) and get photodissociated at less dense regions of cloud (e.g., Caselli et al. (1999); Spezzano et al. (2016); Tafalla et al. (2004)). The gas column density can change due to variation in CO-to-H_2 conversion factor or abundance ratio of optically thick ^{12}CO and optically thin $C^{18}O$ tracers according to metallicity and column density gradients (Bolatto et al., 2013; Pineda et al., 2010).

5.4.6 Physical parameters of the clump C2

The C1, which is currently forming the protostar L1157-mm, shows supersonic turbulent motions in $C^{18}O$ lines. The dust temperature was found to be $\sim$ 15 K. Previous studies have already characterised the C1 using dust continuum and line mapping observations at different spatial and spectral resolutions (Gueth et al., 1997). In this section we determined the properties of C2 to characterize its evolutionary state. The clump C2 has a peak dust temperature (T_d) $\sim$ 12 K and peak column density $\sim 9 \times 10^{21}$ cm^{-2}. As discussed earlier, there exist blue-red asymmetry in ^{12}CO lines towards centre of C2 and the $C^{18}O$ peaks at the velocity of the self-absorption indicating the presence of an inward motion (Fig. 5.10 and Fig. 5.11). The lack of high-velocity wings in the line profile suggests that the region is not affected by the outflow though the southern edge of the blue-shifted lobe of the outflow

spatially coincides with the outer periphery of C2. The outflow is almost in the plane-of-sky with the inclination angle of 10°(Gueth et al., 1996). We quantified the outflow energetics with its mass and kinetic energy as 0.05 $M_\odot$ and 1.2×10^{43} ergs, respectively. The sources of uncertainty in the estimation of the outflow parameters depend on the velocity boundary between the high velocity wings and the ambient velocity and the inclination angle with respect to the line-of-sight. The gravitational binding energy of the C2 is calculated as 0.53 $\times 10^{43}$ ergs. Thus, the outflow has the potential to disturb the ambient gas and may affect C2 in future. The motion of the gas molecules around C2 is very quiescent with subsonic turbulence and high $C^{18}O$ intensity. Fig 5.9 (c) shows that the subsonic non-thermal motions are mostly associated with the region around C2. The properties of prestellar or starless cores in low mass star forming regions like Taurus and Ophiuchus have been studied in detail (di Francesco et al., 2007; Gregersen & II, 2000; Motte et al., 1998; Onishi et al., 2002) and the values found here for C2 are consistent with the typical properties of starless core.

The measure of non-thermal line-widths using molecular line diagnostics can be used to investigate whether the core is virialised or not. We derived the virial mass of C2 using the averaged total velocity dispersion of $C^{18}O$ line. If the mass of the clump is less than the virial mass, the cloud is not gravitationally bound and may expand. We derived the virial mass using the formula (MacLaren et al., 1988),

$$M_{vir} = \frac{k\sigma^2 R}{G} \tag{5.4}$$

where k depends on the density distribution, G is the Gravitational constant and R is the cloud radius. The total velocity dispersion is given by the equation,

$$\sigma = \sqrt{\frac{kT_{kin}}{\mu_{m_H}} + \sigma_{nt}^2} \tag{5.5}$$

Assuming a Gaussian velocity distribution and density profile distribution as $\rho = r^{-2}$, we can express the above equation also in terms of solar mass as $M_{virial} = 126\Delta v^2 R$, where Δv is the FWHM velocity of $C^{18}O$ lines in km s^{-1} along the line-of-sight and R, the radius in parsec units. By approximating C2 as an ellipse on the sky projection, the radius of the core was estimated as $\sqrt{FWHMx} \times \sqrt{FWHMy}$, where FWHMx and FWHMy are the full-width at half maximum diameters along major and minor axis, respectively. The value of average FWHM velocity of the gas was calculated as 0.5 km s^{-1}. We calculated the effective radius of C2 as ~ 0.1 pc using FWHM of major axis ~ 1.3 $'$ and minor axis ~ 0.7 $'$. The virial mass of C2 was estimated as ≈ 3.1 $M_\odot$. The major contribution of uncertainty in the calculation of the virial mass comes from the uncertainty in the distance estimation which is ~ 1%. There

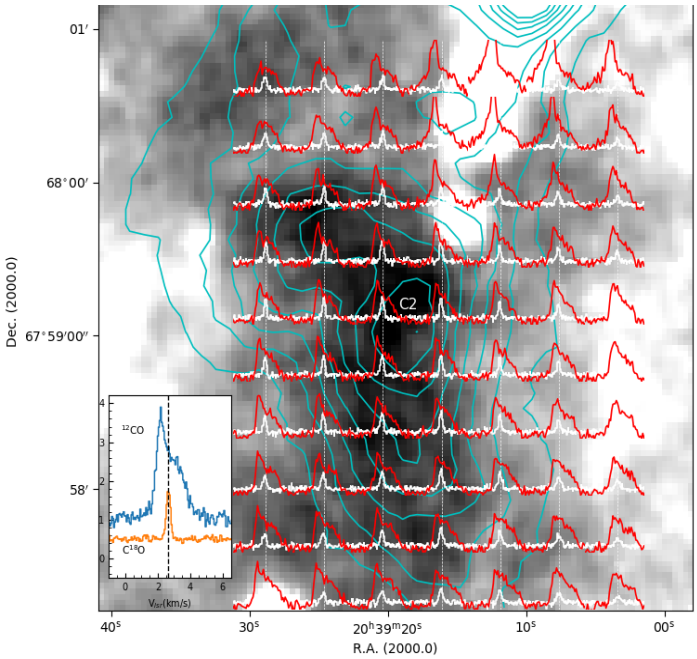

Figure 5.11: ^{12}CO (red) and C^{18}O (white) profiles overlayed on 12 μm *WISE* emission map with C2 marked. The contours in cyan color show the 250 μm dust intensity emission and the contour levels are in range 50-120 MJy/sr in steps of 10 MJy/sr. In the inset shown two profiles for ^{12}CO (in blue) and C^{18}O lines (in orange) averaged over half-maximum contour in intensity map of N_2H^+ line.

is a variation of 5% in the value of virial mass due to distance uncertainty. We summed up all the pixels with column density values falling within the derived radius of clump C2 in moment zero map of C^{18}O line. The total gas mass of C2 is calculated as $\sim 2.5\pm0.3$ M$_\odot$. We found that the clump C2 is on the verge of being gravitationally bound since $M_{virial} \approx M_{gas}$. The dust mass around clump C2 is calculated as ≈ 5 M$_\odot$ using same region as used in the calculation of gas mass.

The N_2H^+ line traces the dynamics of the dense central part of the core while the C^{18}O line traces the dynamics of the surrounding less dense material in the envelope. We studied the core-to-envelope motion around C1 and C2 by comparing the centroid velocity of N_2H^+ and C^{18}O lines and the velocity dispersion. As can be noticed, the velocities of the different tracers match with each other as shown in Fig 5.9 also. The average difference in centroid velocities of C^{18}O and N_2H^+ around clump C2 is 0.03 ± 0.02 km s^{-1} and around core C1 is 0.06 ± 0.02 km s^{-1} which means that the velocities of the different tracers differ on average by less than one fifth or one third of the sound speed. This good match rules out any significant relative motions between different density regimes of the gas and, in particular, rules out any possibility of systematic drift between the dense cores (traced by N_2H^+) and

the surrounding gas (traced by $C^{18}O$). This result is in good agreement with the previous studies that probed relative motion between the dense inner region and envelope of the cores (Ayliffe et al., 2007; Kirk et al., 2007a; Walsh et al., 2004). The line width obtained in $C^{18}O$ line is found to be relatively broader (by 1-2 channels around core C1) when compared with that of N_2H^+ (1-0) as shown in Fig 5.12. The difference in line-width around core C1 is within a channel spacing for both the tracers. The motions in C2 is subsonic in both $C^{18}O$ and N_2H^+ lines as compared to that of C1. This behaviour of line broadening is consistent with the previous studies where starless cores are expected to have less turbulent motions and protostellar cores show more broader line-width (Kirk et al., 2007a).

The N_2H^+ and $C^{18}O$ lines can be used to find out the extent of chemical evolution of the dense cores. N_2H^+ can only form in significant amounts after $C^{18}O$ freezes out on dust grains since both the molecules form by competing reactions (Caselli et al., 1999). N_2H^+ is observed to be good tracer of gas at densities $\sim 10^5$-10^6 cm^{-3} whereas $C^{18}O$ will deplete at these densities (Tafalla et al., 2002). At later stages of evolution when the central protostar formation has taken place, the N_2H^+ will get destroyed due to rise in temperature and CO molecules will start forming. We used the integrated intensity of $C^{18}O$ and N_2H^+ lines to calculate the ratio of intensities. If this ratio, $R > 1$, it implies that the core has not evolved to the extent that the carbon molecules could freeze out on the surface of dust grains and therefore, chemically young. We averaged the intensity values around the starless core C2 where significant ($\geq 3\sigma$) emission of N_2H^+ is obtained. The ratio is found to be greater than 1 which implies that the core has not yet chemically evolved. C1 core shows highly enhanced distribution of N_2H^+ line. This may be due to the significant depletion or photodissociation of $C^{18}O$ molecules in the core which usually play a role for the destruction of N_2H^+ (Caselli et al., 1999). N_2H^+ in C2 core is also enhanced, but not as much as C1 core. This can be also explained by overabundance of $C^{18}O$ molecules than C1 core.

5.5 Conclusions

We present results of a study conducted on a molecular cloud L1157 which is part of a cloud complex L1148/1157. Currently, formation of a Class 0 protostar, L1157-mm, having a spectacular bipolar outflow is taking place. The extreme youth of the protostar implies that the initial conditions that guided the cloud to form a star may still be preserved. We made R-band polarimetry of the cloud to trace magnetic field geometry of the cloud. We also made observations in ^{12}CO, $C^{18}O$ and N_2H^+ ($J = 1 - 0$) lines to investigate the kinematics of the material associated with the cloud. The main results obtained are summarized below.

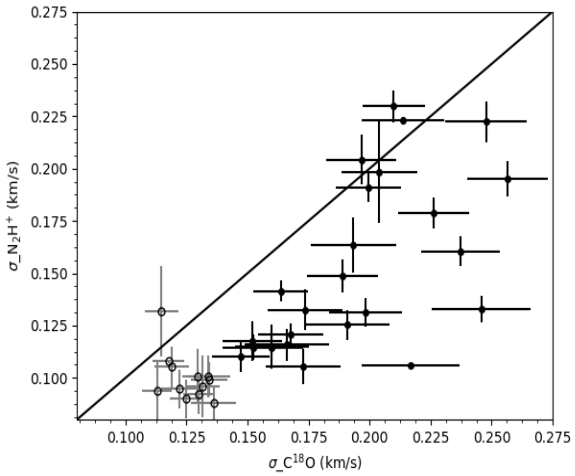

Figure 5.12: Variation of velocity dispersion measured in $C^{18}O$ and N_2H^+ profiles. The filled circles are the points near C1 and unfilled circles are around C2.

1. We estimated distance to the L1148/1157 complex using the YSOs associated with the cloud complex. The distances of the YSOs are estimated based on the parallax measurements and the proper motion values obtained from the *Gaia* DR2 database. The estimated distance is 340 ± 3 pc.

2. We obtained polarization measurements of 62 stars projected towards the direction of L1157 (within a region of $0.3^\circ \times 0.3^\circ$field). Based on the degree of polarization vs. distance plot for the stars observed by us and those from the (Heiles, 2000) catalog, we present additional evidence of the presence of the cloud at ~ 340 pc distance.

3. Using the *Filfind* algorithm on the dust column density map of L1157 obtained from the *Herschel* data, we traced a filament which is found to be ~ 1.2 pc in length and oriented at a PA of 79° (east-west segment). Near to the protostar, the filament changes its orientation and becomes almost perpendicular (north-south segment). Using the *Radfil* algorithm, the average filament width is estimated as ~ 0.09 pc and the radial distribution of the material is fitted with a Plummer-like density profile of power-law index of $p = 3$. Using the *Clumpfind* algorithm we identified two cores (C1 and C2) that are found to be located on the filament. In one of these cores is where L1157-mm is currently embedded.

4. The ICMF traced by our R-band polarization measurements of the stars background to the cloud is found to be well ordered at $\sim 0.2 - 2$ pc scale. The geometry of the ICMF inferred from the *Planck* 353 GHz data was found to be in good agreement with our

R-band polarization results. The strength of the magnetic field calculated based on our data is found to be $\sim 50\ \mu$G. The ICMF is oriented at a PA of $127^\circ \pm 12^\circ$.

5. Based on the relative orientations between the ISMF, CMF, filament and outflow and the presence of an hour-glass morphology of the magnetic field at the core scale with its symmetry axis orthogonal to the major axis of the flattened pseudodisk suggest that magnetic field has played an important role in the evolution of L1157 to become a star forming core.

6. We made ^{12}CO, C^{18}O and N_2H^+ line observations of the entire region covering L1157 cloud. The C^{18}O is detected at points all along the ~ 1.2 pc long filament and found to correlate well with the dust emission. A blue-red asymmetry is observed in ^{12}CO towards both C1 and C2 with C^{18}O peaking at the systemic velocity of the cloud signifying infall motion of the material. We found no significant change in V_{lsr} velocity along the filament except at the location where the north-south segment changes its direction towards the east-west segment of the filament. The N_2H^+ ($J = 1 - 0$) line also shows a systematic change in the velocity across C1 suggestive of the presence of a bulk motion in the gas.

7. The east-west segment of the filament presents a sinuous structure. It is believed that the sinuous features seen in clouds are believed to occur due to cloud-ISM interaction. The dynamical state of such interactions depends on the Reynolds number which is found to be ~ 3 in L1157. For such a low value ($\lesssim 10$) of Reynolds number, the cloud motion through ambient medium can cause mass loss by ablation and can form long sinuous filaments.

Chapter 6

Molecular line study of the cloud complex LDN 1147/L1158 complex

6.1 Introduction

In the previous chapter, we studied the gas kinematics of structurally simple cloud having a single filament and two cores associated with, L1157 belonging to the cloud complex L1147/1158. As mentioned in the previous chapter, the distance to L1147/1158 complex is found to be 340±3 pc based on the distances of the three YSOs for which *Gaia* DR2 parallax and proper motion measurements are available. Thus, L1147/1158 together with L1172/1174 form a part of a bigger complex which are both spatially and kinematically associated. However, both the complexes show differences in terms of their capacity to form stars. While L1172/1174 contains a Herbig Be star, HD 200775, surrounded by a sparse cluster of YSOs, L1147/1158 is found to be associated with a Herbig Ae star, PV Cep, and star formation happening at isolated clouds, namely, L1148 (Kauffmann et al., 2011), L1152 (Benson et al., 1988), L1155, and L1157 (198, 1988).

The cloud has been mapped by (Snell, 1981) in the ^{12}CO and ^{13}CO (J=1-0) transitions with 4′ beam. The complex has been part of full ^{13}CO line survey program of the Cepheus and the Cassiopeia constellation (Yonekura et al., 1997). But the observations were made with coarse resolution of 2.6′ with 8′ grid. This region contains various morphologies of filaments such as a long rectilinear and curved shaped structures as shown in Fig. 6.1. The details of how they were extracted will be discussed further in the chapter. To understand the formation of filaments, cores and subsequent star formation in relatively less active environment, we have investigated the filaments and dense cores of the full L1147/1158

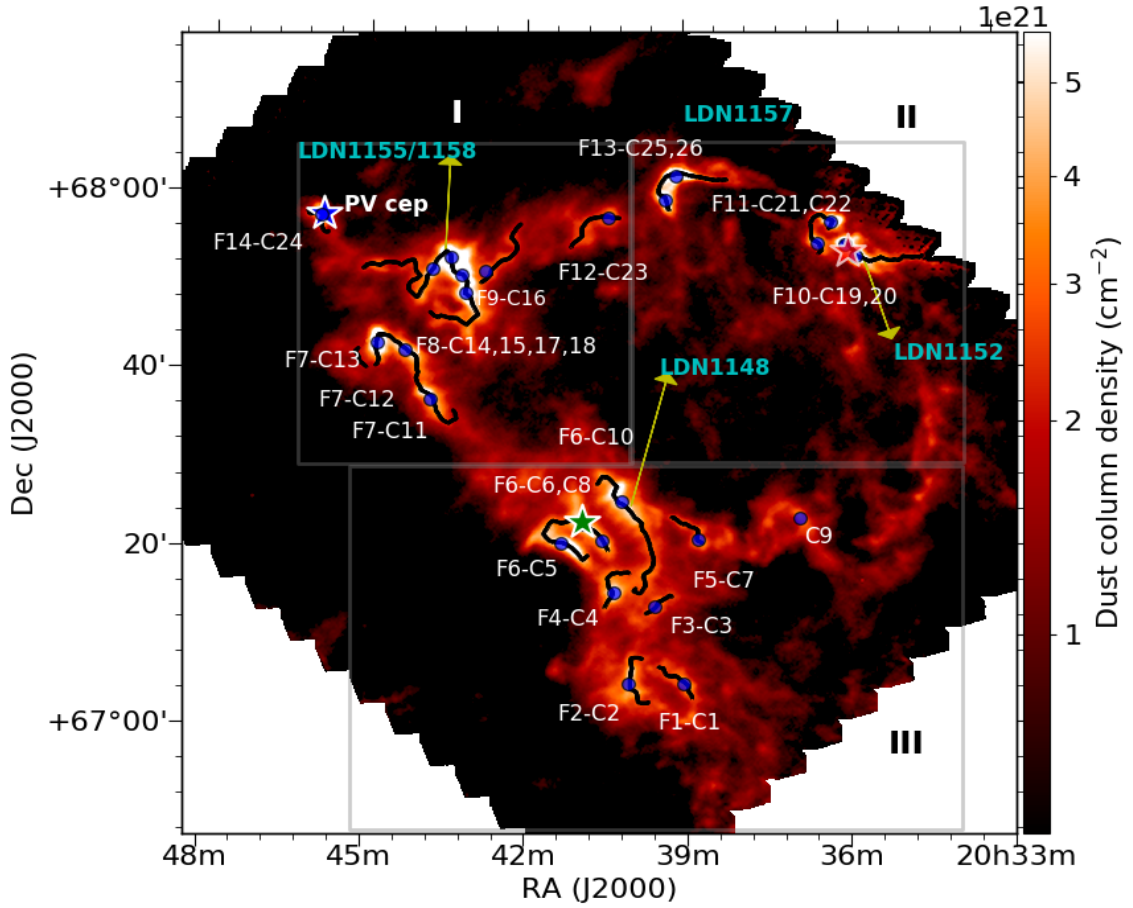

Figure 6.1: Dust column density distribution of the L1147/1158 complex. The high density skeletons are identified by black lines. Blue filled circles show extracted clumps. Different clouds L1157, L1155, L1152, L1148 regions are labelled.

complex with the same telescope and same velocity resolution of 0.05 km s^{-1}. The complex is of size ~1.5°× 1.5°.

6.2 Observations and data reduction

We have carried out On-The-Fly (OTF) mapping towards the whole cloud L1147/1158 with the 14 m diameter single-dish telescope of Taedeuk Radio Astronomy Observatory in Daejeon, South Korea from December 23, 2019-January 6, 2020 and from January 23 - 28 January, 2020. The pointing accuracy was achieved to be $\leq 5''$ using a standard R Cas and X Cygnus source in the SiO line. C^{18}O line which reveals the dynamics of high density regions of cloud was simultaneously observed with ^{13}CO line. We divided the complex L1147/1158 in four tiles so that all the dense structures in dust map can be covered using molecular line

mapping. Each tile has a size of $36^{'} \times 36^{'}$. Spectral resolution of 0.05 kms^{-1} was used and typical rms noise in one channel was ~0.099 K for $C^{18}O$ and ~0.1 K for ^{13}CO lines. The half-power beam width is $44^{''}$ at frequency of 109 GHz. The map is sampled at a grid size of $20^{''}$ which corresponds to spatial resolution of ~0.034 pc at a distance of 340 pc. The details of reduction and baseline fitting have already been discussed in Chapter 2. We obtained a total of 47,000 spectra over the mapped region of $1.2^{\circ} \times 1.2^{\circ}$ size in both the lines.

6.3 Analysis and results

6.3.1 Identification of filaments and clumps

Fig. 6.1 shows the dust column density distribution of L1147/1158 complex taken from Herschel Gould Belt Survey Archive (Di Francesco et al., 2020). We used *Filfinder* algorithm to extract the high density structures in the full complex. The whole column density map was divided in terms of individual complexes and *Filfinder* was applied individually. A global threshold of three times the background value, 2.1×10^{21} cm^{-2} has been used in each region with a flattening percentile ~ 98. The derived skeletons have been pruned up on the basis of branch threshold criteria and longest possible skeletons were extracted out. A set of 14 filaments were obtained over the full complex. Their detailed properties are discussed in further sections.

We used *Astrodendrogram* on the dust column density map with min_delta value as 2.88×10^{21} cm^{-2} which is 4 × background column density. The threshold is chosen such that well defined local maxima can be extracted. The background column density, σ ~ is 0.7×10^{21} cm^{-2}. We identified a total of 26 cores numbered from 1 to 26 in Fig. 6.1. Different properties like position, peak flux, effective radius (R_{eff}), major and minor axis which are all direct outputs of Astrodendro are derived. The R_{eff} calculated in the algorithm is defined as $R_{eff} = \sqrt{\sigma_{major} \times \sigma_{minor}}$, where σ_{major} and σ_{minor} are rms sizes along the major and the minor axis, respectively. The kinematical properties of these sources like systematic velocity, velocity dispersion, gas mass, virial mass will be discussed in further sections.

6.3.2 Gas distribution of the complex

- **^{13}CO (1-0) and C^{18}O (1-0) emission:** Fig. 6.2 shows the averaged spectra of the ^{13}CO and $C^{18}O$ (1-0) lines emission towards the mapped region of the filamentary structures of L1147/1158 complex.

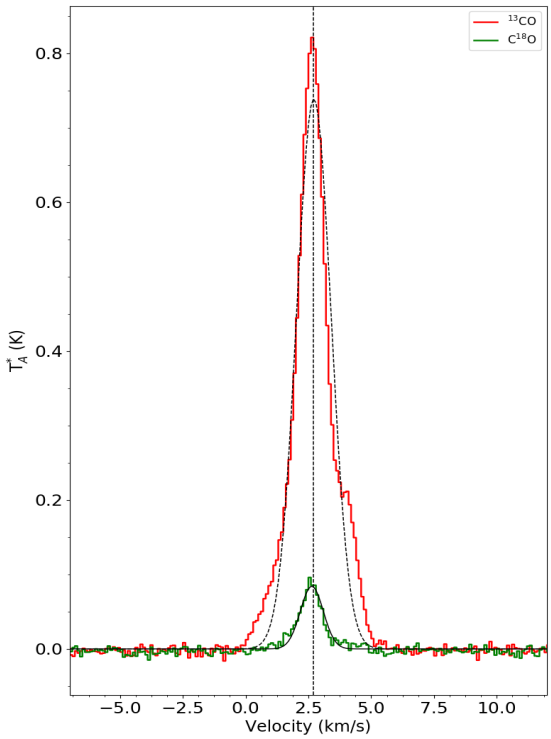

Figure 6.2: ^{13}CO (J = 1-0), C^{18}O (J = 1-0) averaged spectra of the whole mapped region. The black dashed line represents the intensity peak at systematic velocity of the cloud ~ 2.7 km s^{-1}. The x-axis is labelled with the velocity in units of km s^{-1}.

There is only peaked profile seen in the averaged spectrum of ^{13}CO line suggesting that there is presence of only one cloud component along the line-of-sight which is fitted with a single Gaussian function. However, the C^{18}O line shows a deviation from the Gaussian fit on both lower and higher velocity ends. There is an extra shoulder around 4 km s^{-1}which contributes to the deviation. This is an extra cloud component at $\sim$ 4 km s^{-1}on the western side of L1148-IRS. On the lower velocities, there is an extended tail from 1.5 km s^{-1}. We obtained a peak velocity of 2.71 km s^{-1}based on a Gaussian fit to the ^{13}CO (1-0) line. The averaged spectrum of C^{18}O also shows a single peak at 2.63 km s^{-1}. The line width of ^{13}CO is found to be $\sim$ 1.62 km s^{-1}while C^{18}O is quite narrower with a line width of $\sim$ 1 km s^{-1}. The detailed pixel-by-pixel analysis will be discussed in further sections.

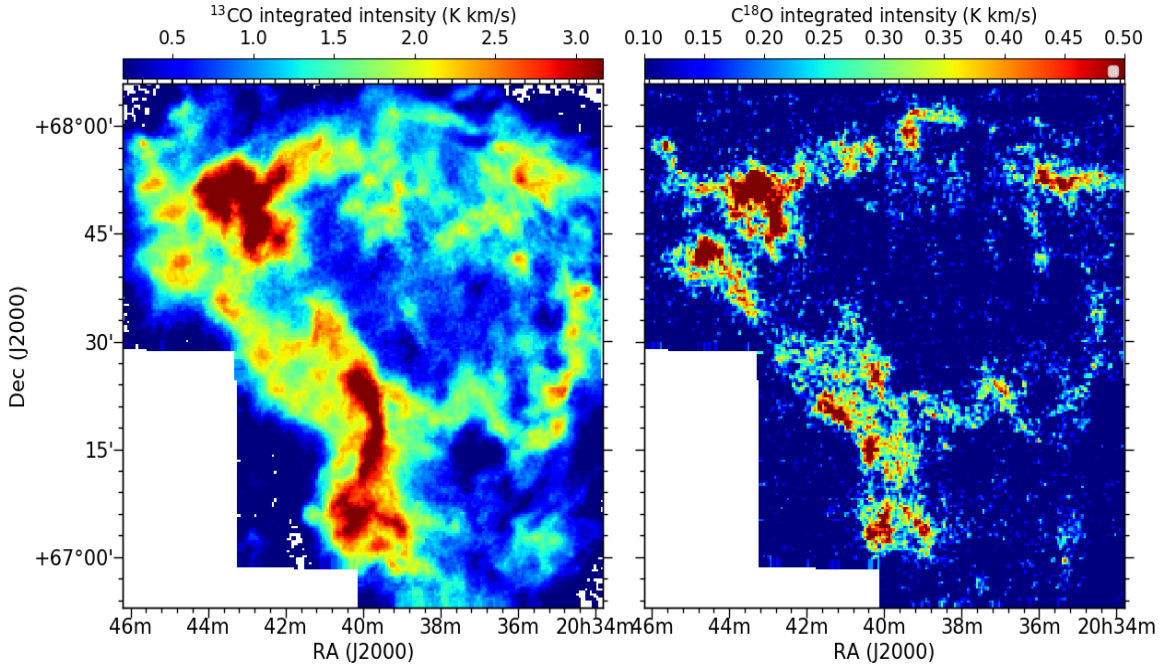

Figure 6.3: Integrated intensity maps of ^{13}CO (left) and C^{18}O (right) emission lines. The integrated intensity is shown using colorscale.

Fig. 6.3 shows the distribution of ^{13}CO and C^{18}O gas for the filamentary region. The moment maps for ^{13}CO and C^{18}O are created by using those channels having temperature values exceeding 0.1 K (approximately 3 times the rms level per channel) respectively. The integrated intensity distribution of ^{13}CO is shown in Fig. 6.3 (left panel). The ^{13}CO is integrated over a velocity range of -0.5 to 5.3 km s^{-1}. The ^{13}CO distribution is more extended in different parts of the complex where north-east and south-west branch show the maximum emission.

The distribution of $C^{18}O$ (1-0) emission is shown in Fig. 6.3 (right) in units of K kms^{-1}. The intensity levels are taken from 0.1-0.99 K kms^{-1} in steps of 3σ= 0.1 K kms^{-1}. The velocity channels used for the summation are in the range of 0.6-4.9 km s^{-1}. The $C^{18}O$ distribution in almost correlating well with the extracted filaments obtained from dust column density map shown in Fig. 6.1. The highest $C^{18}O$ emission, $\sim$ 1 K km s^{-1}is seen near the core L1155 arc like structures.

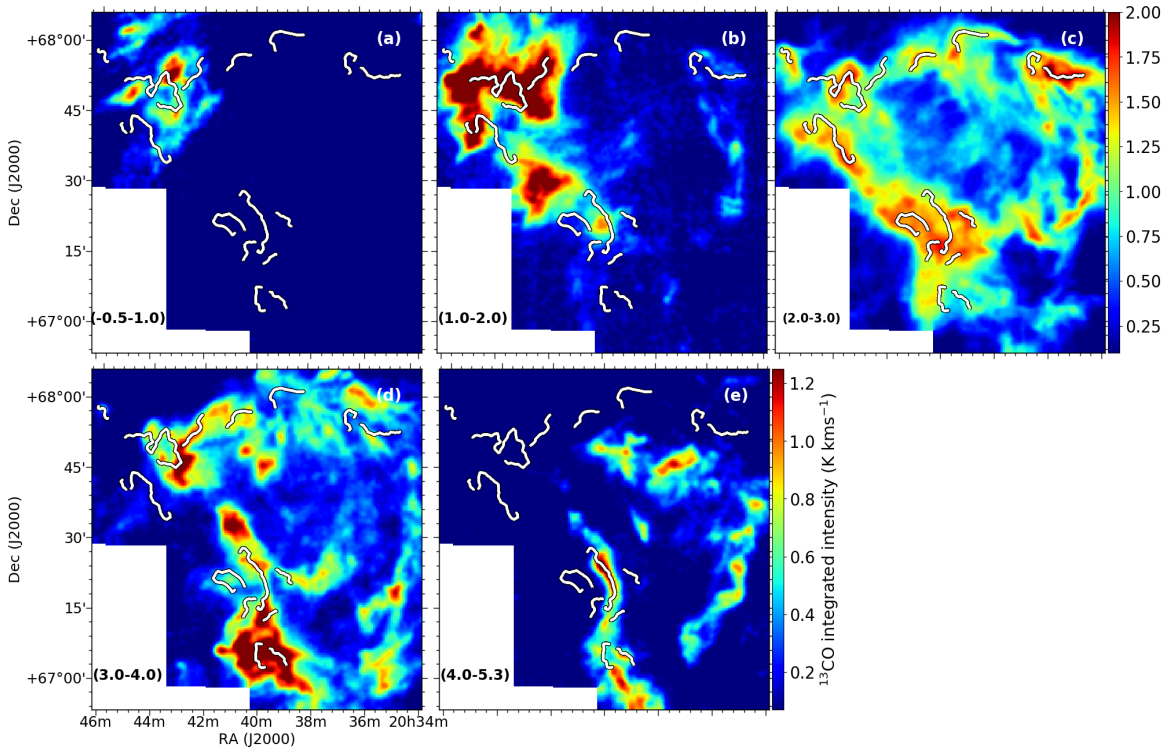

Figure 6.4: Channel maps for ^{13}CO lines. Each channel shows the velocity range used for the integrated emission. The intensity is in the units of K km s^{-1}. Each panel shows emission higher than the threshold of the map.

Fig. 6.4 shows the channel maps of ^{13}CO line over the velocity range from -0.5 to 5.3 km s^{-1}. The distribution of ^{13}CO emission is quite diffuse over the full velocity range. However, most of the structures are seen in the velocity range of 2.0 <v$\leq$ 3.0 km s^{-1}, Fig. 6.4 (d). The $C^{18}O$ integrated emission looks highly structured. The maximum emission is obtained in the L1155 region and L1148 complex. The gas motion is preferentially from east to west. In panel (e), we notice that there is an enhanced emission towards the extreme south of the mapped region.

Fig. 6.5 shows the channel maps of $C^{18}O$ emission towards the filamentary structure. Each channel map is obtained by integrating the emission over 1.0 km s^{-1}velocity

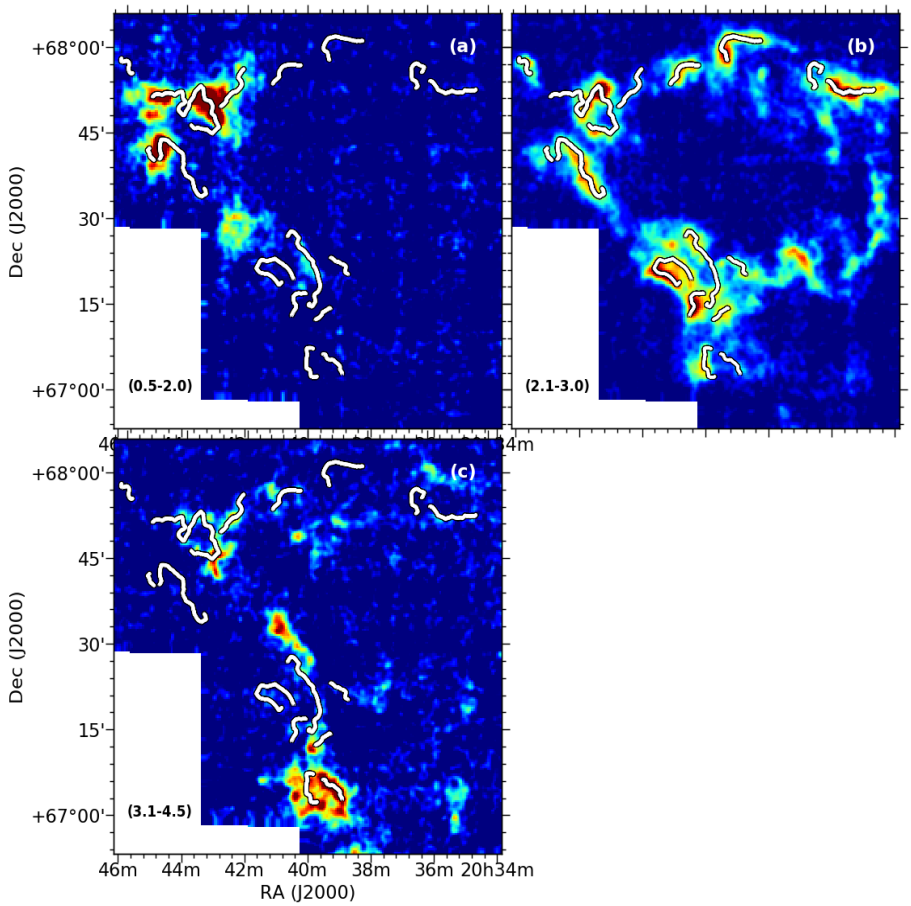

Figure 6.5: Channel maps for $C^{18}O$ lines. The solid white lines represent high density skeletons derived from *Filfinder*. Each channel shows the velocity range used for the integrated emission. The intensity is in the units of K km s^{-1}. The background intensity is 0.02 K km s^{-1}.

intervals. These channel maps help us to examine the gas distribution in the filament for a given velocity interval. Panel (a) shows the channel map in $C^{18}O$ emission from 0.5 to 2.0 km s^{-1}. The north-eastern part of the complex shows very bright emission in contrast to the southern and western parts of the complex which is devoid of any significant $C^{18}O$ emission. The next panel (b) shows the emission in the velocity range 2.1-3.0 km s^{-1}. We notice that this velocity range covers almost the full complex with a good correlation with the extracted filaments (shown in white solid lines). Panel (c) shows the $C^{18}O$ emission in velocity range 3.1-4 km s^{-1}. This map is selectively showing brighter emission towards the southern most part of the complex. However, the northern part of the complex shows $C^{18}O$ structures. Overall, the $C^{18}O$ gas is distributed from north-east to south-west in velocity space. The north-east region is blue-shifted while south-west region is red-shifted with respect to systematic velocity

of the cloud. The distribution of $C^{18}O$ lines is almost clumpy tracing high density regions. The study of individual regions and their corresponding spectra will be discussed further in detail.

The regions in the whole complex show different morphology and state of star formation. While eastern part of complex shows comma shaped structures and two YSOs, the southern part contains V source, which is likely a brown dwarf candidate (Kauffmann et al., 2011). The northern eastern region has PV Cep at the top but no star formation is going on in the extended parallel structures. Considering different state of star forming activity in the complex, the region is divided in three parts as shown in Fig. 6.1: L1155 (identified as I), L1152 (identified as II) and L1148 (identified as III).

6.3.3 Gas kinematics of filaments in L1155 region (I)

The region I contains five filaments F7, F8, F9, F12 and F14 extracted using Filfinder and are mostly aligned towards the north-east direction. All of them hosts a number of cores.

This region contains a Herbig star called PV cep towards the extreme north which shows a filament F15 and core C26. To understand the gas and dust column distribution, we plotted the kinematic parameters from $C^{18}O$ line and dust in Fig. 6.6. We estimated H_2 column density from Herschel data and to compare the $C^{18}O$ gas properties, the emission from both should be taken at same pixel grid. The *Herschel* grid, at a resolution of 36″ is convolved to TRAO beam size at 44″. The whole $N(H_2)$ map was regridded to pixel grid of TRAO, at 20″. This filament is oriented towards north-eastern part of the cloud. The cloud shows a tail like structure extended towards the south direction. The bottom part of the cloud lies at blue-shifted velocity with respect to v_{lsr} of the cloud, $\sim$ 2 km s^{-1}as seen in channel maps. All the positions along the filament show intensities greater than 3σ in $C^{18}O$ emission. We plotted dust column density in panel (a) and dust temperature in panel (b). The values of $N(H_2)$ ranges from 2-8 $\times$ 10^{21} cm^{-2}. The average column density is 4 $\times$ 10^{21} cm^{-2} with a dispersion of 2 $\times$ 10^{21} cm^{-2}. The dust temperature shown in panel (b) shows less values towards both the ends of F26 with peak around core position but higher at core position ($T_d \sim$ 16 K) since it is a protostellar core. The values range from 14 to 16 K with mean value as 14 K and dispersion as 1 K. PV Cep is a bright Herbig Ae/Be star situated towards north-eastern part of the cloud. Goodman & Arce (2004) found that this is moving with high velocity and has escaped from the NGC 7023 nebula studied in previous chapter. The centroid velocity as shown in panel (c) ranges from 2.4 to 2.7

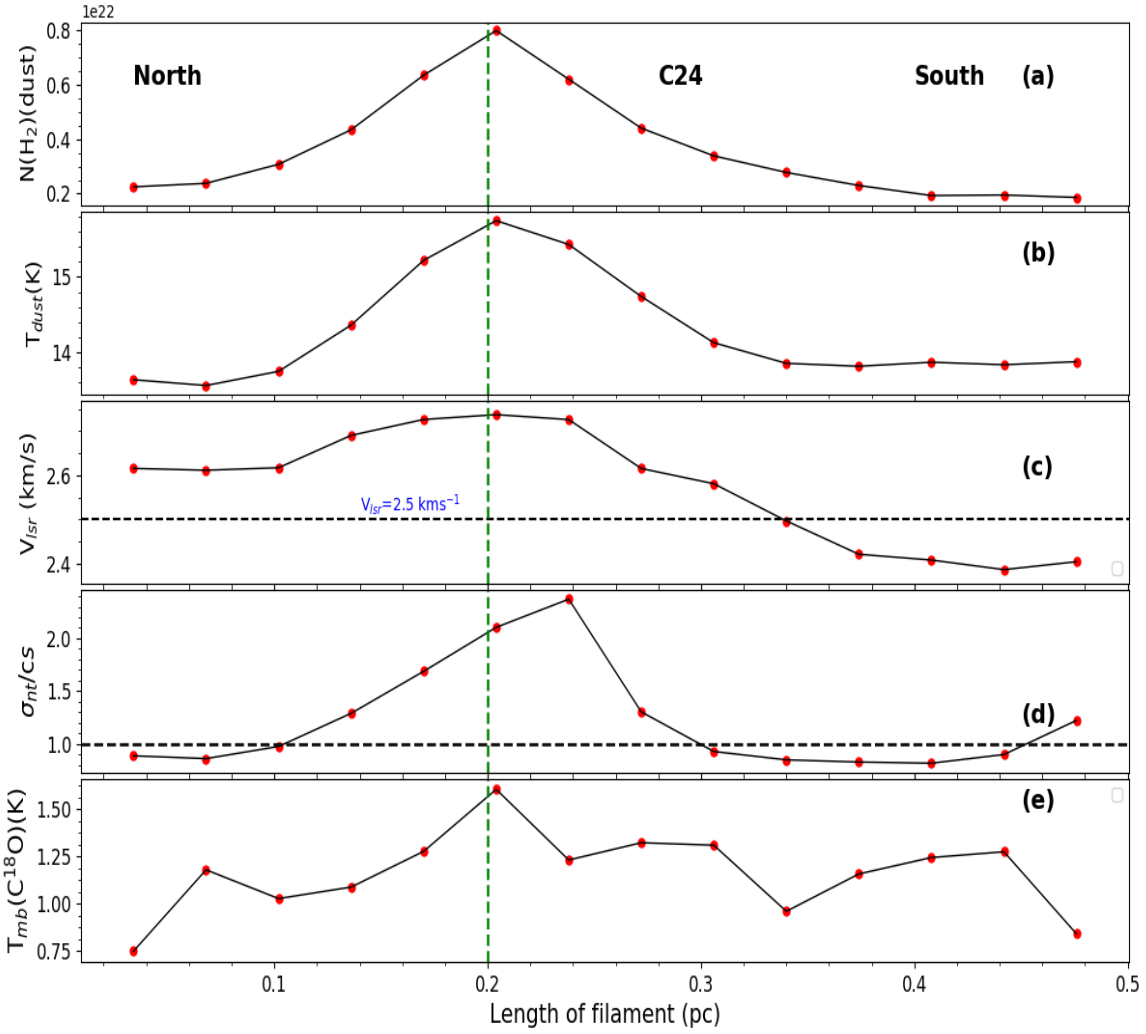

Figure 6.6: Dust and gas properties for filament containing PV Cep star. (a) Variation of dust column density as a function of distance along the filament. The extreme northern part is taken as the reference. (b) Variation of dust temperature along the length of filament. (c) Centroid velocity in red filled circles. The black dotted line shows the systematic velocity of the cloud. (d) Variation of Mach number (σ_{nt}/c_s) (e) Main beam temperature from the $C^{18}O$ line.

km s^{-1}. This filament possesses a mean centroid velocity as 2.6±0.1 km s^{-1}. The central velocity of the ambient gas which is associated with the cloud having PV Cep source is 2.5 km s^{-1}(Cohen et al., 1981) using CO observations. The horizontal line in panel (c) denotes systematic velocity of the cloud. The top part of the filament shows red-shifted velocity and decreases down towards the length of filament.

The variation of Mach number is shown in panel (d). The gas motions around peak of core is highly turbulent as the Mach number, M ≥ 2 around the extent of core whereas the ends of filament shows subsonic motions with M 1. The details about non-thermal motions used in calculation of Mach number are given in Chapter 3. The main beam temperature, T_{mb} (panel (e)) ranges from 0.75 to 1.5 K. The peak at ∼ 1.5 K is seen at position of core.

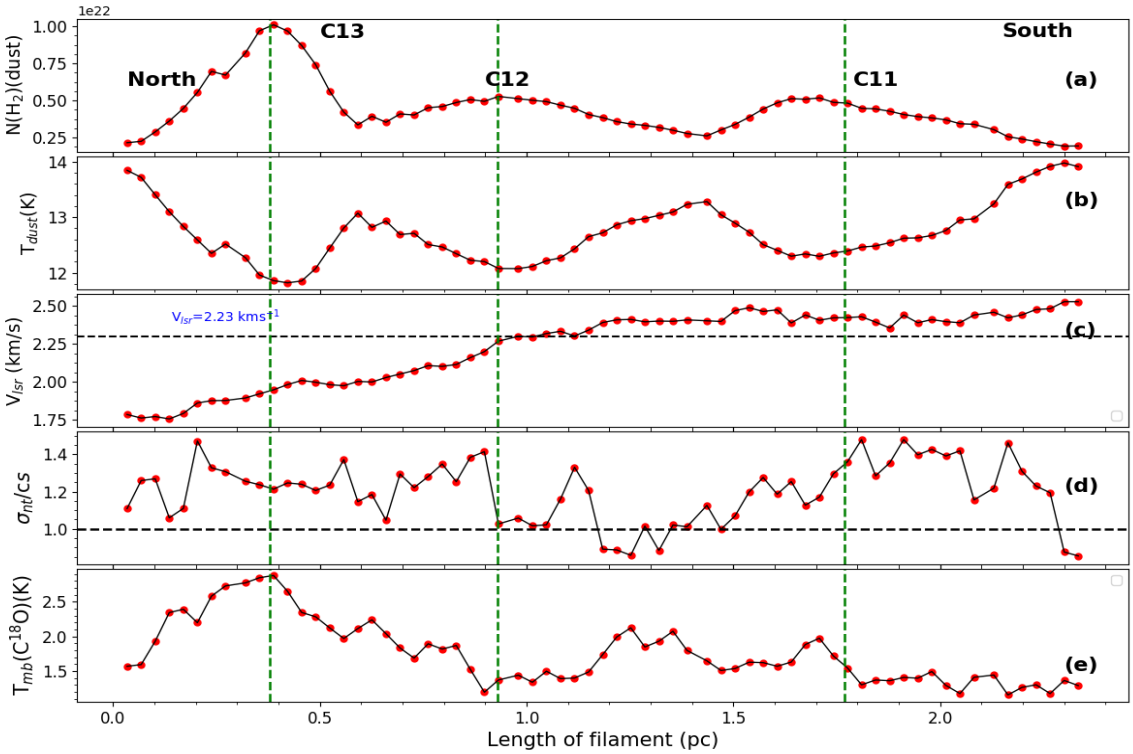

Figure 6.7: Dust and gas properties for filament containing L1155E, F7 filament. The details about each panel is same as given in Fig. 6.6.

The region towards extreme east of complex containing L1158 cloud, also called L1155E and referred as F7 in this work. Three cores C11, C12 and C13 are embedded on this filament. The average spectrum of this region shows single component in ^{13}CO line except at few positions along the skeletons. All the positions along the crest of filament show spectral profiles in both the lines having emission greater than

3σ emission. This part was considered as one of the regions in MAMBO mapping using 1.3 mm continum emission which also discusses the presence of three clumps (Kauffmann et al., 2008).

We present the comparison of dust and gas properties in Fig. 6.7. The dust column density ($N(H_2)$) shown in panel (a) shows multiple peaks in the variation along the filament and the peak positions coincides with the position of cores which are embedded in the filament. The maximum $N(H_2)$ is 1×10^{22} cm^{-2} at the position of C13 and minimum is 0.25×10^{22} cm^{-2}. The dust temperature, T_d in panel (b) is higher towards the northern edge and southern edge with decrease in values towards the position of cores. Mean T_d is 12.7±0.5 K. The range of T_d is 12-14 K.

By fitting a single Gaussian component to the $C^{18}O$ profiles, we derived the best fit parameters at each pixel along the skeleton of the filament. Panel (c) shows the centroid velocity at each pixel along the crest. For the purpose of comparison, the V_{lsr} of the cloud is taken as the average of all the centroid velocities which is obtained using Gaussian fitting for all the pixels in the skeleton (shown in black dotted line). The average $V_{lsr} \sim 2.23$ km s^{-1}. Some of the profiles show double component in ^{13}CO lines, however this analysis considers only the profile lying around the systematic velocity of the cloud. There is a steep gradient in the velocity values starting from 0.034 pc to 0.9 pc and then the velocity becomes constant till 2.5 pc length. The best fit value, V_{lsr} ranges from 1.75 to 2.5 km s^{-1}. Panel (d) shows the distribution of the Mach number which tells us that the filament is almost overall transonic with the values ranging between 0.8 to 1.5. The main beam temperature, T_{mb} obtained from $C^{18}O$ line is shown in panel (e). The initial parts of the filament till 0.4 pc shows higher temperatures (~ 2-2.5 K) and then gradually falls along the length. The core C13 shows the highest peak of $T_{mb} \sim 2.8$ K but other cores does not show brighter $C^{18}O$ emission. The range of $T_{mb} \sim 1$ to 2.8 K. The region lying nearer to L1155E filament, F8 shows a curved structure with one end extending towards the northern part of the complex. Fig. 6.8 shows the color composite image where red is channel map from 2.3 to 4 km s^{-1}, green is dust column density map and blue is moment0 map of $C^{18}O$ line integrated from 0.5 to 2.2 km s^{-1}. After inspecting the spectral cube data, we plotted average spectrum of the region around L1155 as shown in Fig. 6.8 (bottom right inset). There is presence of two velocity components in the L1155 region which are separated by more than 2-3 channels of velocity resolution. This implies that there are two cloud components present along the line-of-sight. One of the components in $C^{18}O$ line is lying at 1.5 km s^{-1}and other at 2.9 km s^{-1}. Most of the region in arc like emission possessing two components of cloud along the line-of-sight. In the

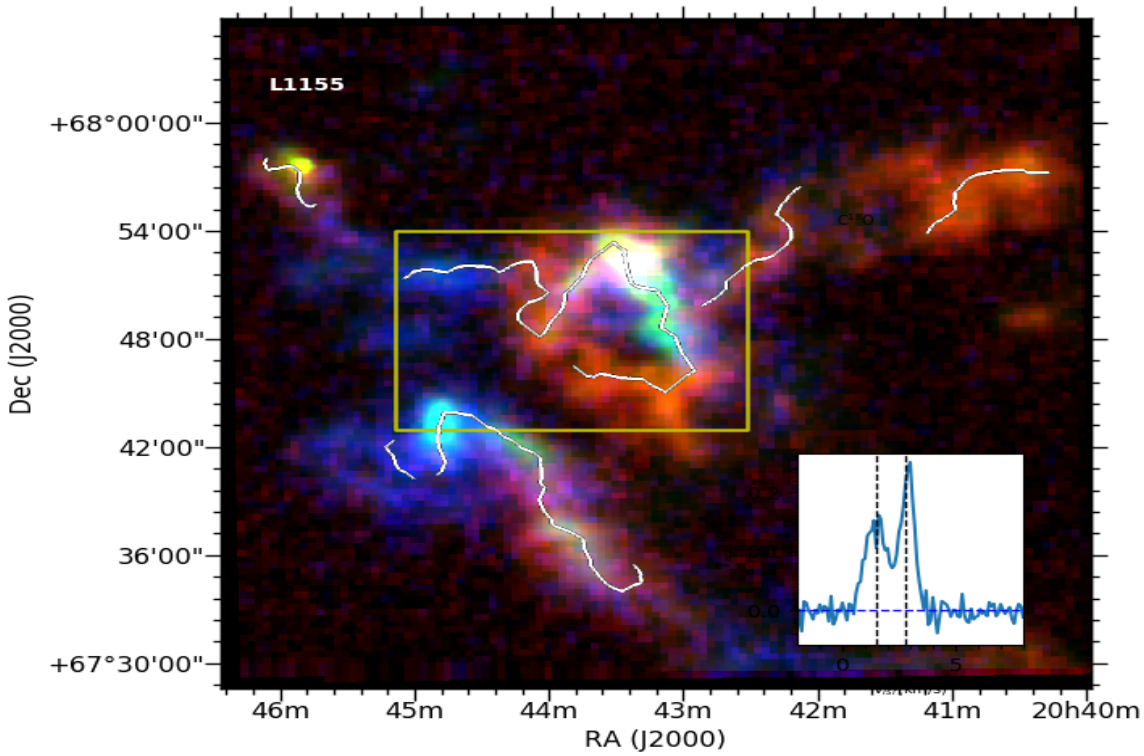

Figure 6.8: Color composite image of L1155 region ($15' \times 15'$) where red is the channel map taken from 2.3-4 km s^{-1}, green is dust column density and blue is 0.5-2.2 km s^{-1}. The bottom right panel shows the average profile in the marked region for $C^{18}O$ emission.

integrated intensity map of $C^{18}O$ line, the total emission will be summation of these two components. To disentangle the spatial distribution of two velocity components along the marked rectangular region, we made moment 0 maps in two different ranges. The northern branch of this filament does show only emission in velocity range 2-3 km $s^{-1}$where the curved part has emission from both the components although brighter in red channel 2.3-4 km s^{-1}. We studied the kinematics of two velocity components separately using dust and gas emission along the line-of-sight.

Harjunpaa et al. (1991) has studied this L1155 region using point switching observations using FCRAO telescope using ^{13}CO (1-0) line. The eastern part of the cloud, L1155C- C1, C2 shows two components 2.6 km $s^{-1}$and 4.1 km s^{-1}using NH_3 observations. The integrated intensity images shows high different high density structures in $C^{18}O$ map which not necessarily coincides with the high density peaks. We checked different velocity intervals if that is an overlap or velocity coherent structures.

To disentangle the velocity structure of these cloud components, we studied the gas properties separately. Fig. 6.9 shows the comparison of gas properties in two cloud

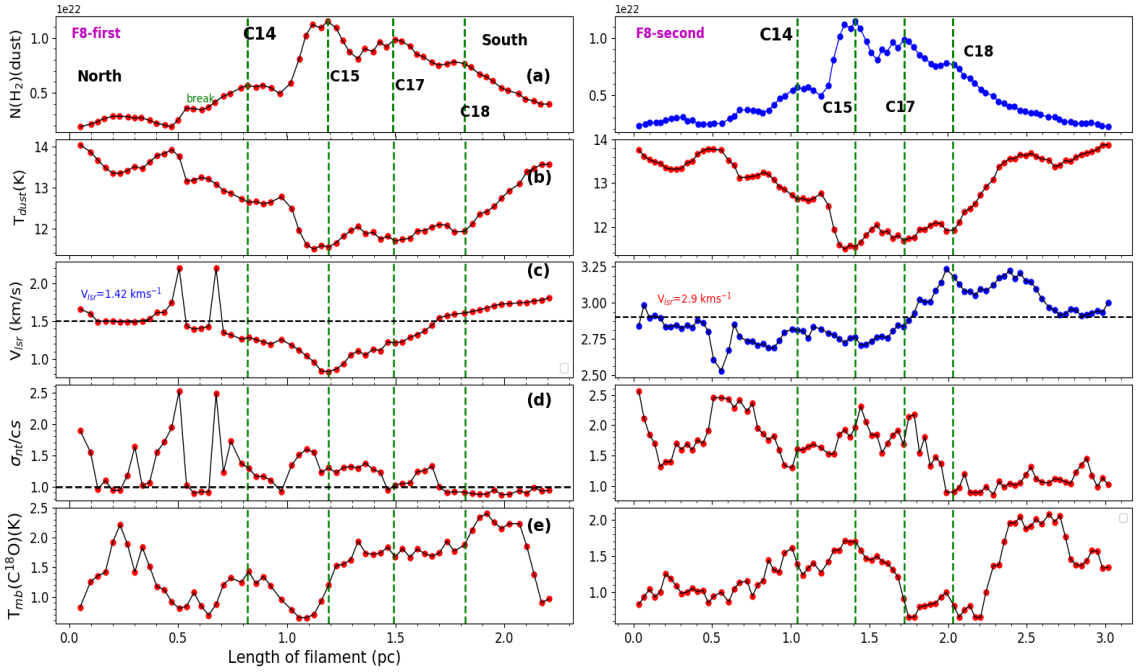

Figure 6.9: Dust and gas properties for filament containing L1155E, F8 filament containing two cloud components along the line-of-sight.

components with total dust emission present. We found that the first component is at lower velocities around 1.4 km s^{-1}. Left panel shows the properties along the first component. All the positions along the crest do not have emission greater than 3σ from the blue-shifted cloud component. There is break towards the north east branch at a distance of 0.5 pc (shown in Fig. 6.9). First two panels show the distribution of dust column density and temperature. Out of all four cores, C15 shows the maximum column density of around 1.1 $\times$ 10^{22} cm^{-2}. Both the ends of the filament show higher temperature. There is a gradient in velocity $\sim$ 1.0 km s^{-1}pc^{-1} along the filament length starting from distance of 1.2 to 2.2 pc. In panel (d), there is a very high mach number at the position of break.

The filament, F9 towards the western side in this region is aligned 90°. Fig. 6.10 shows the comparison of dust and gas properties along the length of filament. The front edge of the filament (towards east) is taken as the reference. The column density from dust in panel (a) shows that the values range from 1.7 to 2.96 $\times$ 10^{21} cm^{-2} with an average of 2.4$\pm$0.3 $\times$ 10^{21} cm^{-2}. The dust temperature in panel (b) shows that the eastern branch is cooler than the western branch. T$_d$ ranges from 13.8 to 14.4 K and mean is 14.1$\sim$0.2 K. The third parameter from gas emission varies from 2.9 to 3.2 km s^{-1}and average centroid velocity is 3.0$\sim$0.1 km s^{-1}. Panel (d) shows the variation of Mach

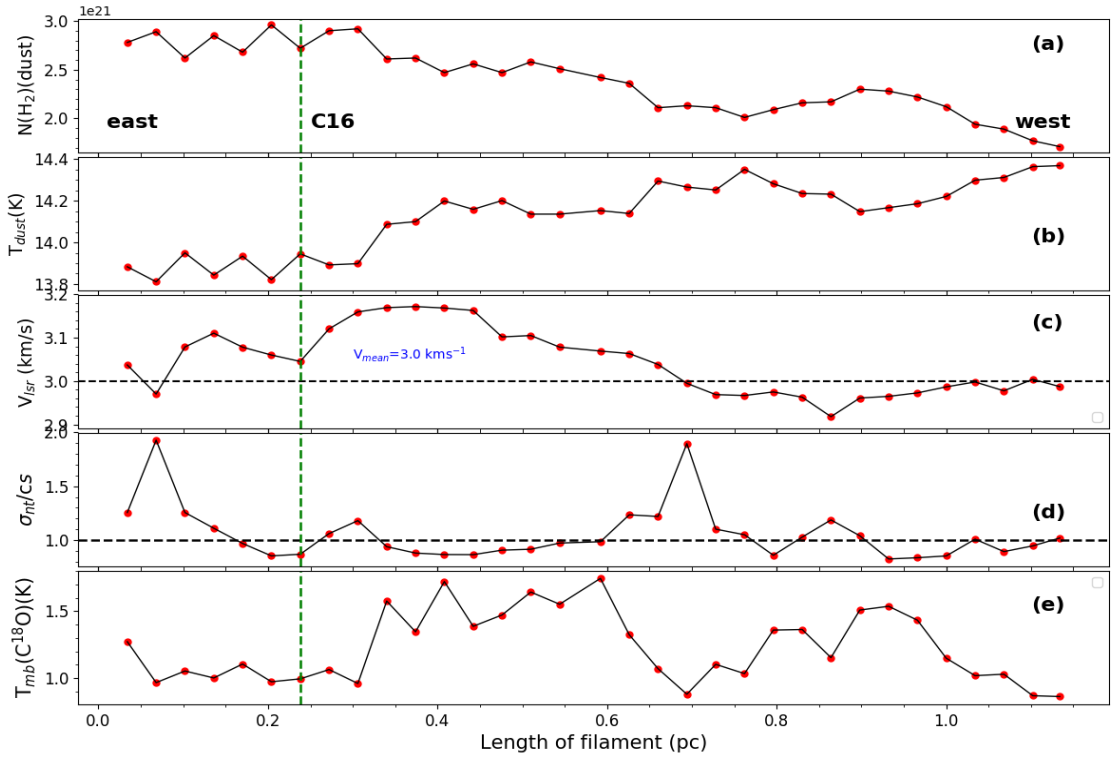

Figure 6.10: Dust and gas properties for filament F9 filament.

number where the value approaches a value of 2 at 0.1 pc and then goes to subsonic values with M less than 1.0. The range of Mach number is 0.82 to 1.93. Mean Mach number is 1.05±0.25. T_{mb} varies from 0.86 to 1.74 K with mean value as 1.23±0.26 K. The middle part of filament shows higher temperature as compared to the extreme ends.

6.3.4 Gas kinematics of L1152 complex filament (II)

This region II contains four filaments F10, F11 (L1152 cloud) and F13 (L1157 cloud) (see Fig. 6.1. The region around L1157 filament, F13 has already been studied in detail in chapter 5 using a set of tracers, ^{12}CO , $C^{18}O$, N_2H^+ (1-0) observations. There are two cores embedded in it where one is protostellar core and other one is starless core. There is another cloud, L1152 identified as F10 which shows tail like structure extending towards extreme west. To understand the velocity field and line emission in comparison to the high density column of dust, we plotted the gas and dust properties together in Fig. 6.11. Panel (a) of Fig. 6.11 shows the variation of H_2 column density and dust temperature along the length of filament. The reference is

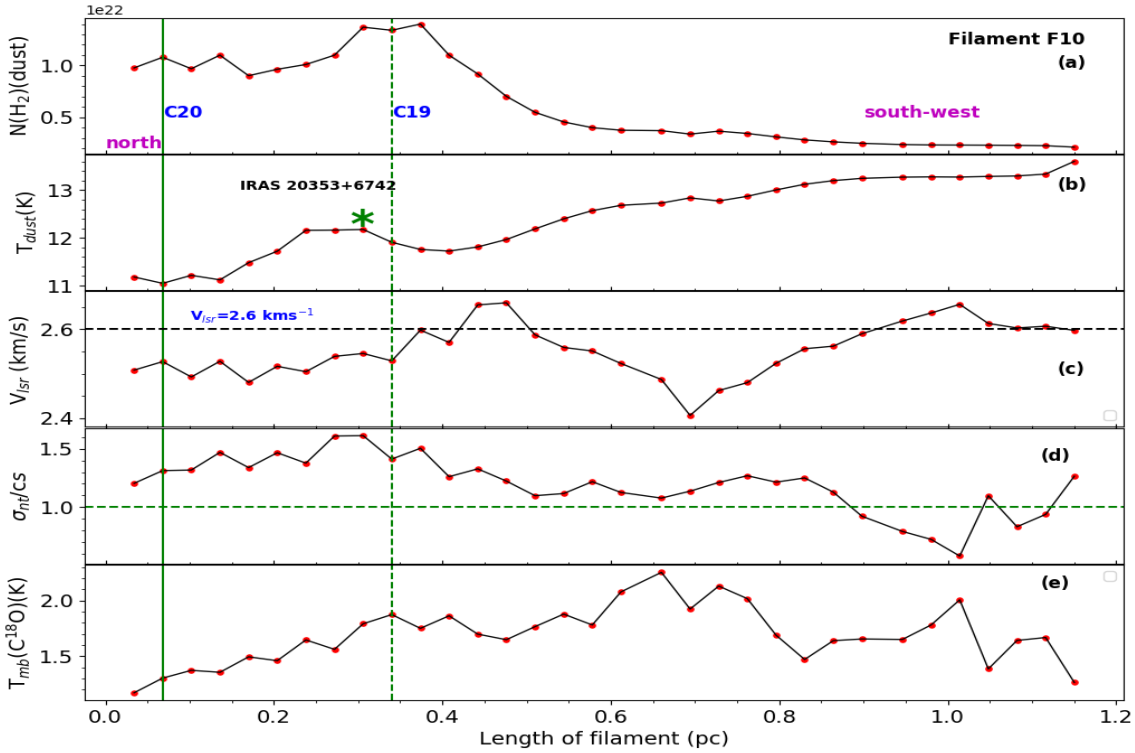

Figure 6.11: Variation of dust parameters and $C^{18}O$ gas parameters as a function of distance along the skeleton line.

taken from north-east region of filament. The $N(H_2)$ values range from 2-14 $\times$ 10^{21} cm^{-2}. The mean $N(H_2)$ is 6±4 $\times$ 10^{21} cm^{-2}. The dust temperature shown in panel (b) ranges from 11 to 14 K. The mean temperature of F3 is 13±1 K. There is an IRAS source (labelled in panel (b)) near C19 which shows an increase in dust temperature.

This filament region exhibits a single velocity component in $C^{18}O$ emission and therefore, there is only single cloud component present along the line-of-sight. The whole spectrum was fitted with a single gaussian function using python programs. We included only those along the high density skeletons where the signal-to-noise (SNR) ratio $C^{18}O$ is greater than 3. We derived the optimum parameters T_{peak}, centroid velocity, velocity dispersion. Panel (C) shows the variation of centroid velocity along the distance of filament. The horizontal line shows the systematic velocity of $\sim$ 2.63 km s^{-1}. Caselli et al. (2002b) calculated the systematic velocity by taking average hyperfine spectrum of N_2H^+ lines over the L1152 cloud. There is sharp change in the velocity of filament at a distance of 0.7 pc. The range of centroid velocity is from 2.3 to 2.7 km s^{-1}.

The third optimum parameter, velocity dispersion was also obtained from gaussian fitting. In order to trace whether the motion along the filament is subsonic or supersonic, we calculated the non-thermal velocity dispersion. Since we have value of dust temperature of each pixel, the non-thermal component was calculated independently at each pixel. Panel (d) shows the variation of Mach number which is ratio of σ_{nt} with respect to isothermal sound speed. We notice a transition from transonic motion to subsonic motion along the length of filament. The Mach number varies from 0.6-1.6. The average mach number is 1.2±0.2 implying the overall motion as subsonic only.

Panel(e) shows the variation of main beam temperature of $C^{18}O$ line. Those identified clumps have been taken for kinematical analysis where it lies in 2-3 velocity channels and the number of pixels over which it is distributed is greater than 3. The maximum value of T_{mb} is higher at 0.7 pc which has higher dust temperature ($\sim$ 13.5 K) present. The regions around core positions do not show peaks in $C^{18}O$ temperature which might be because of depletion in the core. There is a curved high density structure identified as F11, in front of L1152 cloud. The two dust peaks C21 on southern part and C22 on northern side are shown. There is a YSO present on the curved structure. The kinematical properties are shown in Fig. 6.12. The variation of $N(H_2)$ shows two bumps around core positions C21, C22. First half of the plot shows the properties of southern filament and the other half for northern part of F11. The column density ranges from 2.3-7.3 $\times$ 10^{21} cm^{-2}. Average value is 4±1 $\times$ 10^{21} cm^{-2}. There is a break at the centre which has very low density but high temperature around 13 K. The length

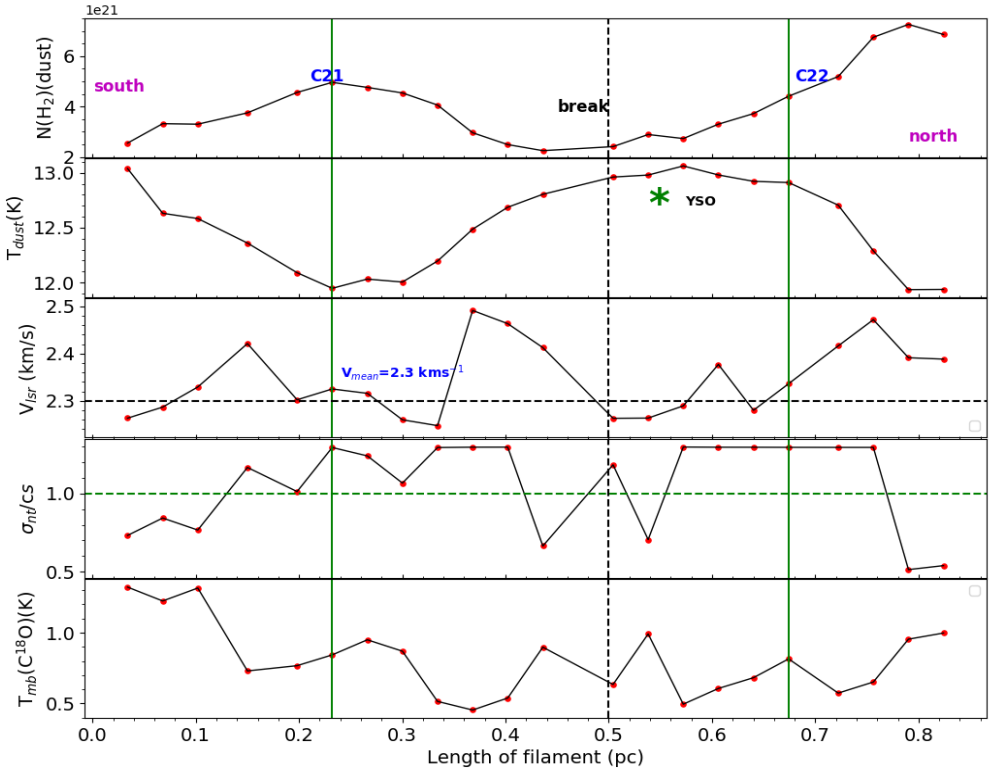

Figure 6.12: Variation of dust parameters and $C^{18}O$ gas parameters as a function of distance along the skeleton line of F11 filament.

of both the filaments is similar. The dust temperature shown in panel (b) range from 12-13 K with average as 12.5±0.4 K. In panel (c), we show the variation of gaussian fitted parameter, centroid velocity which shows many fluctuations along the length. We do not find any unidirectional change in the velocity. The values vary from 2.2-2.5 km s^{-1}. Mean v_{lsr} is 2.3±0.1 km s^{-1}. Mach number shown in panel (d) vary from 0.5 to 1.3 with average as 1.1±0.3. Both the filaments are almost subsonic. The T_{mb} in panel (e) is higher at both the edges of filament with low values at the points in between. Mean T_{mb} is 0.8±0.2 K. The values range from 0.45 to 1.32 K.

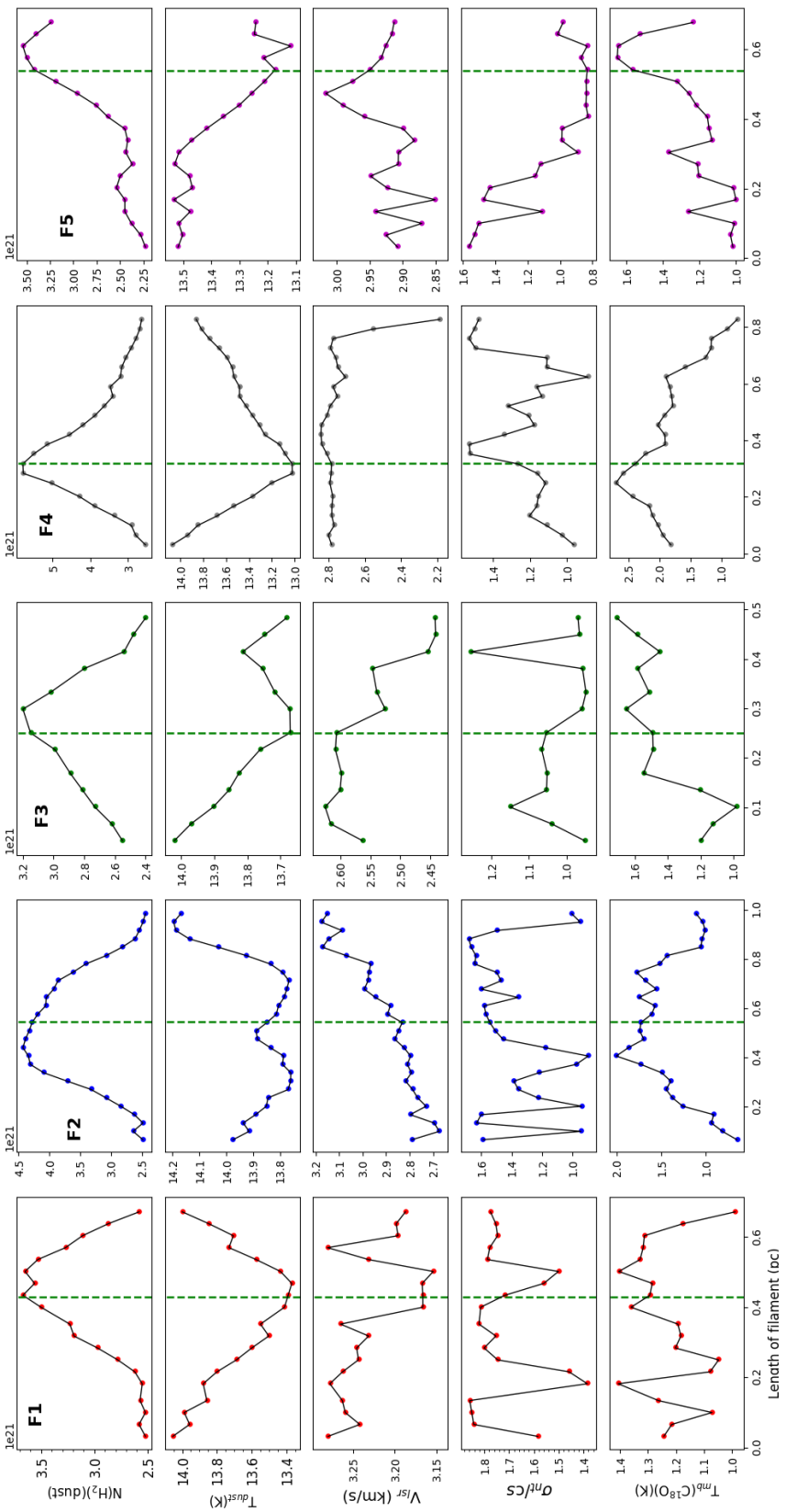

Figure 6.13: *First row:* Variation of dust column density with respect to the distance. *Second row:* Variation of dust temperature with distance. *Third row:* Velocity centroid as a function of position along the length. *Fourth row:* Mach number *Fifth row:* Main beam (T_{mb}) temperature. Vertical green dashed line shows the position of clump in each filament.

6.3.5 Gas kinematics of L1147-L1148 filaments (III)

In this section, we discuss the filaments and cores in region III containing L1147 and L1148 clouds. This region contains parallel high density filaments. The region hosts seven filaments F1- F7 where F7 being the longest with length 2.1 pc. This group of filaments host seven clumps as extracted from Astrodendro algorithm except C9. The physical properties of these cores are tabulated in table 6.1. Four of the clumps identified as C5, C6, C8 and C10 lie on the parallel filaments. There is a protostar L1148-IRS ($L_{int} \sim 0.10$ L$\odot$ (Kauffmann et al., 2011) on F6.

There are a number of shorter filaments F1, F2, F3, F4 and F5 with lengths ranging from 0.4-0.8 pc. The longer ones F6 and F7 have lengths 1.6 and 2.1 pc respectively. We compare the gas and dust properties together for all five filaments in Fig. 6.13. The north-eastern point in each filament is taken as reference which is shown with a filled triangle in Fig. 6.1. The dust and gas properties of filaments F1-F5 are shown in Fig. 6.13. Each column represents the properties of F1 (left) to F5 (extreme right). First row shows the distribution of column density. All the filaments have higher values at the position of core and less dust temperature in second row. There is high temperature on an average towards the ends of all the filaments as compared to the positions around core.

The distribution of centroid velocity for F1-F5 is shown in third row. There is a change in the velocity for F1, F2, F3 and F5 but a constant velocity around 2.8 km s^{-1}in F4. The fourth row presents the distribution of non-thermal motions along the filament lengths. Almost all the filaments show signs of transonic motions with Mach number lying between 1-2. The T_{mb} shown in fifth row for F2, F4 and F5 follows the distribution of dust column density in first row. There is a peak at the position of cores and gradually falls towards the ends of filament. On contrary, F3 shows high T_{mb} towards the whole length of filament except at initial distances (around 0.1 pc). This filament is overall $C^{18}O$ brighter. Similarly, F1 also exhibits higher T_{mb} within an average of $\sim 1.2\pm0.1$ K.

Further, we study the variation of properties along the filament F6 passing through the region containing Very Low Luminosity Object (VeLLO). The elongated structure are aligned towards the south-eastern direction. It harbors three cores, C5 on the left most branch, C6 and C8 on the other parallel branch of F6 where C8 is the protostellar core with a VeLLO. It is defined as an protostellar object with low internal luminosity $\leq$0.1 L$\odot$ which are deeply embeddded in the parent molecular cloud (Dunham et al., 2008).

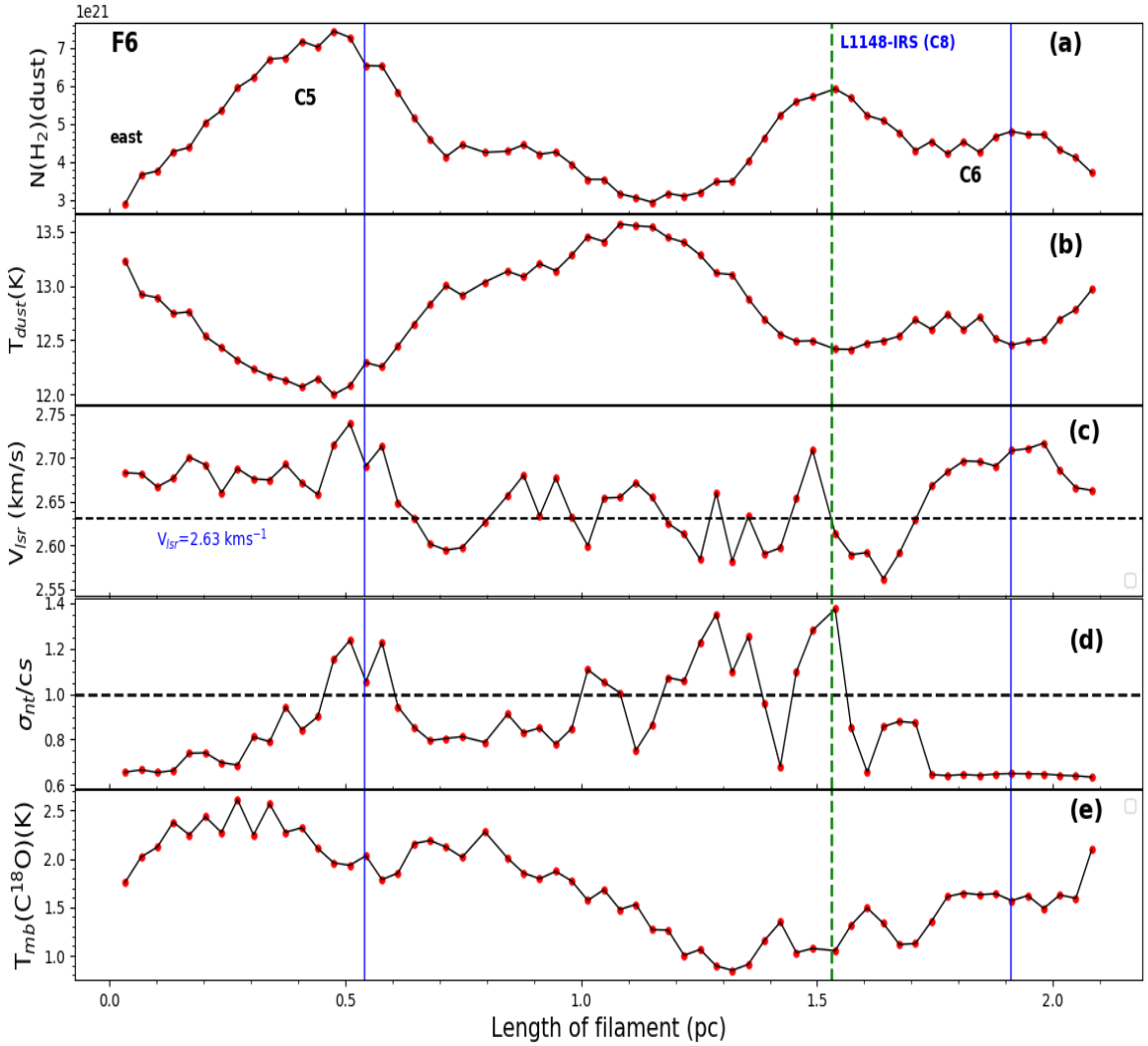

Figure 6.14: (a) Comparison of properties of dust emission and gas for filament F6 (containing VeLLO) with respect to the distance.

L1148-IRS drives a compact CO outflow with length ~ 5 arcsec, about 1800 au in projection. This confirms the presence of L1148-IRS as a clear-cut protostar, and the association was found out through the velocity. The outflow was detected in interferometeric observations using PdBI where single-dish observations using IRAM 30-m telescope did not reveal it.

Fig.6.14 shows the comparison of dust and gas properties along the filamentary region L1147 and L1148 region. Panel (a) shows the variation of gas column density along the length of the filament. The value of dust column density varies from 3-9 $\times$ 10^{21} cm^{-2}. The mean column density is 4.7 $\times$ 10^{21} cm^{-2} with the dispersion of 1.2 $\times$ 10^{21} cm^{-2}. Panel (b) shows the variation of dust temperature along the filament. It shows a dip in

the dust temperature at two positions which corresponds to the derived core positions. The range is from 12-13.5 K with the mean value as 12.8±0.4 K. The centroid velocity of the filament varies from 2.55 to 2.73 km s^{-1}. The V_{lsr} of the cloud has been found out as 2.64 km s^{-1}using N_2H^+ (1-0) observations shown by dashed line in panel (c). The mean centroid velocity over the length of filament is 2.65±0.04 km s^{-1}.

Panel (d) shows the distribution of Mach number which ranges from 0.6 to 1.5. The filament shows supersonic motions around length 0.5 pc at the position of core. The region around L1148-IRS shows the signatures of supersonic non-thermal motions. The Mach number is almost constant from 1.7 to 2 pc distance.

Panel (e) shows the variation of T_{mb} along the length of filament. The value ranges from 0.85 to 2.6 K with the average value as 4.3 K and dispersion as 0.6 K. Around L1148-IRS, it shows a decrease in $C^{18}O$ temperature which could be because of depletion in the core. The region around VeLLO does not show a $C^{18}O$ peak but the dust column density shows density $\sim 6\times 10^{21}$ cm^{-2}. As this is a protostellar core, the gas could have depleted at this position as N_2H^+ (1-0) has been significantly detected in previous studies. The N_2H^+ derived systematic velocity is found out as 2.6 km s^{-1}. The extent of chemical depletion is reported with a factor of 10.

Fig. 6.15 (a) shows the distribution of column density as a variation of distance for filament F4. The dust column density varies from 2.5 to 6.3×10^{21} cm^{-2}. The average column density is 3.7×10^{21} cm^{-2} with a dispersion of 1.1×10^{21} cm^{-2}. Panel (b) shows the variation of dust temperature along the filament. The range of dust temperature is 12-14 K. The mean dust temperature with the standard deviation is 13.5±0.5 K. Panel (c) shows the centroid velocity derived using Gaussian fitting of the spectral line. Some positions along the filament show two cloud components, one at 2.3 km $s^{-1}$and other at 4 km s^{-1}. The values vary from 2.0 to 2.5 km s^{-1}. The average centroid velocity with the standard deviation is 2.26±0.13 km s^{-1}.

The filament is overall subsonic as shown by Mach number values in panel (d). The Mach number, throughout the length of filament, ≤ 1 with the values ranging from 0.6 to 0.9. The main beam temperature using $C^{18}O$ lines (in panel (e)) shows the values from 0.8 to 2.3 K with the average value 1.4 ± 0.4 K. The values starts increasing sharply till 0.7 pc and gradually falls till the extent of core. At distance greater than 1.2 to 1.8 pc, the T_{mb} is almost constant $\sim$ 1 K. Again, there is slight increase at 2 pc with value 1.8 K which is consistent with low dust temperature and high column densities.

Table 6.1: Properties of core derived using Astrodendro algorithm in L1147/L1148 complexes

Core Name	RA	Dec	R	M_{LTE}	M_{dust}	M_{vir}
(1)	(2)	(3)	(4)	(5)	(6)	(7)
	(°)	(°)	(pc)	M⊙	M⊙	M⊙)
C1	309.764075	67.080366	0.135	3.46	3.81	9.15
C2	310.019538	67.080625	0.247	9.36	13.03	13.83
C3	309.893239	67.226624	0.109	1.51	2.22	3.90
C4	310.085909	67.251000	0.300	11.91	16.23	13.77
C5	310.331411	67.344594	0.254	12.10	17.50	10.68
C6	310.141929	67.348062	0.063	0.55	1.28	1.94
C7	309.689979	67.350824	0.115	1.93	2.86	4.81
C8	310.230593	67.379201	0.099	1.32	3.45	4.58
C9	309.214405	67.389465	0.086	1.46	1.42	3.81
C10	310.050928	67.421880	0.311	10.71	24.91	13.68
C11	310.952987	67.613623	0.189	6.58	9.03	8.51
C12	311.070341	67.704293	0.116	2.33	4.16	4.68
C13	311.204999	67.719329	0.144	6.14	9.30	7.04
C14	310.791540	67.814389	0.062	0.30	2.08	2.68
C15	310.810191	67.847507	0.087	1.11	4.21	5.59
C16	310.694808	67.854698	0.080	0.68	1.43	4.81
C17	310.944498	67.857452	0.068	1.10	1.82	4.28
C18	310.860393	67.879159	0.100	2.86	6.30	7.59
C19	308.931913	67.879500	0.067	1.51	3.60	4.85
C20	308.980030	67.900564	0.067	0.93	3.21	4.00
C21	309.114465	67.904509	0.121	1.37	3.06	6.63
C22	309.045104	67.944824	0.136	1.05	3.79	6.86
C23	310.107876	67.955645	0.094	1.85	1.83	3.38
C24	311.484225	67.956964	0.113	1.95	4.01	6.08
C25	309.839377	67.988246	0.103	2.32	4.33	3.26
C26	309.783878	68.032479	0.137	2.98	10.19	5.84

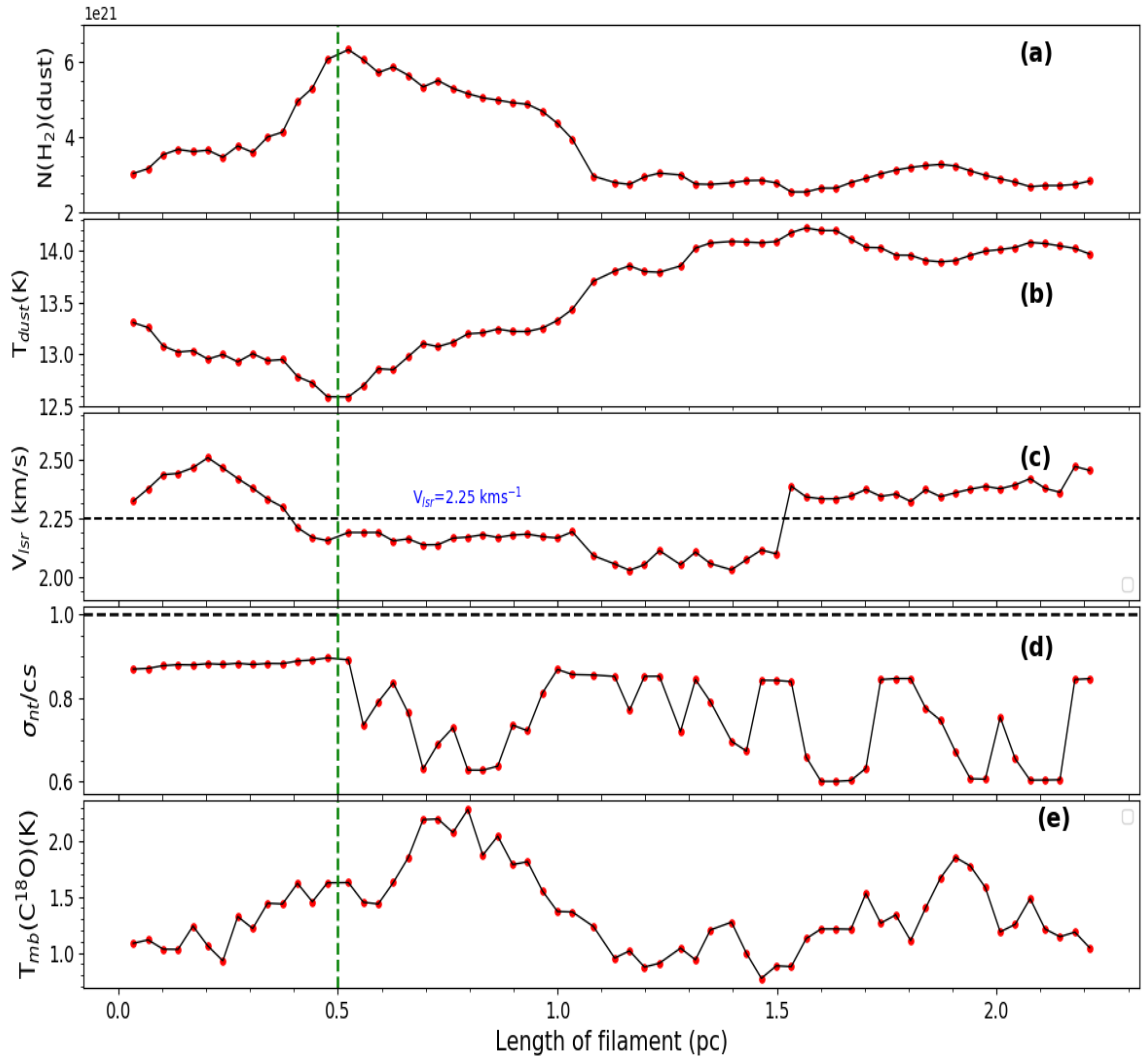

Figure 6.15: (a) Variation of dust column density along the skeleton of filament F7. The x-axis is the distance with the northern part as the reference. (b) Variation of the dust temperature with distance. (c) Centroid velocity (d) Mach number (e) Main-beam temperature

6.3.6 Core properties

Fig. 6.1 shows the distribution of the extracted cores in the L1147/1158 complex using *Astrodendrogram* algorithm. Table 6.1 shows the summary of the positions, size and kinematical properties of the extracted clumps derived using dust and gas observations. The positions of the clumps, RA and Dec are the centroid positions of the peak column densities as shown in Column 2 and 3. The size is given by the effective radius in column 4 which is geometric mean of major and minor axis derived from the algorithm. ^{13}CO traces the gas with densities between 10 and 10^4 cm^{-3}, as

the line becomes optically thick at the dense regions above this densities (Pineda et al., 2008). This density makes it an appropriate tracer to estimate the turbulent pressure of the medium around dense cores. $C^{18}O$ line traces the densities above 10^4 cm^{-3} and an important tracer to understand the kinematics of high density regions. After applying Astrodendrogram on the dust column density map, we derived a sample of 26 clumps and their physical properties. The fitting parameters V_{lsr} and δV for $C^{18}O$ lines allow us to examine the global velocity structure of the gas along the line-of-sight and across cloud spatial structures. At the typical densities higher than 10^4 cm^{-3}, we used ^{13}CO (optically thick) and $C^{18}O$ (optically thin) line to calculate the Local thermal equilibirium (LTE) parameters like excitation temperature, optical depth and hydrogen column density (see section 3.3.2). We determine the excitation temperature from the peak antenna temperature from ^{13}CO line at each pixel assuming that the ^{13}CO is optically thick. Column 5 shows the LTE gas mass of each core. The largest uncertainty in the column density can come from the excitation temperature of the ^{13}CO line. The hydrogen column density involves a conversion factor to convert from $C^{18}O$ column density. This conversion factor may vary significantly with respect to the excitation, abundance, opacity and resolution. For milky way, with a number of observational studies, a factor of $X_{CO} = 0.5 \times 10^{20}$ cm^{-2} (K km $s^{-1})^{-1}$ was recommended for the clouds within 500 pc of the galaxy with an uncertainty of a factor of 2 (Bolatto et al., 2013). The excitation temperature derived is an upper limit since the line may get saturated. The masses derived from $C^{18}O$ and ^{13}CO lines are smaller than dust emission by a factor of 4. We calculated virial mass (column 7) for each clump assuming a spherical density distribution. Hence, the total mass of each clump was found by summing up the pixels within the extent which is twice the FWHM size of each source.

Fig. 6.16 shows the average profiles of all the cores obtained in ^{13}CO (shown in blue) and $C^{18}O$ (shown in red) emission. Some of the cores show single peaked profile in $C^{18}O$ line which means there is a single cloud component present along the line-of-sight. While there are cores which show multiple components in optically thin $C^{18}O$ line like core C14, C15, C16, C17 and C18.

Fig.6.17 shows the distribution of mass and radius of all the clumps extracted in the complex. More number of cores are distributed towards the eastern part of the complex. The value of mass ranges from 0.3 to 12 $M_\odot$. The size of cores which is the effective radius in the table ranges from 0.06 to 0.25 pc. This range of sizes is well consistent with typical core sizes given in Bergin & Tafalla (2007) (0.03-0.2 pc). The typical

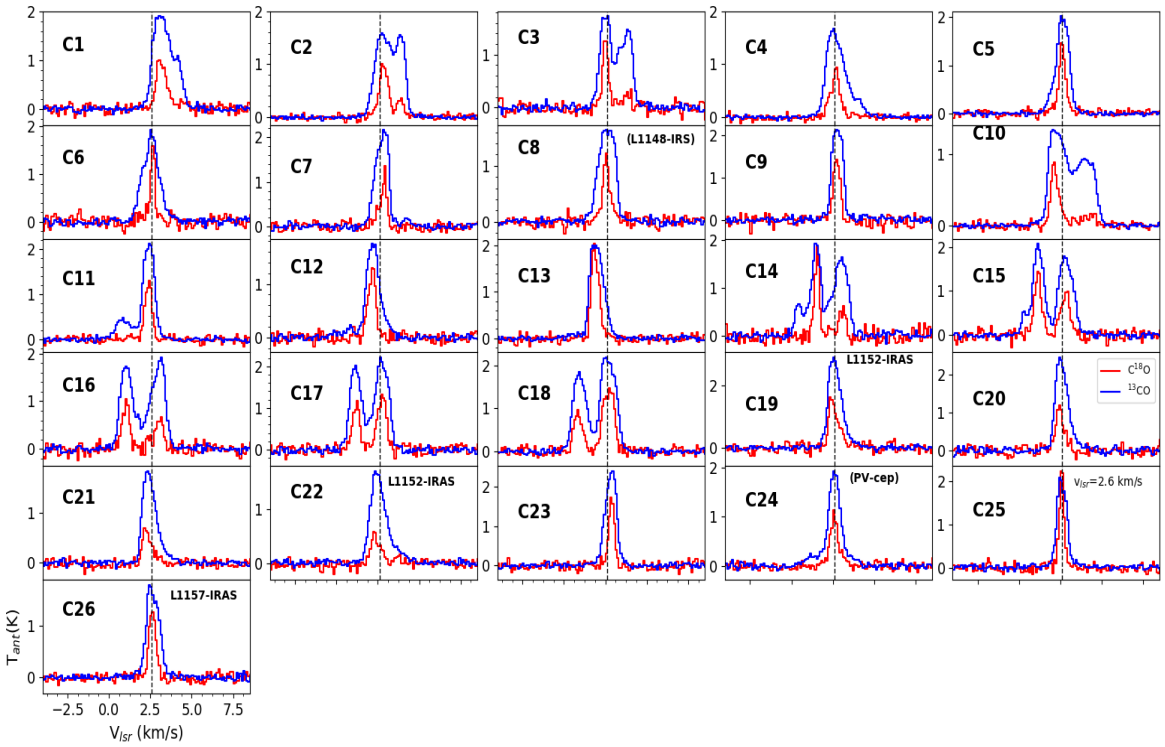

Figure 6.16: Average profiles of all the extracted cores. Red spectrum shows $C^{18}O$ emission and blue shows ^{13}CO emission.

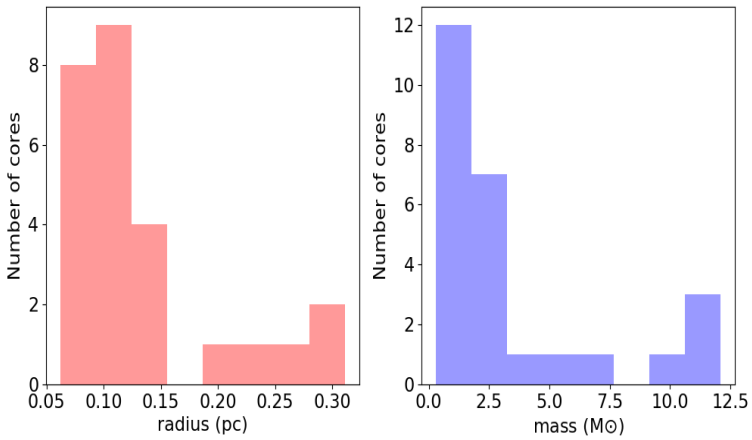

Figure 6.17: Histogram of mass (left) and radius (right) for all the cores.

uncertainties are due to the error in Gaussian fitting. We assign the scales of 0.5 pc or above as belonging to the cloud.

6.4 Discussion

We estimated the kinematical properties of cores and filaments using ^{13}CO and C^{18}O (1-0) line observations. As mentioned earlier, the region was divided into three parts based on the star forming activity. We characterised the velocity structure of the filaments and found that some of the filaments are velocity coherent whereas some of them exhibit a velocity gradient along the length of filaments.

All the regions in this complex show different physical conditions. The first region is part of the north-east branch having PV cep at the northern most part of the cloud. We have analysed the gas properties of this region and found that the single filaments appearing in dust continum emission are not from a single cloud component rather two cloud components along the line-of-sight. One cloud component is at 2.2 km s^{-1}and other one at 3.8 km s^{-1}. It could be two cloud cores with an orbiting motion. The filament F7 forming the sharp edge of the boundary contains three cores along the length of filament. The second filament towards the eastern side, F8 shows two components of cloud along the line-of-sight. There are four cores along the filament.

The other two filaments are aligned perpendicularly to F7 and F8 with relatively shorter in length. The magnetic field structure is shown in Fig. 6.18 where *Planck* polarization vectors are shown in cyan lines. The vectors are perpendicular to the filaments except F9 and F10. The mean polarization fraction is 4.5% ± 1.4% and the polarization angle along with the standard deviation is 131°±10°with respect to the north towards east.

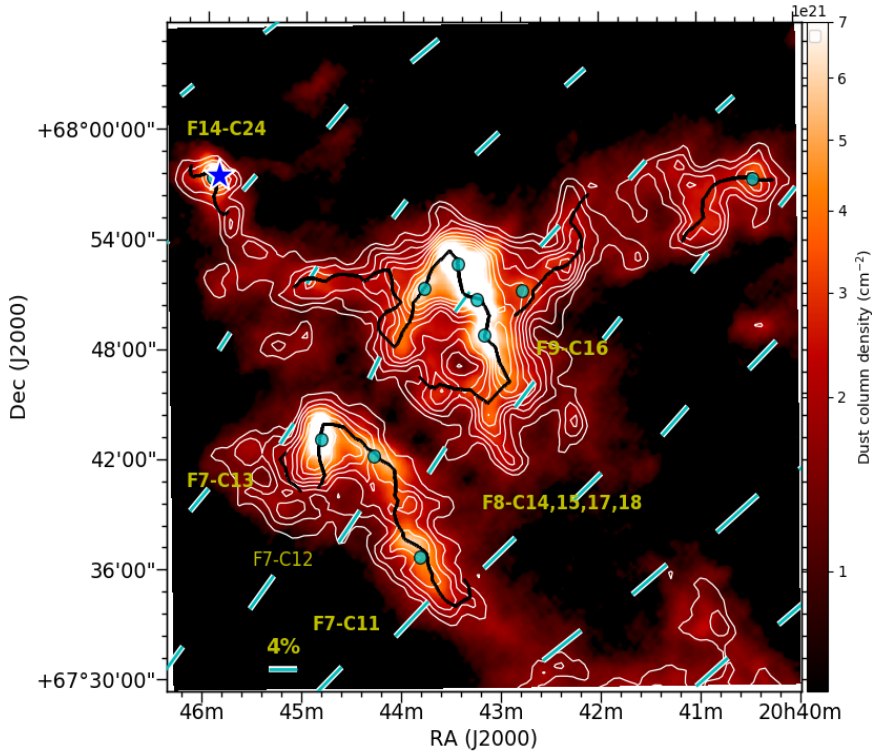

Figure 6.18: The dust column density map for I region containing L1155 cloud and PV cep star. The cyan lines show Planck polarization vectors. Blue line show the skeletons of F7, F8, F9, F12 and F14. White contours are the integrated intensity emission using $C^{18}O$ lines. The levels range from 0.15-0.69 K km s^{-1}in steps of 0.06 K km s^{-1}.

Fig. 6.19 shows the integrated intensity map of $C^{18}O$ overplotted over dust column density map of L1152 complex. The high density skeleton of extracted filaments and cores are shown with blue lines and cyan filled circles. We used the emission from velocity value -0.5 to 4.3 km $s^{-1}$where the signal is greater than 0.1 K. The high density skeletons are well traced by $C^{18}O$ integrated emission. There are three filaments in this region with the clumps embedded.

We note that the peaks in $C^{18}O$ emission towards the tail of F10 are not consistent with the present dust emission. The Planck polarization vectors on the dust column density image are shown with cyan vectors. The mean polarization fraction is $6\% \pm 2\%$ and mean magnetic field as inferred from the Planck polarization vectors is 131±9°with respect to north. The orientation of the filaments, F10 and F13 as given by Filfinder is 80°and 82°, respectively with respect to north. The length of both the filaments is similar ~ 1 pc. F11 is at the front edge of F10 with two clumps at both the branches. The distribution of non-thermal motions in F10 is between subsonic to transonic. The simple consequence of presence of transonic nature of non-thermal nature is that these could be playing role in supporting the cloud

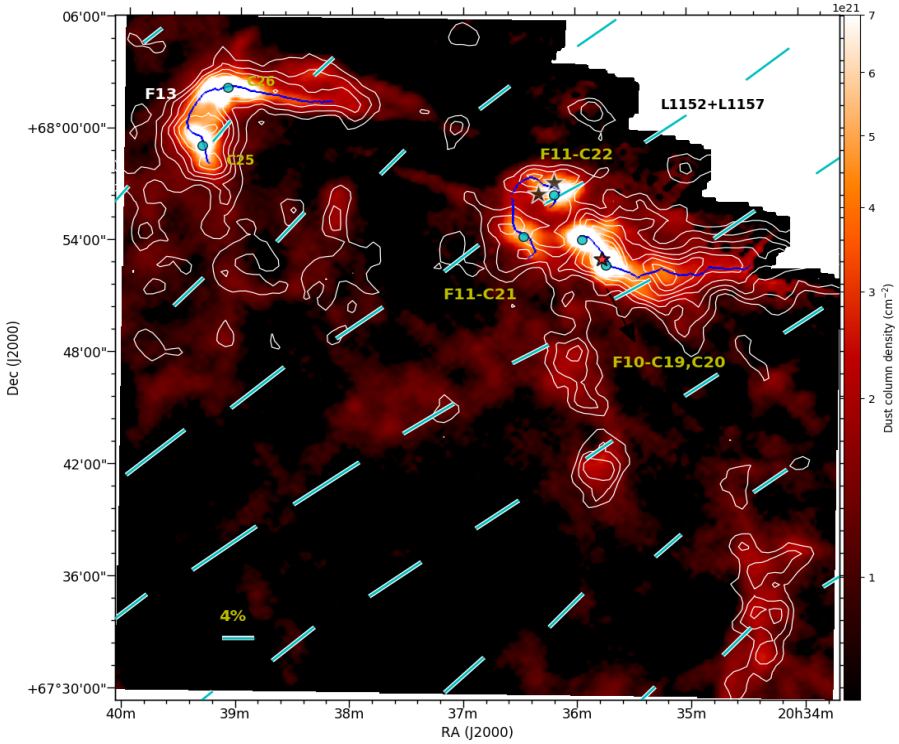

Figure 6.19: The dust column density map for II region. The cyan lines show Planck polarization vectors. Blue line show the skeletons of F10, F11, F13. White contours are the integrated intensity emission using $C^{18}O$ lines. The levels range from 0.15-0.69 K km s^{-1}in steps of 0.06 K km s^{-1}.

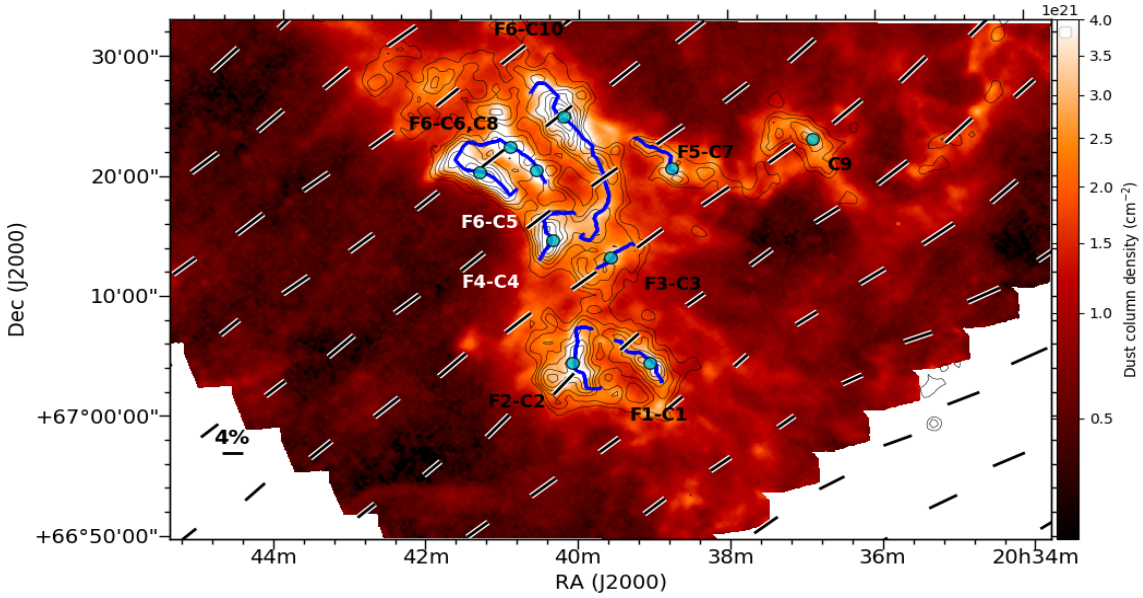

Figure 6.20: The dust column density map for III region. The cyan lines show Planck polarization vectors. Blue line show the skeletons of F10, F11, F13. White contours are the integrated intensity emission using $C^{18}O$ lines. The levels range from 0.15-0.69 K km s^{-1}in steps of 0.06 K km s^{-1}.

against gravity. This contribution is likely to happen if the resulting turbulent motions are created from local microscopic motions of gas molecule which is responsible in supporting cloud against gravity (Chandrasekhar & Fermi, 1953).

This region shows three parallel filaments which are aligned in similar way like the ones in region I. Though there are some smaller filaments towards the extreme south of the region. The mean polarization fraction is $6\% \pm 1\%$ and polarization angle with the standard deviation is $131^\circ \pm 7^\circ$with respect to the north towards east. We did not find any twisting of magnetic field lines in this complex with the same orientation in all three regions.

The velocity dispersion in small five filaments towards the south of complex show almost transonic nature throughout the length of filaments. To find out mass of the complex, we summed up the pixel values within a contour of 1×10^{21} cm^{-2}. The total mass of the cloud is found out as 720 $M_\odot$. The filaments found in this complex are not related to a group of velocity coherent fibers unlike Taurus molecular cloud, NGC 1333 rather smaller filaments with a gradient in the velocity. The gas is in more earliest stages of star formation as there are more prestellar cores as compared to the protostellar cores. Although the filaments and cores exhibit almost similar velocity structures, there are localised gas motions in the form of longitudinal velocity gradients.

6.5 Conclusions

We present the high resolution detailed study of the L1147/1158 complex using ^{13}CO and C^{18}O (1-0) lines by combining with the dust properties using Herschel data. The main conclusion from our study are as follows. We extracted 14 filaments of the full complex using *Filfinder* algorithm. The length of filaments range from 0.4 to 4 pc with average length as 4 pc. We extracted 26 clumps using *Astrodendro* algorithm which are distributed over north-eastern, south-east and north-east parts of the cloud. The kinematics of almost all the clumps show non-thermal motions from subsonic to transonic along their length. Few filaments show velocity gradients along the length of filaments. The cloud presents different kinematical properties and different environmental conditions in the full complex. Morphologically, the south-west and north-east boundary of the cloud seen in dust well as gas emission shows a sharp edges. The regions around L1157 and L1152 cloud also shows tail like features which could be in the effect of a common physical mechanism. We also found out a similar preferential distribution of material towards east in L1172/L1174 complex. The morphology and orientation of the clouds and the cores inside them would contribute to the mechanism underlying their formation and evolution. The detailed study on the orientation of the clouds and their cores will be discussed in the next chapter.

Chapter 7

Kinematics of star-forming molecular clouds in Cepheus Flare Region

7.1 Introduction

The detailed velocity structure has been studied in previous chapters using molecular line data. The front side (north-western side) of the complex show sharp edges. One of the mechanisms proposed for the formation of filamentary molecular clouds is the converging flows (e.g., Ballesteros-Paredes et al., 1999; Hennebelle et al., 2007; Hennebelle & Pérault, 1999; Inoue & Inutsuka, 2009; Vázquez-Semadeni et al., 2006) driven by stellar feedback or turbulence. Stellar feedback processes like the expansion of HII regions (Bania & Lyon, 1980; Passot et al., 1995; Vazquez-Semadeni et al., 1995), stellar-winds and supernova blast waves (de Avillez, 2000; de Avillez & Breitschwerdt, 2005; de Avillez & Mac Low, 2001; Gazol-Patiño & Passot, 1999; Kim et al., 2011; McCray & Kafatos, 1987; Ntormousi et al., 2011) can generate converging streams of gas that assemble to become molecular clouds, either in the Galactic plane or at relatively high Galactic latitudes. The energy input from supernovae and stellar winds can also eject material vertically up (e.g., Benjamin & Danly, 1997; McKee, 1993; Spitzer, 1990) which then flows back into the plane of the disk ($v_{gas} < v_{esc}$) through the diffuse magnetized ISM.

Magnetic fields may play a crucial role in the dynamics of cloud motion through the ISM. Using 2-D numerical simulations Mac Low et al. (1994) showed that even a moderate level of magnetic field aligned parallel to the direction of the shock motion can help a cloud to stabilize against disruptive instabilities (see also Jones et al., 1996). The magnetic field was found to have an even more dramatic impact when the motion of the cloud was considered transverse to the field lines (Jones et al., 1996). In this case, the field lines at

the leading edge of the cloud get stretched creating a magnetic shield which quenches the disruptive Rayleigh-Taylor and Kelvin-Helmholtz instabilities and thus help the cloud to survive longer. By varying magnetic field orientation angle with respect to the cloud motion and also by varying the cloud-background density contrast and the cloud Mach number, Miniati et al. (1999), based on 2-D numerical simulations showed that for large enough angles, the magnetic field tension can become significant in the dynamics of the motion of clouds having high density contrast and low Mach number. Gregori et al. (1999, 2000), using three-dimensional numerical simulations of a moderately supersonic cloud motion through a transverse magnetic field, showed that the growth of dynamical instabilities get significantly enhanced due to the increase in the magnetic pressure at the leading edge of the cloud caused by the the effective confinement of the magnetic field lines.

The Gould Belt is a distribution of stars and molecular clouds that forms a circular patter in the sky having an inclination of $\sim 20^{\circ}$ with respect to the Galactic plane (Gould, 1879). The minimum and the maximum Galactic latitudes of the Gould Belt are toward the Orion and the Scorpio-Centaurus constellations respectively. The Cepheus Flare region is considered to be a part of the Gould Belt (e.g., Kirk et al., 2009). This region is identified as having a complex of nebulae that extends 10°-20° out of the plane of the Galactic disk at a Galactic longitude of 110° (Clemens & Barvainis, 1988; Dobashi et al., 2005; Dutra & Bica, 2002; Hubble, 1934; Lynds, 1962; Taylor et al., 1987). Five associations of dark clouds are found towards this region, namely, L1148/1157, L1172/1174, L1228, L1241, and L1247/1251. There are signposts of current star formation in these cloud complexes (e.g., Kirk et al., 2009).

Several shells and loops are identified in the direction of the Cepheus Flare. The Cepheus Flare Shell with its center at the Galactic coordinates of $l \sim 120^{\circ}$ and $b \sim 17^{\circ}$, is considered as an expanding supernova bubble at distance of ~ 300 pc (Grenier et al., 1989; Olano et al., 2006). Based on a study of the HI distribution in the region of the Cepheus Flare, Heiles (1969) speculated the possibility of the presence of two sheets most likely representing an expanding or colliding system at a distance range of 300-500 pc. Presence of a giant radio continuum region *Loop III* centered at $l = 124 \pm 2^{\circ}$, $b = +15.5 \pm 3^{\circ}$ and extending across 65° (Berkhuijsen, 1973), possibly formed as a consequence of multiple supernova explosions, and identification of an HI shell by Hu (1981) at $l = 105^{\circ}$and $b = +17^{\circ}$ suggest that the ISM towards the Cepheus Flare region is in a state of energetic motion.

Based on a study on the kinematics of the gas in LDN 1157, a dark star forming cloud associated with the cloud complex LDN 1147-LDN 1158, Sharma et al. (2020) showed that the southern boundary of the east-west segment was found to present a sinuous feature. Using the proper motion and parallax measurements of YSOs associated with L1147/1158

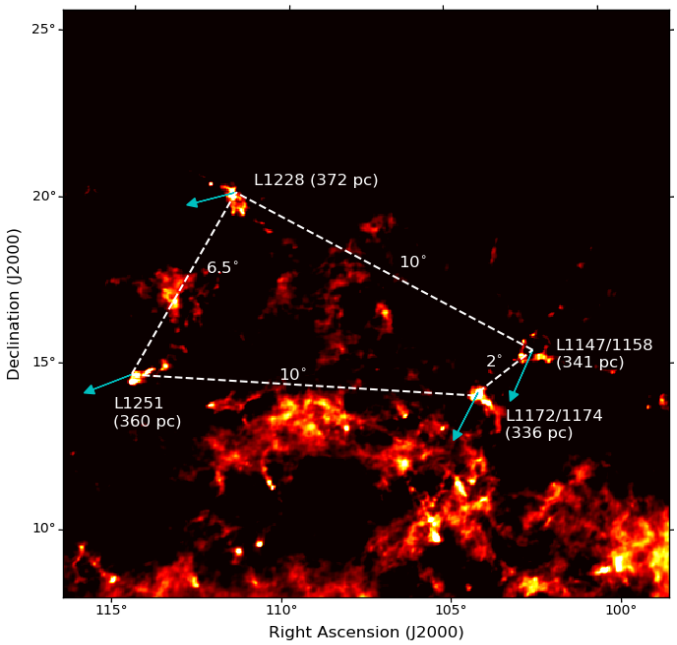

Figure 7.1: Proper motion values of sources associated with L1147/1158, L1172/1174, L1228 and L1251. The darker and lighter shaded ellipses are drawn using 3 and 5 times the median absolute deviation values of the distance and the proper motions respectively. The sources lying outside of the 5 times the MAD ellipse are identified using squares symbols.

and L1172/1174 they suggested that the feature could be produced due to the motion of the cloud through the ISM. In this paper, we studied the motion of the clouds in two more cloud complexes, LDN 1228 (hereafter L1228; Lynds, 1962) and LDN 1251 (hereafter L1251; Lynds, 1962). They are located in the direction of the Cepheus Flare region (Yonekura et al., 1997) and show signs of active star formation (Kun et al., 2009). Both these clouds are situated towards the east of L1147/1158 and L1172/1174 cloud complexes at an angular separation of ~ 10° (Fig. 7.1). The Galactic locations of L1228 and L1251 are $l \sim 111.3°$, $b \sim +19.7°$and $l \sim 114.7°$, $b \sim +14.5°$respectively. Using the parallax measurements of the YSOs associated with the clouds from the *Gaia* DR2, we find that both L1228 (372±12 pc) and L1251 (360±15 pc) are located at distances similar to L1147/1158 and L1172/1174 but show different radial velocities (Benson & Myers, 1989; Lee et al., 2007; Yonekura et al., 1997). Using the proper motion measurements of the YSO population identified in L1147/1158, L1172/1174, L1228 and L1251 and assuming that kinematically both YSOs and the clouds are coupled, we estimated the motion of the clouds on the plane of the sky.

The plane of the sky component of the magnetic fields towards a region are inferred from the observations made in optical (e.g., Alves et al., 2008, 2014; Goodman et al., 1990; Neha et al., 2016; Soam et al., 2013; Vrba et al., 1976), near infrared (e.g., Chapman et al.,

2011; Clemens et al., 2018; Goodman, 1995; Goodman et al., 1992; Sugitani et al., 2010), far-infrared (e.g., Chuss et al., 2019; Clemens et al., 2018; Pillai et al., 2020) and sub-mm wavelengths (Benoît et al., 2004; Dotson et al., 2010a; Planck Collaboration et al., 2016b; Rao et al., 1998; Vaillancourt et al., 2007). In optical and NIR wavelengths when background starlight passes through the asymmetric dust grains that are aligned with their minor axis parallel to the ambient magnetic fields gets polarized due to selective absorption (Davis & Greenstein, 1951). As a result, the polarization position angles become parallel to the magnetic field orientation allowing us to trace the projected field line. In far-infrared and sub-mm wavelengths (Benoît et al., 2004; Vaillancourt et al., 2007) thermal dust emission is found to be linearly polarized with the polarization position angles lying perpendicular to the ambient magnetic field orientations providing us the information on the projected field lines. The magnetic field geometry traced by the polarization measurements made with the *Planck* are used not only to infer the Galactic magnetic field geometry, but also to place new constraints on the dust grain properties (Planck Collaboration et al., 2016a, 2015b, 2016b,c). The plane of the sky component of the magnetic field geometry was inferred for all the four clouds using the *Planck* polarization measurements and the relationship between the projected direction of motion and the field orientations are studied to understand the effects of the cloud movement and its interaction with the ISM. By combining this with the radial velocity measurements of the clouds, we estimated their space velocity also.

This paper is organized in the following manner. We begin with a description on the data in section 7.2 followed by a discussion on the YSO population in each cloud in section 7.3.1. The calculation of the space velocity of the clouds are presented in section 7.3.2. The motion of the clouds are discussed with respect to the orientation of the projected magnetic field using the *Planck* polarization measurements in section are discussed further in section 7.3 followed by a summary of the results in section 7.4.

7.2 The Data

7.2.1 The Gaia DR2

The *Gaia* second data release DR2 provides five-parameter astrometric solution, namely, positions on the sky (α, δ), parallaxes, and proper motions for more than 1.3 billion sources (Gaia Collaboration et al., 2018). The limiting magnitude is $\sim$ 21 in G-band. Uncertainties in the parallax values are in the range of up to 0.04 milliarcsecond for sources with G $<$ 15, around 0.1 mas for sources with G=17. For the sources at the fainter end, with G$\sim$20, the uncertainty in parallax is of the order of 0.7 mas. For the uncertainties in the corresponding

proper motion values are up to 0.06 mas/yr for G < 15 mag, 0.2 mas/yr for G = 17 mag and 1.2 mas/yr for G = 20 mag. Because, the conversion from parallax to distance is known to become non-trivial when the observed parallax is small compared to its uncertainty especially in cases where $\sigma_{\varpi}/\varpi \gtrsim 20\%$ (Bailer-Jones, 2015). As a result, by adopting an exponentially decreasing space density prior in distance, Bailer-Jones et al. (2018) estimated distances of more than one billion sources using the *Gaia* parallax measurements. The distances to the YSOs studied in this chapter are obtained from the catalogue provided by Bailer-Jones et al. (2018) while the proper motion values are obtained from the *Gaia* DR2 (Gaia Collaboration et al., 2018) catalog. We used only those values for which the ratio, m/Δm (where m is the distances and the proper motions and Δm is the corresponding uncertainties), is less than or equal to 3.

7.2.2 The Planck polarization measurements

We used the 353 GHz (850 μm) data. The 353 GHz channel is the highest-frequency polarization-sensitive channel of the Planck. We produced the geometry of the magnetic fields in the vicinity of L1147/1158, L1172/1174, L1228 and L1251 based on these data. We selected images containing the clouds and smoothed them down to the 80 resolution to obtain a good signal-to-noise (SNR) ratio. The dust emission is linearly polarized with the electric vector normal to the sky-projected magnetic field, therefore the polarization position angles were rotated by 90° to infer the projected magnetic field.

7.2.3 Identification of clumps from the Herschel column density maps

The dust column density maps of the four clouds L1147/1158, L1172/1174, L1228 and L1251 were obtained from the Herschel Gould Belt Survey Archive. We identified clumps in the column density maps of the four clouds using the *Astrodendro* algorithm, which is a Python package to identify and characterize hierarchical structures in images and data cubes. A dendrogram is a tree diagram which identifies the hierarchical structures of 2-dimensional and 3-dimensional datasets. The structures start from the local maximum with the volumes getting bigger when it merges with the surroundings with lower flux densities and stop identifying structures when they meet neighbouring structures (Rosolowsky et al., 2008). The dendrogram method identifies emission features at successive isocontours in emission maps which are called *leaves* and find the intensity values at which they merge with the neighbouring structures (branches and trunks). In order to extract the structures, three parameters need to be defined : min_value, min_delta and min_npix. The parameter, min_value is an emission threshold above which all the structures are identified and min_delta

is contour interval which decides the boundary between the distinct structures. The initial threshold and the contour step size are selected as a multiple of the σ, the rms of the intensity map. In our analysis, we are interested in the denser regions which are identified as leaves.

In each cloud, the minimum threshold was selected as a multiple of background of the column density values, $\sim 0.7 \times 10^{21}$ cm^{-2}. In this work, we used the column density maps at $36''$ resolution. In order to identify the real structures, we used the condition on the size of the clump as that the area within each ellipse should be higher than the area within 5 pixels. Second, we excluded the clumps where the area of the each source is higher than the area subtended by a beam. Here, we used the Herschel column density map for the source extraction with the beam size $\sim 36''$. In addition to that, to consider only the elongated clumps, we used only those clumps where the aspect ratio is less than 0.833 (Chen et al., 2020). Since we are interested in the orientation of cores embedded within the large clouds, we removed those clumps from our sample that are lying on the edges of the dust column density maps as that leads to the artificial clumps. The structures identified as clumps are all have the area larger than the area of the beam.

7.3 Results and Discussion

7.3.1 Population of YSOs, distance, proper motion and radial velocity

The star forming regions in the Cepheus Flare was extensively studied by Kirk et al. (2009), Kun et al. (2009), Yuan et al. (2013). The YSOs used in this study are taken from the above three works. We obtained the *Gaia* DR2 data for the three YSO candidates that are located in the direction of L1147/1158 cloud complex (Kirk et al., 2009). These sources are listed in Table 7.1. Columns 1-5 give source names, right ascension, declination, Galactic longitude and latitude. Columns 6-10 give the distances obtained from the Bailer-Jones et al. (2018) catalog, $\mu_{\alpha\star}$ (= $\mu_\alpha \cos\delta$) and μ_δ along with the uncertainties obtained from the *Gaia* DR2 (Gaia Collaboration et al., 2018) catalog. The distance and proper motion values of these three sources associated with L1147/ 1158 cloud complex are shown in Fig. 7.2 using open circles ($\mu_{\alpha\star}$) and triangles (μ_δ) in magenta. The median and the standard deviation values of the distances and $\mu_{\alpha\star}$ and μ_δ are found to be 341±3 pc, 7.753±0.317 mas/yr and -1.514±0.045 mas/yr respectively. These values are given in columns 2, 3 and 4 of Table 7.2.

Recently, Saha et al. (2020) made a study of the YSO candidates in the direction of L1172/1174 based on the *Gaia* DR2 data. They obtained the *Gaia* DR2 data for a total of 19 known YSOs that they obtained from Kirk et al. (2009), Kun et al. (2009) and Yuan et al. (2013). The filled circles and triangles in grey show results for L1172/1174. The median and

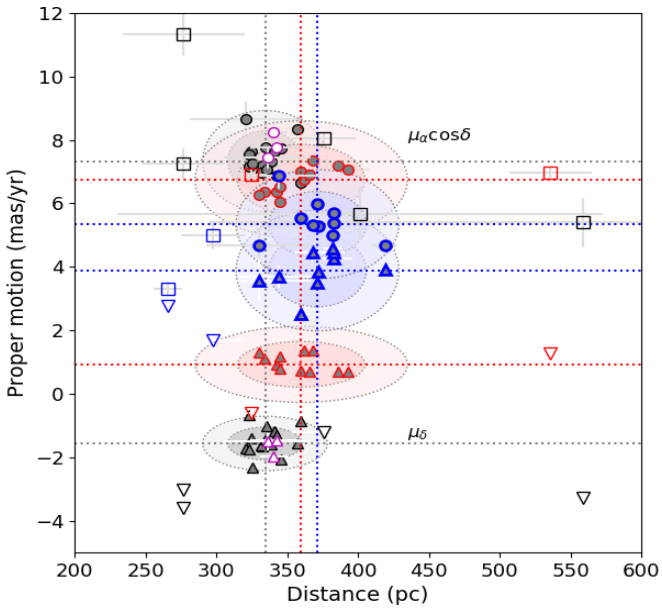

Figure 7.2: Proper motion vs. distance plot for stars towards L1147/1158 (magenta), L1172/1174 (grey), L1228 (blue) and L1251 (red). The $\mu_{\alpha\star}$ and μ_δ are represented using circles and triangles respectively. Sources listed in Table 7.1 for L1147/1158, L1172/1174, L1228, L1251 are shown using magenta, grey, red and blue symbols. The darker and lighter shaded ellipses are drawn using 3 and 5 times the MAD values of the distance and the proper motions respectively. The sources falling outside of the 5 times the MAD ellipse are identified using squares ($\mu_{\alpha\star}$) and inverted triangles (μ_δ).

median absolute deviation (MAD), more robust against outliers, for the distances, $\mu_{\alpha\star}$ and μ_δ are 335±9 pc, 7.333±0.319 mas/yr and -1.566±0.172 mas/yr respectively. In Fig. 7.2, we also draw ellipses with 3×MAD (darker shade) and 5×MAD (lighter shade) for L1172/1174. Of the 19 sources found towards L1172/1174, four sources are found to fall outside the ellipses drawn with 5×MAD. These sources are shown using open squares ($\mu_{\alpha\star}$) and inverted triangles (μ_δ) respectively. The sources that are falling within the 5×MAD ellipses are considered for our study. The three sources identified in the direction of L1147/1158 are also found to fall within the 5×MAD ellipses obtained for L1172/1174 cloud. These sources are listed in Table 7.1.

The YSO candidates towards L1228 and L1251 are obtained from the source list provided by Kun et al. (2009). We obtained *Gaia* DR2 data for 12 and 13 sources towards L1228 and L1251 respectively. The results are shown using the filled circles and triangles in blue (L1228) and red (L1251) respectively. The median and MAD of the distances, $\mu_{\alpha\star}$ and μ_δ for L1228 are 372±12 pc, 5.345±0.344 mas/yr and 3.882±0.380 mas/yr respectively and for L1251 are 360±15 pc, 6.745±0.372 mas/yr and 0.928±0.240 mas/yr respectively. Two sources each belonging to L1228 and L1251 are found to fall outside the ellipses drawn with

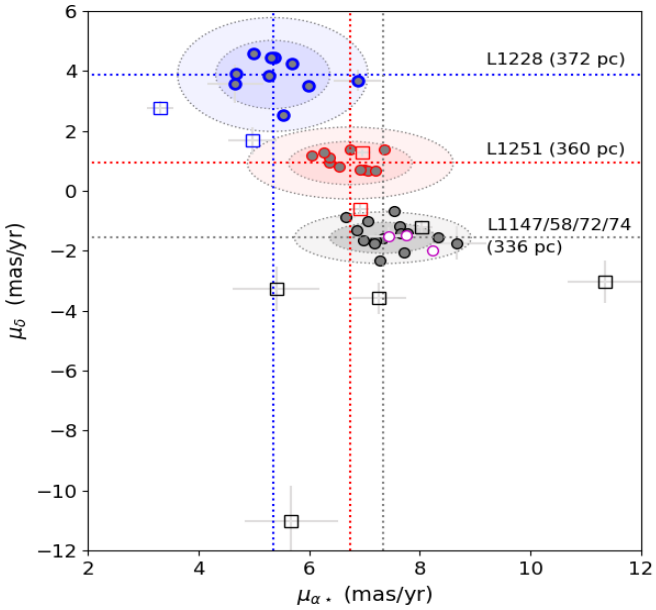

Figure 7.3: Proper motion values of sources associated with L1147/1158, L1172/1174, L1228 and L1251. The darker and lighter shaded ellipses are drawn using 3 and 5 times the median absolute deviation values of the distance and the proper motions respectively. The sources lying outside of the 5 times the MAD ellipse are identified using squares symbols.

5×MAD which are identified using open squares and inverted triangles in blue (L1228) and red (L1251) respectively. The sources that are falling within the 5×MAD ellipses towards L1228 (10) and L1251 (11) respectively are listed in Table 7.1. The mean and the MAD values of the distance and the proper motions obtained for L1147/1158, L1172/1174, L1228 and L1251 complexes are given in columns 2, 3 and 4 of Table 7.2.

A clustering of the sources associated with each cloud complex is quite evident. It is also apparent that both L1147/1158 and L1172/1174 are located at similar distances from us even though they are ∼2° apart in the sky. This implies that they are spatially ∼ 10 pc apart. L1228 which is located at an angular distance of ∼10° away from both L1148/1157 and L1172/1174 is located at slightly further away at ∼360 pc from us. This translates to a spatial separation of ∼60 pc. L1251 which is spatially at a separation of ∼6° away from L1228 is located at a further distance at ∼370 pc. L1251 is also at a spatial separation of ∼10° away from both L1148/1157 and L1172/1174. In Fig. 7.3 we show the $\mu_{\alpha\star}$ and μ_δ values for L1148/1157 and L1172/1174 (grey + magenta), L1228 (blue) and L1251 (red). The median values are identified using dotted lines and the ellipses are drawn using 3×MAD (darker shade) and 5×MAD (lighter shade). The square symbols show the sources that falling outside 5×MAD ellipses in Fig. 7.2 and hence not considered in this study. In proper motion domain also, all but one in L1148/57/72/74 are falling within the 5×MAD ellipses drawn in Fig. 7.3. There is

a clear clustering of sources implying that the YSO candidates associated with the clouds are moving coherently in space.

In earlier studies, L1228 was considered to be a cloud lying closer to us at a distance of ~ 200 pc (e.g., Kun et al., 2008). Kinematically also this cloud differs from the rest of the clouds belonging to the Cepheus flare region. At least three centers of star formation was identified towards L1228 (e.g., Kun et al., 2008). Recently, Zucker et al. (2020) estimated distances to the molecular clouds by inferring the distance and extinction to stars lying projected on the clouds using optical and near-infrared photometry and the *GAIA* DR2 parallax measurements. Based on their results, the distances provided for the regions enclosed within the Galactic coordinates $l \sim 102°$-$115°$and $b \sim 14°$-$21°$are found to be in the range of ~ 330 pc to ~ 380 pc. This is quite consistent with the distances estimated for the four molecular clouds presented here using the YSO candidates associated with the cloud which is the most direct method of estimating distances to molecular clouds.

7.3.2 The Space motion and the 3D distribution of the clouds

For any velocity, it can always be broken down into components along two perpendicular axes. For stars, the space velocity includes some motion along the line of sight, that is, either towards or away from us which is called the radial velocity and some motion across the sky, perpendicular to the radial velocity which is called the proper motion. Thanks to the *Gaia* mission, now we have parallax and proper motion measurements for over billion stars with unprecedented accuracy. Though the high-resolution spectroscopy of stars can provide the measurements of radial velocity, it is still not possible to get the measurements made for YSOs as they are typically fainter in magnitudes. On the other hand, it is not possible to measure the proper motion of the molecular clouds as they are not point sources but their radial velocities can be measured using molecular line observations. Therefore by combining the radial velocity measurements of a molecular cloud and the proper motion measurements of the YSOs associated with it and by assuming that both the YSOs and the clouds share the same velocity in space as these clouds are the birth places of the YSOs, we can determine the actual motion of a molecular cloud through the space.

The proper motions of the sources measured by the *Gaia* are in the equatorial system of coordinates. To understand the motion of objects in the Galaxy, we need to transform the proper motion values from the equatorial to the Galactic coordinate system $\mu_{l\star} = \mu_l \cos b$ and μ_b. We transformed the proper motion values using the expression (Poleski, 2013),

$$\begin{bmatrix} \mu_{l\star} \\ \mu_b \end{bmatrix} = \frac{1}{cosb} \begin{bmatrix} C_1 & C_2 \\ -C_2 & C_1 \end{bmatrix} \begin{bmatrix} \mu_{\alpha\star} \\ \mu_\delta \end{bmatrix} \tag{7.1}$$

where the term $cosb = \sqrt{C_1^2 + C_2^2}$ and the coefficients C_1 and C_2 are given as,

$$\begin{aligned} C_1 &= sin\delta_G\ cos\delta - cos\delta_G\ sin\delta\ cos(\alpha - \alpha_G) \\ C_2 &= cos\delta_G\ sin(\alpha - \alpha_G) \end{aligned} \tag{7.2}$$

The equatorial coordinates (α_G, δ_G) of the North Galactic Pole are taken as 192°.85948 and 27°.12825, respectively (Poleski, 2013). The mean values of $\mu_{l\star}$ and μ_b calculated from the YSO candidates found towards the four cloud complexes are given in columns 5 and 6 of Table 7.2. If we assume that the cloud and the YSO candidates are expected to share similar kinematics as a result of them being born inside the cloud, then the arrows should also represent the motion of the clouds on the sky plane. Presence of reflection nebulosity around a number of these YSO candidates provide evidence of their clear association with the cloud. The plane of the sky component of the direction of motion (θ_{pos}^{motion}) calculated using the mean values of $\mu_{l\star}$ and μ_b are given in the column 7 of Table 7.2. The arrows drawn in yellow in Fig. 7.5 show the sense of the motion of the sources on the sky plane with respect to the Galactic north increasing to the east.

The radial velocity of L1147/1158 and L1172/1174 regions are obtained by us in the previous chapters (Chapter 3, 4 and 5). The radial velocities are found to be ~2.6 km s^{-1}for L1147/1158 and ~2.7 km s^{-1} L1172/1174 respectively. Our results are consistent with the values obtained by Yonekura et al. (1997) based on a large-scale ^{13}CO (J=1-0) survey of the Cepheus-Cassiopeia region. The radial velocity of L1228 and L1251 are found to be -7.8 km s^{-1}(Benson & Myers, 1989) and -4.0 km s^{-1}(Benson & Myers, 1989; Lee et al., 2007) respectively. Benson & Myers (1989) obtained the radial velocities based on the seven-component fit to the spectra using the hyperfine structure fitting. The radial velocity of the cloud complexes are converted from the local standard of rest (LSR) system to the heliocentric system. The V_r values calculated for L1147/1158, L1172/1174, L1228 and L1251 are -11.4 km s^{-1}, -11.0 km s^{-1}, -20.1 km s^{-1}, and -15.1 km s^{-1}respectively. The two tangential velocity components along the Galactic longitude and latitude are calculated using $V_l = 4.74d \times \mu_{l\star}$ and $V_b = 4.74d \times \mu_b$, respectively. The factor 4.74 is the ratio of the au expressed in kilometer and the number of seconds in a tropical year. The d is the median distance to the cloud. The V_l and V_b values thus calculated are 5.4 km s^{-1} and -10.8 km s^{-1} respectively for L1147/1158, .

Then we calculated the velocities U, V, W directed along the rectangular Galactic coordinate axes using the expressions (e.g., Bobylev & Bajkova, 2019),

$$\begin{bmatrix} U \\ V \\ W \end{bmatrix} = \begin{bmatrix} cosl\ cosb & -sinl & -cosl\ sinb \\ sinl\ cosb & cosl & -sinl\ sinb \\ sinb & 0 & cosb \end{bmatrix} \begin{bmatrix} \mathrm{V}_r \\ \mathrm{V}_l \\ \mathrm{V}_b \end{bmatrix} \tag{7.3}$$

The velocity U is directed from the Sun toward the Galactic center with the positive direction being toward the Galactic center, V is positive in the direction of Galactic rotation, and W is positive directed to the north Galactic pole. The values of (U, V, W) for L1147/L1158 and L1172/1174 cloud complexes are (−3.3, −14.3, −13.2) km s^{-1} with a standard deviation of (0.6, 0.3, 0.9) km s^{-1}. To determine the motion of the complexes with respect to the Galactic frame of reference, we transformed the heliocentric velocities to the LSR velocities by subtracting the motion of the Sun with respect to the LSR from the heliocentric velocities.

In a number of studies (e.g., López-Corredoira & Sylos Labini, 2019; Trick et al., 2019) the velocity components of the motion of the Sun with respect to the LSR estimated by Schönrich et al. (2010) of (U, V, W)$_\odot$ = ($11.1^{+0.69}_{-0.75}$, $12.24^{+0.47}_{-0.47}$, $7.25^{+0.37}_{-0.36}$) km s^{-1} are used. However, recently, based on the *Gaia* DR2 data, the velocity components of the Sun's motion have been re-evaluated using, for example, stars (Ding et al., 2019; Li et al., 2019), open star clusters (Bobylev & Bajkova, 2019), OB star samples (Bobylev & Bajkova, 2018) and white dwarfs (Rowell & Kilic, 2019). We used the most recent values of (U, V, W)$_\odot$ = (7.88, 11.17, 8.28)±(0.48, 0.63, 0.45) km s^{-1} obtained by Bobylev & Bajkova (2019) for the transformation from the heliocentric to the LSR velocities. The value of (u, v, w) estimated for L1148/L1157 and L1172/1174 cloud complexes is found to be (4.6, −3.1, −4.9) km s^{-1} with a standard deviation of (0.6, 0.3, 0.9) km s^{-1}.

The motion of the complex is presented on a rectangular (x, y, z) co-ordinate system with the Sun as the origin as shown in Fig. 7.4. The Ox axis runs parallel to the Sun-Galactic center direction, Oy in the Galactic plane but perpendicular to the Ox and Oz is perpendicular to the Galactic plane. The positive direction in Ox, Oy and Oz being the direction toward the Galactic center, in the direction of the Galactic rotation and towards the Galactic North pole, respectively. We computed the position of the complexes (X, Y, Z) as (-79, 315, 84) pc for L1147/1158, (-127, 326, 127) pc for L1228 and (-142, 319, 90) pc for L1251. The resultant velocity is found to be ∼ 8.5 km s^{-1}, 7.4 km s^{-1}, 12.3 km s^{-1}and 8.5 km s^{-1}for L1147/1158, L1172/1174, L1228 and L1251 respectively. The cloud L1228 which is located further away at 372 pc is the one located at a height of 127 pc above the Galactic mid-plane. Recently, Alves et al. (2020) studied the 3-D distribution of all the cloud complexes around solar neighbourhood and showed that the distribution is inconsistent with the perception that these

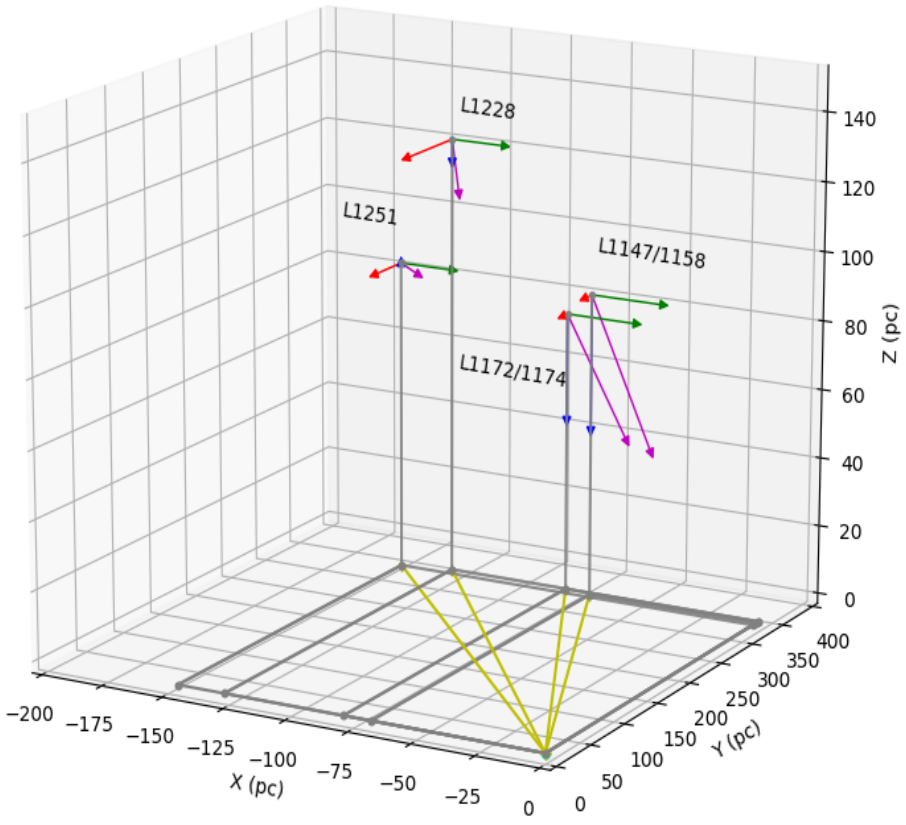

Figure 7.4: The 3-D motion of L1147/1158 and L1172/1174 complexes is presented on a rectangular coordinate system with the Sun as the origin. The X-axis, Y-axis, and Z-axis run parallel to the Sun-Galactic center vector, perpendicular to the Sun-Galactic center vector and perpendicular to the Galactic plane respectively. The positive direction of X-, Y- and Z-axis is the direction towards the Galactic center, in the direction of Galactic rotation and towards the Galactic North pole respectively. The arrows in green, red and blue represent the components of velocity in the X-, Y- and Z-axis respectively. The arrow in magenta represents the resultant velocity of the complex. The line in yellow shows the projection of the distance of the complex on the Galactic plane. The scale of the vectors is taken as eight times the magnitude of velocity.

clouds are part of the Gould Belt system. In stead they found the clouds to be distributed as a spatially and kinematically coherent structure, known as Radcliffe Wave, seems to be undulating. They described the 3-D distribution with a damped sinusoidal wave on the plane of the Milky Way. The Cepheus Flare region falls on the near end of this structure which appears to be elevated from the Galactic plane.

Odenwald & Rickard (1987) and Odenwald (1988) have catalogued a number of high-latitude cometary/filamentary objects gleaned from the IRAS images (similar to the four clouds presented here) and suggested that their morphologies can be explained as a result of cloud-ISM interaction. A flow of velocity of V around an object of length L can be characterized using the Reynolds number (R_e=ρLV/μ), where ρ is the ambient fluid density, and μ is the fluid viscosity. Whether the passage of a body through a fluid results in turbulent motion is assessed from the value of R_e which is related to the ratio of the rate at which vorticity is produced to the rate at which it is destroyed via diffusion. While flows of extremely low ($\approx$10) and intermediate ($\approx$50) values of R_e are expected to show a smooth laminar flow pattern and an irregular structures and vortices respectively, higher values of R_e($\gg$100) is expected to produce a fully turbulent flow. Odenwald (1988) suggested that for a relatively low value of R_e ($\lesssim$10), the mass lost by ablation due to the motion of a cloud through ambient medium can form long sinuous filaments.

Following the procedure from Odenwald & Rickard (1987) and Odenwald (1988), we made a rough estimate of the value of R_e for L1147/1158, L1172/1174, L1228 and L1251 and found it to be $\sim$ 3. Major contribution of uncertainty in the calculation of R_e comes from the large uncertainty in the estimation of the density and the viscosity of the ambient medium. We ignored the effects of magnetic field in our calculation as the offset between the projected magnetic field and the direction of the cloud's motion is $\sim 30°$. Studies with various values of offsets between the orientation of the magnetic field lines and the direction of the cloud motion have shown that only for large enough offsets magnetic fields play a significant role in the dynamical evolution of the cloud (Jones et al., 1996; Mac Low et al., 1994; Miniati et al., 1999). The number density of the ambient medium is estimated as 0.09 cm^{-3} adopting a density of 0.17 cm^{-3} along the Galactic plane and an exponential scale height of 125 pc (Odenwald, 1988). Assuming that the cloud is in pressure equilibrium with the ambient medium, we estimated the temperature of the ambient medium as $\sim 10^6$ K using the average values of the number density and temperature of the cloud calculated from the dust emission. We used V = 7 km s^{-1} and L= 1 pc in the calculation. The low value of R_e is consistent with the smooth morphology of the cloud structures especially the sinuous morphology depicted by L1157 (Sharma et al., 2020).

7.3.3 Motion of the cloud complexes with respect to the magnetic field

The plane of the sky magnetic field (B_{pos}) vectors obtained from the *Planck* polarization measurements of the region containing all the four complexes are shown in Fig. 7.5. The B_{pos} vectors are overplotted on the *Herschel* column density maps. The outer most contour drawn in Fig. 7.5 corresponds to a column density of 1×10^{21} cm^{-2}. This corresponds to an extinction of $A_V \approx 0.5$ magnitude determined using the relationship between the column density and the extinction derived by Draine (2003) for R_V =3.1 extinction law. While the vectors lying within the contour are considered as providing information on the cloud B_{pos}, the ones lying outside are considered as providing information on the ambient or background or ICMF orientation surrounding each cloud (see chapter 5). The B_{pos} vectors lying within (B_{pos}^{cloud}) and outside (B_{pos}^{ICMF}) of this contour are identified separately using the lines drawn in red+white and white colors respectively. We find no significant difference between the distributions of B_{pos}^{cloud} and B_{pos}^{ICMF} vectors in L1147/1158, L1228 and L1251 which is very much evident from Fig. 7.5 also. This implies that the clouds are threaded by the ambient magnetic fields.

As discussed in the earlier chapters, we find a change in the orientation of the B_{pos}^{cloud} and B_{pos}^{ICMF} vectors of L1172/1174 which is more prominent as we move to the south and the south-eastern direction of the cloud. The orientation of the B_{pos}^{cloud} and B_{pos}^{ICMF} in each cloud are obtained by calculating the median value of all the vectors lying within and outside of the 1×10^{21} cm^{-2} contour. The values of θ_{Bpos}^{cloud} and θ_{Bpos}^{ICMF} thus obtained are listed in column 10 of Table 7.2. The θ_{Bpos}^{cloud} and the θ_{Bpos}^{ICMF} determined for each cloud is shown using thick lines in red and cyan in Fig. 7.5.

In previous chapters we discussed the gas dynamics of L1147/1158 and L1172/1174 in detail. In L1147/1158, we noted that the cloud complex has strikingly sharp edges to its southern side which is the side facing the Galactic plane. The sharp edges of the southern side of L1147/1158 were noted by Harjunpaa et al. (1991) also. The projected direction of motion of L1147/1158 is found to be ~157° with respect to the Galactic north. The results imply that L1147/L1158 is moving towards the Galactic plane. Interestingly, the sharp edges are developed towards the leading edge of the cloud motion. It is possible that these sharp edges are created as a result of the interaction of the cloud with the ambient medium through which it is travelling. The projected magnetic field orientations found inside and outside the cloud boundary are found to be at an angle of 183±7° and 186±6°. These values are consistent with the magnetic field orientation estimated for L1157 in chapter 5 using optical polarization measurements of background stars. The position angle in the Galactic coordinate system was 184±11°. The directional offset between the inner and outer magnetic fields is found to be 3°. The projected offsets between the direction of motion of the cloud and the

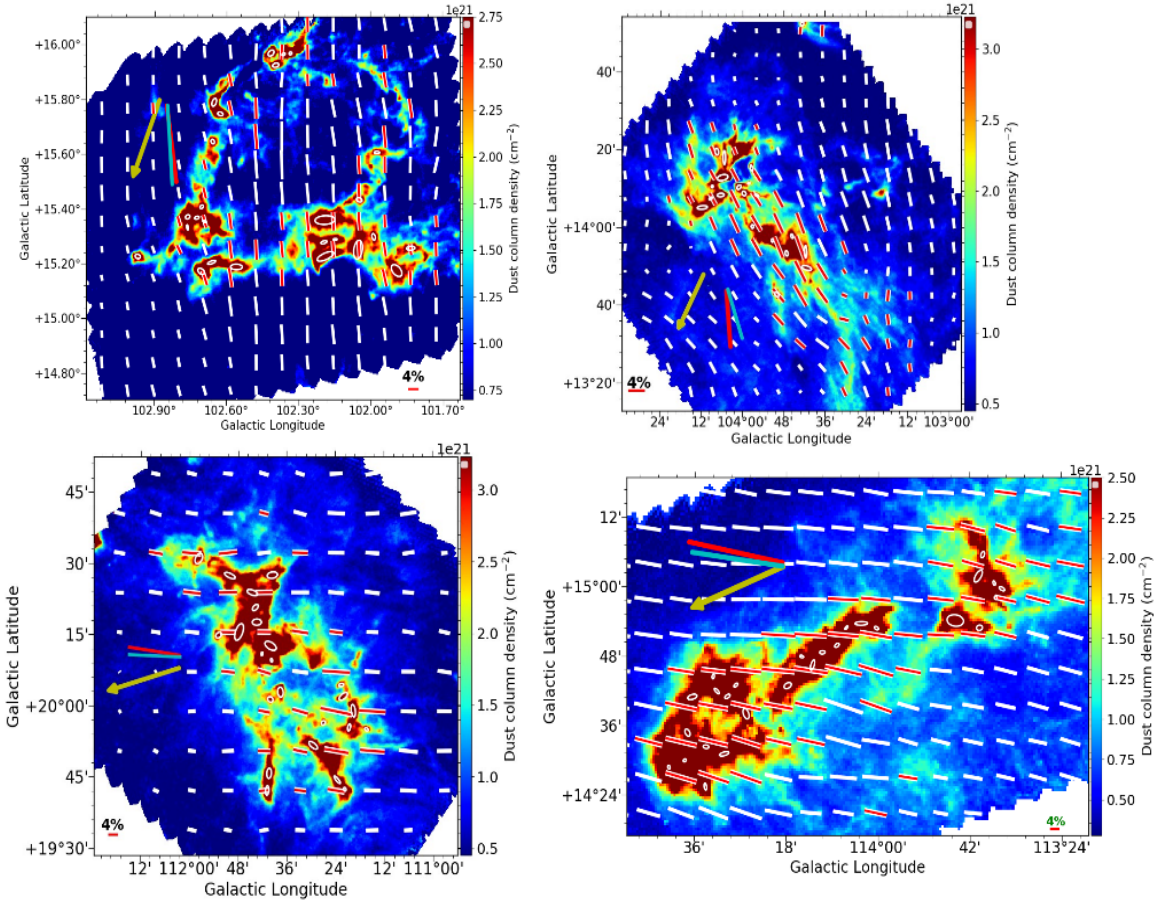

Figure 7.5: Planck polarization vectors (white) plotted over the column density maps of the clouds produced using the *Herschel* images. The vectors identified with the red+white vectors corresponds to a column density of 1×10^{21} cm^{-2} which are considered as representing the cloud magnetic field geometry. The arrow drawn in yellow shows the direction of motion of the clouds. The thick lines drawn in red and cyan are the mean value of the cloud and the background magnetic field orientations respectively.

magnetic field orientation inside and outside the cloud boundary are 26°and 29°respectively. Thus the projected motion of the cloud is almost aligned with the ambient magnetic field direction.

L1172/1174 which seems to be both spatially and kinematically associated with L1147/1158 shows a significant difference in the projected magnetic field orientation especially to its northern and southern regions. The field orientation to the north of L1172/1174 is consistent with the field orientation seen towards L1147/1158. However, it is to the south-eastern side of L1172/1174 that the magnetic field orientation becomes more complex. The projected magnetic field orientations inside and outside of the cloud are 208±11° and 196±23° respectively. The directional offset between the inner and outer magnetic fields in L1172/1174 is found to be 12°. The complex magnetic field orientation in the vicinity of the complex is evident from the relatively high dispersion (by a factor of two to three compared to the values found towards the other three clouds) found for the field vectors lying outside the cloud. Similar to L1147/L1158, L1172/1174 is also found to be moving towards the Galactic plane. The projected direction of motion of L1172/1174 is estimated to be 152° which is quite consistent with the direction of the motion of L1147/1158. Thus the offsets between the direction of motion of the cloud and the magnetic field orientations found inside and the outside of the cloud are 56° and 44° respectively.

Among the four clouds studied here, L1228 is located at a height of 127 pc above the Galactic plane. The direction of motion of the cloud is found to be almost parallel to the magnetic field direction at 105°. The projected orientation of the magnetic field inside and outside
the inner and outer magnetic fields in L1228 is found to be 4°. The projected direction of motion is at an offset of 21° and 17° with respect to the projected magnetic fields within and outside of the cloud respectively. L1251 is an elongated cloud having a remarkable cometary morphology which is believed to have been formed as a consequences of its interaction with a supernova bubble as described by Grenier et al. (1989). The elongation of the cloud is in the east-west direction. Two IRAS point sources, associated with molecular outflows, are located in the eastern head region of the cloud while no sign of current star formation was identified in the western region which forms the tail of the cloud (e.g., Kun et al., 2008). Based on the morphology of the cloud produced using the extinction maps generated from the star counts, Balázs et al. (2004) suggested that the cloud resembles a body flying at hypersonic speed across an ambient medium. The projected direction of motion of the cloud is found to be at a direction of 105°. The projected orientation of the magnetic field inside and outside of L1251 is found to be 79±6° and 81±6° respectively and the angular offset between the two fields is 2°. The offset between the projected directions of the motion of the

cloud and the inner and the outer magnetic fields are 19° with respect to the local projected magnetic field orientation. It is interesting to note that while the cometary morphology of the cloud is oriented parallel to the direction of motion, the diffuse material lying towards the south-western region close to the head of the cloud show distribution along the field lines.

The inner and outer magnetic fields in all the four clouds are found to be parallel to each other suggesting that the inner magnetic fields are inherited from the ambient fields and that the formation of the of the clouds have not affected the cloud geometries much. As discussed in chapter 5, in a magnetic field mediated cloud formation scenario, the field lines guide the material (Ballesteros-Paredes et al., 1999; Van Loo et al., 2014), to form the filamentary structures first that are expected to be oriented perpendicular to the ambient magnetic field which then undergo fragmentation to form cores (Könyves et al., 2015; Polychroni et al., 2013). As the accumulation of the material is helped by the magnetic field lines, the ICMF direction is expected to get preserved deep inside the cores (Hull et al., 2013; Li et al., 2009, 2015), expecting a parallel orientation between the ICMF and the core magnetic field.

The magnetic field lines aligned with the cloud motion was studied in two-dimensional numerical simulations by Mac Low et al. (1994) and shown that the magnetic fields help the cloud to stabilize against disruptive instabilities. Further, using two-dimensional numerical study, Miniati et al. (1999) explored the effect of a uniform magnetic field oriented oblique with respect to a moving interstellar cloud. They carried out the study for several values of inclination ranging from the aligned case to the transverse case, for several values of Mach number and density contrast parameter which is the ratio between the cloud and the ambient density. They found that for angles larger than 30°, the magnetic field lines get stretched and would tend to wrap around the cloud amplifying the magnetic field significantly at the expense of the kinetic energy of the cloud.

In all the clouds, the field orientations are smooth and well ordered. In L1148/1157, L1228 and in L1251, the offsets between the projected direction of the motion and the projected magnetic fields are $\lesssim$30°. No draping of the magnetic fields towards the leading edges of the clouds are noticed even in the case of the cometary cloud L1251. However, the offset between the projected direction of the motion and the projected magnetic fields is $\gtrsim$30° and one would expect an amplification of the field strength towards its leading edge. Among the four clouds studied here, L1172/1174 is the only cloud that shows an apparent hub-filament structure and forming a massive star, HD 200775, and a sparse cluster in the hub. It is interesting to note that in L1172/1174, the deviation in magnetic field as we move from L1147/1158 occurs at the location of the cloud and then as we move towards the eastern/south-eastern sides of L1172/1174, the field geometry becomes complex. It could be possible that a large offset between the cloud motion and the magnetic fields might have

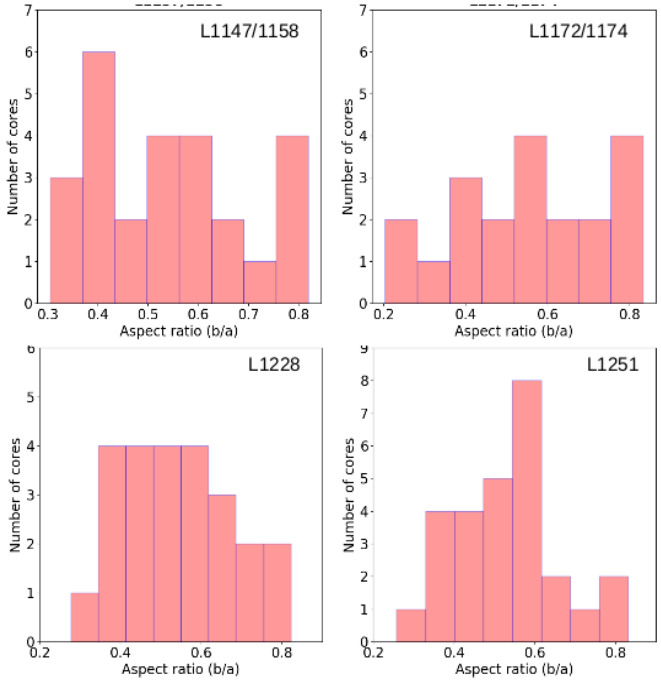

Figure 7.6: Histogram of the aspect ratios of the clumps extracted from the four clouds.

helped the cloud to amass material quickly and initiate the formation of a massive star like HD 200775. Whether the modification of the magnetic fields occur due to the formation of the cloud or the bend in the magnetic field facilitated the formation of the cloud is unclear.

7.3.4 Relative orientations of clumps, magnetic field and motion of the clouds

We derived the properties like the right ascension and the declination of the identified clumps, their effective radius, major and minor axis and the position angle of the major axis of the clumps (θ_{pos}^{clump}) identified using the *Astrodendro*. The reference for position angle is taken from the positive x-axis increasing counter-clockwise. The derived clumps are identified and drawn as ellipses in Fig. 7.5. We extracted 30 clumps each in L1147/1158 and in L1172/1174, 26 in L1228 and 36 in L1251 complex. After applying all the selection criteria mentioned in the section 7.2.3, the final number of clumps are 26 in L1147/1158, 20 in L1172/1174, 24 in L1228 and 27 in L1251 complex. These extracted cores are shown in Fig. 7.5 as ellipses. The distribution of the aspect ratio of the identified clumps in each cloud are shown in Fig. 7.6. The clumps in L1147/1158 and L1172/1174 show full range of aspect ratio ranging from 0.3 to 0.8 while in L1228 and in L1251, the aspect ratios peak between 0.4-0.6.

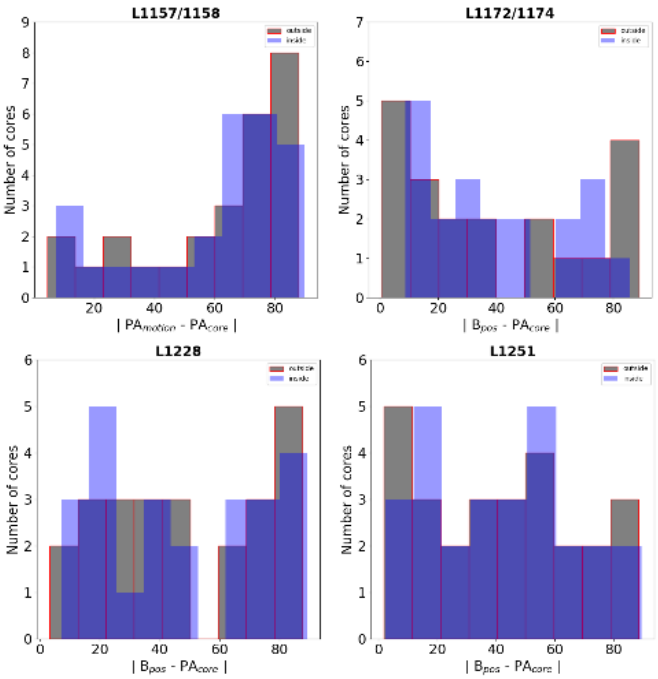

Figure 7.7: Histogram of the offsets between θ_{pos}^{clump} with respect to the θ_{Bpos}^{cloud} (grey) and θ_{Bpos}^{bg} (blue).

The clumps extracted in all the four clouds are mostly associated with the filamentary structures which is consistent with the results obtained from the Herschel Gould Belt Survey (André et al., 2014, 2010; Könyves et al., 2010). Theoretically, this association is interpreted as the longitudinal fragmentation of thermally supercritical filaments into cores (e.g., Inutsuka & Miyama, 1992, 1997). However, in the presence of turbulence, the filaments cease to become quiescent structures in which perturbations grow slowly. In the case when the clouds are in motion through the ambient interstellar medium, like the four clouds studied here, they interact with it generating turbulence in the cloud structure (Gregori et al., 1999, 2000; Jones et al., 1996; Mac Low et al., 1994; Miniati et al., 1999). Under this scenario we made an attempt to examine the properties of the clumps associated with these clouds with respect to the directions of the B_{pos}^{cloud} and B_{pos}^{bg} and the direction of their motion.

The offset angles, $\Delta\theta_{Bcloud}^{clump} = \theta_{pos}^{clump}$ - θ_{Bpos}^{cloud}, $\Delta\theta_{BICMF}^{clump} = \theta_{pos}^{clump}$ - θ_{Bpos}^{ICMF}, and $\Delta\theta_{motion}^{clump} = \theta_{pos}^{clump}$ - θ_{pos}^{motion} are calculated. The distributions of $\Delta\theta_{Bcloud}^{clump}$ (in blue) and $\Delta\theta_{BICMF}^{clump}$ (in grey) for all the four clouds are shown in Fig. 7.7. Towards L1147/1158, the major axis of the clumps are oriented predominantly orthogonal to both ICMF and the inner magnetic fields. Of the 26 clumps identified, in 17 (65%) of them, both $\Delta\theta_{BICMF}^{clump}$ and $\Delta\theta_{Bcloud}^{clump}$ are found to be $\geq 60°$. This is consistent with the conclusion drawn by Soler (2019) who found that the projected magnetic fields are mostly perpendicular across all the column density values in this

region. In L1172/1174, the major axis of the clumps are aligned more parallel to the cloud magnetic field and the ICMF. It is important to note that the sources which are considered here are not the ones with spherical shape (aspect ratio $\gtrsim 0.83$). The core L1174 showing two well separated peaks in the column density plot got filtered out due to our selection criteria. L1172 is a protostellar core which has also been considered as rounded core by Kauffmann et al. (2008) using c2d Bolocam data. Of the 20 clumps identified in L1172/1174, 10, 4 and 6 clumps show $\Delta\theta^{clump}_{Bcloud}$ <30°, 30° < $\Delta\theta^{clump}_{Bcloud}$ ⩽60° and $\Delta\theta^{clump}_{motion}$ > 60° respectively. Statistics of the distribution of $\Delta\theta^{clump}_{BICM}$ is also found to be similar to that of $\Delta\theta^{clump}_{Bcloud}$. In both L1228 and L1251, $\Delta\theta^{clump}_{BICM}$ and $\Delta\theta^{clump}_{Bcloud}$ seems to be distributed evenly showing lack of any preferred orientation.

In 11 clumps in L1147/1158, the offset between the clump major axis and the motion of the cloud falls within 30°< $\Delta\theta^{clump}_{motion}$ ≤60°and in another 11, the values are >60° suggesting that the major axis of the clumps tend to be oriented more perpendicular to the direction of motion. In L1172/1174 and L1228, the $\Delta\theta^{clump}_{motion}$ distribution seems to be more random. In L1251, 13 clumps show the values of $\Delta\theta^{clump}_{motion}$ ≤30° implying that the major axis of the clumps are aligned with the direction of the motion of the cloud. In fact, the cloud shows a blunt head and a tail which is filamentary is aligned almost parallel to the direction of the motion and it is here that the major axis of the majority of the clumps also aligned along both the filament and the direction of the motion of the cloud.

The distribution of differences between the core elongation and the inner magnetic field is shown in Fig. 7.7 for the four cloud complexes. Since there is not a significant dispersion within the inner magnetic field vectors, we consider the mean value for all the vectors within the contour level $\sim 1 \times 10^{21}$ cm^{-2}. We searched for possible correlation between the core elongation and the parsec scale magnetic field. Panel (a) and (b) for L1158 and L1172 suggest a bimodal distribution whereas panel (c) and (d) shows a random distribution of the differences for L1228 and L1251. This suggests that there is not any systematic trend on the relation between core elongation and magnetic field.

We also studied the relative orientation between major axis of cores and direction of motion. The distribution of difference between core elongation and angle of cloud motion is shown in Fig. 7.8. Panel (a) for L1157/1158 shows a preferential distribution towards 90°implying that most of the cores are perpendicular to the direction of motion. Panel (b) for L1172/1174 and L1228 show a random distribution whereas panel (d) for L1251 shows bimodal distribution with more cores lying predominantly along the the direction of motion. It is interesting to note that the direction of motion is also along the direction of magnetic field for the cloud. This suggests that the core orientations in L1251 is correlated with the direction of motion. Since it exhibits a cometary shaped morphology which is well consistent

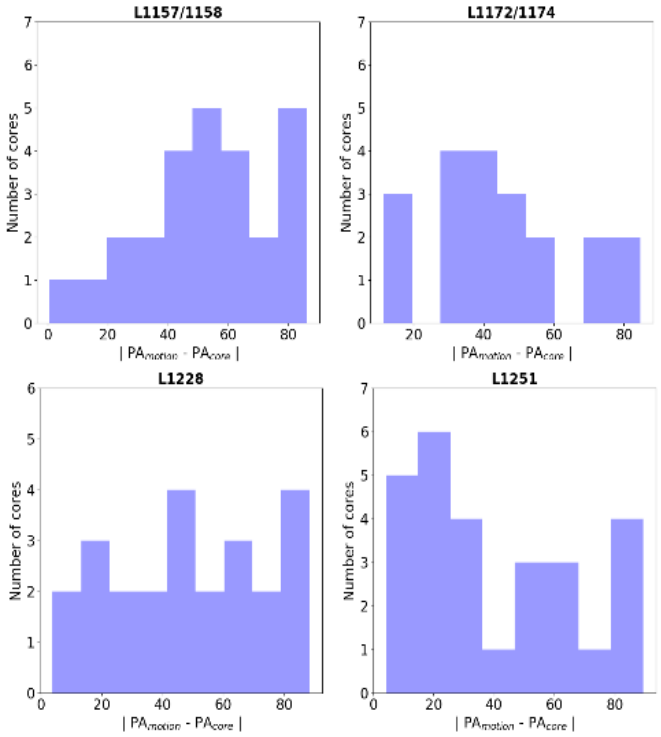

Figure 7.8: Histogram of the offsets between θ_{pos}^{clump} with respect to the direction of motion.

with the simulations suggested by Miniati et al. (1999), it might be possible that the core formation within the complex is governed by the direction of motion in the galaxy.

The difference in core angles and background magnetic field could provide hints about the relative importance of magnetic fields at the cloud-scale as compared to other factors like turbulence in gas motions and various feedback mechanisms. The general accepted paradigm is that the clouds with stronger magnetic field should have their cores major axes aligned perpendicular to the field as it is easier to gravitationally contract or collapse the material along the field lines. Previous studies also discussed that on the scales of 1-5 pc, the dense filaments tend to align perpendicular to the surrounding B-field (Cox et al., 2016). One of the complex here shows a bimodal distribution of offsets between core major axis and B-field direction. The different distribution of the core and B orientation could tell us about the star formation activity of the cloud. The L1158/L1147 complex as discussed show a well ordered B-field and filaments are oriented along the field lines. Since all the derived cores are associated with the filaments, we expect that the core elongation agrees with the filament orientations. Most of the cores are perpendicular to the background as well core-scale magnetic field. The region overall is quiescent and showing low star formation activity. Again, similar to core axis and B-field relation, there is preferential distribution of

cores orientation perpendicular to the direction of motion. This region could be in the effect of the kinematic motion of the cloud in space which is governing the formation of cores.

Contrary to this, L1172/1174 is very active star forming region with a curved B-field morphology. The bimodality of difference in core axis and B-field is not found when compared with the direction of motion. It is completely random which could be because that the formation of cores in this region is regulated mostly by the star formation activity in the complex not by motion as the stellar feedback from HD 200775 is affecting the head part of the complex (see chapter 3).

The L1228 complex at relatively higher galactic latitude is again quiescent region with more number of prestellar cores distributed in the complex. The randomness of difference between core axis and motion could be again the effect of feedback in the cloud but the formation might be governed by the large-scale magnetic field. There is bimodality satisfied within the core-angles also similar to filament distributions. The L1251 complex has a strikingly cometary shape along the direction of motion. Overall, these complexes of Cepheus Flare region showing different star-forming activity shows a diverse distribution of core orientation with respect to magnetic field and the direction of motion. This suggests that the relative orientation of clumps might be a consequence of individual star-forming properties and the physical conditions present in each cloud.

7.4 Conclusions

We present results of a study conducted on four molecular cloud complexes situated in the Cepheus Flare region, L1147/1158, L1172/1174, L1228 and L1251. Using the *Gaia* DR2 data for the YSOs associated with these clouds we estimated a distance of 372±12 pc and 360±15 pc for L1228 and L1251 respectively implying that all the four complexes are located at similar distances from us. Using proper motions of the YSOs, radial velocity of the clouds and assuming that both are kinematically coupled, we estimated the space velocity and their positions in the Galaxy. All the four clouds are found to be located at a Galactic height in the range of $\sim 80-130$ pc. The space velocity of the clouds are found to be 8.5 km s^{-1}, 7.4 km s^{-1}, 12.3 km $s^{-1}$and 8.5 km $s^{-1}$for L1147/1158, L1172/1174, L1228 and L1251 respectively. The clouds are found to be in motion at an offset of $\sim 30^{\circ}$ with respect to the ambient magnetic fields inferred from the *Planck* polarization measurements except in the case of L1172/1174 in which the offset is $\sim 45^{\circ}$. The inner and outer magnetic field orientations are found to be nearly parallel suggesting that the cloud magnetic fields are inherited from the ICMF. We extracted a total of 26, 20, 24 and 27 clumps in L1147/1158, L1172/1174, L1228 and L1251 respectively using Astrodendro algorithm. In L1147/1158,

the major axis of the clumps are found to be oriented predominantly orthogonal to both ICMF and cloud magnetic fields while in L1172/1174, the major axis of the clumps are found to be aligned more parallel to the field lines. In L1228 and L1251 the offset between the major axis of the clumps and the field lines are oriented more randomly. With respect to the motion of the clouds, there is a marginal trend of the clump major axis being more perpendicular in L1147/1158 and more parallel in L1251. In L1172/1174 and L1228 the clump major axis are oriented more randomly.

Table 7.1: *Gaia* results of YSOs associated with the L1147/1158 and L1172/1174 complexes.

Source Name	RA	Dec	l	b	D	μ_α	$\Delta\mu_\alpha$	μ_δ	$\Delta\mu_\delta$
	(°)	(°)	(°)	(°)	(pc)	(mas/yr)	(mas/yr)	(mas/yr)	(mas/yr)
(1)	(2)	(3)	(4)	(5)	(6)	(7)	(8)	(9)	(10)
L1147/1158									
2MASS J20361165+6757093	309.048672	+67.952608	102.4221	+15.9738	336^{20}_{-22}	7.436	0.351	-1.514	0.284
IRAS 20359+6745	309.082855	+67.942131	102.4205	+15.9573	343^{12}_{-13}	7.753	0.189	-1.469	0.143
PV Cep	311.474902	+67.960735	102.9697	+15.2315	341^{6}_{-7}	8.228	0.126	-1.976	0.110
L1172/1174									
FT Cep	314.845315	+68.245467	103.9926	+14.4053	339^{4}_{-4}	7.333	0.087	-1.599	0.079
2MASS J21002024+6808268	315.084447	+68.140772	103.9661	+14.2704	341^{9}_{-10}	7.630	0.147	-1.182	0.158
2MASS J21005550+6811273	315.231481	+68.190885	104.0418	+14.2596	332^{12}_{-13}	7.205	0.184	-1.649	0.280
NGC 7023 RS 2	315.359984	+68.177338	104.0621	+14.2140	325^{6}_{-6}	7.652	0.104	-1.416	0.121
NGC 7023 RS 2B	315.362884	+68.177214	104.0627	+14.2131	360^{12}_{-13}	6.667	0.174	-0.865	0.189
LkHα 425	315.400352	+68.139576	104.0418	+14.1785	332^{6}_{-6}	6.971	0.106	-1.638	0.117
HD 200775	315.403923	+68.163263	104.0616	+14.1924	357^{5}_{-5}	8.336	0.079	-1.566	0.083
NGC 7023 RS 5	315.427117	+68.215960	104.1093	+14.2191	323^{8}_{-8}	7.530	0.148	-0.668	0.164
FU Cep	315.444875	+68.145894	104.0577	+14.1696	335^{4}_{-4}	7.770	0.071	-1.428	0.078
FV Cep	315.558650	+68.233141	104.1549	+14.1923	321^{25}_{-30}	8.666	0.528	-1.736	0.568
LkHα 428 N	315.617758	+68.058287	104.0301	+14.0642	343^{6}_{-6}	6.868	0.098	-1.319	0.107
FW Cep	315.637634	+68.124746	104.0878	+14.1008	336^{2}_{-2}	7.054	0.044	-1.017	0.043
NGC 7023 RS 10	315.747855	+68.108939	104.1022	+14.0590	323^{4}_{-4}	7.174	0.079	-1.738	0.075
EH Cep	315.851719	+67.985134	104.0295	+13.9501	326^{7}_{-7}	7.269	0.140	-2.330	0.128
2MASS J21035938+6749296	315.997585	+67.824847	103.9389	+13.8053	346^{8}_{-8}	7.722	0.152	-2.061	0.133

Continued on next page...

Table 7.1 – ...continued from previous page

Source Name	RA (°)	Dec	l	b	D	μ_α	$\Delta\mu_\alpha$	μ_δ	$\Delta\mu_\delta$
	(°)	(°)	(°)	(°)	(pc)	(mas/yr)	(mas/yr)	(mas/yr)	(mas/yr)
(1)	(2)	(3)	(4)	(5)	(6)	(7)	(8)	(9)	(10)
L1228									
2MASS J20584668+7740256	314.694891	+77.673875	111.7897	+20.1974	344^{25}_{-30}	6.877	0.423	3.691	0.363
2MASS J21005285+7703149	315.220237	+77.054169	111.3338	+19.7352	383^{12}_{-13}	5.684	0.146	4.250	0.147
2MASS J21012919+7702373	315.370747	+77.043700	111.3465	+19.7019	383^{8}_{-7}	5.381	0.087	4.458	0.082
2MASS J21012919+7702373	315.372805	+77.043769	111.3468	+19.7016	372^{5}_{-5}	5.271	0.064	3.854	0.061
2MASS J21013267+7701176	315.385687	+77.021545	111.3299	+19.6859	382^{6}_{-6}	4.996	0.080	4.591	0.076
2MASS J21014960+7705479	315.456720	+77.096668	111.3299	+19.6859	368^{12}_{-14}	4.996	0.080	4.591	0.076
2MASS J21020488+7657184	315.520565	+76.955170	111.2933	+19.6216	371^{2}_{-1}	5.982	0.024	3.490	0.023
†2MASS J21030242+7626538	315.759650	+76.448351	110.9023	+19.2695	330^{33}_{-40}	4.666	0.512	3.579	0.638
2MASS J21030242+7626538	315.761082	+76.448379	110.9025	+19.2692	360^{6}_{-5}	5.537	0.066	2.519	0.096
2MASS J21055189+7722189	316.466412	+77.371980	111.7800	+19.7100	419^{9}_{-8}	4.686	0.095	3.910	0.091
L1251									
2MASS J22351668+7518471	338.819607	+75.313082	114.5620	+14.7206	362^{6}_{-6}	6.745	0.074	1.382	0.065
2MASS J22352542+7517562	338.855984	+75.298960	114.5626	+14.7037	360^{13}_{-13}	7.004	0.158	0.719	0.133
2MASS J22352722+7518019	338.863513	+75.300554	114.5652	+14.7041	393^{14}_{-15}	7.063	0.150	0.686	0.135
2MASS J22381872+7511538	339.578072	+75.198277	114.6731	+14.5234	368^{12}_{-12}	7.360	0.132	1.370	0.130
2MASS J22374953+7504065	339.456610	+75.068466	114.5776	+14.4271	343^{3}_{-3}	6.356	0.038	0.928	0.038
2MASS J22392717+7510284	339.863479	+75.174575	114.7260	+14.4662	334^{6}_{-7}	6.373	0.090	1.100	0.085
2MASS J22381522+7507204	339.563569	+75.122351	114.6302	+14.4597	386^{16}_{-17}	7.202	0.169	0.684	0.168
2MASS J22382962+7514266	339.623507	+75.240739	114.7056	+14.5542	345^{14}_{-16}	6.537	0.211	0.798	0.209
2MASS J22384046+7508413	339.668708	+75.144805	114.6660	+14.4655	345^{17}_{-18}	6.052	0.221	1.168	0.218

Continued on next page...

Table 7.1 – ...continued from previous page

Source Name	RA (°)	Dec	l	b	D	μ_α	$\Delta\mu_\alpha$	μ_δ	$\Delta\mu_\delta$
	(°)	(°)	(°)	(°)	(pc)	(mas/yr)	(mas/yr)	(mas/yr)	(mas/yr)
(1)	(2)	(3)	(4)	(5)	(6)	(7)	(8)	(9)	(10)
2MASS J22391466+7507162	339.811230	+75.121196	114.6864	+14.4267	366^{11}_{-11}	6.914	0.135	0.704	0.136
2MASS J22410470+7510496	340.269829	+75.180475	114.8221	+14.4196	330^{8}_{-9}	6.257	0.132	1.289	0.120

†There are two sources within 1″ search radius.

Table 7.2: *Gaia* results of YSOs associated with the L1147/1158 and L1172/1174 complexes.

Complex	D	μ_α	μ_δ	$\mu_{l\star}$	μ_b	θ^M_{pos}	V_{lsr}	(u, v, w)	$^\dagger\theta^B_{pos}$
	(pc)	(mas/yr)	(mas/yr)	(mas/yr)	(mas/yr)	(°)	(km s^{-1})	(km s^{-1})	(°)
(1)	(2)	(3)	(4)	(5)	(6)	(7)	(8)	(9)	(10)
L1147/1158	341±3	7.753±0.317	-1.514±0.045	3.100±0.128	-7.256±0.237	157	2.7	4.7, -3.7, -6.1	3, 6
L1172/1174	336±7	7.483±0.283	-1.540±0.197	3.361±0.302	-6.769±0.408	152	2.5	4.6, -3.1, -4.9	28, 16
L1228	372±12	5.345±0.344	3.882±0.380	6.539±0.280	-1.736±0.352	105	-7.8	3.7, -11.6, -1.4	84, 88
L1251	360±15	6.745±0.372	0.928±0.240	6.336±0.261	-2.530±0.326	112	-4.0	3.7, -7.6, 0.3	79, 81

†Projected magnetic field orientation of inside and outside of the cloud.

Chapter 8

Core orientations and magnetic fields in molecular clouds showing asymmetric morphology

8.1 Introduction

In molecular clouds, the filamentary structures are ubiquitous which are believed to be created by compression of material due to multiscale supersonic flows (Alves et al., 2014). Some localised density enhancements will shrink under self-gravity to form prestellar cores and then collapse to become protostellar which will ultimately become stars (Shu et al., 1987). These prestellar cores are the preferential and ideal sites of low mass star formation in nearby dark clouds like Taurus and Perseus. Previous studies based on the optical inspection of the Palomar sky plate and molecular line observations in NH_3, N_2H^+ showed that the dense cores are typically of size $\sim$ 0.1 pc and contain a few solar mass of subsonic material at temperatures of 10 K and with an average volume density $\sim 10^4$ cm^{-3} (Benson & Myers, 1983; Myers & Benson, 1983). The correlation of dense core positions with the locations of highly embedded YSOs led to the fact that some cores are forming stars currently or some of them have started it very recently. On the basis of association of YSO or IRAS source, the cores are broadly divided into two categories: prestellar and protostellar core. Cores are observed in dust continuum and molecular line observations. The results from the *Herschel* Gould Belt survey suggests that the cores are mostly being embedded in the filaments (Alves et al., 2014; André et al., 2010; Klessen & Hennebelle, 2010). The association is consistent with the theoretical prediction that the thermally supercritical filaments experience a longitudinal fragmentation into cores (Inutsuka & Miyama, 1992).

The significance of magnetic fields on the star formation process has been a subject of ongoing debate (e.g., Crutcher, 2012; Li et al., 2014). It is widely accepted that the magnetic fields along with the other physical factors like turbulence and gravity are the key agents affecting star formation process at different scales and different evolutionary stages (Ballesteros-Paredes et al., 2007; McKee & Ostriker, 2007). A number of observations were carried out to understand the dynamical importance of magnetic fields (Alves et al., 2008; Commerçon et al., 2011; Palau et al., 2013; Sugitani et al., 2010).

The cloud-scale magnetic field at the lower densities can affect the compression in turbulence-induced shocks and channel the flows towards the high density regions (Heyer et al., 2008). The core-scale magnetic field regulates the gas dynamics within the cores like removing angular momentum in collapsing cores. The correlation between magnetic field in dense cores and the core orientation is well established in starless and star-forming regions. In continuation with that, the magnetic fields at the intermediate scales connecting the large scale magnetic field to the field within cores can have a significant effect on their dynamics and the structure. Li et al. (2017) suggested a bimodal distribution of cloud and magnetic field alignment which can be either parallel or perpendicular and found magnetic field as a primary regulator of star formation rate using Planck polarization observations. But how the morphology of dense core structures are affected due to large-scale magnetic field orientation is less explored.

Observational studies conducted by Poidevin et al. (2014) on the cores extracted from 350 μm Herschel observations to investigate the core orientations in Lupus I cloud with respect to the large-scale magnetic field. The environment plays an important role in shaping the prestellar cores through ram pressure and magnetic pressure (Chen & Ostriker, 2018). Cores are usually either oblate or prolate shaped structures as suggested by MHD simulations (Banerjee et al., 2009; Chen & Ostriker, 2018) . There are anisotropic gas flows along the magnetic field lines during the formation and evolution of cores which lead to the preferential orientation of the cores along the background magnetic field lines. Chen et al. (2020), by combining simulations and observational results from the archive, studied a sample of three clouds and investigated whether there is any systematic relation between the core orientation and the cloud-scale magnetic field.

Optical polarization of starlight is used as a technique to trace the plane-of-sky magnetic field geometry which typically works in regions of low extinction (A_V ~1-5). Thus, optical polarimetry is mainly applicable towards the low density parts of the clouds. This is because the non-spherical dust grains believed to be aligned with their major axes perpendicular to the magnetic field causes selective extinction making the starlight polarized. At higher extinctions, the background starlight gets extinguished completely making it impossible to

measure any polarization (e.g., Alves et al., 2008; Goodman et al., 1990; Hiltner, 1949; Soam et al., 2013; Vrba et al., 1976). The polarized thermal dust emission is used as a technique to trace the plane-of-sky magnetic field geometry of regions with high obscurations. This is because the non-spherical dust grains that are believed to be aligned with their major axes perpendicular to the magnetic field emit radiation which is polarized in a direction parallel to the major axis of the dust grains. The all-sky maps of polarized dust emission from dust using the *Planck* satellite at wavelengths of 353 GHz emission gives an important insight into the Galactic magnetic field in the star-forming regions.

In this chapter we present results from our study of seven isolated starless clouds that manifest asymmetry in their physical appearance with sharp edges on one side and an extended distribution on the opposite side. The asymmetry in their appearance suggests that these clouds may have had interaction with some external influence during the process of their formation. The questions that we are trying to investigate are the following:

1. What is the relationship between the magnetic field orientations inside the clouds inferred from the *Planck* polarization and the envelope field inferred from the optical polarization measurements of background starlight?

2. What is the relationship between the magnetic field orientation with the elongation seen in the clouds?

3. How the core major axes are oriented with respect to both inside and outside magnetic field directions?

Of the seven clouds, for two of them we obtained polarization measurements of stars projected on them in R-band. For the other five, we obtained polarization data from the archive. To infer magnetic field orientation towards the denser regions, we used the *Planck* polarization measurements. While the R-band polarization measurements infer the magnetic field geometry of the outer envelope of the clouds, the *Planck* polarization measurements trace the field orientations towards inner regions of the cores. By combining the results obtained from both the techniques, we have studied the magnetic field geometry from cloud-scale to down to the core-scale. The chapter is organized in the following manner. We begin with a description of the clouds selected for the present study followed by a discussion on the observations and the data reduction. Then we present results from our R-band polarization measurements and describe the procedure adapted to extract the cores in each cloud. We discussed our main results and conclude the chapter with a summary.

8.2 Description on the individual clouds

8.2.1 Clouds observed in this work

In the previous chapters we presented optical polarization measurements of the stars projected on the cloud L1157 and the Planck polarization on four cloud complexes located in the Cepheus Flare region. In this chapter we present results of polarization observations of the stars projected on two isolated, nearby starless clouds, LDN 1512 (hereafter L1512; Lynds, 1962) also known as CB 27 (Clemens & Barvainis, 1988) and LDN 1523 (hereafter L1523; Lynds, 1962) also known as Barnard 29 (Barnard, 1919). Both L1512 and L1523, identified on the DSS image [1] in Fig. 8.1, are peculiar as they show an asymmetry in their overall morphological appearance having a relatively sharp edge on one side and an extended feature on the opposite. Below we describe briefly the information gathered from the literature on the sources for which we observations.

8.2.1.1 L1512

L1512 is classified as a starless core located near the edge of the Taurus-Auriga molecular cloud complex (Lin et al., 2020). Benson & Myers (1989) classified this cloud as an isolated globule based on the fact that this cloud is separated from the nearest neighbouring clouds by several cloud diameter. It is considered to be at a distance of 140±20 pc away from us (Benson & Myers, 1989; Elias, 1978; Hilton & Lahulla, 1995) similar to the distance of the Taurus molecular clouds. The cloud has a V_{lsr} velocity of 7.09 km s^{-1}(Benson & Myers, 1989; Myers et al., 1983). Based on a chemical modelling study of the deuteration profiles of L1512, Lin et al. (2020) suggested that the cloud is 1.4 Myr old. The L1512 envelope shows no significant infall but probably undergoing oscillatory or expansion motion (Lee et al., 2001; Sohn et al., 2007). Falgarone et al. (1998, 2001) noted that the cloud exhibits extremely sharp southern edge and Kim et al. (2016) proposed that the cloud morphology could be caused by external radiation from an A-type main-sequence star located in its vicinity. The ^{12}CO (J=2-1) distribution is found to be highly anisotropic, complex and is concentrated in a network of filamentary structures with the dense core located at the point of convergence of all these filaments (Falgarone et al., 2001). They also found that the gas is far from being in a quiescent state, and various gas motions are detected at different scales. It is suggested that the filaments may be spinning along their long axis, with velocity gradients up to ~8 km

[1]The Digitized Sky Survey (DSS), is a ground-based imaging survey of the entire sky in several colors. The survey, performed with Palomar and UK Schmidt telescopes, produced photographic plates that were later digitized at the Space Telescope Science Institute (STScI) to produce the Hubble Guide Stars Catalog (GSC).

s^{-1} pc^{-1}. The results obtained are interpreted as evidence of an MHD instability developing in filaments that are threaded by a helical magnetic field (Falgarone et al., 2001).

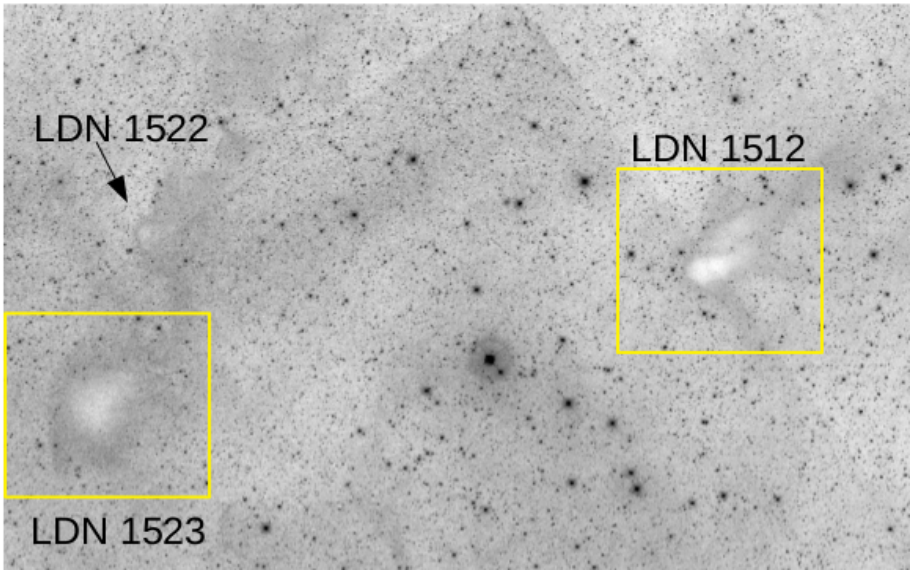

Figure 8.1: Positions of LDN 1512 and L1523 identified on the DSS image. A nearby cloud LDN 1522 is also identified. All the three clouds show sharp edges on their eastern sides.

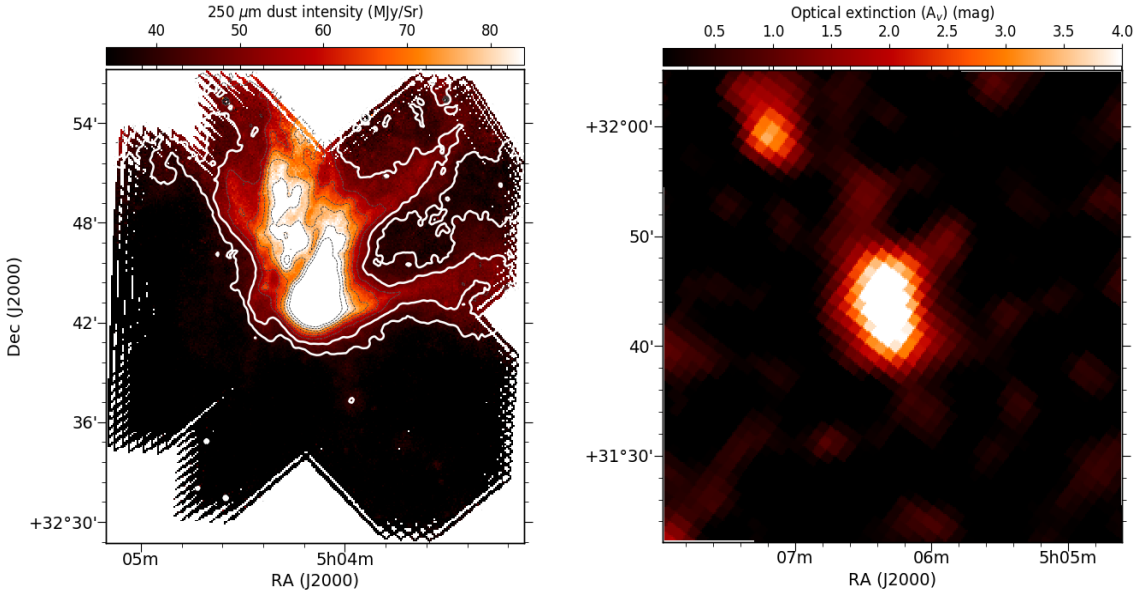

Figure 8.2: **Left:** The Herschel 250 μm SPIRE image of L1512 cloud of size 0.5°×0.5°with intensity contours shown in white lines. **Right:** Extinction map for L1523 cloud of size 0.5°×0.5°produced using the 2MASS data (Dobashi, 2011).

8.2.1.2 L1523

L1523 is located ∼1° to the south-eastern side of L1512. L1523 was also classified as an isolated (Benson & Myers, 1989) starless globule (Beichman et al., 1986). Based on star count method, Tomita et al. (1979) estimated a distance of 200 pc to L1523 whereas in other studies, authors have adopted a distance of 140 pc (e.g., Myers et al., 1983; Wu et al., 1992) considering it to be a part of the Taurus molecular cloud. The cloud has a V_{lsr} velocity of 7.01 km s^{-1}(Myers et al., 1983) similar to L1512. The cloud lacks discernible sharp edges but show asymmetry in the distribution of the diffused material around it very much similar to the distribution of material seen around L1512 (Fig. 8.1). Interestingly, the another cloud L1522 lying to the north of L1523 do show sharp edges to the south-eastern parts of it suggesting that some external agent must be responsible for their appearances. Previous studies found that the ^{13}CO (1-0) line studies for this core shows narrow line-width which indicates the cold and quiescent internal physical conditions (Kim & Hong, 2002; Kim et al., 2008). Having no depletion at the centre of the cloud suggests that the L1523 is chemically evolved core.

8.2.2 Clouds for which the data taken from the archive

In addition to L1512 and L1523, we selected five more molecular clouds that show an symmetry in their morphology and have polarization measurements of the stars projected on them made with the same telescope and the instrument combination.

The details of the five clouds, LDN 1521E (hereafter L1521E), LDN 1517 (hereafter L1517), LDN 1544 (hereafter L1544), LDN 1780 (hereafter L1780) and LDN 183 (hereafter L183) are given in Table 8.2. The number of fields observed and the total number of stars projected on each cloud for which polarization measurements were made are given in the columns 4 and 5 respectively. These are the sources having the ratio, $P/e_p, \geq 3$. In columns 6 we give the distances of the clouds taken from the literature and the respective references are given in column 7. The data for the clouds, L1517, L1780 and L183 are obtained from the previous studies. The fields containing L1521E and L1544 were observed using AIMPOL which we obtained through private communication with the PI.

8.2.2.1 L1521E

LDN 1521E (hereafter L1521E; Lynds, 1962) cloud is located in the Taurus molecular cloud at a distance of $\sim 145^{+12}_{-16}$ pc (Yan et al., 2019). Presence of high abundances of carbon-chain molecules compared to its neighbouring regions made Hirota et al. (2002) to classify it as a very young starless core (Hirota et al., 2002). Tafalla & Santiago (2004) found no C^{18}O (1-0)

depletion towards the centre of the core and estimated a chemical age of $\leq 1.5\times 10^5$ yr. The mass of the core is 1±0.1 $M_\odot$ and the dust temperature is 9.8±0.2 K based on the *Herschel* SPIRE observations (Makiwa et al., 2016). The large scale $C^{18}O$ integrated intensity map clearly shows an extended emission of gas in the north-south direction with sharp gradient to its south side Tafalla & Santiago (2004). In Fig. 8.3 we show the *Herschel* 250 μm image of L1521E. The outermost contour is plotted at 3 times the background rms above the background emission. The cloud shows an extended emission towards the northern side with sharp edges towards its southern boundary.

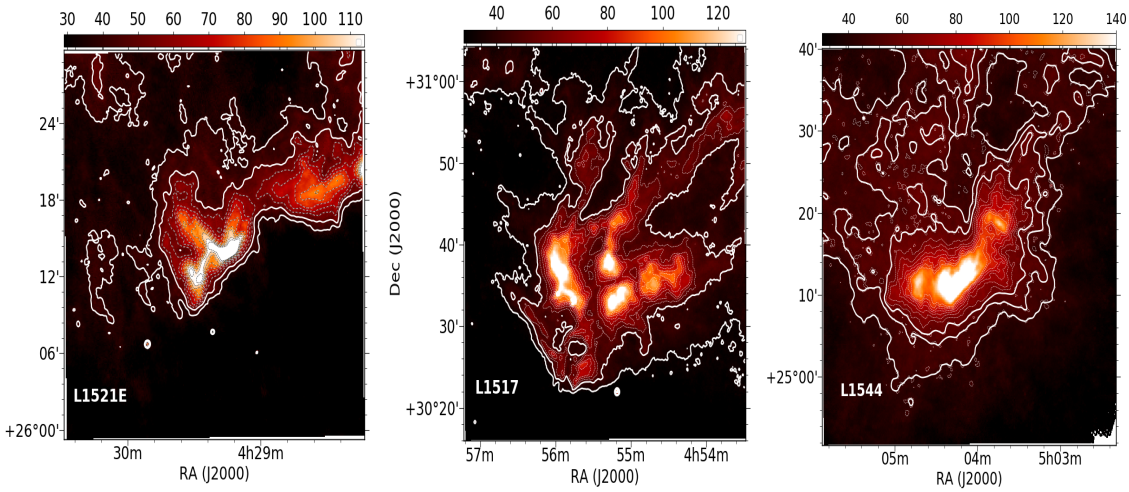

Figure 8.3: The 250 μm image of L1521E, L1517 and L1544. The outermost contour is plotted 3 times the background rms above the background emission.

8.2.2.2 L1517

L1517 is relatively isolated dark cloud which is disturbed by the near pre-main sequence stars AB Aurigae and SU Aurigae. The stars being physically associated with the cloud are heating the surrounding gas (Nachman, 1979). Hacar & Tafalla (2011) studied the fragmentation of the cloud into multiple cores. The V_{lsr} of the cloud is found to be $\sim$ 5.7 kms^{-1} using IRAM 30 m molecular line observations. We assigned a distance of 160±3 pc distance to the cloud based the *Gaia* DR2 distances of the young stars AB Aur and SU Aur which are responsible for illuminating reflection nebulosity (Magakian, 2003; Schneider & Elmegreen, 1979). The CO observations show an extended distribution of the gas to the northwest of the nebulosity and consists of several filamentary structures and optical obscuration (Heyer et al., 1987). Radio observations revealed a number of cores associated with the cloud and one of these, L1517B, was studied in detail owing to its regular shape and molecular freeze out which is a signature of it being in an advanced stage of evolution (Tafalla et al., 2004, 2006). One of

the remarkable feature of the cores in L1517 is that they all appear to be starless (Beichman et al., 1986; Kirk et al., 2007b; Strom et al., 1976). In Fig.8.3 we show the *Herschel* 250 μm image of L1517. The outermost contour is plotted 3 times the background rms above the background emission. The cloud shows a extended emission towards the northern side with sharp edges towards its southern boundary very much similar to L1521E.

8.2.2.3 L1544

L1544 is a prototypical prestellar core (Ward-Thompson et al., 1999) considered to be associated with the Taurus molecular cloud complex. It is found to be highly centrally concentrated with a central density of 2×10^6 cm^{-3} and show very low central temperatures ranging from 5 to 11 K in the inner parts (Crapsi et al., 2007). Evidence of a slow quasi-static contraction (Keto et al., 2015; Tafalla et al., 1998), CO freeze-out and enhanced deuteration (Caselli et al., 1999, 2002b; Vastel et al., 2006) is seen in the core. L1544 shows signatures of chemical differentiation, with and offset seen between the distribution of methanol away from the sharp H_2 column density drop seen toward the southeast of the core (Spezzano et al., 2016, 2017). In Fig. 8.3 we show the *Herschel* 250 μm image of L1544. Here again, the outermost contour is plotted at three times the background rms above the background emission. The cloud shows a extended emission towards the north-eastern side with sharp edges towards its south-western boundary. L1544 also shows signs of chemical differentiation, with methanol residing away from the sharp H_2 column density drop toward the southeast of the core, rich in carbon chain molecules

8.2.2.4 L1780

L1780, also called MBM 33 is a cometary-shaped high latitude ($b \sim 36^\circ$) translucent cloud having a maximum extinction of ~4 magnitude (Snow & McCall, 2006) at a distance of 74±3 pc (Zucker et al., 2019). LDN 1780 show a moderate column density of a few$\times10^{21}$ cm^{-2}. It is one of those few clouds where emission show spatially distinct distributions at different infrared wavelengths, suggesting the presence of spatially different dust populations (Chlewicki et al., 1987; del Burgo & Cambrésy, 2006; Laureijs et al., 1995; Ridderstad & Juvela, 2010). The far-infrared emission at 100 μm and 200 μm, caused mainly by big grains, are found to peak in the western parts of the cloud while the 60 μm emission (mostly due to smaller grains) seems to show a peak at the middle part of the cloud. The polycyclic aromatic hydrocarbon (PAH) emission seems to be strongest towards the tail part of the cloud . The *Herschel* SPIRE 250 μm image of the cloud is shown in Fig. 8.4. The outermost contour is drawn at five times the background rms above the background emission. The image clearly

shows its cometary shape with the head-tail morphology oriented parallel to the east-west direction. The R-band polarization measurements of stars projected on L1780 was carried out by Neha et al. (2018). The magnetic field inferred from the polarization are found to be parallel to the overall cometary shape of the cloud.

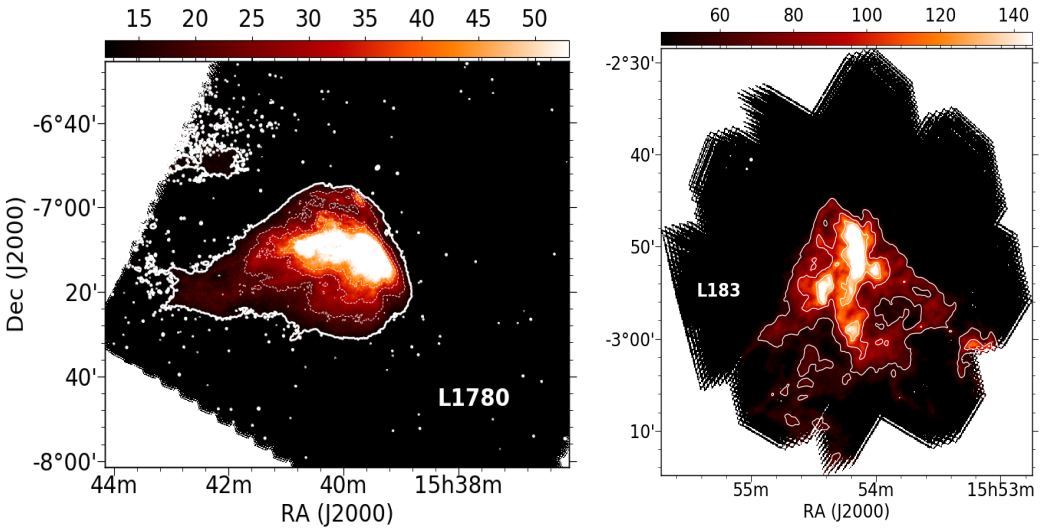

Figure 8.4: The 250 μm image of L1780 and L183. The outermost contour is plotted 3 times the background rms above the background emission.

8.2.2.5 L183

L183 and the nearby L134 form a group of starless clouds at a relatively high Galactic latitide of ($b \sim 37°$). The distance of the cloud is 115±5 pc (Zucker et al., 2019). The cloud contains a very dense, low-temperature cores with prestellar condensations occurring currently and exhibits the coreshine effect (Dickens et al., 2000; Pagani et al., 2004, 2003, 2005). Based on H-band polarimetric observations of stars projected on the cloud, Clemens (2012) suggested that the envelope field oriented almost perpendicular to the field seen at 850 μm is more closely aligned with the rotation axis of the dense gas core. In Fig. 8.4 we show the cloud morphology based on its emission at 250 μm imaged with the *Herschel* SPIRE instrument. The outermost contour is drawn at three times the background rms above the background emission. The cloud shows an asymmetric distribution with sharp boundaries towards the north and diffuse emission seen towards the opposite direction. This north-south elongation was reported by Pagani et al. (2003) who studied this region using the MAMBO 1.2 mm observations.

Table 8.1: Log of the observations.

ID	Cloud Identification	Date of observations
1	L1512	26-30 October, 2017
2	L1523	28 October; 23, 24, 25 November 2016

8.3 Observations and data reduction

Polarization measurements of stars projected on L1512 and L1523 were carried out using the AIMPOL. The polarization measurements were done in the standard Johnson R-band. Table 8.1 shows the log of the observations for L1512 and L1523. A detailed description on the AIMPOL and the data reduction procedure and the whole analysis are explained in chapter 2. Similar to the methodology used in Chapter 7, here also we extracted the *Planck* data from Planck Legacy Archive for the fields containing our sample sources and used Planck polarization data and intensity at 353 GHz frequency band. The I, Q and U maps were constructed at $8^{'}$ resolution using the gnomic projection of the HEALPix all sky maps.

8.4 Polarization results

The right ascension, declination of L1512 and L1523, the number of fields observed and total number of stars observed in the direction of each cloud are given in the columns 1, 2, 3, 4 and 5 of Table 8.2. The distance to the clouds obtained from the literature are given in column 6. The references for the distances to the clouds are in column 7. In total we detected polarization for 134 and 135 stars towards the directions of L1512 and L1523 respectively. After applying the condition that the stars should have the ratio of the degree of polarization (P_{op}%) and the error in the degree of polarization (e_p) greater than 3, we obtained a total of 94 and 97 sources towards L1512 and L1523 respectively which we have used for our further analysis.

The P_{op}% and the polarization position angle (θ_{op} in degree) of the 94 stars projected on L1512 are shown in Fig. 8.5 (Left) using open circles in blue. The values of P_{op} range from ~0.4% to ~6% and the θ_{op} range from ~73° to ~207°. The mean value of P_{op} is found to be 2.5% with a standard deviation of 1.3%. The right panel in Fig. 8.5 shows the histogram of the θ_{op} values in L1512. Based on a Gaussian fit to the data, the mean values of the θ_{op} for the stars projected on the L1512 is found to be 158° with a standard deviation of 16°. The polarization results obtained from the *Planck* data for L1512 is shown in Fig. 8.5 using open circles in red. The *Planck* polarization results are selected from the regions where the 250 μm intensity is greater than three times of the standard deviation above the background

Table 8.2: The R-band polarization measurements.

Name of the clouds (1)	RA (°) (2)	Dec (°) (3)	No. of fields (4)	No. of stars observed (5)	Distance (in parsec) (6)	Ref. (7)
			This work			
L1512	76.044615	+32.720758	7	94	140±20	1, 2
L1523	76.552195	+31.699365	6	97	140	3, 4
			From archive			
L1521E	67.336701	+26.239465	6	98	145^{+12}_{-16}	5
L1517	73.940972	+30.551346	5	99	160±3	6
L1544	76.063518	+25.178058	7	136	130±6	7
L1780	234.922838	-07.167661	6	41	74	8, 9
L183	238.550219	-02.828594		26	115	8, 9

1. Elias (1978), 2. Benson & Myers (1989), 3. Myers et al. (1983), 4. Wu et al. (1992), 5. Yan et al. (2019), 6. Bailer-Jones et al. (2018), 7. Zucker et al. (2020), 8. Zucker et al. (2019), 9. Neha et al. (2018).

intensity. The mean values of the polarization position angles (θ_{plk}) obtained from the *Planck* polarization for L1512 is found to be 158° with corresponding standard deviations of 8°.

The P_{op} and θ_{op} for the 97 stars projected on L1523 are shown in Fig. 8.6 (Left) using open circles in blue. The values of P_{op} range from ~0.5% to ~8% and the θ_{op} range from ~85° to ~233°. The mean value of P_{op} is found to be 2.5% with a standard deviation of 1.3%. The right panel in Fig. 8.6 shows the histogram of the θ_{op} values of the stars projected on L1523. The mean value of θ_{op} for the stars projected on L1523 obtain by making a Gaussian fit to the data is found to be 130° with a standard deviation of 14°. The polarization results obtained from the *Planck* data for L1523 is shown in Fig. 8.6 using open circles in red. Here again, the *Planck* polarization results are selected from the regions where the 250 μm intensity is greater than three times of the standard deviation above the background intensity. The mean values of the polarization position angles (θ_{plk}) obtained from the *Planck* polarization for L1523 is found to be 132° with corresponding standard deviations of 9°.

A total of 98 sources were found towards L1521E having $P/e_p \geq 3$. The P_{op} vs. θ_{op} for these sources are presented in Fig. 8.7 (upper left panel). The P_{op} values are found to range from 1.6% to 6.1% and the θ_{op} values range from 14° to 74°. The mean value of the P_{op} and the corresponding standard deviation are found to be 3.1% and 0.8% respectively. The histogram of the θ_{op} values is shown in Fig. 8.7 (lower left panel). We fitted a Gaussian function to the distribution of the θ_{op} and obtained a mean value of 33° with a dispersion of 8°. The polarization measurements obtained from the *Planck* data selected from regions

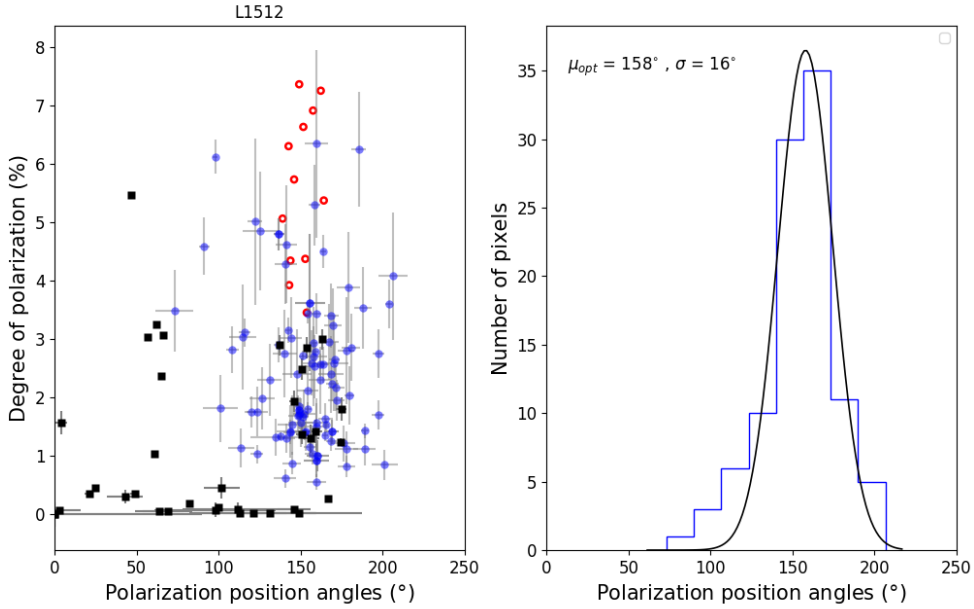

Figure 8.5: The P% vs. θ_{op} plot and histogram plot of θ_{op} for L1512. The blue and red symbols show our R-band and the *Planck* polarization results and the filled squares show the polarization measurements taken from the Heiles (2000) catalog.

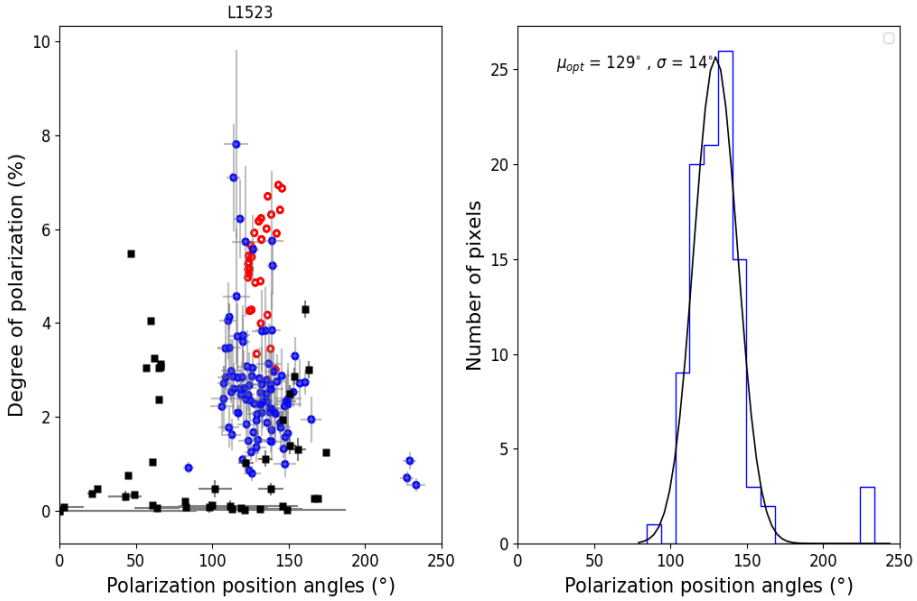

Figure 8.6: The P% vs. θ_{op} plot and histogram plot of θ_{op} for L1523. The blue and red symbols show our R-band and the *Planck* polarization results and the filled squares show the polarization measurements taken from the Heiles (2000) catalog.

having the 250 μm intensity greater than three times of the standard deviation above the background intensity for L1521E are shown in Fig. 8.7 (upper left panel) using open circles in red. The mean value of the θ_{plk} is found to be 30° with a standard deviation of 6°.

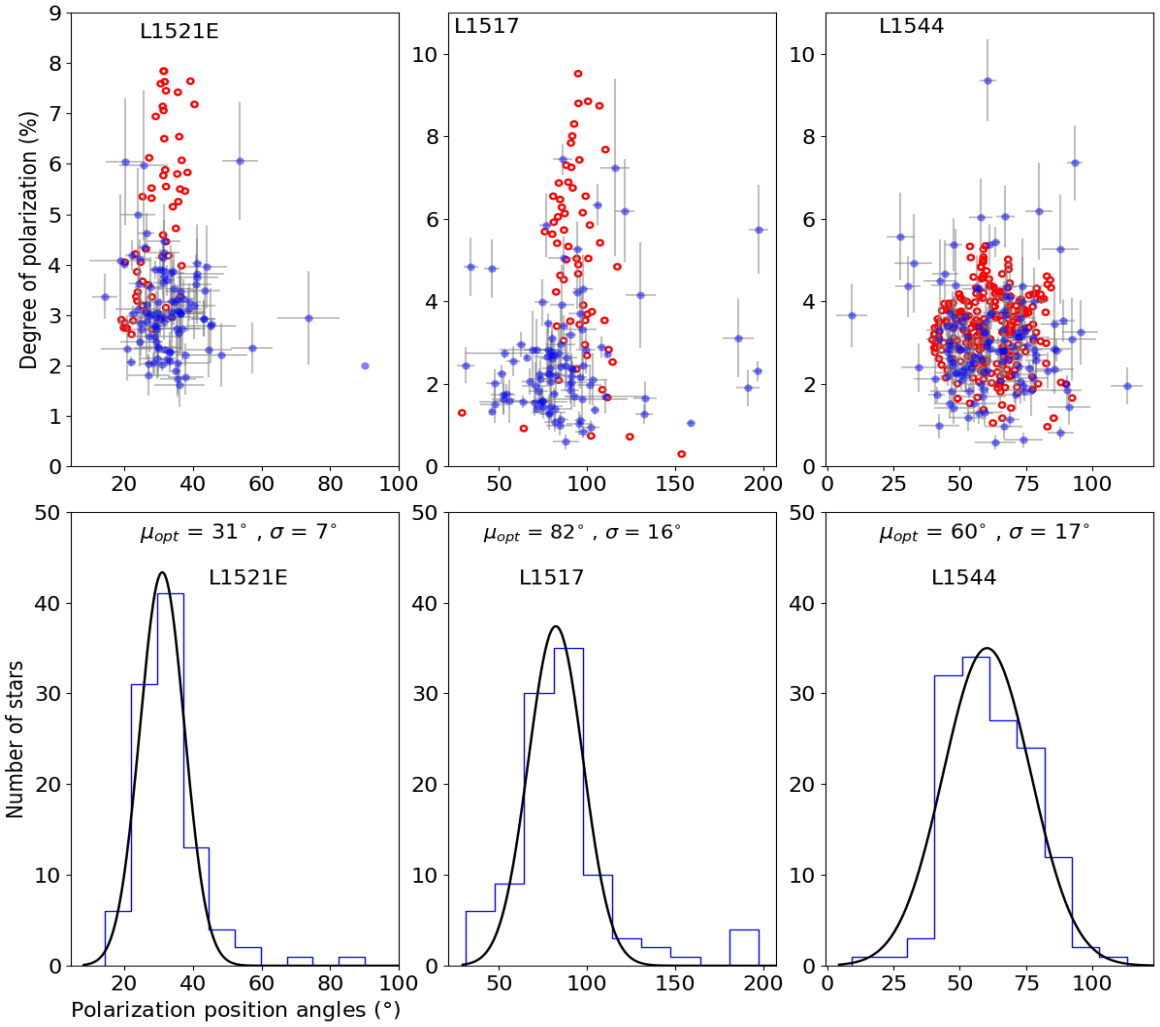

Figure 8.7: **Left:** Variation of the degree of polarization as a function of polarization position angle for L1521E, L1517, L1544 cloud. **Right:** Histogram of polarization angles from optical measurements.

Polarization measurements of 99 stars with P/e$_p$ ≥3 were obtained from the five fields observed towards L1517. The fields are mostly covering L1517A, L1517B and regions surrounding the Herbig Ae star, AB Aur. The P$_{op}$ and the θ_{op} values are found to range from 0.6% to 7.4% and 31° to 197° respectively. The P$_{op}$ vs. θ_{op} for the 99 sources are shown in Fig. 8.7 (top middle panel). The mean value of the P$_{op}$ is found to be 2.6% ± 1.4%. The mean value of the θ_{op} obtained from a Gaussian fit to the data is found to be 83° with a

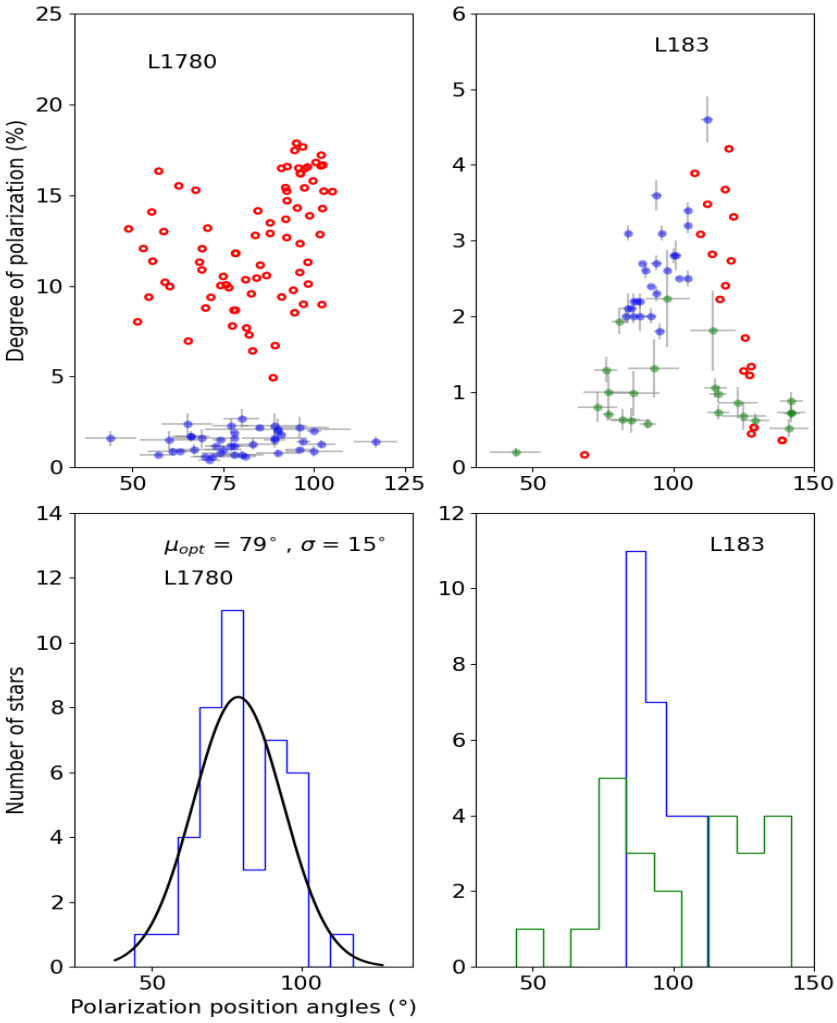

Figure 8.8: **Left:** Variation of P(%) with the distance for the sources with polarization measurements for L1521E, L1517, L1544 cloud. **Right:** Histogram of polarization angles from optical measurements.

standard deviation of 14°. The *Planck* polarization measurements selected from regions with the 250 μm intensity greater than three times of the standard deviation above the background intensity for L1517 are shown in Fig. 8.7 (upper middle panel) using open circles in red. The mean value of the θ_{plk} is found to be 93° with a standard deviation of 19°.

A total of 136 stars having P/e$_p$, $\geq$ 3 were obtained towards L1544 which are distributed all around the periphery of the cloud. The P$_{\rm op}$ and $\theta_{\rm op}$ values range from 0.6% to 9.3% and 9° to 113° respectively. The P$_{\rm op}$ vs. $\theta_{\rm op}$ for 136 sources are shown in Fig. 8.7 (top right panel). The mean value of the P$_{\rm op}$ is found to be 3.0% $\pm$ 1.3%. Based on a Gaussian fit to the $\theta_{\rm op}$ values we estimated a mean value 60° $\pm$ 16°. The *Planck* polarization measurements

from the regions having the 250 μm intensity values greater than three times of the standard deviation above the background intensity towards L1544 are shown in Fig. 8.7 (upper right panel) using open circles in red. We estimated the mean value of θ_{plk} as 61° with a standard deviation of 11°.

We obtained polarization measurements for 41 stars projected on L1780. Polarization results are shown in Fig. 8.8 (upper left panel). The observed stars are distributed mainly around the high density parts of the cometary cloud. The P_{op} and θ_{op} values range from 0.4% to 2.7% and 44° to 117° respectively. The mean value of the P_{op} is found to be $1.4\% \pm 0.6\%$ which is the lowest among the seven cloud studied here. The consistent with the classification of the L1780 as a translucent cloud. A Gaussian fit to the θ_{op} values gave a mean of $77° \pm 14°$. The mean value of *Planck* polarization measurements obtained from the regions having the 250 μm intensity values greater than three times of the standard deviation above the background intensity is found to be 84° with a standard deviation of 15°for L1780. The P_{plk} vs. θ_{plk} plot is shown in Fig. 8.8 (upper left panel) using open circles in red.

Polarization measurements of 26 stars projected on L183 are shown in Fig. 8.8 (upper right panel). The P_{op} and θ_{op} values range from 1.8% to 4.6% and 31° to 197° respectively. Majority of the polarization measurements from regions located to the south of the dense region of the cloud. The mean value of the P_{op} is found to be $2.6\% \pm 0.6\%$. Because of small number statistics, we calculated the mean from the data for θ_{op} as 94°with a standard deviation of 8°. Polarization measurements of sources projected towards the dense regions of L183 was carried out by Clemens (2012) in H-band. They obtained polarization measurements for 35 sources of which 23 sources have P/ep $\geq$ 3. These values are shown in Fig. 8.8 (upper right panel) using open circles in green. The degree of polarization in H-band range from 0.2% to 2.2% and the position angles range from 44° to 142°with a mean values of 0.9% and 103°respectively. The estimated mean value of the *Planck* polarization measurements obtained from the regions having the 250 μm intensity values greater than three times of the standard deviation above the background intensity is found to be 120° with a standard deviation of 14°.

8.5 Extraction of cores

The positions the cores associated with the seven clouds and their properties are obtained using the python package *ASTRODENDRO* algorithm. We adopted a procedure similar to what we used in Chapter 7 to identify cores. The dendrogram method identified emission features at successive isocontours in emission maps which are called "leaves" and found the intensity values at which they merge with the neighbouring structures (branches and trunks).

We supplied an emission threshold above which all the structures are identified and contour intervals which decides the boundary between the distinct structures. The initial threshold and the contour step size are selected as a multiple of the σ, the rms of the intensity map. In our analysis, we are interested in the dense cores which are identified as leaves.

In our analysis, we used the Herschel Spire 250 μm intensity map available on Herschel Science Archive in the units of MJy/sr. The L1523 cloud has not been observed using Herschel telescope. We used Doabshis extinction map for this cloud at an angular resolution of $1^{'}$. For each core, we estimated the core positions, the major and the minor axes, the effective radius of the core, and the position angle in degrees which is measured counter-clockwise from the positive x-axis. The core major and minor axes are calculated from the intensity-weighted second moment in the direction of the major axis or perpendicular to the major axis. The derived properties of the cores are presented in Table 8.3. A total of 20 cores were identified in seven clouds studied here. The core right ascension, declination are given in the columns 2 and 3. The aspect ratios of the cores, the orientation of the major axis measured from the north increasing to the east is given in column 5. The sources having aspect ratio higher than 0.83 were removed from the analysis to consider only elongated cores. The smallest structure that can be considered as real is of size $\sim$ 0.75 FWHM (Miville-Deschênes et al., 2017). We selected only those sources where the derived radius is larger than 2-3 pixels with the beam size of 250 μm intensity map. In addition to that, we considered only those sources lying within the asymmetric structure of the cloud (shown by white contours in fig. 8.13, 8.14,8.12 (right panel)).

8.6 Distances of the observed stars from GAIA DR2

The magnetic field geometry of a cloud is traced using the polarisation measurements of the stars that are background to the cloud. With the availability of the *GAIA* DR2 data, we can get the distance information of the stars having polarization measurements and examine whether they are all actually lying behind the cloud or not. The distances of the stars projected on L1512 and L1523 are obtained from the Bailer-Jones et al. (2018) catalogue by making a search around each star for a *GAIA* detection. We obtained a *GAIA* counterpart for 93 out of 94 stars projected on the L1512 cloud within a separation of $5''$. Sources were checked manually and confirmed for their true associations. The P_{op} versus distance and the θ_{op} versus distance plots for the stars projected on the L1512 are shown in Fig. 8.9 (a) and (b) respectively using open circles in red. Towards L1523, we found a *GAIA* counterpart for all the 97 stars projected on the cloud within a separation of $5''$ around each star. Again, sources were checked manually to confirm their associations with our sources. These sources are

plotted in the P_{op} versus distance and the θ_{op} versus distance plots shown in Fig. 8.9 (a) and (b) respectively using open circles in blue.

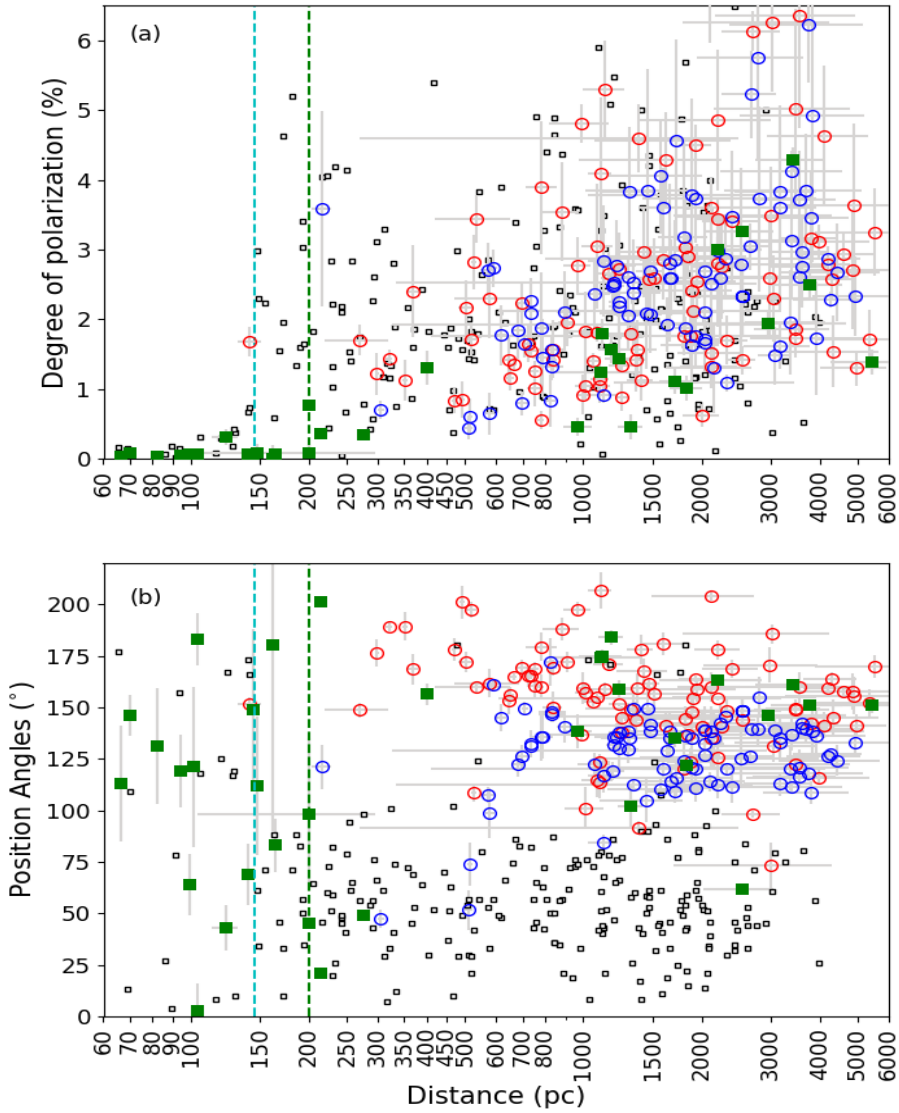

Figure 8.9: **(a)** Variation of P_{op} with the distance for the sources with polarization measurements for L1512 cloud (red filled circles). The filled squares show the polarization measurements of stars from a circular regions of radius 5°about L1512 obtained from the Heiles (2000) catalogue. The grey filled boxes represent Heiles polarization measurements of stars in a circular region of 10°around Taurus cloud. (b) Variation of the θ_{op} as a function of distance.

For the reason that there are no reliable distance estimates available for L1512 and L1523 but rather a distance of 140 pc (Benson & Myers, 1989; Elias, 1978; Hilton & Lahulla, 1995; Myers et al., 1983; Wu et al., 1992) is assigned heuristically just because of their proximity

to the Taurus molecular cloud. Therefore we made an attempt to estimate the distance to both the clouds by using the polarization measurements of the stars projected on the clouds. The P% versus distance (pc) plots are used to bracket the cloud distances (e.g., Alves & Franco, 2007; Neha et al., 2018). The sources foreground to a cloud show a relatively low degree of polarization compared to those behind it since the background stars will have an additional contributions from the dust grains associated with the cloud. Thus compared to the P% of the stars foreground to the cloud, the background sources will have a relatively high degree of polarization. The distance to the closest foreground star (with a significantly low polarization) and the background star which is closest to the cloud (with a significantly high polarization) will allow us to bracket the cloud distance. Henceforth to bracket a clouds' distance, it is necessary to have sufficient number of stars lying to both foreground and background of the cloud.

Among the sources projected on the L1512, the closest star to us is at a distance of ∼140 pc and the next nearest star is at a distance of ∼270 pc. In the case of L1523, the nearest star is located at a distance of ∼220 pc and the next closest is at a distance of ∼300 pc. Therefore, to obtain more stars which are closer to us, we searched for additional stars within a circular region of radius of 5° around both L1512 and L1523 in the catalogue produced by Heiles (2000). We found a total of 25 stars within the searched region and have distances in the Bailer-Jones et al. (2018) catalogue. The degree of polarization (P_H) and the position angle (θ_H) as a function of distance is shown in Fig. 8.9 (a) and (b) using square symbols in green. It is interesting to note that the stars from the Heiles (2000) catalogue show relatively low value of polarization till a distance of ∼200 pc. The mean value of P_H for the sources having distances ≤ 200 pc is found to be 0.1% and the corresponding θ_H is found to be 119°. The mean value of P_H and θ_H for the sources with distances ≥200 pc are found to be 1.8% and 148°which is close to the average of the mean position angles obtained for L1512 (=158°) and L1523 (=130°). The P_H for the sources lying at distances ≤200 pc is significantly lower than those lying at distances >200pc.

As both L1512 and L1523 are lying near to the Taurus molecular cloud and are often considered as a part of it, we obtained the polarization results of the stars projected on the Taurus molecular cloud from within a circular region of radius 10°from the Heiles (2000) catalogue again and obtained their distances from the Bailer-Jones et al. (2018) catalogue. These sources are plotted in Fig. 8.9 (a) and (b) using open square symbols. The degree of polarization of the sources lying projected on the Taurus molecular cloud and located at distances $\lesssim$ 150 pc are found to be significantly lower than those lying beyond this distance. A sudden jump in the values of the degree of polarization for the sources located at distances $\gtrsim$ 150 pc suggests that the Taurus molecular cloud is located at around 150 pc consistent with

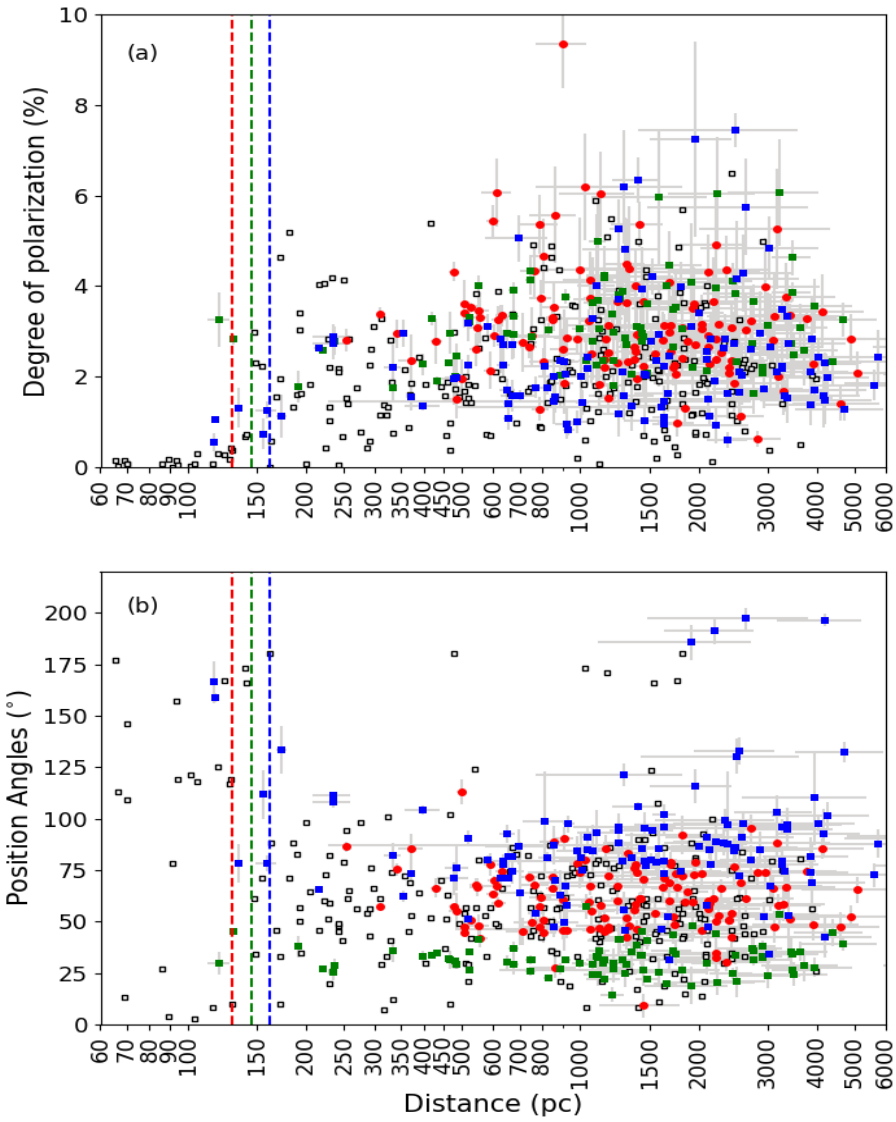

Figure 8.10: P_{op} versus distance (a) and the θ_{op} versus distance (b) for the stars projected on L1521E (green), L1517 (blue) and L1544 (red). The squares in grey represent the around the Taurus molecular cloud.

the recent estimates of the distance to the cloud using the *Gaia* DR2 results and the Panstarrs photometry (Zucker et al., 2020). The sources lying at distances $\lesssim$ 150 pc show a large spread in the values of the position angles. However, for the sources located at distances $\gtrsim$ 150 pc, the position angles show a distribution around a mean value of $\sim 50^{\circ}$ which is almost perpendicular to the mean values of position angles obtained for the sources towards L1512 and L1523. It is interesting to note that among the stars selected from the Heiles (2000) catalogue around L1512, the sources at distances $\leq$140 pc show position angles consistent

with those found towards the Taurus molecular cloud. But the position angles of the majority of the sources (except one star located at a distance of >230 pc) is more consistent with the values found for the sources projected on L1512 and L1523. Based on the results from the stars obtained from the Heiles (2000) catalogue and those projected on L1512 and L1523, we estimate a distance of ~200 pc to both the clouds.

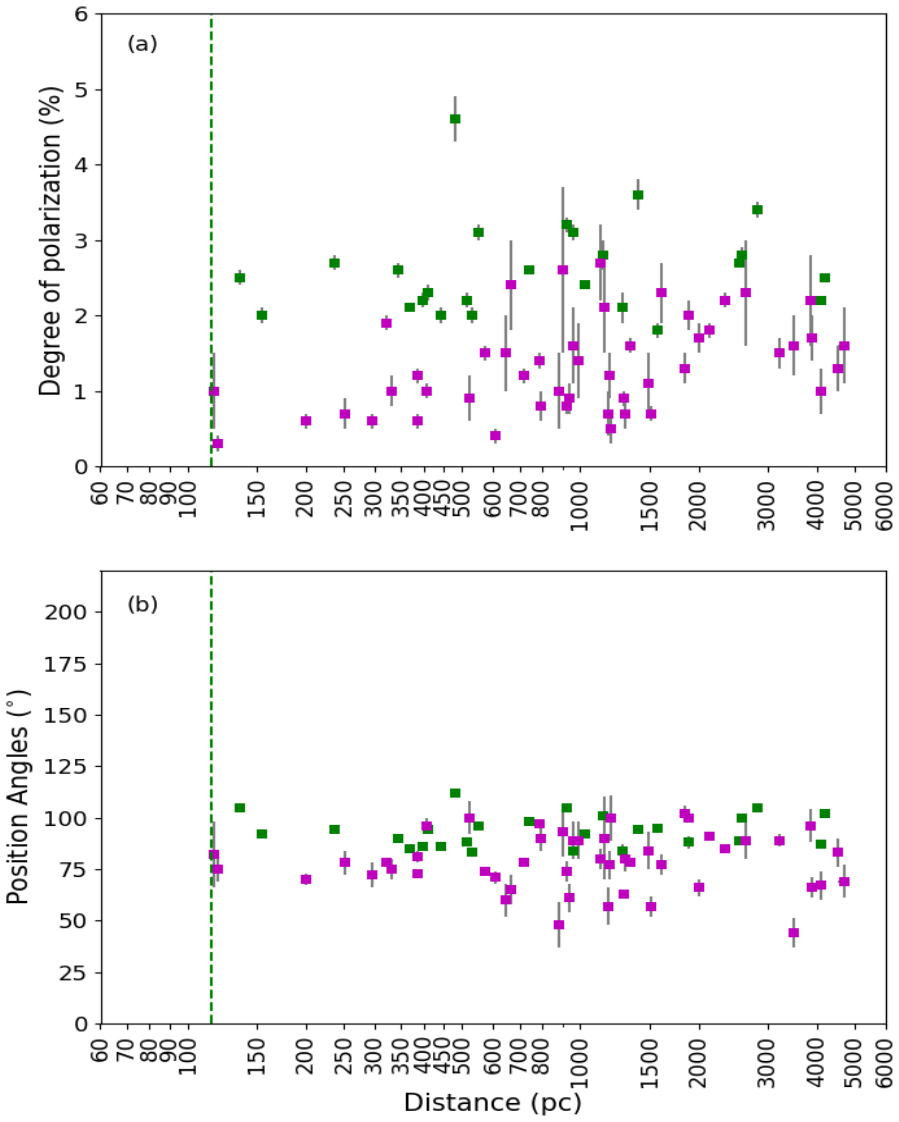

Figure 8.11: P_{op} versus distance (a) and the θ_{op} versus distance (b) for the stars projected on L1780 (maroon) and L183 (green). The squares in grey represent the around the Taurus molecular cloud.

In Fig. 8.10 we show the P_{op} versus distance and the θ_{op} versus distance plots for the stars projected on L1521E (green), L1517 (blue) and L1544 (red). The dotted lines are drawn

at the distances of the clouds mentioned in Table 8.2. These three clouds are plotted together as they are considered to be at similar distances and a part of the Taurus molecular cloud. The position angles of the stars lying towards the Taurus molecular cloud (open square) are found to be consistent with the position angles of the sources projected on L1521E, L1517 and L1544 which supports the argument that these clouds are indeed a part of the Taurus molecular cloud. As it is evident from the plots that majority of the sources project on L1521E, L1517 and L1544 are background to the clouds, the magnetic field inferred from the polarization measurements would represent the field geometry of the clouds.

The P_{op} versus distance and the θ_{op} versus distance plots for the stars projected on L1780 (maroon) and L183 (green) are show in Fig. 8.11. The vertical dotted line is drawn at 115 pc. It is evident that all the stars observed towards both the clouds are located behind the clouds and hence the observed polarization in the starlight is most likely due to the dust component residing in the cloud. The L1780 shows relatively low values of P_{op} as compared with the other clouds studied here though the θ_{op} values of the stars are consistent with those in L183.

8.7 The magnetic field geometry and the asymmetric cloud morphology

For all the clouds except L1523, the projected magnetic field geometry traced by the R-band polarization results (B_R) are presented on the *Herschel* 250 μm images containing the clouds L1512 in Fig. 8.12 (Left), L1521E, L1517, L1544 in Fig. 8.13 and L1780, L183 in Fig. 8.14. Since L1523 was not observed with the *Herschel* telescope, we overplotted the polarization results on the extinction map of L1523 produced by Dobashi (2011) using the 2MASS data as shown in Fig. 8.12 (Right). The $\theta_{op} \leq$ two times the standard deviation about the mean are plotted in the left panels of Figures 8.12, 8.13 and 8.14 using the lines drawn in cyan and the $\theta_{op} >$ two times the standard deviation about the mean are shown using the lines drawn in grey. The projected magnetic field traced using the *Planck* polarization vectors (B_{Plk}) are represented using the vectors drawn in yellow in the left panels of Figures 8.12, 8.13 and 8.14. The length of the vectors corresponds to the values of P_{op} and the direction corresponds to the θ_{op} measured from the north increasing towards the east.

The optical polarization traces the field lines towards the outer low-density regions of the cloud and the *Planck* polarization is more efficient in tracing the field orientations towards the denser parts of the cloud. Therefore ideally we should use R-band polarization measurements to trace magnetic field geometry towards the low-density extended regions of the seven clouds studied here and the *Planck* polarization measurements to trace the field lines towards

the high-density cores of the clouds. However, as can be seen from the Figures that the R-band polarization measurements are for sources that are located around the immediate neighbourhood of the clouds while the *Planck* polarization measurements are available for the full extend of the clouds.

The advantage of using the R-band polarization of the stars is that as the distance information to the individual stars are known and since the majority of them towards all the seven clouds studied here are background, we are certain that the measured polarization is actually due to the dust grains belonging to the cloud and hence traces the clouds' projected field geometry. Thus the projected magnetic field directions traced by the R-band polarization measurements are compared with those from the *Planck* measurements towards the low-density outer regions of the cloud. Because the polarization detected in R-band is clause by the dust grains due to selective absorption, when the same dust grains emit, causes polarization which is detected by the *Planck*. Hence the polarization measurements made in the R-band and the *Planck* should be consistent towards the low-density parts of the cloud. Such agreements between the polarization measurements made in the optical and in the sub- or milli-meter wavelengths are seen in other studies also (e.g., Gu & Li, 2019; Soler et al., 2016; Ward-Thompson et al., 2009). In addition to this, since polarization in R-band gives field geometry with relatively higher spatial resolution when compared to the *Planck* polarization measurements, the R-band results are used to examine field distortions at smaller scales. Below we discuss the results obtained for individual clouds.

L1512: Irrespective of whether L1512 is associated with the Taurus molecular cloud or is located at a further distance (~200 pc), it is certain that the majority of the stars observed by us in the direction of L1512 are background sources and hence are tracing the projected magnetic field geometry of the cloud as shown in Fig. 8.12 (Left). The orientations of the B_R and the B_{Plk} are in excellent agreement (both showing an orientation of 158°). The consistency of the B_R and the B_{Plk} is even higher when we compare the θ_{op} within two standard deviation about the mean as shown by the vectors drawn in cyan. Because the optical polarization traces the field lines towards the outer low-density regions of the cloud and the *Planck* polarization is more efficient in tracing the field orientations towards the denser parts of the cloud, the agreement seen here suggests that the cloud is threaded by the same magnetic field from outer low-density medium to the high density regions of L1512. The projected field is aligned along the asymmetric morphology of the cloud. There is a curvature in the field lines along the northwest and southeast direction. The field lines are found to be tracing the two filaments seen to the western parts of the cloud. The degree of polarization (measured from both R-band and the *Planck*) is relatively lower towards the region showing sharp edges than in the opposite diffuse region which could be due to the

lack of aligned dust grains there. It could also be due to a tangled magnetic field causing depolarization.

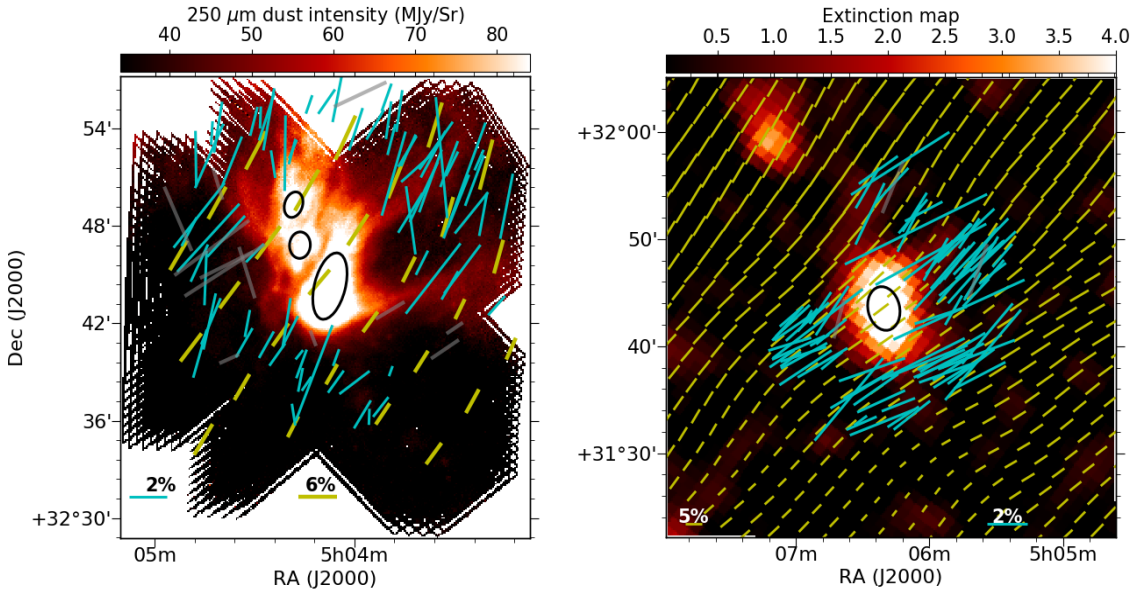

Figure 8.12: **Left:** Polarization results for L1512 overplotted on the on the *Herschel* 250 μm image. The R-band and the *Planck* polarization vectors are shown in the cyan and the yellow colors respectively. The length of the vectors corresponds to the degree of polarization and the direction corresponds to the position angles measured from the north and increasing towards the east. Two vectors corresponding to 2% (for the R-band) and 5% (for the *Planck*) polarization at a position angle of 90° are shown for reference. **Right:** The polarization results for L1523 overplotted on the extinction map produced using 2MASS data (Dobashi, 2011) as no *Herschel* observations are available for L1523.

L1523: The cloud shows a diffused tail towards the north-western parts of the cloud similar to the direction in which L1512 shows the extension. The B_R (130°) and the B_{Plk} (132°) are found to be in excellent agreement in L1523 also implying that the inner cloud magnetic field is inherited from the envelope magnetic field. Here again, the agreement is more pronounced as we consider the θ_{op} within two standard deviation about the mean as shown by the vectors drawn in cyan in Fig. 8.12 (Right). Both B_R and B_{Plk} show highly ordered distribution. The magnetic field orientation between the region to the south-western and the north-eastern parts of the cloud show a small variation. It is at the position of the cloud where the change is occurring. Whether the change in the field orientation is caused because of the formation of the cloud or the formation of the cloud occurred because of the bend in the field created by the two components of the magnetic field is unclear. In the case of a weaker magnetic field, gas dynamics is not controlled by the field and hence forced to follow the motion of

the gas (Körtgen & Banerjee, 2015). However, as the field strength increases, the field lines dominate the gas dynamics helping the clouds to remain coherent.

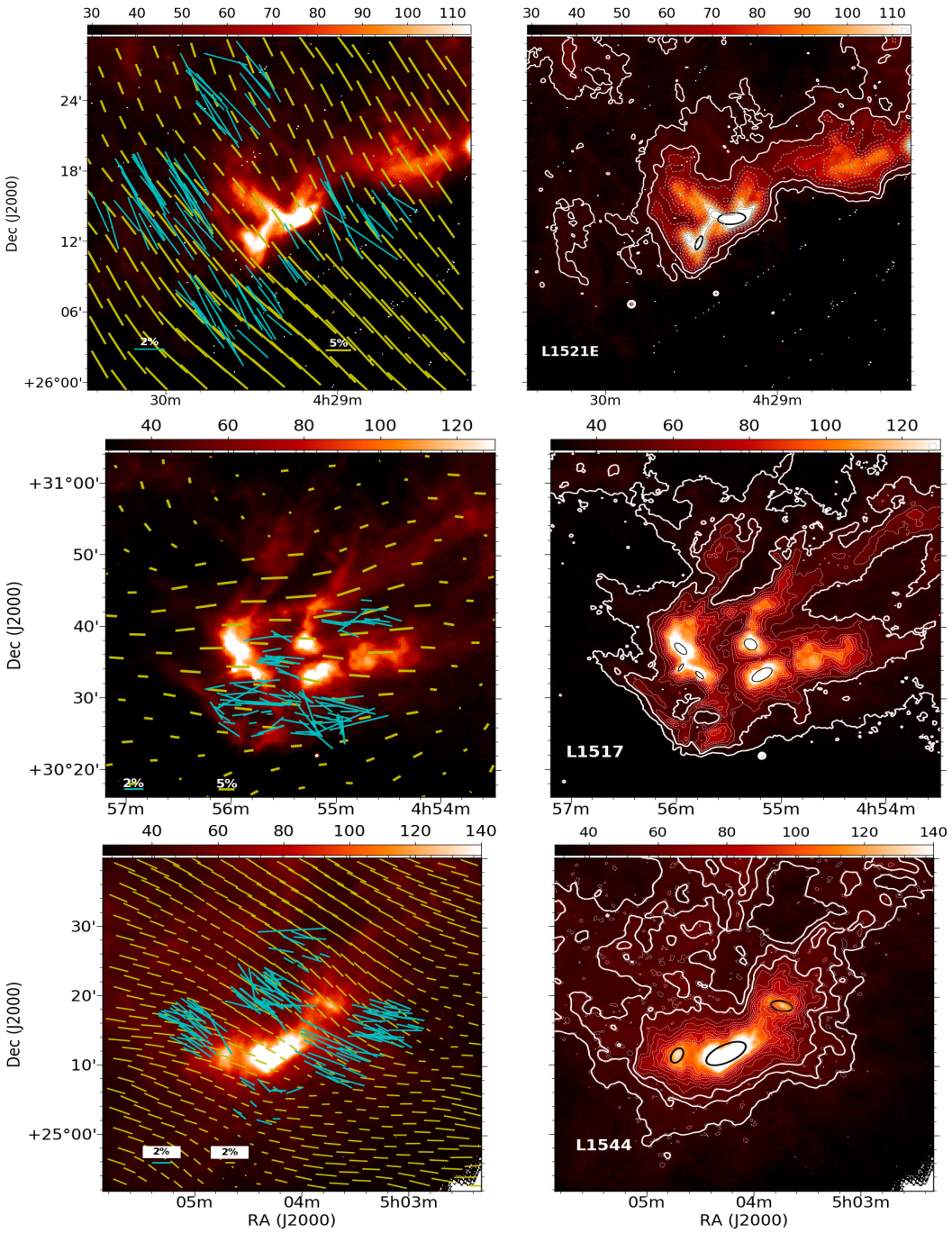

Figure 8.13: **Left:** Optical R-band polarization vectors in cyan overplotted on Herschel 250 μm image of L1521E, L1517, L1544 clouds. Yellow vectors shows the *Planck* polarization measurements. **Right:** Distribution of the extracted cores identified using the *Astrodendro* algorithm shown by ellipses.

L1521E: The field orientations inferred from both the techniques are in excellent agreement implying that the inner magnetic field is inherited from the envelope field in L1521E also. The field orientations follow the extended cloud structure of the cloud. The H_2 density at the peak position of the core is estimated to be 1.3-5.6×10^5 cm^{-3} (Hirota et al., 2002). They also noted that though the H_2 density is high enough to excite the inversion transitions of NH_3, these lines are found to be very faint in L1521E. Tafalla & Santiago (2004) compare the emission of two molecules, $C^{18}O$ and N_2H^+ which are known to have different depletion behaviors. While $C^{18}O$ gets heavily depleted at densities of a few 10^4 cm^{-3}, N_2H^+ remains at gas phase up to densities of ∼10^6 cm^{-3}. Thus the ratio between the integrated intensities of $C^{18}O$ and N_2H^+ is a good indicator of depletion which is found to be 3.4 in L1521E implying that this core is chemically less processed and therefore youngest core known with a contraction age of $\lesssim 1.5\times10^5$ yr (Tafalla & Santiago, 2004). However this age is not compatible with models of core formation via ambipolar diffusion, as they require evolutionary times of the order of 1 Myr. In that case, a more dynamical core formation scenario is required to create such a highly contracted core on a short time scale as estimated by using chemical models (Tafalla & Santiago, 2004). The sharp edges to the southern side and a more extended distribution of material to the opposite direction could be a result of some external compression acted from the southern direction along the field lines that might have created the cloud.

L1517: Here again there is an excellent agreement between the field lines in the inner parts of the clouds (93°) to the field lines in the outer envelope (83°) of the cloud. Kirk et al. (2006) mapped the linear polarization emission from L1517B (one of the five cores in the cloud) at 850 μm. The weighted mean of position angle was estimated as 106°which is at an offset of 13°with the B_{Plk} and at an offset of 23°from the B_R . Kirk et al. (2006) also reported a shift in the position angles from the north (84°) to the middle (94°) and to the southern parts (156°) of L1517B. It is evident from the Fig. 8.13, that there are changes in the large-scale magnetic field orientation around the cloud as found towards the north-east and south-west corners of the figure where field rotations are most likely causing a reduction in the degree of polarization possibly due to depolarization. Hacar & Tafalla (2011) have made a detailed study of L1517 in molecular lines and 1.2 dust continuum emission. They identified four filaments and five starless cores, embedded in these filaments, that are at different evolutionary stages. These filamentary structures stretch parallel to the direction of the extended emission and also to the direction of the magnetic fields. The magnetic fields towards the south of cloud near AB Aur shows more disoriented vectors with relatively large dispersion which could be because of the effects from this Herbig Ae star. Opposite to that, the vectors in the north of cloud shows more ordered pattern.

L1544: The B_R (60°) shown in cyan vectors are found to be in excellent agreement with the B_{Plk} (61°) implying that the field lines inside the cloud are threaded with the fields from the envelope. Both B_R and B_{Plk} are mostly oriented perpendicular to the high density emission structures seen towards the cloud. The JCMT-SCUBA maps of 850 μm thermal emission from dust in L1544 was obtained by Ward-Thompson et al. (2000). The weighted mean position angle of the magnetic field inferred is found to be at an offset of 23° with the B_R and ~ 37° with B_{Plk}. In is interesting to note that towards the southern tip of the cloud both optical and the *Planck* polarization values show a change in the field direction from ~60° to ~90°. The degree of polarization shows a drop at this location consistently in measurements made in both the techniques. The magnetic field towards the diffused extended region is found to be more parallel to the magnetic field orientation.

L1780: Again, the B_R (77°) and the B_{Plk} (84°) agree very well not only with respect to the mean orientation but also to the overall field morphology traced with the two techniques. The field lines remarkably follow the cloud structure. The cloud presents a cometary morphology with a broad high density part to the west and a diffuse narrow part to the east. The structure shows a curvature from east to west which is strikingly traced by the field lines as well. Towards the head, the field lines rotate by almost 90°with respect to the field lines in the tail part. The degree of polarization here is significantly lower compared to the other regions as traced by both the techniques.

L183: The R-band measurements made by us are for the background stars lying towards the southern parts of the cloud while the H-band polarization measurements made by Clemens (2012) are for the background sources lying to the northern parts of the cloud. The magnetic fields inferred from the H-band polarization measurements made by Clemens (2012) are shown using the vectors drawn in white. Though the field orientations inferred from both R-band and H-band are in good agreement with the *Planck* polarization measurements, there are differences seen between the H-band and the *Planck* magnetic field orientations towards the western parts of the cloud where a reduction in the degree of polarization is seen. There could be two components of magnetic field orientation here which is causing a depolarization resulting in the reduction. The maps generated using the R-, H- and *Planck* present a smooth and ordered field geometry over the entire field containing the cloud. The magnetic field is predominantly perpendicular to the north-south elongation of the cloud. The weighted mean position angle of the magnetic field, averaged over the 16 positions observed by Ward-Thompson et al. (2000) in 850 μm is 46°. This represents the magnetic field geometry of the high density inner regions of the cloud which is at an offset of 74°, 57°and 48° with respect to the magnetic fields inferred by the *Planck*, H-band and R-band

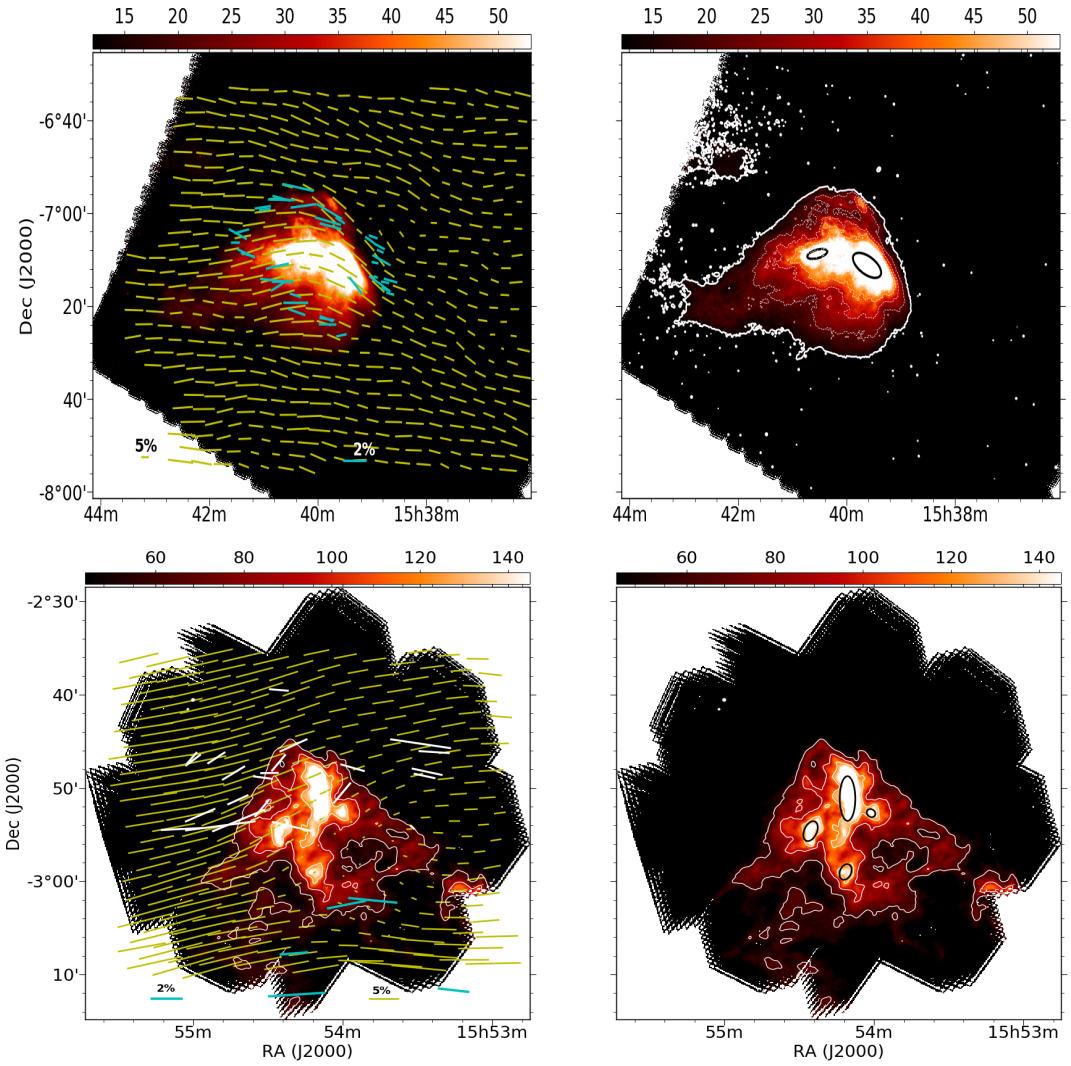

Figure 8.14: Optical R-band polarization vectors in cyan overplotted on the *Herschel* 250 μm images of L1780 (top) and L183 (bottom) clouds. Yellow vectors show the *Planck* polarization measurements. **(b):** Distribution of the extracted cores identified using the *Astrodendro* algorithm are shown by ellipses.

polarization measurements. This is the only cloud where we find the sharp edged northern and extended diffuse emission to the southern parts of the cloud are perpendicular to the magnetic field orientation.

8.8 Relative orientation between the magnetic field and the core orientations

In the previous section, we discussed the magnetic field orientation with respect to the asymmetric distribution of the material around the clouds. In this section we looked at the relative orientation between the core major axis and the ambient and the core-scale magnetic fields. Because the R-band polarization measurements trace the envelope magnetic fields or the fields at the periphery of the clouds, we define this as the ambient (θ_{opt}) magnetic fields. The core-scale magnetic field defined by θ_{plk} is calculated by taking an average of the nearest three Planck polarization vectors around the core centre. The θ_{plk} thus obtained are listed in the column 6 of Table 8.3. A total of 21 cores are identified in seven cores studied here. A maximum of five core in L1517, four in L183, three each in L1512 and L1544, two each in L1521E and L1780 and one in L1523. The extracted cores in each cloud are shown in the right panels of Figures 8.12, 8.13 and 8.14. In L1512, the major axis of the three extracted cores are almost parallel to each other and parallel to the ambient magnetic field. Interestingly, the core major axis orientation is along the asymmetric morphology of the cloud. In contrast, in L183, though three of the four core with their major axis oriented parallel to each other, the ambient magnetic field is oriented perpendicular.

8.9 Discussion

Magneto-hydrodynamic simulations carried out by various authors Heitsch et al. (2009); Seifried et al. (2020) show that the there is a significant of magnetic field orientation (from low to high field strengths) in the formation of clouds. The star-forming cores or starless cores are considered to the consequence of fragmentation of the clouds. As the relative orientation of filaments and B-field are correlated in nearby cloud complexs (Planck Collaboration et al., 2016c; Soler, 2019; Soler & Hennebelle, 2017) the cores, being the nested structures will have effect from the magnetization of the cloud. In that regard, the clump shape and orientation are important indicator of clump dynamics and fate of star formation.

Chen & Ostriker (2018) showed that a sample of more than 100 pretsellar cores and found that the environment plays an important role in shaping the prestellar cores through ram pressure and magnetic pressure. We expect that the cores tend to align perpendicular to the local magnetic field where the flow of material will be preferential to favour the collapse mechanism. The orientation of the cores are not aligned or randomly oriented with respect to the large-scale magnetic field. If the cores orientation has significant effect of the large-scale magnetic field, we expect the core major axis to be parallel to the magnetic field lines with

Table 8.3: Position angle of cores, magnetic field using R-band optical polarization and Planck polarization measurements.

Core	RA	Dec	(b/a)	$\theta^{\ddagger}_{maj}$	θ_{pla}	$\lvert\theta_{pla}-\theta_{maj}\rvert$	$\lvert\theta_{opt}-\theta_{maj}\rvert$
Id	(°)	(°)		(°)	(°)	(°)	(°)
(1)	(2)	(3)	(4)	(5)	(6)	(7)	(8)
L1521E, θ_{opt} = 32°±7°							
C1	67.36626	26.19997	0.35	159	37	58	51
C2	67.31869	26.23470	0.45	94	31	63	64
L1517, θ_{opt} = 83°±14°							
C1	73.79654	30.55554	0.49	123	79	44	41
C2	73.94581	30.55403	0.38	42	86	44	41
C3	73.99066	30.57162	0.27	150	87	63	66
C4	73.99151	30.61505	0.47	41	90	49	42
C5	73.82441	30.62605	0.79	41	82	41	42
L1512, θ_{opt} = 158°±16°							
C1	76.03063	32.73859	0.47	165	142	23	7
C2	76.06828	32.78068	0.80	176	143	33	18
C3	76.07625	32.82231	0.70	161	147	14	3
L1544, θ_{opt} = 60°±16°							
C1	76.06606	25.19548	0.45	118	60	58	58
C2	76.180594	25.19019	0.62	153	69	84	87
C3	75.93618	25.31015	0.50	77	40	37	17
L1523, θ_{opt} = 130°±14°							
C1	76.58531	31.72597	0.73	13	126	67	64
L1780, θ_{opt} = 79°±15°							
C1	234.90594	-7.18877	0.46	61	68	7	17
C2	235.13476	-7.14786	0.33	102	97	5	23
L183, θ_{opt} = 93°±8°							
C1	238.54740	-2.98351	0.66	160	132	28	67
C2	238.60597	-2.91059	0.57	158	122	36	65
C3	238.54418	-2.85220	0.33	180	120	60	87
C4	238.50488	-2.87830	0.85	42	126	84	51

‡ Position angle of the major axis of the cores.

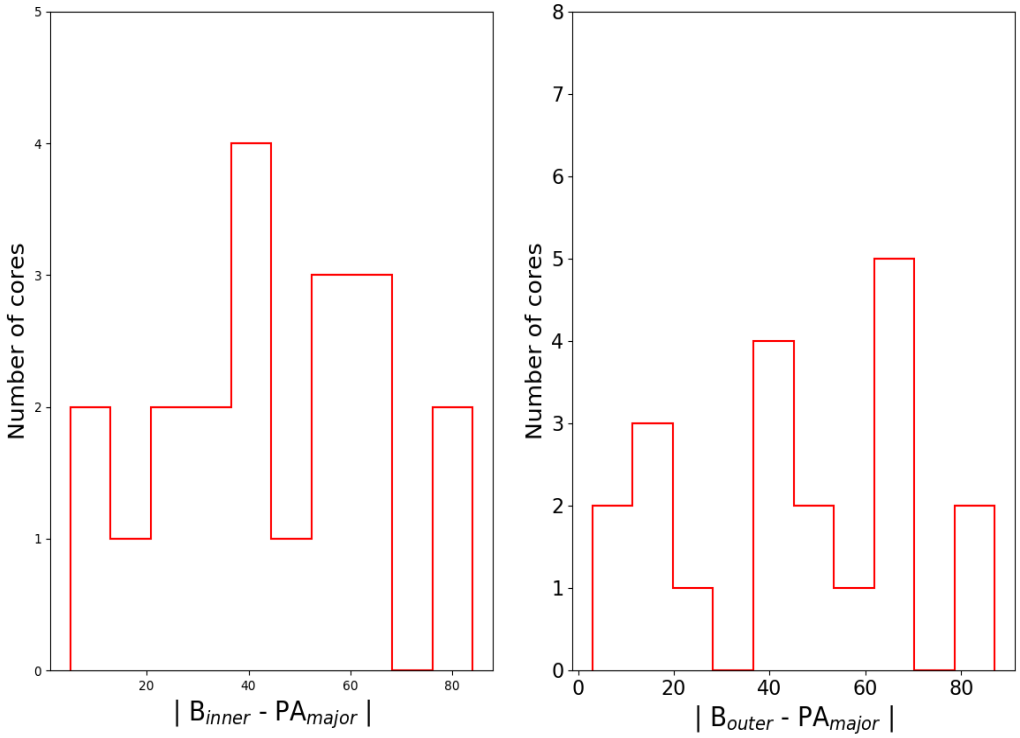

Figure 8.15: **Left:** Distribution of difference of inner magnetic field and position angle of major axis. **Right:** Difference of outer magnetic field and position angle of major axis.

a significant effect on the gas motions. But we notice that all the cores extracted shows a random orientations with respect to the magnetic field. The position angle of the R-band or Planck polarization show a well defined direction of magnetic field in all the cores. That implies that the core orientation might not have a significant effect from the magnetic field as per the standard theory. There might be other factors that can contribute to shaping the core morphology. The magnetic field plays a crucial role in the formation of cloud and governing the overall dynamics (Körtgen & Banerjee, 2015). When the overall cloud evolve as a consequence of internal dynamics and stellar feedback effects, the clumps will also grow accreting material turning into a non-spherical structures. Hence, clump shape and orientation might be an indicator of formation mechanism.

We have studied the large-scale magnetic field structure using Planck polarization and small scale variations using optical polarization at the outer periphery of the cloud. The cloud magnetic field is parallel to intercloud magnetic field in each cloud. One common factor in all the selected clouds here is the asymmetric shape of all the clouds on one side of the map. The results suggest that the asymmetric shape is parallel to the derived magnetic field structures. Kim et al. (2016) investigated a samples of starless cores using AKARI

and molecular line observations to conclude that the external feedback from the stars or the isotropic interstellar radiation field might play a crucial role in the evolution of the cores.

The asymmetric shape of far-infrared emission in L1512, L1523 and L1517 have a nearby heating sources. In addition, the magnetic field is along the direction of aysmmetric structure. The orientation of the cores are also the magnetic field.

The other two high-latitude cloud L1780 and L183 again show asymmetric emission. In L1780, the results are well consistent with the simulations carried out by Miniati et al. (1999) where the B-field lines are along the cloud morphology. The case of L183 shows two directions of magnetic field, one along the structures in the cloud towards the head part and other is perpendicular to the magnetic field.

8.10 Conclusions

In this chapter we presented our R-band polarization measurements of over 200 stars projected on two small, isolated starless clouds L1512 and L1523. These two sources were chosen as they both show an asymmetry in their cloud morphology having sharp edges on one side and an extended emission on the opposite direction to trace the plane of the sky magnetic field geometry of these clouds. In addition to these, we also present results of five additional clouds, L1521E, L1517, L1544, L1780 and L183, which also show asymmetric morphology similar to L1512 and L1523. We obtained data for these five clouds from the archive. The main goals of the study were (a) to investigate the relationship between the magnetic field orientation with the elongation seen in the clouds; (b) to investigate relationship between the magnetic field orientations inside the clouds inferred from the *Planck* polarization and the envelop field inferred from the optical polarization measurements of background starlight; (c) to examine the relative offsets between the core major axes orientation with respect to both inside and outside magnetic field directions. The results obtained from this study are given below:

1. Based on the distribution of the degree of polarization and the position angles of the stars projected on the clouds L1512 and L1523 (measured by us in R-band) with respect to the distances of the stars obtained from the *GAIA* DR2, we show evidence for both the clouds to be located at further away (~200 pc) from the distance at which the Taurus molecular cloud is located.

2. In all the seven clouds studied here, the magnetic fields inferred from the R-band polarization and the *Planck* polarization measurements are in excellent agreement

suggesting that it is the same dust population which is possibly responsible for the production of polarization that is detected in the two techniques.

3. In six out of seven clouds studied in this chapter, the projected magnetic field is aligned with the asymmetric morphology of the cloud. The one cloud, L183, show the asymmetry morphology to be oriented perpendicular to the ambient magnetic field.

4. A total of 21 cores are extracted from the seven clouds. The major axis of the three cores found in L1512 are not only found to be parallel to each other but also parallel to both the projected magnetic fields and the asymmetry of the cloud morphology. In contrast, in L183, for three out of four cores, though their major axis are parallel to each other and parallel to the cloud elongation, but are almost perpendicular to the orientation of the ambient magnetic field.

5. The orientation of the core major axis with respect to the (projected) ambient and the core magnetic field shows a random distribution.

Chapter 9

SUMMARY AND FUTURE WORK

9.1 Summary and concluding remarks

The aim of the studies carried out in this thesis is to understand the process of filament formation and their evolution to cores by studying the relative role played by the physical factors like gravity, turbulence and magnetic fields. Specifically, the main questions addressed in this work are: (1) What are the dynamical properties of the filaments and cores in the vicinity of a massive star?, (2) How the filaments, in general evolve in the case of less active region?, (3) How the magnetic fields will affect the evolution of the clouds?, (4) What is the role played by the motion of clouds in the core morphology?

We have described the detailed study of the dynamics of two cloud complexes L1172/ L1174 and L1147/L1158 in the Cepheus Flare region using sub-millimetre molecular line and magnetic field observations. The gas emission was complimented with the available dust continuum emission. Both the clouds offered two different physical conditions based on the current star formation activity. One part of the work in L1172/L1174 was motivated by the feedback effects of a young star on the surrounding ambient gas. I characterized the high-density structures and clumps using various algorithms and studied their kinematical properties in considerable detail using various tracers with different critical densities. The importance of the magnetic field structures was studied using optical polarization and Planck polarization taken from the archive. I also studied the importance of clump orientation and magnetic field at cloud and core scale in a sample of clouds that show asymmetric distribution in far-infrared emission. We have also found accurate distances for all the clouds in Cepheus Flare region and the kinematical studies of high density structures in the cloud complexes. The orientations of the core have been estimated and their relation with the magnetic field and the direction of motion.

The main work of the thesis has been explained from chapters 3-8.

Table 9.1: Skills and software expertise learnt during the thesis tenure.

Software	**Application**
Python	Polarization results, statistical plots, color-composite images
Herschel Interactive Processing Environment (HIPE)	Convolution and regridding of images
IRAF	Photometery of images
CLASS	Single dish radio data reduction.
Healpy	Planck polarization maps
Observation experience	
Band	**Observation**
Optical	Polarimetric and photometric observations using 1.04-m ST
Radio	Molecular line mapping using 14-m Single dish radio telescope.

9.1.1 Dynamical state of gas surrounding HD 200775

In chapter 3, we have addressed the scenario of formation of dense core in the vicinity of high mass star. The detailed kinematics of the gas emission around NGC 7023 was mapped using ^{12}CO , C^{18}O (1-0) lines. NGC 7023 is a reflection nebula illuminated by HD 200775 and shows asymmetric distribution of dust around the central star HD 200775. There is a cavity present on the western side of the star. The high density regions were mapped by tracers with more critical density but different optical depths, N_2H^+ (1-0) and CS (2-1) lines. We extracted the filaments and clumps using *Filfinder* and *Astrodendro* algorithms. Various properties such as centroid positions, major & minor axis and position angles were used in the clump analysis. The longest skeletons were used for to study the kinematics of each filament. The radial profile of each filament also was constrained by fitting a Plummer and Gaussian functions to the mean average profile of column density. To visualise the distribution of gas in different velocities, we made channel maps for both the tracers and found that the gas emission is quite clumpy in different velocity channels. The high velocity gas is found to be present around central star potentially affecting the high density low velocity gas. From the analysis of spectral profiles, it is evident that the regions around the HD 200775 are under the effect of stellar radiation as there are features of bulk motions. In order to study the kinematics of the filaments, we fitted a Gaussian function to the spectral profiles with the SNR ≥ 3 if there is single cloud component along the line-of-sight. Using Local thermodynamical equilibrium (LTE), we calculated the parameters of all the clump

like optical depth, column density, excitation temperature. We compared the gas mass of each core with the virial mass to find out whether the core is gravitationally stable or not. We constructed the *Planck* polarization map for the region and compared with the optical polarization map and the high density structures. The magnetic field lines are perpendicular to the filaments on the eastern side whereas parallel on the western side. We found out that the field lines are more disturbed towards the eastern side which is because of the presence of high velocity gas and the material is more turbulent. The findings in this chapter suggest that the structures are being shaped by the magnetic field lines. The filaments show supersonic turbulent motions and exhibit tail like morphology.

9.1.2 Interplay of magnetic field and gas dynamics in L1172

This chapter explores one of the morphology of filamentary structures: Hub-filament or Head tail. We investigated the dynamics of the long filament which emerges like a tail from the hub containing a massive star by using large scale molecular line observations. The gas distributed in different velocity ranges is that clumpy and there is less spread of velocity in both the tracers unlike the head region, NGC 7023. By making use of the crest of filament extracted using *Filfinder*, we characterised the velocity structure by fitting a single Gaussian model to each line profile of $C^{18}O$ as there is single velocity component present along the line-of-sight. We found a positive longitudinal velocity gradient ~ 0.2 km $s^{-1}pc^{-1}$ along the length suggesting there may be accretion of the material away from the hub and towards the high density core. The magnetic field lines (inferred using optical as well as Planck polarization) are well correlated with the morphology of the filament and follows the curvature as well. We conclude that this filament is not in well accordance with the hub-filament systems.

9.1.3 Distance, magnetic field, and kinematics of filamentary cloud LDN 1157

In chapter 5, we studied a small cloud which is morphologically simple showing comma shape. The distance of the cloud was found out to be 340 pc. The presence of a protostellar core with a class 0 protostar ejecting out a bipolar outflow and a starless core embedded in the filament makes it an interesting example. We mapped the magnetic field morphology of the cloud using R-band polarization observations. The magnetic field lines is almost perpendicular to the east-west branch of the filament but parallel to the bipolar outflow. The correlation of magnetic field lines at small scale (using sub-millimeter polarization) with the lines at the outer periphery of the cloud shows that the morphology is preserved.

9.1.4 Molecular line study of the cloud complex LDN 1147/L1158 complex

In chapter 6, we further extended our study to the whole L1147/L1158 complex to explore the reasons behind different star formation activity in the two complexes. We extracted a set of filaments and cores using dust column density map. We analysed the kinematics of each region in detail by using ^{13}CO and C^{18}O (1-0) molecular lines. We found out that the some of the filaments show two velocity components suggesting that there are two clouds along the line-of-sight. We found out the gas mass, dust mass and virial mass of all the extracted cores by using LTE analysis. We also presented the magnetic field maps of each region in this complex and found that a majority of filaments are perpendicular to the magnetic field lines (as seen in *Planck* polarization observations).

9.1.5 Motion of four clouds in Cepheus Flare region

The study carried out in chapter 7 is quite interesting in the direction of exploring motions of clouds in Cepheus Flare clouds. The complexes L1147/L1158, L1172/L1174, L1228 and L1251 were studied to calculate their direction of motions assuming the YSOs are kinematically coupled with the cloud material. We estimated the space velocity and positions of these clouds in the Galaxy. The space velocity of the clouds are calculated by combining the transverse and radial motion and the values are found to be 8.5 km s^{-1}, 7.4 km s^{-1}, 8.5 km s^{-1}and 12.3 km s^{-1}for L1147/1158, L1172/1174, L1251 and L1218 respectively. To understand the role of magnetic fields in governing the motion and shaping the core morphology, we estimated the possible offsets between various orientations. We used Astrodendro method for extracting the sources. The correlations suggest that the cores in L1157/L1158 are preferentially perpendicular to the magnetic field whereas in L1172/L1174 they are aligned more parallel. For the case of motion, the cores are perpendicular to the direction of motion in L1147/L1158 whereas more parallel in case of L1251. Other clouds L1228 and L1172/L1174 show random alignment with the motion.

9.1.6 Importance of core orientations and magnetic fields in clouds showing asymmetric morphology

In this chapter, we systematically investigate a sample of clouds showing asymmetric dust distribution. To understand the possible origin of the morphology and its correlation with the magnetic fields, we mapped the magnetic field morphology of the clouds using optical polarization and the Planck polarization measurements. We used Astrodendro method for

extracting the cores and the correlates their position angle with direction of magnetic field. We find that the distribution of offsets between the position angle of cores with the magnetic fields is random. One possible explanation of this could be that the orientations are a local property of each region and depends on the environment of star-forming region.

With the work done in this thesis, we present for the first time the large-scale molecular line maps of the whole complexes L1147/L1158 and L1172/L1174 at a velocity resolution of ~ 0.1 km s^{-1}and an angular resolution of $44''$ with a pixel size of $20''$. We have discussed the velocity structure of the filaments and cores in great detail. Our observational results provide substantial evidences that the subsonic to supersonic turbulence along with magnetic fields are indeed controlling the star formation process. This will help in better understanding the origin of diverse star formation activity of the clouds and constraining the star formation theories. In addition to that, we also present first time study of the various correlations of the motion of the clouds with the large scale magnetic field and core orientations. This specific study about the motion of the clouds with respect to the magnetic fields and the core orientation will give important insights into the topological features of the clouds.

9.2 Future perspectives

- The complete understanding of star formation regarding the role of turbulence and magnetic fields still requires more observational constraints and comparison with the theoretical models. With the large-scale observations of filaments and cores in for example, L1172/L1174, we estimated a longitudinal velocity gradient. Theoretical studies proposed that the accretion could be taking place completely from the surrounding material. Keeping in the mind projected structures in the plane-of-the sky (ignoring the effects of inclination angles of the filaments), we could acquire knowledge only about motion of gas along the filaments. I intend to study the filamentary structures with a better angular resolution so that the width of the filaments can be better constrained. By sampling the transverse motion with a possible velocity gradient, if present, we can better constrain the kinematics of the whole filament. The intended proposed study will create better insights in the understanding of filament formation and their kinematical structure.

- The morphology of the clouds are believed to be affected by the motion of the clouds and their interaction with various factors like magnetic fields. In our work, we showed that the difference between the motion and magnetic fields can shape the morphological features of the clouds and the small structures, cores. It will be interesting to extend the study to more star-forming regions within Gould Belt survey.

References

, 1988, Infrared Astronomical Satellite (IRAS) Catalogs and Atlases.Volume 7: The Small Scale Structure Catalog., vol. 7

Abergel A., Boulanger F., Mizuno A., Fukui Y., 1994, , 423, L59

Alecian E., Catala C., Wade G. A., et al., 2008, , 385, 391

Ali A., Harries T. J., Douglas T. A., 2018, , 477, 5422

Allen A., Li Z.-Y., Shu F. H., 2003a, , 599, 363

Allen A., Shu F. H., Li Z.-Y., 2003b, , 599, 1, 351

Alves F. O., Franco G. A. P., 2007, , 470, 2, 597

Alves F. O., Franco G. A. P., Girart J. M., 2008, , 486, L13

Alves F. O., Frau P., Girart J. M., Franco G. A. P., Santos F. P., Wiesemeyer H., 2014, , 569, L1

Alves J., Zucker C., Goodman A. A., et al., 2020, , 578, 7794, 237

An J. H., Sellgren K., 2003, , 599, 312

Andre P., 1996, , 67, 901

André P., Di Francesco J., Ward-Thompson D., Inutsuka S.-I., Pudritz R. E., Pineda J. E., 2014, Protostars and Planets VI, 27–51

André P., Men'shchikov A., Bontemps S., et al., 2010, , 518, L102

Andre P., Ward-Thompson D., Barsony M., 1993, , 406, 122

Aniano G., Draine B. T., Gordon K. D., Sandstrom K., 2011, , 123, 1218

Arce H. G., Borkin M. A., Goodman A. A., Pineda J. E., Beaumont C. N., 2011, , 742, 2, 105

Arce H. G., Santiago-García J., Jørgensen J. K., Tafalla M., Bachiller R., 2008, , 681, 1, L21

Arnal E. M., Morras R., Rizzo J. R., 1993, , 265, 1

Arzoumanian D., André P., Didelon P., et al., 2011, , 529, L6

Arzoumanian D., André P., Könyves V., et al., 2019, , 621, A42

Arzoumanian D., André P., Peretto N., Könyves V., 2013, , 553, A119

Avery L. W., Chiao M., 1996, , 463, 642

Ayliffe B. A., Langdon J. C., Cohl H. S., Bate M. R., 2007, , 374, 4, 1198

Bachiller R., Pérez Gutiérrez M., Kumar M. S. N., Tafalla M., 2001, , 372, 899

Bailer-Jones C. A. L., 2015, , 127, 994

Bailer-Jones C. A. L., Rybizki J., Fouesneau M., Mantelet G., Andrae R., 2018, , 156, 58

Balázs L. G., Ábrahám P., Kun M., Kelemen J., Tóth L. V., 2004, , 425, 133

Ballesteros-Paredes J., Hartmann L., Vázquez-Semadeni E., 1999, , 527, 285

Ballesteros-Paredes J., Klessen R. S., Mac Low M. M., Vazquez-Semadeni E., 2007, in Protostars and Planets V, edited by B. Reipurth, D. Jewitt, K. Keil, 63

Bally J., Langer W. D., Stark A. A., Wilson R. W., 1987, , 312, L45

Banda-Barragán W. E., Parkin E. R., Federrath C., Crocker R. M., Bicknell G. V., 2016, , 455, 2, 1309

Banerjee R., Vázquez-Semadeni E., Hennebelle P., Klessen R. S., 2009, , 398, 1082

Bania T. M., Lyon J. G., 1980, , 239, 173

Barnard E. E., 1919, , 49, 1

Baschek B., Beltrametti M., Koppen J., Traving G., 1982, , 105, 300

Beichman C. A., Myers P. C., Emerson J. P., et al., 1986, , 307, 337

Benjamin R. A., Danly L., 1997, , 481, 2, 764

Benoît A., Ade P., Amblard A., et al., 2004, , 424, 571

Benson P. J., Ladd E. F., Myers P. C., Campbell B. G., Walmsley C. M., 1988, in Bulletin of the American Astronomical Society, vol. 20, 693

Benson P. J., Myers P. C., 1983, , 270, 589

Benson P. J., Myers P. C., 1989, , 71, 89

Bergin E. A., Alves J., Huard T., Lada C. J., 2002, , 570, 2, L101

Bergin E. A., Tafalla M., 2007, , 45, 339

Berkhuijsen E. M., 1973, , 24, 143

Berné O., Joblin C., Rapacioli M., Thomas J., Cuillandre J.-C., Deville Y., 2008, , 479, L41

Bertoldi F., 1989, , 346, 735

Bertoldi F., McKee C. F., 1990, , 354, 529

Bisbas T. G., Wünsch R., Whitworth A. P., Hubber D. A., Walch S., 2011, , 736, 142

Blitz L., 1993, in Protostars and Planets III, edited by E. H. Levy, J. I. Lunine, 125–161

Bobylev V. V., Bajkova A. T., 2018, Astronomy Letters, 44, 11, 676

Bobylev V. V., Bajkova A. T., 2019, Astronomy Letters, 45, 3, 109

Bolatto A. D., Wolfire M., Leroy A. K., 2013, , 51, 1, 207

Bontemps S., Andre P., Terebey S., Cabrit S., 1996, , 311, 858

Buckle J. V., Fuller G. A., 2002, , 381, 77

Cambrésy L., 1999, , 345, 965

Caselli P., Benson P. J., Myers P. C., Tafalla M., 2002a, , 572, 238

Caselli P., Myers P. C., Thaddeus P., 1995, , 455, L77

Caselli P., Walmsley C. M., Tafalla M., Dore L., Myers P. C., 1999, , 523, 2, L165

Caselli P., Walmsley C. M., Zucconi A., Tafalla M., Dore L., Myers P. C., 2002b, , 565, 1, 344

Cazaux S., Martín-Doménech R., Chen Y. J., Muñoz Caro G. M., González Díaz C., 2017, , 849, 2, 80

Cernis K., 1987, , 133, 355

Chandrasekhar S., Fermi E., 1953, , 118, 113

Chapman N. L., Davidson J. A., Goldsmith P. F., et al., 2013, , 770, 151

Chapman N. L., Goldsmith P. F., Pineda J. L., Clemens D. P., Li D., Krčo M., 2011, , 741, 21

Chen C.-Y., Behrens E. A., Washington J. E., et al., 2020, , 494, 2, 1971

Chen C.-Y., Li Z.-Y., King P. K., Fissel L. M., 2017, , 847, 2, 140

Chen C.-Y., Ostriker E. C., 2018, , 865, 1, 34

Chiang H.-F., Looney L. W., Tobin J. J., 2012, , 756, 168

Chiang H.-F., Looney L. W., Tobin J. J., Hartmann L., 2010, , 709, 470

Chlewicki G., Laureijs R. J., Clark I. O., Wesselius P. R., 1987, in NASA Conference Publication, edited by C. J. Lonsdale Persson, vol. 2466 of NASA Conference Publication, 113–116

Chuss D. T., Andersson B. G., Bally J., et al., 2019, , 872, 2, 187

Ciolek G. E., Basu S., 2000, , 529, 925

Clark F. O., 1991, , 75, 611

Clarke S. D., Whitworth A. P., Duarte-Cabral A., Hubber D. A., 2017, , 468, 2, 2489

Clemens D. P., 2012, , 748, 18

Clemens D. P., Barvainis R., 1988, , 68, 257

Clemens D. P., El-Batal A. M., Cerny C., Kressy S., Schroeder G., Pillai T., 2018, , 867, 1, 79

Cohen M., Kuhi L. V., Harlan E. A., Spinrad H., 1981, , 245, 920

Colín P., Vázquez-Semadeni E., Gómez G. C., 2013, , 435, 1701

Commerçon B., Hennebelle P., Henning T., 2011, , 742, 1, L9

Cox N. L. J., Arzoumanian D., André P., et al., 2016, , 590, A110

Crapsi A., Caselli P., Walmsley M. C., Tafalla M., 2007, , 470, 1, 221

Crutcher R., 2005, in The Magnetized Plasma in Galaxy Evolution, edited by K. T. Chyzy, K. Otmianowska-Mazur, M. Soida, R.-J. Dettmar, 103–110

Crutcher R. M., 2012, , 50, 29

Cudlip W., Furniss I., King K. J., Jennings R. E., 1982, , 200, 1169

Curran R. L., Chrysostomou A., 2007, , 382, 2, 699

Dale J. E., Bonnell I. A., Clarke C. J., Bate M. R., 2005, , 358, 1, 291

Dale J. E., Bonnell I. A., Whitworth A. P., 2007a, , 375, 4, 1291

Dale J. E., Clark P. C., Bonnell I. A., 2007b, , 377, 535

Dale J. E., Ngoumou J., Ercolano B., Bonnell I. A., 2013, , 436, 3430

Dame T. M., Hartmann D., Thaddeus P., 2001, , 547, 2, 792

Davis L., 1951, Physical Review, 81, 5, 890

Davis Jr. L., Greenstein J. L., 1951, , 114, 206

de Avillez M. A., 2000, , 315, 479

de Avillez M. A., Breitschwerdt D., 2005, , 436, 585

de Avillez M. A., Mac Low M.-M., 2001, , 551, 1, L57

del Burgo C., Cambrésy L., 2006, , 368, 3, 1463

Dhabal A., Mundy L. G., Rizzo M. J., Storm S., Teuben P., 2018, , 853, 2, 169

di Francesco J., Evans II N. J., Caselli P., et al., 2007, Protostars and Planets V, 17–32

Di Francesco J., Keown J., Fallscheer C., et al., 2020, arXiv e-prints, arXiv:2010.09894

Dibai E. A., 1958, , 2, 429

Dickens J. E., Irvine W. M., Snell R. L., et al., 2000, , 542, 870

Dickman R. L., 1978, , 37, 407

Ding P.-J., Zhu Z., Liu J.-C., 2019, Research in Astronomy and Astrophysics, 19, 5, 068

Dobashi K., 2011, , 63, S1

Dobashi K., Uehara H., Kandori R., et al., 2005, , 57, S1

Dotson J. L., Vaillancourt J. E., Kirby L., Dowell C. D., Hildebrand R. H., Davidson J. A., 2010a, , 186, 406

Dotson J. L., Vaillancourt J. E., Kirby L., Dowell C. D., Hildebrand R. H., Davidson J. A., 2010b, VizieR Online Data Catalog, J/ApJS/186/406

Draine B. T., 2003, , 41, 241

Draine B. T., 2011, Physics of the Interstellar and Intergalactic Medium

Dunham M. M., Crapsi A., Evans II N. J., et al., 2008, , 179, 249

Dutra C. M., Bica E., 2002, aap, 383, 631

Egan M. P., Shipman R. F., Price S. D., Carey S. J., Clark F. O., Cohen M., 1998, , 494, 2, L199

Elias J. H., 1978, , 224, 857

Elmegreen B. G., 1998, in Origins, edited by C. E. Woodward, J. M. Shull, H. A. Thronson, Jr., vol. 148 of Astronomical Society of the Pacific Conference Series, 150

Elmegreen B. G., Kimura T., Tosa M., 1995, , 451, 675

Elmegreen B. G., Lada C. J., 1977, , 214, 725

Elmegreen B. G., Scalo J., 2004, , 42, 1, 211

Falgarone E., Panis J. F., Heithausen A., et al., 1998, , 331, 669

Falgarone E., Pety J., Hily-Blant P., 2009, , 507, 1, 355

Falgarone E., Pety J., Phillips T. G., 2001, , 555, 1, 178

Federrath C., 2016, , 457, 1, 375

Fehér O., Juvela M., Lunttila T., et al., 2017, , 606, A102

Fiege J. D., Pudritz R. E., 2000a, , 311, 1, 85

Fiege J. D., Pudritz R. E., 2000b, , 534, 291

Field G. B., Goldsmith D. W., Habing H. J., 1969, , 155, L149

Fierlinger K. M., Burkert A., Diehl R., et al., 2012, in Advances in Computational Astrophysics: Methods, Tools, and Outcome, edited by R. Capuzzo-Dolcetta, M. Limongi, A. Tornambè, vol. 453 of Astronomical Society of the Pacific Conference Series, 25

Fischera J., Martin P. G., 2012, , 542, A77

Fleming B., France K., Lupu R. E., McCandliss S. R., 2010, , 725, 159

Franco G. A. P., Alves F. O., 2015, , 807, 5

Froebrich D., 2005, , 156, 2, 169

Fuente A., Martin-Pintado J., Bachiller R., Neri R., Palla F., 1998a, , 334, 253

Fuente A., Martin-Pintado J., Rodriguez-Fernández N. J., Cernicharo J., Gerin M., 2000, , 354, 1053

Fuente A., Martin-Pintado J., Rodriguez-Franco A., Moriarty-Schieven G. D., 1998b, , 339, 575

Fukuda N., Hanawa T., Sugitani K., 2002, , 568, L127

Fukuda N., Miao J., Sugitani K., et al., 2013, , 773, 2, 132

Gaia Collaboration, Brown A. G. A., Vallenari A., et al., 2018, , 616, A1

Gaia Collaboration, Prusti T., de Bruijne J. H. J., et al., 2016, , 595, A1

Galli D., Shu F. H., 1993a, , 417, 220

Galli D., Shu F. H., 1993b, , 417, 243

Gazol-Patiño A., Passot T., 1999, , 518, 748

Geen S., Hennebelle P., Tremblin P., Rosdahl J., 2016, , 463, 3129

Gerin M., Phillips T. G., Keene J., Betz A. L., Boreiko R. T., 1998, , 500, 329

Gold T., 1952, , 112, 215

Goldsmith P. F., 2001, , 557, 2, 736

Goldsmith P. F., Heyer M., Narayanan G., Snell R., Li D., Brunt C., 2008, , 680, 428

Gómez G. C., Vázquez-Semadeni E., Zamora-Avilés M., 2018, , 480, 3, 2939

Goodman A. A., 1995, in From Gas to Stars to Dust, edited by M. R. Haas, J. A. Davidson, E. F. Erickson, vol. 73 of Astronomical Society of the Pacific Conference Series

Goodman A. A., Arce H. G., 2004, , 608, 2, 831

Goodman A. A., Bastien P., Menard F., Myers P. C., 1990, , 359, 363

Goodman A. A., Benson P. J., Fuller G. A., Myers P. C., 1993, , 406, 528

Goodman A. A., Jones T. J., Lada E. A., Myers P. C., 1992, , 399, 108

Goodman A. A., Jones T. J., Lada E. A., Myers P. C., 1995, , 448, 748

Górski K. M., Hivon E., Banday A. J., et al., 2005, , 622, 759

Gould B. A., 1879, Resultados del Observatorio Nacional Argentino, 1, I

Greaves J. S., Holland W. S., Minchin N. R., Murray A. G., Stevens J. A., 1999, , 344, 668

Gregersen E. M., Evans Neal J. I., Mardones D., Myers P. C., 2000, , 533, 1, 440

Gregersen E. M., II N. J. E., 2000, The Astrophysical Journal, 538, 1, 260

Gregori G., Miniati F., Ryu D., Jones T. W., 1999, , 527, L113

Gregori G., Miniati F., Ryu D., Jones T. W., 2000, , 543, 2, 775

Grenier I. A., Lebrun F., Arnaud M., Dame T. M., Thaddeus P., 1989, , 347, 231

Griffin M. J., Abergel A., Abreu A., et al., 2010, , 518, L3

Gu Q., Li H.-b., 2019, , 871, 1, L15

Gueth F., Guilloteau S., Bachiller R., 1996, , 307, 891

Gueth F., Guilloteau S., Dutrey A., Bachiller R., 1997, , 323, 943

Guetter H. H., 1968, , 80, 473, 197

Guetter H. H., Vrba F. J., 1989, , 98, 611

Habart E., Abergel A., Boulanger F., et al., 2011, , 527, A122

Hacar A., Kainulainen J., Tafalla M., Beuther H., Alves J., 2016, , 587, A97

Hacar A., Tafalla M., 2011, , 533, A34

Hacar A., Tafalla M., Kauffmann J., Kovács A., 2013, , 554, A55

Hamaker, J. P., Bregman, J. D., 1996, Astron. Astrophys. Suppl. Ser., 117, 1, 161

Harjunpää P., Kaas A. A., Carlqvist P., Gahm G. F., 1999, , 349, 912

Harjunpaa P., Liljestrom T., Mattila K., 1991, , 249, 493

Haworth T. J., Harries T. J., Acreman D. M., 2012, , 426, 203

Haworth T. J., Harries T. J., Acreman D. M., Rundle D. A., 2013, , 431, 3470

Heiles C., 1969, , 156, 493

Heiles C., 2000, , 119, 923

Heitsch F., 2013, , 776, 62

Heitsch F., Stone J. M., Hartmann L. W., 2009, , 695, 248

Hennebelle P., Falgarone E., 2012, , 20, 55

Hennebelle P., Mac Low M. M., Vazquez-Semadeni E., 2007, arXiv e-prints, arXiv:0711.2417

Hennebelle P., Pérault M., 1999, , 351, 309

Herbig G. H., 1960, , 4, 337

Hernández J., Calvet N., Briceño C., Hartmann L., Berlind P., 2004, , 127, 1682

Heyer M., Dame T. M., 2015, , 53, 583

Heyer M., Goldsmith P. F., Yıldız U. A., Snell R. L., Falgarone E., Pineda J. L., 2016, , 461, 3918

Heyer M., Gong H., Ostriker E., Brunt C., 2008, , 680, 1, 420

Heyer M. H., Vrba F. J., Snell R. L., et al., 1987, , 321, 855

Hildebrand R. H., 1983, , 24, 267

Hildebrand R. H., 1988, , 29, 327

Hildebrand R. H., Dragovan M., Novak G., 1984, , 284, L51

Hiltner W. A., 1949, , 163, 283

Hilton J., Lahulla J. F., 1995, , 113, 325

Hirota T., Ito T., Yamamoto S., 2002, , 565, 1, 359

Hoang T., Lazarian A., 2008, , 388, 1, 117

Hoang T., Lazarian A., 2009, , 697, 1316

Hu E. M., 1981, , 248, 119

Hubble E., 1934, , 79, 8

Hull C. L. H., Plambeck R. L., Bolatto A. D., et al., 2013, , 768, 159

Hull C. L. H., Plambeck R. L., Kwon W., et al., 2014, , 213, 13

Iffrig O., Hennebelle P., 2017, , 604, A70

Inoue T., Inutsuka S.-i., 2009, , 704, 161

Inutsuka S.-i., Inoue T., Iwasaki K., Hosokawa T., 2015, , 580, A49

Inutsuka S.-I., Miyama S. M., 1992, , 388, 392

Inutsuka S.-i., Miyama S. M., 1997, , 480, 2, 681

Jeong I.-G., Kang H., Jung J., et al., 2019, Journal of Korean Astronomical Society, 52, 227

Johnstone D., Bally J., 1999, , 510, 1, L49

Jones R. V., Spitzer Jr. L., 1967, , 147, 943

Jones T. W., Ryu D., Tregillis I. L., 1996, , 473, 365

Kainulainen J., Hacar A., Alves J., Beuther H., Bouy H., Tafalla M., 2016, , 586, A27

Kauffmann J., Bertoldi F., Bourke T. L., Evans II N. J., Lee C. W., 2008, , 487, 993

Kauffmann J., Bertoldi F., Bourke T. L., Myers P. C., Lee C. W., Huard T. L., 2011, , 416, 2341

Keto E., Caselli P., Rawlings J., 2015, , 446, 4, 3731

Kim C.-G., Kim W.-T., Ostriker E. C., 2011, , 743, 1, 25

Kim G., Lee C. W., Gopinathan M., Jeong W.-S., Kim M.-R., 2016, , 824, 2, 85

Kim H. G., Hong S. S., 2002, , 567, 1, 376

Kim H. G., Kim B. G., Jung J. H., 2008, , 8, 6, 686

Kim J.-G., Kim W.-T., Ostriker E. C., 2018, , 859, 68

Kirk H., Johnstone D., Tafalla M., 2007a, , 668, 1042

Kirk J. M., Ward-Thompson D., André P., 2007b, , 375, 3, 843

Kirk J. M., Ward-Thompson D., Crutcher R. M., 2006, , 369, 1445

Kirk J. M., Ward-Thompson D., Di Francesco J., et al., 2009, , 185, 198

Klessen R. S., Heitsch F., Mac Low M.-M., 2000, , 535, 887

Klessen R. S., Hennebelle P., 2010, , 520, A17

Koch E. W., Rosolowsky E. W., 2015, , 452, 3435

Koenig X. P., Allen L. E., Gutermuth R. A., Hora J. L., Brunt C. M., Muzerolle J., 2008, , 688, 1142

Köhler M., Habart E., Arab H., et al., 2014, , 569, A109

Könyves V., André P., Men'shchikov A., et al., 2010, , 518, L106

Könyves V., André P., Men'shchikov A., et al., 2015, , 584, A91

Körtgen B., Banerjee R., 2015, , 451, 3, 3340

Krumholz M. R., Crutcher R. M., Hull C. L. H., 2013, , 767, L11

Kun M., 1998, , 115, 1, 59

Kun M., Balog Z., Kenyon S. J., Mamajek E. E., Gutermuth R. A., 2009, , 185, 451

Kun M., Kiss Z. T., Balog Z., 2008, Star Forming Regions in Cepheus, vol. 4, 136

Kwon W., Fernández-López M., Stephens I. W., Looney L. W., 2015, , 814, 43

Ladd E. F., Hodapp K. W., 1997, , 474, 2, 749

Larson R. B., 1981, , 194, 809

Laureijs R. J., Fukui Y., Helou G., Mizuno A., Imaoka K., Clark F. O., 1995, , 101, 87

Law C. Y., Li H. B., Leung P. K., 2019, , 484, 3, 3604

Lazarian A., 1995, , 453, 229

Lazarian A., 2003, , 79, 881

Lazarian A., Hoang T., 2007, , 378, 910

Lee C. W., Myers P. C., Plume R., 2004, , 153, 2, 523

Lee C. W., Myers P. C., Tafalla M., 1999, , 526, 788

Lee C. W., Myers P. C., Tafalla M., 2001, , 136, 703

Lee H. M., Draine B. T., 1985, , 290, 211

Lee J.-E., Di Francesco J., Bourke T. L., Evans Neal J. I., Wu J., 2007, , 671, 2, 1748

Lemaire J. L., Field D., Maillard J. P., et al., 1999, , 349, 253

Li C., Zhao G., Yang C., 2019, , 872, 2, 205

Li H.-b., Dowell C. D., Goodman A., Hildebrand R., Novak G., 2009, , 704, 891

Li H.-b., Fang M., Henning T., Kainulainen J., 2013, , 436, 4, 3707

Li H. B., Goodman A., Sridharan T. K., et al., 2014, in Protostars and Planets VI, edited by H. Beuther, R. S. Klessen, C. P. Dullemond, T. Henning, 101

Li H.-B., Jiang H., Fan X., Gu Q., Zhang Y., 2017, Nature Astronomy, 1, 0158

Li H.-B., Yuen K. H., Otto F., et al., 2015, , 520, 7548, 518

Lin S.-J., Pagani L., Lai S.-P., Lefèvre C., Lique F., 2020, , 635, A188

Lindegren L., Hernández J., Bombrun A., et al., 2018, , 616, A2

Loinard L., Torres R. M., Mioduszewski A. J., et al., 2007, The Astrophysical Journal, 671, 1, 546

Looney L. W., Tobin J. J., Kwon W., 2007, , 670, L131

López-Corredoira M., Sylos Labini F., 2019, , 621, A48

Lynds B. T., 1962, , 7, 1

Mac Low M.-M., McKee C. F., Klein R. I., Stone J. M., Norman M. L., 1994, , 433, 757

Mac Low M. M., Ossenkopf V., 2000, , 353, 339

Machida M. N., Matsumoto T., Hanawa T., Tomisaka K., 2006, , 645, 2, 1227

Mackey J., Lim A. J., 2011, , 412, 2079

MacLaren I., Richardson K. M., Wolfendale A. W., 1988, , 333, 821

Magakian T. Y., 2003, , 399, 141

Makiwa G., Naylor D. A., van der Wiel M. H. D., et al., 2016, , 458, 2, 2150

Mangum J. G., Emerson D. T., Greisen E. W., 2007, , 474, 2, 679

Mardones D., Myers P. C., Tafalla M., Wilner D. J., Bachiller R., Garay G., 1997, , 489, 719

Matsumoto T., Nakazato T., Tomisaka K., 2006, , 637, L105

Matthaeus W. H., Pouquet A., Mininni P. D., Dmitruk P., Breech B., 2008, , 100, 8, 085003

Matthews B. C., McPhee C. A., Fissel L. M., Curran R. L., 2009, , 182, 143

McCray R., Kafatos M., 1987, , 317, 190

McCutcheon W. H., Vrba F. J., Dickman R. L., Clemens D. P., 1986, , 309, 619

McKee C. F., 1993, in Back to the Galaxy, edited by S. S. Holt, F. Verter, vol. 278 of American Institute of Physics Conference Series, 499–513

McKee C. F., Ostriker E. C., 2007, , 45, 565

McKee C. F., Ostriker J. P., 1977, , 218, 148

McKee C. F., Zweibel E. G., Goodman A. A., Heiles C., 1993, in Protostars and Planets III, edited by E. H. Levy, J. I. Lunine, 327

Melioli C., de Gouveia Dal Pino E. M., de La Reza R., Raga A., 2006, , 373, 2, 811

Mellema G., Arthur S. J., Henney W. J., Iliev I. T., Shapiro P. R., 2006, , 647, 1, 397

Men'shchikov A., André P., Didelon P., et al., 2010, , 518, L103

Miao J., White G. J., Nelson R., Thompson M., Morgan L., 2006, , 369, 143

Miao J., White G. J., Thompson M. A., Nelson R. P., 2009, , 692, 382

Miniati F., Jones T. W., Ryu D., 1999, , 517, 242

Miville-Deschênes M. A., Salomé Q., Martin P. G., et al., 2017, , 599, A109

Morgan L. K., Urquhart J. S., Thompson M. A., 2009, , 400, 1726

Motte F., Andre P., Neri R., 1998, , 336, 150

Mouschovias T., 2001, in Magnetic Fields Across the Hertzsprung-Russell Diagram, edited by G. Mathys, S. K. Solanki, D. T. Wickramasinghe, vol. 248 of Astronomical Society of the Pacific Conference Series, 515

Mouschovias T. C., 1991, , 373, 169

Mouschovias T. C., Ciolek G. E., 1999, in NATO ASIC Proc. 540: The Origin of Stars and Planetary Systems, edited by C. J. Lada, N. D. Kylafis, 305

Mouschovias T. C., Spitzer Jr. L., 1976, , 210, 326

Myers P. C., 1983, , 270, 105

Myers P. C., 2009, , 700, 1609

Myers P. C., Benson P. J., 1983, , 7, 238

Myers P. C., Heyer M., Snell R. L., Goldsmith P. F., 1988, , 324, 907

Myers P. C., Linke R. A., Benson P. J., 1983, , 264, 517

Myers P. C., Mardones D., Tafalla M., Williams J. P., Wilner D. J., 1996, , 465, L133

Nachman P., 1979, , 39, 103

Nakano T., 1984, , 9, 139

Nakano T., 1998, , 494, 587

Neha S., Maheswar G., Soam A., Lee C. W., 2018, , 476, 4, 4442

Neha S., Maheswar G., Soam A., Lee C. W., Tej A., 2016, , 588, A45

Ntormousi E., Burkert A., Fierlinger K., Heitsch F., 2011, , 731, 13

Nutter D., Kirk J. M., Stamatellos D., Ward-Thompson D., 2008, , 384, 2, 755

Odenwald S. F., 1988, , 325, 320

Odenwald S. F., Rickard L. J., 1987, , 318, 702

Offner S. S. R., Klein R. I., McKee C. F., 2008, , 686, 2, 1174

Olano C. A., Meschin P. I., Niemela V. S., 2006, , 369, 2, 867

Onishi T., Mizuno A., Kawamura A., Tachihara K., Fukui Y., 2002, , 575, 2, 950

Ortiz-León G. N., Loinard L., Dzib S. A., et al., 2018, The Astrophysical Journal, 869, 2, L33

Ostriker E. C., Stone J. M., Gammie C. F., 2001, , 546, 980

Ostriker J., 1964, , 140, 1056

Pabst C., Higgins R., Goicoechea J. R., et al., 2019, , 565, 618

Padoan P., Juvela M., Goodman A. A., Nordlund Å., 2001, , 553, 227

Pagani L., Bacmann A., Motte F., et al., 2004, , 417, 605

Pagani L., Lagache G., Bacmann A., et al., 2003, , 406, L59

Pagani L., Pardo J.-R., Apponi A. J., Bacmann A., Cabrit S., 2005, , 429, 181

Palau A., Fuente A., Girart J. M., et al., 2013, , 762, 2, 120

Palmeirim P., André P., Kirk J., et al., 2013, , 550, A38

Passot T., Vazquez-Semadeni E., Pouquet A., 1995, , 455, 536

Pelkonen V. M., Juvela M., Padoan P., 2009, , 502, 3, 833

Peretto N., André P., Könyves V., et al., 2012, , 541, A63

Peretto N., Fuller G. A., 2009, , 505, 1, 405

Pereyra A., Magalhães A. M., 2004, , 603, 584

Perez M. R., Grady C. A., 1997, , 82, 407

Perryman M., 2009, Astronomical Applications of Astrometry: Ten Years of Exploitation of the Hipparcos Satellite Data

Pillai T. G. S., Clemens D. P., Reissl S., et al., 2020, Nature Astronomy

Pineda J. E., Caselli P., Goodman A. A., 2008, , 679, 1, 481

Pineda J. L., Goldsmith P. F., Chapman N., et al., 2010, , 721, 1, 686

Planck Collaboration, Adam R., Ade P. A. R., et al., 2016a, , 586, A135

Planck Collaboration, Ade P. A. R., Aghanim N., et al., 2014, , 571, A1

Planck Collaboration, Ade P. A. R., Aghanim N., et al., 2015a, , 576, A104

Planck Collaboration, Ade P. A. R., Aghanim N., et al., 2015b, Astronomy and Astrophysics, 576, A106

Planck Collaboration, Ade P. A. R., Aghanim N., et al., 2016b, Astronomy and Astrophysics, 586, A138

Planck Collaboration, Ade P. A. R., Aghanim N., et al., 2016c, , 586, A141

Podio L., Codella C., Gueth F., et al., 2016, , 593, L4

Poglitsch A., Waelkens C., Geis N., et al., 2010, , 518, L2

Poidevin F., Ade P. A. R., Angile F. E., et al., 2014, , 791, 1, 43

Poleski R., 2013, arXiv e-prints, arXiv:1306.2945

Polychroni D., Schisano E., Elia D., et al., 2013, , 777, 2, L33

Punanova A., Caselli P., Pon A., Belloche A., André P., 2016, , 587, A118

Purcell E. M., 1979, , 231, 404

Rao R., Crutcher R. M., Plambeck R. L., Wright M. C. H., 1998, , 502, L75

Rapacioli M., Joblin C., Boissel P., 2005, , 429, 193

Rautela B. S., Joshi G. C., Pandey J. C., 2004, Bulletin of the Astronomical Society of India, 32, 159

Rector T. A., Schweiker H., 2013, , 145, 35

Ridderstad M., Juvela M., 2010, , 520, A18

Rizzo J. R., Morras R., Arnal E. M., 1998, , 300, 497

Rosolowsky E. W., Pineda J. E., Kauffmann J., Goodman A. A., 2008, , 679, 2, 1338

Rowell N., Kilic M., 2019, , 484, 3, 3544

Sagar R., Kumar B., Omar A., 2013, ArXiv e-prints

Saha P., Gopinathan M., Kamath U., et al., 2020, , 494, 4, 5851

Sandford II M. T., Whitaker R. W., Klein R. I., 1982, , 260, 183

Sato F., Mizuno A., Nagahama T., Onishi T., Yonekura Y., Fukui Y., 1994, , 435, 279

Scalo J., Elmegreen B. G., 2004, , 42, 1, 275

Scarrott S. M., Rolph C. D., Tadhunter C. N., 1991, , 249, 131

Schnee S., Enoch M., Noriega-Crespo A., et al., 2010, , 708, 1, 127

Schneider S., Elmegreen B. G., 1979, , 41, 87

Schönrich R., Binney J., Dehnen W., 2010, , 403, 4, 1829

Seifried D., Walch S., Haid S., Girichidis P., Naab T., 2018, , 855, 2, 81

Seifried D., Walch S., Weis M., et al., 2020, , 497, 4, 4196

Sharma E., Gopinathan M., Soam A., et al., 2020, , 639, A133

Shu F. H., Adams F. C., Lizano S., 1987, , 25, 23

Snell R. L., 1981, , 45, 121

Snow T. P., McCall B. J., 2006, , 44, 1, 367

Soam A., Lee C. W., Maheswar G., Kim G., Neha S., Kim M.-R., 2017, , 464, 2, 2403

Soam A., Maheswar G., Bhatt H. C., Lee C. W., Ramaprakash A. N., 2013, , 432, 1502

Soam A., Maheswar G., Lee C. W., et al., 2015, , 573, A34

Sohn J., Lee C. W., Park Y.-S., Lee H. M., Myers P. C., Lee Y., 2007, , 664, 928

Soler J. D., 2019, , 629, A96

Soler J. D., Alves F., Boulanger F., et al., 2016, , 596, A93

Soler J. D., Hennebelle P., 2017, , 607, A2

Soler J. D., Hennebelle P., Martin P. G., Miville-Deschênes M. A., Netterfield C. B., Fissel L. M., 2013, , 774, 2, 128

Spezzano S., Bizzocchi L., Caselli P., Harju J., Brünken S., 2016, , 592, L11

Spezzano S., Caselli P., Bizzocchi L., Giuliano B. M., Lattanzi V., 2017, , 606, A82

Spitzer Lyman J., 1990, , 28, 71

Stahler S. W., Yen J. J., 2010, , 407, 2434

Stamatellos D., Whitworth A., 2005, How Well Determined is the Core Mass Function of ρ OPH?, vol. 327, 319

Stamatellos D., Whitworth A. P., Ward-Thompson D., 2007, , 379, 4, 1390

Stephens I. W., Dunham M. M., Myers P. C., et al., 2017, , 846, 1, 16

Stephens I. W., Looney L. W., Kwon W., et al., 2013, , 769, L15

Stone J. M., Norman M. L., 1992, , 390, L17

Stone J. M., Ostriker E. C., Gammie C. F., 1998, , 508, 1, L99

Straizys V., Cernis K., Kazlauskas A., Meistas E., 1992, Baltic Astronomy, 1, 149

Strom K. M., Strom S. E., Vrba F. J., 1976, , 81, 320

Sugitani K., Nakamura F., Tamura M., et al., 2010, , 716, 299

Suzuki T., Ohishi M., Hirota T., 2014, , 788, 2, 108

Tafalla M., Hacar A., 2015, , 574, A104

Tafalla M., Mardones D., Myers P. C., Caselli P., Bachiller R., Benson P. J., 1998, , 504, 900

Tafalla M., Myers P. C., Caselli P., Walmsley C. M., 2004, , 416, 191

Tafalla M., Myers P. C., Caselli P., Walmsley C. M., Comito C., 2002, , 569, 815

Tafalla M., Santiago J., 2004, , 414, L53

Tafalla M., Santiago-García J., Myers P. C., Caselli P., Walmsley C. M., Crapsi A., 2006, , 455, 577

Taylor D. K., Dickman R. L., Scoville N. Z., 1987, , 315, 104

Testi L., Palla F., Prusti T., Natta A., Maltagliati S., 1997, , 320, 159

The P. S., de Winter D., Perez M. R., 1994, , 104, 315

Tomisaka K., 1998, , 502, L163

Tomita Y., Saito T., Ohtani H., 1979, , 31, 407

Trick W. H., Coronado J., Rix H.-W., 2019, , 484, 3, 3291

Tritsis A., Tassis K., 2016, , 462, 4, 3602

Tsamis Y. G., Rawlings J. M. C., Yates J. A., Viti S., 2008, , 388, 898

Umemoto T., Iwata T., Fukui Y., et al., 1992, , 392, L83

Urquhart J. S., Morgan L. K., Thompson M. A., 2009, , 497, 3, 789

Vaillancourt J. E., Chuss D. T., Crutcher R. M., et al., 2007, in Infrared Spaceborne Remote Sensing and Instrumentation XV, vol. 6678 of Society of Photo-Optical Instrumentation Engineers (SPIE) Conference Series, 66780D

Van Loo S., Keto E., Zhang Q., 2014, , 789, 1, 37

Vastel C., Caselli P., Ceccarelli C., et al., 2006, , 645, 2, 1198

Vazquez-Semadeni E., Passot T., Pouquet A., 1995, , 441, 702

Vázquez-Semadeni E., Ryu D., Passot T., González R. F., Gazol A., 2006, , 643, 245

Vrba F. J., Strom S. E., Strom K. M., 1976, , 81, 958

Walsh A. J., Myers P. C., Burton M. G., 2004, , 614, 1, 194

Wang J.-W., Lai S.-P., Eswaraiah C., Clemens D. P., Chen W.-P., Pandey A. K., 2017, , 849, 2, 157

Ward-Thompson D., Kirk J. M., Crutcher R. M., Greaves J. S., Holland W. S., André P., 2000, , 537, L135

Ward-Thompson D., Motte F., Andre P., 1999, , 305, 143

Ward-Thompson D., Sen A. K., Kirk J. M., Nutter D., 2009, , 398, 394

Waters L. B. F. M., Waelkens C., 1998, , 36, 233

Watt G. D., Burton W. B., Choe S. U., Liszt H. S., 1986, , 163, 194

Werner M. W., Uchida K. I., Sellgren K., et al., 2004, , 154, 309

Whittet D. C. B., 2005, in Astronomical Polarimetry: Current Status and Future Directions, edited by A. Adamson, C. Aspin, C. Davis, T. Fujiyoshi, vol. 343 of Astronomical Society of the Pacific Conference Series, 321

Whitworth A., 1979, , 186, 59

Williams J. P., Bergin E. A., Caselli P., Myers P. C., Plume R., 1998, , 503, 689

Williams J. P., de Geus E. J., Blitz L., 1994, , 428, 693

Witt A. N., Gordon K. D., Vijh U. P., Sell P. H., Smith T. L., Xie R.-H., 2006, , 636, 303

Wu Y., Huang M., He J., 1996, , 115, 283

Wu Y., Zhou S., Evans Neal J. I., 1992, , 394, 196

Yan Q.-Z., Zhang B., Xu Y., et al., 2019, , 624, A6

Yonekura Y., Dobashi K., Mizuno A., Ogawa H., Fukui Y., 1997, , 110, 21

Yuan J.-H., Wu Y., Li J. Z., Yu W., Miller M., 2013, , 429, 954

Zamora-Avilés M., Vázquez-Semadeni E., González R. F., et al., 2019, arXiv e-prints

Zhou S., Evans Neal J. I., Koempe C., Walmsley C. M., 1993, , 404, 232

Zhou S., Wu Y., Evans II N. J., Fuller G. A., Myers P. C., 1989, , 346, 168

Zonca A., Singer L., Lenz D., et al., 2019, Journal of Open Source Software, 4, 35, 1298

Zucker C., Chen H. H.-H., 2018, , 864, 152

Zucker C., Speagle J. S., Schlafly E. F., et al., 2019, , 879, 2, 125

Zucker C., Speagle J. S., Schlafly E. F., et al., 2020, , 633, A51

Zuckerman B., Evans N. J. I., 1974, , 192, L149

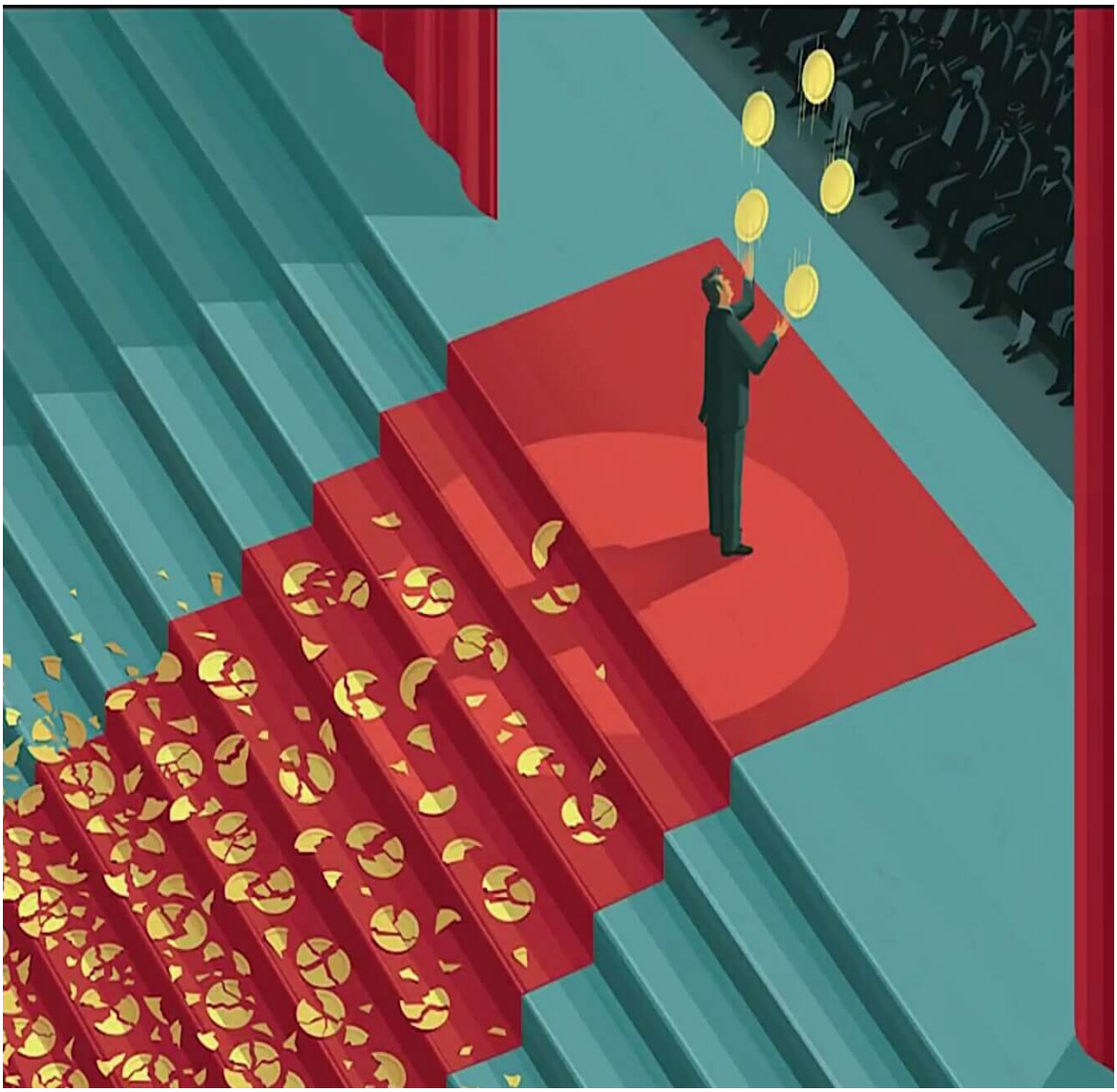

-Lessons learnt from my supervisors